A MICROFLUIDIC PLATFORM TO STUDY REAL-TIME TUMOUR CELL AND

TUMOUR SPHEROID RESPONSE TO CHRONIC AND TRANSIENT HYPOXIA

by

Samantha Marie Grist

B.A.Sc. (Hons.), Simon Fraser University, 2010

A THESIS SUBMITTED IN PARTIAL FULFILLMENT OF

THE REQUIREMENTS FOR THE DEGREE OF

DOCTOR OF PHILOSOPHY

in

THE FACULTY OF GRADUATE AND POSTDOCTORAL STUDIES

(ELECTRICAL AND COMPUTER ENGINEERING)

THE UNIVERSITY OF BRITISH COLUMBIA

(Vancouver)

May 2016

Abstract

Cell-based screening of cancer treatments is used early in the drug development process to test the efficacy and toxicity of treatment candidates prior to animal and human testing. Current cell-based screening methods offer limited predictive capacity, contributing to the high percentage of drugs that fail during the clinical trial stage (80-95% for cancer treatments). One shortcoming of traditional cell-based screening platforms is their inability to recreate many aspects of the natural environment of tumour cells, which can affect treatment response. One important aspect of the microenvironment that can affect cell behaviour and treatment response is oxygenation. Irregular blood vessel formation can cause tumour oxygenation to be much lower than that of surrounding tissue, and spatial and temporal variations in oxygen can be present. Temporal variations can occur at timescales up to several cycles/hour: changes that are too fast to recreate using standard technologies like well plates due to their long diffusion distances.

This thesis presents a novel microfluidic platform to expose cells to both chronic and time-varying oxygen profiles and study their response. Microfluidics technology is combined with 3-D cell culture in tumour spheroids, which can better recreate other aspects of the tumour microenvironment (such as cell-cell and cell-matrix interactions) than traditional 2-D culture. The functionality of the oxygen control device is verified using both finite-element modelling and integrated optical oxygen sensors. Two novel methods for oxygen sensor microfabrication are presented, and the functionality of sensors during long-term experiments is studied. Precise oxygen control is demonstrated using the microfluidic system, with oxygen switching times of <10 minutes. Because 3-D cultures present imaging challenges confounding their data analysis, new, on-chip strategies for improved imaging of 3-D cultures are studied.

Finally, this thesis demonstrates the utility of the platform with preliminary biological experiments. Long-term culture of breast tumour cells is demonstrated, and the response of the cells to oxygen changes is analyzed. The microfluidic platform allowed us to observe for the first time that tumour spheroids can reversibly swell and shrink under changing oxygen conditions. Finally, a preliminary evaluation of the suitability of the platform for drug screening experiments is presented.

Preface

Over the course of my graduate program, I have published two journal papers (with one additional review paper and one further paper in preparation) and seven conference papers/posters as first author or co-first author on my thesis work. Some of the material from these first-author publications has been included in this thesis; this section summarizes the sections in which each publication is included. In the following paragraphs, publications and my contribution to each are listed in the order in which their material first appears in the thesis document. All sections including material from each publication are mentioned in the same paragraph; as such, each publication is only listed once. For cases in which both a conference paper and journal paper were published on related work, both papers are included in the same paragraph. In addition to these publications, during my UBC graduate program I have contributed as a co-author on two further journal papers on the development of the 3-D cultures used in my thesis work, and also published one co-first author journal paper, seven co-authored journal papers, and five co-authored conference papers on projects in areas of electrical/biomedical engineering research unrelated to my thesis work (primarily on silicon photonic biosensors). This work is not included in my thesis; however, these publications are included in the full list of publications to which I contributed during my graduate degree, in Appendix A.

Portions of section 1.1.2 of the Introduction, as well as section 2.5.3 are in preparation as a journal article:

> J1. S. M. Grist[†] and S. S. Nasseri,[†] T. Poon, C. Roskelley, and K.C. Cheung, "On-chip clearing of arrays of 3-D cell cultures and micro-tissues".

S.S. Nasseri and I contributed equally to this work and ran all experiments together. I designed and fabricated the microfluidic devices used in the work and conducted the quantitative data analysis and prepared the manuscript figures. I have written or rewritten all of the introductory material in thesis section 1.1.2, and all of the methods and results in thesis section 2.5.3 with the exception of the sections on cell culture and spheroid preparation and clearing solution preparation. This work was also presented as a conference paper (reproduced with permission from CBMS, Chemical and Biological Microsystems Society) and oral presentation in:

C1. Samantha M. Grist*, S. Soroush Nasseri*, Tak Poon, Cynthia Ni, Calvin Roskelley, and Karen C. Cheung. "μSee3D: On-chip tissue clearing for imaging 3D cell cultures", presented at the 19th International Conference on Miniaturized Systems for Chemistry and Life Sciences (*MicroTAS 2015*), Gyeongju, Korea, 2015.

Portions of sections 1.2 and 1.4 of the Introduction, as well as sections 3.5 and 3.6 and Chapter 4 have been published as a journal article:

J2. S. Grist, J. Schmok, M.-C. Liu, L. Chrostowski, and K. C. Cheung, "Designing a Microfluidic Device with Integrated Ratiometric Oxygen Sensors for the Long-Term Control and Monitoring of Chronic and Cyclic Hypoxia," *Sensors*, vol. 15, p. 20030, 2015.

I designed the system and experiments, conducted the simulations, ran the majority of the experiments and conducted the majority of the data analysis (and supervised those that I did not run and analyze), prepared the figures, and wrote the majority of the manuscript. K. C. Cheung originally wrote the section on "Importance of Precise Oxygen Control in Hypoxia Studies", and I have edited and added to this work. Some of this work was originally presented as a poster:

P1. Samantha M. Grist, Andy Liu, Selim Gawad, Lukas Chrostowski, and Karen C. Cheung. "A microfluidic device with integrated oxygen sensors for the cell-based screening of cancer treatments under transient hypoxia". *SLAS 2015*.

For this poster presentation I ran all of the experiments, analyzed the data, and prepared and presented the poster, and the work won the best poster award at SLAS2015.

A version of section 1.3 and parts of section 1.4 has been published as a review article:

J3. Samantha M. Grist, Lukas Chrostowski and Karen C. Cheung. 2010. "Optical Oxygen Sensors for Applications in Microfluidic Cell Culture". *Sensors* 2010, 10(7).

I conducted the research for this review paper and wrote this manuscript under the supervision of L. Chrostowski and K.C. Cheung.

A version of section 1.3.3.3 of the Introduction as well as section 3.2.2 has been published as a journal article:

J4. S. M. Grist, N. Oyunerdene, J. Flueckiger, J. Kim, P. C. Wong, L. Chrostowski and K. C. Cheung, "Fabrication and laser patterning of polystyrene optical oxygen sensor films for lab-on-a-chip applications," *Analyst*, vol. 139, pp. 5718-5727, Nov 21 2014.

I developed the fabrication process, ran the majority of the experiments and data analysis, wrote the manuscript, and prepared the figures. N. Oyunerdene conducted the laser cutting part of the fabrication process, the AFM measurements were conducted with J. Flueckiger and the ToF-SIMS studies and analysis were run by J. Kim and P. C. Wong using samples prepared and treated by me.

A version of sections 2.3 and 2.4 was published in a conference paper and poster presentation (reproduced with permission from CBMS, Chemical and Biological Microsystems Society):

C2. Samantha Grist[*], S. Soroush Nasseri[*], Tak Poon, Meng-Chi (Andy) Liu, Calvin Roskelley, and Karen C. Cheung. "Two-photon imaging for long-term tumour model monitoring in a microfluidic device", presented at the 19th International Conference on Miniaturized Systems for Chemistry and Life Sciences (*MicroTAS 2015*), Gyeongju, Korea, 2015.

S. S. Nasseri and I contributed equally to this work and ran the experiments together. I designed the device, was involved with all of the experiments and data analysis, and wrote the majority of the manuscript and prepared the figures.

A version of section 2.5.2 was also published in a conference paper and poster presentation (reproduced with permission from CBMS, Chemical and Biological Microsystems Society):

C3. S. M. Grist*, E. Cheng*, L. F. Yu, and K. C. Cheung, "Modulated two-photon imaging of whole spheroids for three-dimensional cell cultures", presented at the 18th International Conference on Miniaturized Systems for Chemistry and Life Sciences (*MicroTAS 2014*), San Antonio, Texas, 2014.

E. Cheng and I contributed equally to this work and ran all of the experiments together. I was involved in all experiments, developed the quantitative data analysis scripts, and wrote the majority of the manuscript and prepared the figures.

A version of section 3.2.1 has been previously published as a conference paper and poster (reproduced with permission from CBMS, Chemical and Biological Microsystems Society):

C4. Samantha M. Grist, Lukas Chrostowski, Karen C. Cheung, "Thin film patterning using a water-soluble etch mask", The 16th International Conference on Miniaturized Systems for Chemistry and Life Sciences (*MicroTAS 2012*), Okinawa, Japan, October 26-November 1, 2012.

I developed the fabrication process, ran all experiments and data analysis, and wrote the manuscript under the supervision of L. Chrostowski and K. C. Cheung.

Portions of section 3.4.1 have been presented as a conference paper and oral presentation:

C5. Samantha M. Grist, Selim Gawad, Carmen Bayly, Linfen Yu, Lukas Chrostowski, and Karen C. Cheung. "3D Cell culture with integrated oxygen control and measurement". Proceedings of the Canadian Medical and Biological Engineering Conference 2014 (*CMBEC37*). 2014. 862909-862909-14.

I developed the system and ran the majority of the experiments, conducted the data analysis, wrote the manuscript, and prepared the figures for this publication. This paper was awarded third place in the best student paper competition at CMBEC37.

A part of section 5.2.1 has been published as a conference paper and poster (reproduced with permission from CBMS, Chemical and Biological Microsystems Society):

C6. Samantha M. Grist, Jonathan C. Schmok, S. Soroush Nasseri, Meng-Chi (Andy) Liu, Lukas Chrostowski, and Karen C. Cheung. "A Microfluidic Platform to Study Real-time Tumour Spheroid Response to Chronic/Transient Hypoxia", presented at the 19th International Conference on Miniaturized Systems for Chemistry and Life Sciences (*MicroTAS 2015*), Gyeongju, Korea, 2015.

I developed the system, ran the experiments, conducted the majority of the data analysis, wrote the manuscript, and prepared the figures for this publication.

The off-chip characterization of the effects of doxorubicin on monolayer and spheroid viability (Figure 5.15) was carried out by S. Soroush Nasseri. I helped to design the experiment, analyzed the data, and created the figure.

Table of Contents

List of Tables

List of Figures

List of Abbreviations

Abbreviation	Definition
2-D	Two-dimensional
2-P	Two-photon (microscopy)
3-D	Three-dimensional
AFM	Atomic force microscopy
BABB	Benzyl alcohol and benzyl benzoate; a tissue clearing solution
BE	Bead edge
CCD	Charge-coupled device
CLARITY	Tissue clearing protocol which supports the tissue with a hydrogel matrix while removing the lipids using electrophoresis or detergents
$Clear^T$, $Clear^{T2}$	Tissue clearing protocols using formamide ($Clear^T$) or formamide and polyethylene glycol ($Clear^{T2}$)
DIC	Differential interference contrast
DMEM	Dulbecco's modified Eagle's medium
DPBS	Dulbecco's phosphate buffered saline
EGFP	Enhanced green fluorescent protein
FBS	Fetal bovine serum
FRUIT	Tissue clearing protocol using fructose and urea
FUCCI	Fluorescence ubiquitination cell cycle indicator
GFP	Green fluorescent protein
GUI	Graphical user interface
HBSS	Hank's balanced salt solution
HIF	Hypoxia-inducible factor
LED	Light-emitting diode
LoB	Limit of blank
LoD	Limit of detection
MCF-7	Michigan Cancer Foundation; breast cancer cell line
MFY	Macrolex fluorescent yellow
NA	Numerical aperture
NMuMG	Normal murine mammary gland (cell line)
PBS	Phosphate buffered saline
PDMS	Poly (dimethylsiloxane); silicone elastomer
PEBBLE	Probes encapsulated by biologically localized embedding
PMT	Photomultiplier tube

PS	Polystyrene
PtOEPK	Platinum(II) octaethylporphyrin ketone; a luminescent oxygen-sensitive indicator dye
PtTFPP	Platinum (II)-5,10,15,20-tetrakis-(2,3,4,5,6-pentafluorphenyl)-porphyrin; a luminescent oxygen-sensitive indicator dye
PVA	Polyvinyl alcohol
RI	Refractive index
RPMI	Roswell Park Memorial Institute; cell culture media
SeeDB	See Deep Brain: a fructose-based tissue clearing protocol
SPIM	Single-plane illumination microscopy
VEGF	Vascular endothelial growth factor
YFP	Yellow fluorescent protein

Acknowledgements

First and foremost, I am immensely grateful to my supervisors, Professor Karen C. Cheung and Professor Lukas Chrostowski, for their support, advice, and encouragement as I undertook this unique and fascinating project. I sincerely appreciate having had the opportunity and freedom to learn from them and work in so many different areas during my PhD, including optics, microfabrication, biology, and photonics. I am also grateful to Professor Boris Stoeber and Professor Shuo Tang, who have served on my departmental committee and asked many important questions over the past few years that have helped to shed insight into various aspects of this project, as well as Professor Cyril Leung for serving as the chair of my departmental defense. I also wish to sincerely thank Professor Kevin Bennewith and Professor James Piret for their valuable feedback when serving as committee members, Professor Torsten Mayr for his beneficial comments and suggestions as external examiner, and Professor William Jia for serving as the chair of my university defense.

I am very lucky to have received graduate funding during my PhD, and offer my gratitude to all of the agencies that have recognized my work and granted me scholarships and fellowships as well as travel funding over the past 6 years: the Natural Sciences and Engineering Research Council of Canada, the Canadian Breast Cancer Foundation – BC/Yukon Region, the Killam Trusts, UBC, the UBC Department of Electrical and Computer Engineering, ICICS, the Society for Lab Automation and Screening, and the Canadian Cancer Society. I am also grateful to CMC microsystems for providing funding to aid in the microfabrication processes undertaken during my graduate program, as well as for providing various software tools and services that were used as a part of this project.

I also wish to recognize all of my co-authors and collaborators on the work that led to this thesis. Many of the cell culture experiments were carried out with S. Soroush Nasseri and Dr. Loïc Laplatine, and I am truly grateful for their assistance and collaboration and have greatly enjoyed working with and learning from them during the course of this project. I also sincerely thank Jonathan C. Schmok for his assistance in running sensor calibration and measurement experiments as well as his significant contributions to various data analysis scripts as well as the software for the microscope automation system. The cell-based experiments undertaken as a part

Chapter 1 Introduction

1.1 Platforms for *in vitro* Screening of Cancer Treatments

Cell-based drug screening methods are used early in the drug development process to identify potential cancer treatments by studying effects such as changes in cell phenotype in response to the potential treatment [1]. The purpose of these early stages of screening is to identify drug candidates and determine their efficacy and safety before proceeding to the later stages of screening in animal models and clinical trials. Cell-based screening involves testing drug candidates on human primary cells or immortalized cell lines in *in vitro* environments and analyzing the cells' response to the drug. The ideal cell-based screening method would accurately predict the results of the later stages of testing, in order to minimize the resources wasted on drug candidates that ultimately prove to be ineffective or unsafe. This is a challenging goal to achieve because many different things can affect a tumour's response to a drug, including the environment around the cells. Traditional screening platforms are lacking in their predictive ability, as is evidenced by the high attrition rate during the clinical trial stages of testing (80% [2] to 95% [3] of the cancer treatment candidates that enter phase I clinical trials never make it to market authorization). As a result, there has been much analysis as to why current screening methods offer limited predictive utility as well as how they may be improved [2-4].

1.1.1 Traditional Platforms: 2-D Cell-Based Screening

Traditional *in vitro* screening of cancer treatments has used assays in which the treatments are tested on cells that are grown in two-dimensional (2-D) monolayers in environments like petri dishes. The treatments are commonly tested by their ability to kill or stop the proliferation of immortalized cell lines that proliferate in an unrestrained manner [4]; as a result, many traditional cancer therapies target the proliferative abilities of cancer cells. More recent development has also focused on targeted cancer therapies, which target specific genetic subtypes of cancer with the goal of producing more personalized cancer treatments [5]. Although this method has yielded great successes, such as imatinib to target a phenotype of chronic myeloid leukemia, targeted drugs are not always found to be effective in clinical trials because the binding of the drug to the target does not always have the intended effect in a more complex system [4]. Phenotypic screening, where the effects of a drug on the cell phenotype (or observable trait that is determined by genetics) is observed, can be combined with targeted drug

development and is thought to offer the potential for improved clinical relevance because it identifies only drug-target interactions that have an observable effect on cell phenotype [4].

Another method that has been used since the 1990s is high-throughput drug screening. This method involves screening vast libraries of compounds (hundreds of thousands to millions of compounds) for their activity on a specific target, and has led to many impressive technological improvements such as automation and low-volume assays [6]. High-throughput screening is applicable to a wide range of targets as well as phenotypic screening because it does not require prior understanding of how a compound of interest could interact with the target [6], but it requires impressive parallelization and data analysis capabilities.

Many current assays are limited because drugs' mechanisms of action are sometimes not well understood, targets can work differently in cells within a patient's tumour than in a molecular assay or immortalized cell line, and the actual response of the cell may not be reflected in the single parameter measured [2, 4]. Additionally, tumours can be highly heterogeneous, with different cell phenotypes and different environmental conditions present [4]. Both the characteristics of the cells themselves and the cells' environmental conditions (such as cell-cell and cell-matrix interactions, limitations in drug, oxygen, and glucose delivery, and other factors) can affect their response to the drug. Because traditional, monolayer-based testing cannot reproduce and control these kinds of heterogeneous conditions it is limited in its predictive capability. This means that the ideal cell-based screening assay would use the most relevant types of cells (likely primary tumour cells), expose them to environmental conditions similar to those they experience in tumours, and measure multiple things (viability, protein expression, etc.) within the cells to determine if the drug has the intended effect [2]. More sophisticated cell-based models incorporating aspects of the tumour microenvironment have the potential to form more predictive cell-based assays [4]. These improved, more clinically-relevant models could be combined with other methods such as high-content analysis (where many features within individual cells such as proteins, RNA, and cellular features are analyzed using automated fluorescence microscopy and image processing to extract quantitative data regarding the effects of drugs [7]) to even further improve the predictive ability of cell-based screening [4].

1.1.2 3-D Cell Cultures as Tissue Models

One method of producing more sophisticated cell-based models is the use of three-dimensional (3-D) cell culture. Many factors (including cell-cell and cell-extracellular matrix signalling) influencing cell behaviour are not reproduced in the 2-D monolayer cell cultures commonly employed in traditional screening assays. In contrast, three-dimensional (3-D) cell cultures have the potential to better replicate *in vivo* responses [8]. Another shortcoming of conventional 2-D cultures is their inability to emulate the complex environment existing in the tumour, including spatially and temporally varying levels of drugs and other environmental parameters. An attractive aspect of 3-D cell culture models is their ability to permit cell growth in multicellular spheroids, which can mimic solid tumours [9, 10]. These spheroids can mimic the *in vivo* tumour environment in several ways that the monolayer cultures cannot, including the formation of diffusion gradients in the concentration of drugs and other environmental parameters [11]. These differences lead spheroids to demonstrate higher resistance to anticancer drugs and radiation than monolayers [12].

One important environmental parameter that is known to have a substantial effect on tumour response to treatment, and also forms diffusion gradients within tumour spheroids, is oxygen. Tumours can contain hypoxic, or low-oxygen, regions, which contain cells that can exhibit different behaviour and response to treatment. Multicellular tumour spheroids can also act as models for solid tumours containing hypoxic, quiescent cells [13]. Cellular spheroids are formed by many types of cells and can be large (> 500 μm) masses of cells with a hypoxic or necrotic core formed due to diffusion limitations (of oxygen, glucose, or other nutrients) within the spheroid [14]. Hypoxic cores have been observed in small (100 μm) human osteosarcoma spheroids in normoxic culture [15] using two-photon imaging of hypoxia-responsive element (HRE) activity (mediated by hypoxia-inducible factor (HIF) activation) resulting in enhanced green fluorescent protein (EGFP) fluorescence, while necrotic cores have been observed at diameters of 600 μm in LNCaP (prostate cancer cell) spheroids [16] using embedding and physical sectioning of spheroids. The disadvantage of these large spheroids is that they present a significant imaging challenge.

1.1.2.1   Data Readout Challenges for 3-D Cultures

In order to quantify the results of image-based drug screening assays employing 3-D cell cultures, it is necessary to label (for viability, hypoxia-inducible factors, autophagosomes, or other effects) and image the cultures in 3-D. Imaging the spheroids presents several advantages over non-image-based assays such as those based on the reduction of tetrazolium or resazurin (e.g. MTT, MTS tetrazolium reduction assays), including the ability to observe heterogeneities within spheroids, and the compatibility with high-content screening, in which several features within the same cells are analyzed simultaneously [17, 18]. Image-based screening methods also require fewer cells to obtain a measurement than other types of assays.

Staining of the spheroids can be subject to dye penetration limitations (where the stain is unable to reach all the cells within the 3-D culture), and even with perfect stain penetration, 3-D imaging of cell spheroids is difficult because they are highly scattering [19] due to their inhomogeneous refractive indices, as well as potentially absorbing (although the scattering coefficient (μ_s) of tumour spheroids has been quantified to be much higher than the absorption coefficient (μ_a) by Hargrave *et al.*: $\mu_s = 90\text{-}160$ mm^{-1} vs. $\mu_a = 0.1\text{-}0.4$ mm^{-1} [20]). Imaging through the spheroid to the necrotic region of a 600 μm spheroid would require imaging through 300 μm of cells, which is challenging for most methods of optical sectioning light microscopy. Our group has previously observed image degradation with depth even in small (~80 μm) spheroids stained with the fluorescent DNA-binding stain DAPI; even at depths of 66 μm the fluorescence intensity in confocal microscopy had degraded such that the images yielded were no longer usable for the extraction of cell numbers and other data. An illustration of how the scattering properties of spheroids affect their transmitted light and confocal imaging is presented in Figure 1.1.

Scattering (as well as absorption, to a lesser extent) within the spheroid causes the centres of the spheroids to appear darkened and opaque in transmitted light imaging, and also causes confocal fluorescence images to have nonuniform intensities through the z-stack. Individual slices of the spheroid in the z-stack also often show darkened centres, as the light must travel a longer optical path through the spheroid to image those points than those near the edges. Finally, in addition to

the nonuniform intensities in the z-stack and individual slices, scattering also causes blurring of the image features within the spheroid.
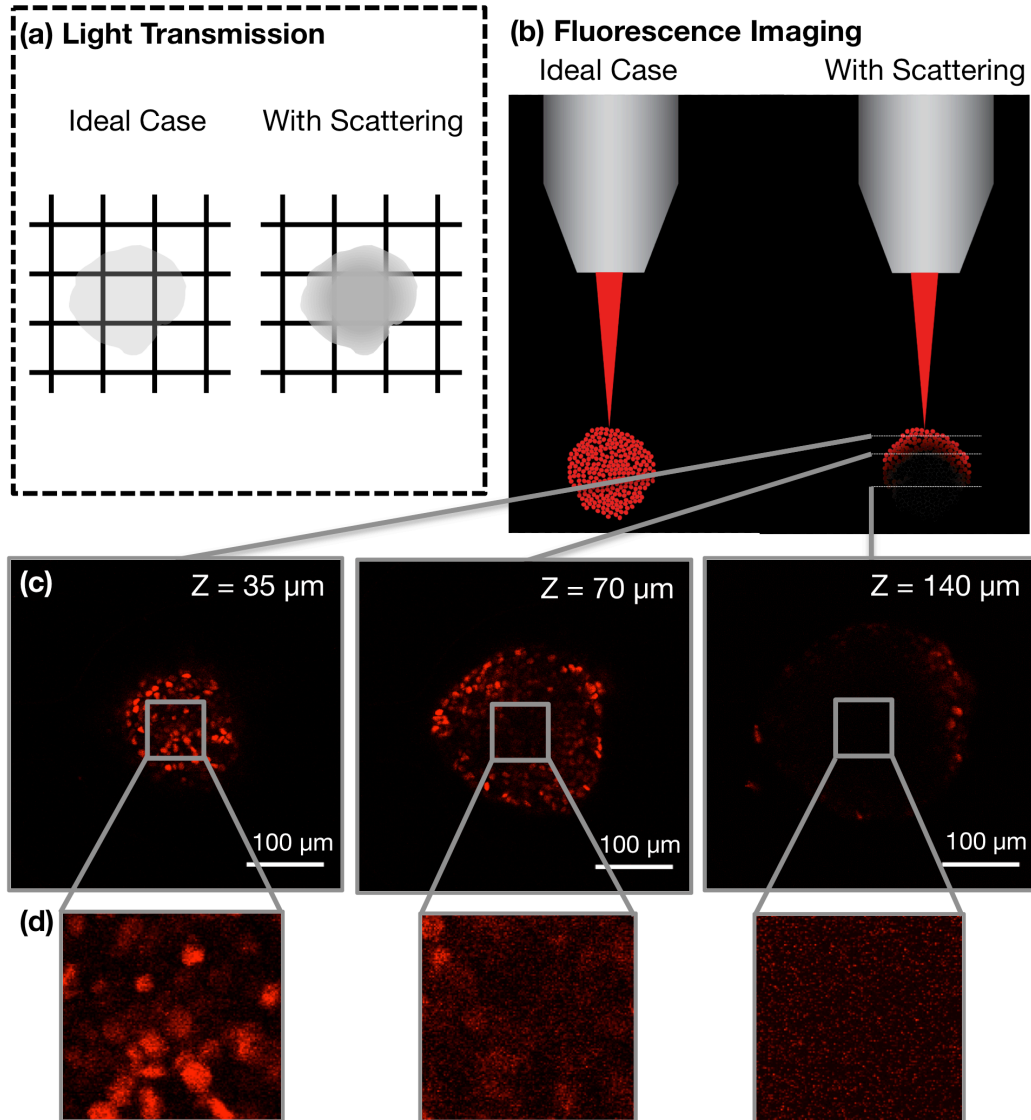
Figure 1.1. Effects of scattering on light transmission and confocal or two-photon fluorescence imaging. **(a)** Illustration showing that scattering causes the spheroid centre to appear dark and opaque in transmitted light imaging. **(b)** Illustration depicting confocal or two-photon fluorescence imaging of a spheroid with and without scattering. In an ideal system with no scattering or absorption, fluorescence intensity would be constant through the depth of the spheroid. Scattering causes nonuniform image intensity in confocal and two-photon fluorescence imaging, with fluorescent cells positioned a longer optical path from the objective appearing dimmer than those closer to the objective. **(c)** Insets show two-photon fluorescence image slices at different depths into a tumour spheroid expressing a fluorescent protein that makes cell nuclei fluoresce orange. Although at 35 μm depth the fluorescence intensity is fairly uniform across the spheroid cross-section, at 70 μm depth the centre of the spheroid appears darker than the edges. At 140 μm into the spheroid, most of the fluorescence intensity is lost. **(d)** In addition to the intensity nonuniformity, scattering also causes blurring of the features in the cross-sectional images, with nuclei in the centre of the spheroid much less well resolved in slices deeper into the spheroid. Cell nuclei in these images express a fluorescent cell cycle reporter, as will be described in section 2.5.1.1.

Histological sectioning, confocal microscopy, multi-photon microscopy, and single-plane illumination microscopy (SPIM), or light sheet microscopy, have all been previously used to image through large cell spheroids [11]. Histological sectioning (embedding the sample in resin or paraffin and subsequently slicing the sample and imaging the physically-sliced sections) is laborious and time-consuming, and can only be used for endpoint analysis. SPIM, which relies on a single-plane 'light sheet' illumination from the side of the sample and measurement with an orthogonal objective from the top or bottom, is the current gold standard for spheroid imaging due to its excellent sample penetration, the possibility for illumination from both sides of the sample, and the further possibility for sample rotation and imaging from multiple different views [11]. The main disadvantages of SPIM systems are that they are currently less readily available than standard confocal systems and they require specialized sample preparation techniques to facilitate the orthogonal microscope arrangement.

Two-photon microscopy, which relies on the excitation of a fluorophore by two photons of twice the excitation wavelength, has the potential to improve the sample penetration depth of scanning laser confocal microscopy. In two-photon microscopy, two photons of approximately double the fluorophore's excitation wavelength are absorbed nearly simultaneously (within $\sim 10^{-16}$s [21]); this requirement for nearly simultaneous absorption of the two photons necessitates a very high incident intensity for the phenomenon to take place. Because of this requirement, two-photon fluorescence has a quadratic dependence on incident light intensity rather than the linear dependence of single-photon confocal [21]. In order to increase the probability of two photons simultaneously interacting with the sample, a mode-locked pulsed laser is used along with spatial focusing of the incident beam [21, 22].

Two-photon microscopy offers increased sample penetration due to three unique properties of the use of two simultaneous higher wavelength photons to excite the sample: lessened sample absorption of the two-photon excitation light due to its longer wavelength outside of the absorption spectrum (and lessened intensity outside of the focal plane makes two-photon absorption in other regions of the sample highly unlikely); higher wavelengths of light are less susceptible to optical scattering; and any excitation scattering that does occur has a reduced

6

impact on the final image due to the lowered probability of excitation [22]. This effective 'single-point excitation' can be defined by the diffraction-limited resolution of the objective lens (assuming approximately even excitation laser intensity over the full aperture of the lens) [23, 24]. The diffraction-limited resolutions (1/e radii) are given by equation 1 for high-numerical aperture (NA = 0.7-1.4) objective lenses [21, 23].

$$\omega_{xy} = \frac{0.325\lambda}{\sqrt{m}NA^{0.91}}, \qquad \omega_z = \frac{0.532\lambda}{\sqrt{m}} \left(\frac{1}{n - \sqrt{n^2 - NA^2}}\right), \qquad (1)$$

where ω_{xy} is the diffraction-limited image resolution in the x-y plane and ω_z is the diffraction-limited image resolution in the z-direction. NA is the numerical aperture of the objective lens, λ is the excitation laser wavelength, n is the refractive index of the lens immersion medium, and m is the excitation order (2 for two-photon).

Two-photon microscopy has been used to image spheroids of various sizes and permitted visualization up to depths of 200-250 μm [13, 25]. It has also been found to yield significantly improved penetration into small (100 μm) spheroids than conventional confocal microscopy [15] and has been used for monitoring drug penetration into spheroids [19]. Another significant advantage of two-photon microscopy, also stemming from its single-point excitation, is its reduced photobleaching of the sample as compared to confocal microscopy [21, 22].

Although two-photon microscopy offers several significant advantages over standard confocal microscopy, two photon microscopes are still less widely available and more expensive than standard confocal microscopes. For applications in high-throughput drug testing, it would be beneficial if the methods used to image the spheroids under test could be adapted and used in a wide variety of industrial and academic environments, and standard confocal is currently the most widely-available standard tool for 3-D microscopy. Confocal microscopy has previously been adapted and optimized for spheroid imaging using water immersion objectives, glass-bottom culture dishes, and laser intensity modulation [26]; using these methods, confocal images down to depths of 320 μm were demonstrated to be analyzable to determine fluorescent protein expression as a function of cell position within the spheroid.

1.1.2.2   Tissue Clearing to Improve Data Readout

Although the use of improved imaging techniques such as SPIM and two-photon microscopy can improve tissue imaging results, even two-photon image quality can be degraded by scattering at imaging depths of ~100 μm. This is a limitation in drug-screening assays, as it restricts the data that can be acquired from inside the cultures without spheroid dissociation. The spheroid microenvironment (like the tumour microenvironment) is heterogeneous, with diffusion gradients of oxygen, nutrients, and drugs. As a result, to fully take advantage of the ability of spheroids to reproduce these effects, it is necessary to obtain data from cells in the various regions of the spheroid. If the imaging depth is limited to 100 μm, cells that are exposed to deficiencies in oxygen, nutrients, or drugs may not be imaged, as the necrotic core regions may not develop until the spheroid reaches ~600 μm in diameter [14]. Although the degradations in image quality that limit the usable imaging depth are due to both scattering and sample absorption, scattering is the dominant effect in tumour spheroid samples.

To address imaging challenges posed by the scattering properties of tissue, a wide array of tissue clearing protocols have been developed and studied; some of the methods and improvements of tissue clearing were reviewed in 2013 by Tuchin *et al.* [27]. These tissue-clearing protocols improve image quality by modifying the optical properties of the tissue in order to reduce scattering effects. Because scattering originates from the refractive index discontinuity within the sample (and largely between the lipid membranes and the media), two main methods have been proposed [28] to clear the tissue: removing the lipids from the tissue, and matching the higher refractive index of the lipids using refractive index matching solutions.

CLARITY is one recently proposed clearing method that supports the tissue within a hydrogel matrix while removing the lipids using electrophoresis [29]. The CLARITY protocol has also been modified to permit lipid extraction using strong ionic detergents, eliminating the need for electrophoresis [30]. A great many other clearing methods have been proposed that operate by matching the tissue refractive index (RI, may also be denoted *n* elsewhere). Glycerol (RI = 1.47) has long been used for clearing, and benzyl alcohol and benzyl benzoate (BABB, RI = 1.56) [31] has also been demonstrated to clear brain tissues; however, these quench many fluorescent proteins because the fluorescence of these proteins is dependent on the presence of water [32].

Additionally, BABB can also interfere with the function of immunofluorescent labels and lipophilic carbocyanine dyes [33].

Other clearing methods have been developed in an effort to preserve the signal from fluorescent proteins. The Sca*l*e process [34] relies on urea to clear tissues and promote tissue hydration; the most effective Sca*l*e solution (Sca*l*eA2, RI≈1.38) contains 4M urea, 10% glycerol (intended to prevent excess hydration and sample swelling), and 0.1% Triton-X-100 detergent. Sca*l*e preserves yellow fluorescent protein (YFP) and other fluorescent protein fluorescence, but requires long incubations of up to two weeks and causes significant sample swelling. A sorbitol-based variation of Sca*l*e (Sca*l*eS) has recently been proposed to address these issues [35]. Another method, named See Deep Brain, or SeeDB, uses increasing concentrations of fructose in water to match the refractive index of tissue [32]. The SeeDB fructose solutions (with a final step of saturated fructose in water at 25°C, RI = 1.49) preserve the fluorescence of both fluorescent proteins and lipophilic dyes, and the full SeeDB process is much faster than the Sca*l*e process (days vs. weeks). Additionally, SeeDB was found to not cause sample volume changes in the brain tissues for which it was developed, unlike Sca*l*e, which causes significant swelling. One limitation of SeeDB is the very high viscosity of its higher concentration steps, which can make solution exchange challenging. Further improving upon the clearing speed, the Clear^T and Clear^{T2} protocols use formamide solutions to clear tissues in a process that only requires hours-long incubations [33]. Clear^T results in excellent clearing with morphological preservation and the preservation of lipophilic dyes using only formamide as the clearing agent, while Clear^{T2}, again based on formamide but with the addition of polyethylene glycol (PEG) to stabilize protein conformation, offers slightly reduced clearing with the advantage of preservation of fluorescent proteins and immunohistochemical labels.

Other recent work has combined elements of these clearing protocols to improve upon these clearing processes. FRUIT combines fructose and urea to decrease solution viscosity compared to SeeDB while limiting the sample expansion caused by the urea [36]. CUBIC, which is designed to prepare whole-body or whole-organ samples for light-sheet microscopy, uses a multi-day two-step clearing process employing hydrophilic reagents based upon Sca*l*e to stabilize fluorescent proteins: first removing the lipids using an aqueous solution of 25 wt% urea,

25 wt%, and 15 wt% Triton X-100; and subsequently matching the refractive index using an aqueous solution of 25 wt% urea, 50 wt% sucrose, and 10 wt% triethanolamine (RI ≈ 1.49) [28].

Most of the aforementioned tissue clearing protocols have been developed to clear neurological tissues and mouse brains; however, different tissue types may have different clearing results and optimal protocols. For example, Boutin and Hoffman-Kim recently compared Clear^{T2}, Sca*l*e, and SeeDB on tissue-engineered neural sphere samples [37]. Although the original demonstration of SeeDB on murine neonatal brain and adult hemi-brain samples showed minimal sample volume change, Boutin and Hoffman-Kim found significant shrinkage in their SeeDB-treated neural sphere samples. It is thus crucial to test different clearing protocols on the tissue of interest, while monitoring the sample during the process could give greater insight as to the effects of each protocol.

There has been very limited work on adapting these clearing protocols to microtissues within a microfabricated device. Das *et al.* have investigated the use of a commercial clearing agent optimized for pancreatic tissue, FocusClear®, on porcine pancreas tissue cores [38]. They fabricated a millimetre-scale custom chamber from glass microscope slides in which to clear a 40-600 μm thick section of tissue with millimetre-scale area. Clearing in the device yielded greatly improved light transmittance and allowed the authors to image pancreatic islet structures in the tissue; however, only one tissue section could be cleared at a time.

1.1.3 Microfluidic Cell Culture

Microfluidic systems (defined as networks of fluidic channels with sub-millimeter dimensions) present one method for improving drug screening platforms because their small size scales facilitate parallelization, spatiotemporal control of chemical concentrations, and the integration of multiple reaction steps within a single device [39]. Additionally, microfluidic models can consume less reagents and are able to reproduce more realistic ratios of cell volume to media volume, or cell volume to scaffold/extra-cellular matrix volume than many traditional models [40]. Microfluidic systems for drug screening have been reviewed by Neuzi *et al.* [41]. These microfluidic advances include devices with connected chambers designed to model the interaction between drugs and different tissues in the body (for example toxicities of drugs and

their metabolites on different tissues) [42], as well as the development of sophisticated 'organs-on-chip', which can create on-chip models of different diseases by modeling mechanical and chemical characteristics of environments in the body, as well as interactions between cell types. Bhatia and Ingber [43] have summarized the development of these 'organ-on-chip' devices in a recent perspective. The enhanced control offered by these types of microfluidic systems (reproducing aspects of more complicated biological systems in a controlled fashion [41]) facilitates the development of more realistic models that can hopefully help us to understand the roles that various aspects of the microenvironment and body systems play in drug response.

Our research group has developed hydrogel-based microfluidic environments for 3-D cell-based drug screening [44-47]. One such work demonstrated on-chip culture of breast tumour cells in size-controlled alginate droplets, cross-linked to form beads which may be immobilized and studied in microfluidic devices [44]. Multicellular spheroids as well as multicellular resistance to doxorubicin in comparison with standard monolayer cultures were observed, similar to results reported in the literature [48, 49]. These droplet-scale cultures present an attractive option for on-chip 3-D cell culture because they afford control over the size of tumour spheroids formed in the device. The beads can be trapped inside a microfluidic chip that is constantly perfused with media, permitting the transport of nutrients, treatments, and waste products to and from the cells. Because the presence of hypoxia in tumours has a major effect on the response of the tumour to treatment, integrating oxygen control into these drug-testing environments could further improve the platform's ability to predict *in vivo* results.

1.2   Hypoxia and Cancer

Tissue hypoxia (or inadequate oxygen levels) in tumours is known to contribute to radiation therapy and anticancer drug resistance, both by reducing the lifetime of free radicals employed by the therapies to cause DNA damage as well as by inducing changes within the cells that increase their resistance [50, 51]. Although hypoxia is often defined as oxygen levels below 8-10 mm Hg (1.05-1.32% of 1 atm), levels below 25-30 mm Hg (3.29-3.95%) have been shown to significantly reduce the efficacy of treatment by X- and γ-radiation as well as certain immunotherapies [50]. Hypoxia is often present within solid tumours because the fast proliferation of tumour cells leads to abnormal vasculature; cells are often present in tumours too

far from blood vessels to receive adequate oxygen supply [52, 53]. Cancer can also result in anemia or other issues that can lead to a reduced ability of blood to carry oxygen [50]. Furthermore, blood vessels in tumours can become blocked and then potentially reopened, leading to cycles of intermittent or transient hypoxia and reperfusion [54-57] that can promote tumour aggressiveness [58]. These cycles can occur at a time scale of approximately 2-5 cycles per hour [59, 60], but traditional cell culture environments such as stationary well plates can only reproduce cycles on the order of hours because of the large distances through which oxygen needs to diffuse through media to reach the cells [61]. The use of microfluidic systems with comparatively smaller diffusion distances, or stirred cultures with convective as well as diffusive transport can address this challenge. Another drawback to the use of traditional culture environments is their use of plastics such as polystyrene, which can sequester oxygen within the polymer matrix for long periods of time because of the polymer's oxygen solubility combined with its relatively low diffusion coefficient [62].

Hypoxia has been quantified in tumours *in vivo* using Clark-type micro-needle electrodes as well as 2-nitroimidazole agents, which bind to low oxygen regions of tissue [62]. Additionally, water-soluble luminescent oxygen probes have been developed for this purpose, and will be discussed in section 1.3.3. 2-nitroimidazole agents such as EF5 offer a high spatial resolution as well as compatibility with various imaging techniques such as magnetic resonance imaging, positron emission spectroscopy, and fluorescence microscopy [62]. EF5 has been widely employed *in vivo* as well as to study oxygen profiles in tissue cultures, and has been recently employed to quantitatively measure the oxygen consumption rates of tumour spheroid cultures [63]. In addition to these exogenous probes, endogenous markers such as the hypoxia-inducible transcription factor HIF-1α can be used to identify hypoxic regions [64, 65].

Tumours can be highly heterogeneous, and this heterogeneity extends to hypoxia as well. There are a variety of regimes and subtypes of hypoxia that can result in different tumour cell behaviour within the same tumour type. Hypoxia can be chronic (caused by blocked or distant blood vessels), acute (caused by temporarily blocked vessels), or cycling (caused by blood vessels that are intermittently closed or blocked and then opened), and differences in the hypoxic oxygen levels between 0%, 0.1%, 1%, and 5% can result in different cell responses due to the

differences in HIF activation, metabolism, and proteomic and genomic changes between these oxygen conditions [64].

1.2.1 Hypoxia-Mediated Resistance to Anticancer Treatments

The effect of hypoxia on resistance to radiation therapy has been identified and studied for over 60 years. Building on work as early as 1935 by J.C. Mottram [66] and others that identified hypoxia as a factor in the efficacy of radiotherapy, in 1953 Gray *et al.* first studied the effect of oxygen on the outcome of radiotherapy and found that tumour cells were approximately 2-3 times less sensitive to X-rays under anoxic than well-oxygenated conditions [67]. More recently, hypoxia has also been identified as a factor in the sensitivity of tumour cells to chemotherapies. In addition to the requirement of molecular oxygen itself for certain therapies such as antibiotics that induce DNA strand breaks [65], a number of adaptations can be made by tumour cells upon exposure to hypoxic environments; these adaptations can lead to either resistance or sensitivity to different chemotherapies. The mechanisms by which hypoxic cells develop resistance and sensitivity to chemotherapeutic agents have also been studied and reviewed in several publications [65, 68-70].

 In 1981, Teicher *et al.* studied the effect of hypoxia (plastic tissue culture flasks flushed with 0% oxygen and 5% CO_2, compared with normoxia defined as air containing 5% CO_2) on EMT6 mouse mammary tumour cells after a 1-hour exposure to various chemotherapies and used colony-forming assays to study the surviving fraction of cells [71]. They grouped chemotherapies into three classes: those that were less effective in hypoxia (e.g. bleomycin: 9 times less sensitive in hypoxia and actinomycin D: nearly 100 times less sensitive in hypoxia at higher (1 μM) drug concentrations, but similar sensitivity at low concentrations), those that were more effective in hypoxia (e.g. Adriamycin (doxorubicin): nearly 10 times more sensitive in hypoxia at high concentrations), and those that were equally effective in hypoxia and normoxia (e.g. 5-fluorouracil). In 1990, the same group studied the effects of chemotherapies *in vivo* on murine FSaIIC Fibrosarcoma, using Hoechst staining as a measure of differentiating between hypoxic and normoxic cell fractions in the tumour [72]. Brightly stained regions (indicative of good tissue blood perfusion) were taken to be normoxic while the darkest regions were taken to be hypoxic. Contrary to their work *in vitro* using EMT6 mouse mammary tumour cells, in this

study they found that the non-Hoechst-stained (potentially hypoxic) cells were 2.2 times less sensitive to Adriamycin (doxorubicin), as well as 2.2 times less sensitive to radiation, than the brightly Hoechst-stained cells. The difference between these two studies is likely due to the diffusion limitations of Adriamycin through the tissue, but could be influenced by a number of other factors that exist *in vivo* but not *in vitro*, including the difference in cell types as well as the heterogeneity, pH conditions, and different hypoxic regimes that can exist in tumours.

More recently, Sullivan *et al.* [73] have exposed MDA-MB-231 human breast cancer cells to several different chemotherapeutic agents under normoxic conditions as well as hypoxia (0.2% oxygen) with a 24-hour hypoxic pre-exposure and compared the treatment efficacy via colony-forming assays. They found that hypoxic conditions led to a 3.5-fold increase in survival for doxorubicin (5 μM), a 4-fold increase for daunorubicin (5 μM), a 4.8-fold increase for etoposide (50 μM), and a 3.6-fold increase for mitoxantrone (1 μM) after a 1-hour exposure to each drug. Strese *et al.* [74] studied the effects of hypoxia (1% oxygen) and anoxia (defined in this work as 0.1% oxygen) on the response of 5 different cell lines representing 5 different cancer types to 19 different chemotherapies. They used commercial hypoxic incubators to expose the cells to hypoxic conditions, and subjected the hypoxic/anoxic cells to a hypoxic/anoxic pre-treatment for 18 hours prior to the 72-hour drug exposure. They quantified their results by analyzing the half-maximal inhibitory concentrations (IC_{50}s; the drug concentration at which half the cell growth is inhibited) of the cells using a non-clonogenic cell viability assay based on the conversion of fluoresceindiacetate to fluorescent fluorescein by live cells. They found that on the MCF-7 breast cancer cells, the IC_{50} of several drugs were lower in hypoxia and anoxia than normoxia, indicating that the drug was more effective in hypoxia/normoxia (e.g. cisplatin IC_{50} was 0.37 times smaller in anoxia and 0.49 times smaller in hypoxia, tirapazamine IC_{50} was 0.055 times smaller in anoxia and 0.062 times smaller in hypoxia). For other drugs on the same cell line, the IC_{50}s were higher in hypoxia and anoxia than normoxia, indicating that the drug was less effective in hypoxia/normoxia (e.g. sorafenib IC_{50} was 1.5 times greater in anoxia and 1.4 times greater in hypoxia, irinotecan IC_{50} was >2.7 times larger in anoxia). Doxorubicin showed an interesting effect on MCF-7 cells in hypoxia and normoxia. Its IC_{50} in anoxia was >2.1 times that in normoxia (indicating resistance to the drug), but its IC_{50} in hypoxia was 0.59 times that in

normoxia (indicating enhanced sensitivity to the drug); between the 1% and 0.1% oxygen levels, the effect of hypoxia on the drug efficacy reversed.

1.2.2 Chronic Hypoxia: Clinical Importance of Oxygen Level

Hypoxia leads to a number of changes and effects within tumour cells, which have been summarized by Höckel and Vaupel [50]. Activation of the hypoxia-inducible transcription factors (HIFs), which regulate the expression of genes involved in angiogenesis, cell survival, and metastasis and help the cell adapt to hypoxia [65, 75], can occur at oxygen levels near 10 mm Hg (1.32%). The rate at which adenosine triphosphate (ATP; a chemical used to transport energy within cells) is produced decreases when oxygen is limited below approximately 10 mm Hg (1.32%) [50], which in turn leads to changes in intracellular ion concentrations due to the reduction of cell membrane function. Under low oxygen conditions, cell metabolism can also shift from oxidative phosphorylation to glycolysis, which produces lactate [64]. Lactate production can lead to acidosis, or extracellular acidification, which can in turn affect the efficacy of anticancer drugs by decreasing their uptake [65]. Hypoxia can also cause proteome changes at oxygen levels ranging from 1-15 mm Hg (0.13-1.97%) [50], including causing the cell cycle to be slowed or arrested. Oxygen levels of 0.2-1 mm Hg (0.026-0.13%) have been found to lengthen the G_1 phase (the first part of the growth or interphase stage of the cell cycle) or arrest cells preferentially in the G_1 phase, while anoxia is thought to cause immediate cycle arrest in any cell cycle state [50]. Slowing or arresting the cell cycle in turn can lead to resistance to cancer therapies, many of which preferentially target proliferative cells. Hypoxia-induced proteomic changes can also lead to apoptosis and necrosis, or alternatively help the cell to adapt to or escape from its environment (for example, by changing its metabolism, stimulating the transcription of vascular endothelial growth factor (VEGF), or proteins associated with tumour invasiveness); genomic changes can also be induced by hypoxia at oxygen levels below 0.2-1 mm Hg (0.026-0.13%) [50]. These changes can in turn lead to tumour progression or metastasis.

Compared to physiological oxygen levels in various tissues of ~3-10% (e.g. 3.8% in muscle and 9.5% in the kidney) [76], approximately 60% of solid tumour mass is either hypoxic or anoxic [77] and the degree of hypoxia has been associated with poor prognosis [78] and tumour

aggressiveness. Based on binding of the 2-nitroimidazole agent EF5 to resected tissue, Evans *et al.* [79] calculated tissue oxygen partial pressure (pO_2) and presented 5 categories to describe oxygen levels within gliomas: physiologic (10%), modest hypoxia (2.5%), moderate hypoxia (0.5%), severe hypoxia (0.1%) and anoxia (0%). Grade 2 tumours on average had modest hypoxia, grade 3 tumours had moderate hypoxia, and grade 4 tumours had severe hypoxia; increased levels of hypoxia were associated with more rapid tumour recurrence.

Hypoxia has also been identified as a potential target for cancer therapies due to its presence in tumour tissue as well as the resistance to many standard cancer therapies that it can facilitate [65]. Hypoxia has been found to increase tumour malignancy by developing cells with more aggressive phenotype [80], and by upregulating genes associated with breast cancer metastasis [81, 82]. A recent review of hypoxia as a target for cancer therapy outlines the two main methods used to target hypoxia: bioreactive prodrugs (inactive compounds that are converted to drugs under hypoxic conditions), and drugs that act on molecular targets present in hypoxic cells (such as the hypoxia-inducible factors, the unfolded protein response, mTOR pathways, or targets downstream of these) [65]. Because of various mechanisms for action, different hypoxia-targeted therapies can target different levels of hypoxia within tumours, further suggesting that the degree of hypoxia in the test environment is important in understanding the efficacy of these drugs.

Two of the regulatory cascades that have been investigated as targets for anticancer therapy are the hypoxia-inducible factor (HIF) pathway, which is involved at hypoxia levels around 1% O_2, and the unfolded protein response, which operates at hypoxia levels < 0.2% O_2 [82, 83]. While investigating hypoxia-induced breast cancer cell migration in the unfolded protein response pathway, Nagelkerke *et al.* [84] found that hypoxia of 1% O_2 stimulated more migration of MDA-MB-231 breast cancer cells than 0.5% O_2 in a gap closure assay. In contrast, at severe hypoxic conditions of 0.1% O_2 the cell migration was not statistically significant compared to normoxic control, which may have indicated that cell survival was more important than cell migration under those conditions. Severe hypoxia (0.1%) was also found to activate different levels of genes compared to 1% hypoxia [85]. It has also been found that the degree of hypoxia can affect autophagy in breast cancer cells: after inducing hypoxia in MCF-7 cells using hypoxic incubation, Bellot *et al.* [86] measured the increase in GFP-LC3 puncta within cells and the

number of autophagic vacuoles and showed that severe hypoxia (0.1% O_2) induced increased autophagy compared to cells cultured under moderate hypoxia (1% O_2).

These results demonstrate the importance of the degree of hypoxia within tumours, and suggest that precise oxygen control is crucial when developing platforms to study specific hypoxic regimes that can exist in tumours. Beyond cancer research and tumour cell culture, this type of precise oxygen control could also have other biological applications. The degree of hypoxia has also been found to be important in regulating embryonic development [87] and stem cell function [88], indicating that hypoxia control platforms could have wider biological relevance.

1.2.3   Oxygen Gradients

In addition to chronic, static hypoxic conditions, there is also evidence that spatially varying oxygen gradients can exist in tumours. To measure oxygen gradients, Helmlinger *et al.* used phosphorescence lifetime imaging to image oxygen profiles in 27-day old human colon adenocarcinoma tumours in immunodeficient mice. They measured gradients near blood vessels decreasing from 14 to 0 mm Hg (1.8% to 0%) over approximately 200 μm [89]. Another work imaged oxygen gradients within mammary adenocarcinomas in rats using phosphorescence lifetime imaging through dorsal skin flap window chambers, and measured gradients between approximately 1-35 mm Hg (0.1%-4.6%) under air breathing conditions [90].

1.2.4   Acute and Cycling Hypoxia

In contrast with chronic hypoxia, which is thought to be primarily caused by diffusion limitations and cellular consumption and exists in cells far from blood vessels, there is also evidence that suggests that acute hypoxia can exist in tumours and have different effects from those of chronic hypoxia. Acute hypoxia in cancer is thought to be caused by a temporary halt to red blood cell perfusion in blood vessels near to the acutely hypoxic region [64]. Large fluctuations in blood flow and oxygenation within tumours have been seen in animal tumour models [56, 83, 91] and human tumours [80, 92, 93]. This could be due to blood clots or other temporary blockages, resulting in a single period of acute hypoxia, or it could be cyclic, leading to cycling hypoxia [64]. Although there have been many different definitions for *in vitro* chronic and acute hypoxic treatment times ranging from minutes to days in the literature as summarized by Bayer and

Vaupel [94] (some of which overlap between acute and chronic), it appears that acute hypoxia may lead to a more aggressive phenotype than chronic hypoxia, although further investigation is necessary to understand this effect [94, 95]. Additionally, acute and cycling hypoxia are thought to lead to genomic instability due to the generation of reactive oxygen species by the hypoxia-reoxygenation cycles [95, 96].

The time scales of cycling hypoxia appear to be widely ranging from several cycles per hour to cycles in days [97, 98], with higher frequencies of a few cycles per hour thought to be caused by endothelial cell contractions [94, 99] and lower frequency cycles of hours to days thought to be caused by vascular remodelling [94]. While chronic or prolonged hypoxia has been found to act as a selective pressure for cells that are resistant to apoptosis [100, 101], intermittent or cyclic hypoxia can also select for genotypes leading to tumour progression and resistance to therapy [102]. The presence of cycling hypoxia (to an even greater degree than chronic hypoxia) has been correlated with a metastatic cell phenotype in several animal models, as reviewed by Dewhirst [98]. A recent study by Ehsan and George has also investigated the effects of cycling hypoxia (between 1% and 20% oxygen) on blood vessel formation by endothelial cells in 3-D culture within custom polymer chambers, and found that the blood vessel formation may depend on the frequency of cycling hypoxia, suggesting that cycling hypoxia may have an effect on angiogenesis [103].

The potential importance of acute and cycling hypoxia in metastasis and blood vessel formation suggest not only that it may be an interesting phenomenon to study in a 3-D culture environment, but also that precise control of the oxygen levels and cycling frequencies during these studies could lead to a more complete understanding of these phenomena.

1.2.5   Conventional Platforms for the Study of Hypoxia

One of the main challenges facing the study of hypoxia is developing an appropriate platform in which to carry out the investigations, as hypoxic oxygen levels are drastically different from atmospheric conditions (21% oxygen). The importance of hypoxia-reoxygenation cycles, as discussed in section 1.2.4, further complicates this study as unintended reoxygenation cycles could impact the results of the experiment. Byrne *et al.* [104] have recently reviewed platforms

for the study of hypoxia. One platform that has been extensively used for the study of hypoxia has been the hypoxic incubator. This type of cell culture incubator has a controlled gas input and can maintain low and precise oxygen levels. The main disadvantages of hypoxic incubators are that they are only capable of recreating one oxygen condition throughout the entire incubator, and that in order to avoid introducing unintended reoxygenation cycles, all media changes and other processing steps must be carried out within a glove box at the same oxygen condition. The first disadvantage has been addressed by the use of modular incubator chambers such as those offered by BioSpherix® or Stemcell™ Technologies. These chambers fit inside cell culture incubators to facilitate the recapitulation of multiple oxygen conditions within the same incubator.

Many groups have used custom vessels or tissue culture flasks flushed with known gas mixtures in order to control the oxygen levels and create hypoxic profiles [71, 103]. Some of these vessels would be subject to long oxygen diffusion times to reach the cells through the static cell culture media, which would in turn create long equilibration times in the system. These vessels would not all have the same oxygen control characteristics, as their dimensions and composition can affect the oxygen profiles within them; for this reason, there is a wide range of oxygen conditions and switching times that have been studied in hypoxic systems and this can create challenges in comparing studies. Plastic vessels such as polystyrene culture flasks, as discussed in section 1.2, can also store oxygen and prevent the recreation of very low oxygen levels within the system [62]; for this reason, glass vessels are preferable. The issue of long equilibration times has been addressed by custom stirred vessels in order to reduce the diffusion limitation on oxygen transport [105]. Other groups induce hypoxia chemically without manipulating the actual oxygen environment using chemicals such as cobalt chloride solutions, which can stabilize HIF-1α and bring on an artificial state of hypoxia [104, 106].

Microfluidics present an elegant solution to this problem due to the level of control that they facilitate over the microenvironment and the oxygen conditions [104]. They offer the unique capability to bring the gases used to control oxygen levels in very close proximity to the cell cultures, as depicted in Figure 1.2. This in turn affords precise control over the oxygen levels and switching times, as will be discussed in detail in section 1.4.

19
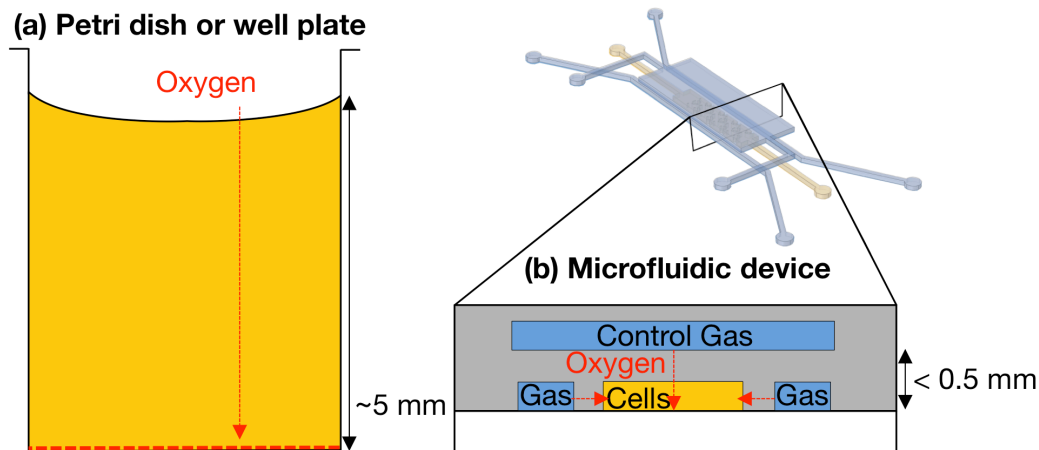
Figure 1.2. Comparison schematic showing approximate gas diffusion distances within traditional culture environments such as petri dishes and well plates **(a)**, and microfluidic devices **(b)**. The use of microfluidic systems allows an order of magnitude decrease in the diffusion distance, which in turn permits faster oxygen switching times.

1.3 Optical Oxygen Sensors

Optical oxygen sensors present an attractive option for sensing oxygen levels inside microfluidic devices because they do not consume oxygen, are easily miniaturized, and are read out optically and thus do not require physical contact between the sensing material and the readout system [107]. These sensors, which can be made by encapsulating an oxygen-sensitive luminescent indicator compound in a polymer film, operate on the principle of luminescence quenching [108]. Both the luminescence intensity and lifetime of these indicators are quenched by the presence of molecular oxygen, so either quantity can be measured to determine the oxygen levels. Ratiometric sensing based upon the comparison of the intensity of an oxygen-sensitive dye with that of an oxygen-insensitive dye encapsulated in the same film has been proposed as a robust sensing mechanism that can be measured with simple fluorescence microscopy equipment, combining some of the advantages of intensity and lifetime sensing systems [107]. A simple ratiometric sensing system employing the colour channels of a colour camera to separate the emission intensities of the two dyes has been proposed and found to be reliable [109].

1.3.1 Theory of Operation

Much of the early work on oxygen sensors focused on Clark-type electrode sensors [110], which detect a current flow caused by reduction of oxygen. These sensors in the Eppendorf needle

probe format have been extensively used to measure tumour hypoxia *in vivo*; however, their invasiveness has limited their designation as the gold standard of hypoxia measurement [111]. Such sensors have been miniaturized and integrated with microfluidic devices to monitor the oxygen consumption of bacteria [112]. The miniaturization of such devices requires microscale electrodes, and this type of sensor consumes oxygen (and thus requires sample stirring for accurate measurements), is easily contaminated by sample contents, and requires electrical connection between the sensor electrodes and the measurement infrastructure [113]. These factors present several significant disadvantages for microfluidic cell culture systems.

Consequently, there has been much interest in the integration of optical oxygen sensors with microfluidic systems. These optical sensors present the advantages that they are easily miniaturized, are not easily contaminated, do not require physical contact between the sensor and optical detector, and do not consume oxygen [113-118]. Most optical oxygen sensors operate on the principle of reversible luminescence quenching of the intensity or excited-state lifetime ([108], as cited in [119]) of a luminescent indicator dye or luminophore. This process occurs when the excited state energy of a fluorescent or phosphorescent indicator molecule is transferred to another molecule such as oxygen rather than being emitted in the form of a luminescence photon [120]. The quenching behaviour can be modeled by the Stern-Volmer equation [121]:

$$\frac{\tau_0}{\tau} = \frac{I_0}{I} = 1 + k_Q \tau_0 pO_2 \text{,}$$

(2)

where pO_2 is the partial pressure of oxygen, k_Q is the quenching rate constant, τ_0 and I_0 are the excited-state lifetime and luminescence intensity in the absence of oxygen, respectively, and τ and I are the excited state lifetime and luminescence intensity at the pressure of interest, respectively. The Stern-Volmer equation may also be written in terms of the dissolved oxygen concentration $[O_2]$ rather than pO_2, requiring different units for k_Q.

There are several excellent reviews of optical oxygen sensors [116, 122], as well as more general optical sensors [123, 124], and oxygen sensors [113]. We published a review of optical oxygen sensors for applications in microfluidic cell culture in 2010 [107], and in recent years, other

21

reviews of optical chemical sensors for integration with microfluidic environments have also been published [125, 126].

1.3.2   Methods of Operation

Optical, luminescence-based oxygen sensing is based on the phenomenon of luminescence quenching by oxygen. As oxygen quenches both the luminescence intensity and excited-state lifetime, there are inherently two different methods of measuring oxygen concentrations or pressures with luminescent probes. This section will present some of the previous work performed using each method, outline the methods' advantages and disadvantages, and evaluate their compatibility with microfluidic systems.

1.3.2.1   Intensity-Based Sensors

Intensity-based oxygen sensing involves only the detection of the luminescence intensity, and as a result is generally easier to implement than lifetime-based detection methods. An example setup for intensity-based detection is presented in Figure 1.3.
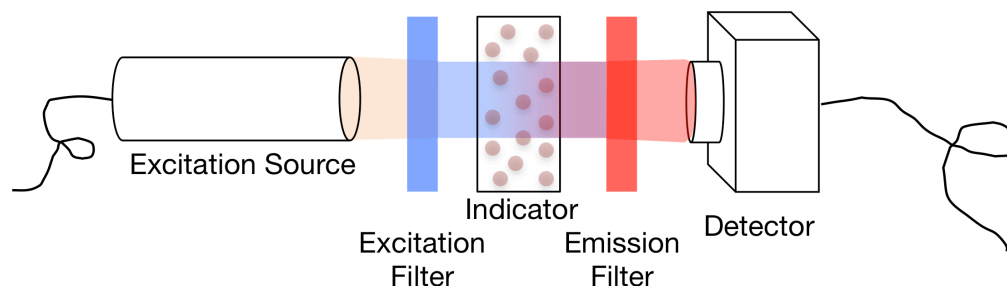
Figure 1.3. Simplified example setup for intensity-based optical oxygen sensing. Figure previously published in [107].

The luminophore is excited by light from an excitation source, which passes through an excitation filter to select the wavelengths best matched to the excitation spectrum of the luminophore. The emitted luminescence intensity is detected after passing through an emission filter to remove any extraneous light not part of the emission spectrum. A detector array such as a Charge-Coupled Device (CCD) can easily be used to detect the emitted luminescence, allowing 2-D oxygen concentration gradients to be determined. The simplified setup depicted in Figure

1.3 does not include any imaging optics, but lenses [127] and even complete fluorescence microscopy setups [118, 128, 129] can be easily integrated into the intensity imaging setup.

Intensity-based sensing suffers from several disadvantages, including susceptibility to photobleaching, leaching, and intensity variations caused by inhomogeneities in the detector pixels (if a 2-D detector is used); dependence on detection optics, sample absorption or scattering, excitation light, and dye layer concentration and film thickness [117]. Nevertheless, intensity-based imaging has been successfully used for *in vivo* sensing applications [128, 130], gaseous oxygen sensing [131], inter- and intra-cellular measurements [132, 133], and microfluidic oxygen sensing [129, 134-136].

Because of these disadvantages of intensity-based sensing, several groups have concluded that lifetime-based optical oxygen measurements (discussed below) are superior to and more robust than intensity-based measurements [117, 137-140] using the same probe molecules. Detection methods based on phosphorescence lifetime also yield improved contrast and suppression of background signal [127]. As such, much of the recent work on luminescent oxygen sensors has focused on lifetime-based sensing methods.

1.3.2.2   Lifetime-Based Sensors

Lifetime-based sensing mechanisms involve the detection of the luminescence lifetime in either the time domain or the frequency domain. Time domain detection generally involves the direct detection of the lifetime itself, while frequency domain detection generally involves determining the luminescence lifetime via a lifetime-dependent phase lag between the excitation and emission light intensity waveforms. For both lifetime-based sensing mechanisms the excitation illumination must be modulated. A simplified example setup for lifetime-based oxygen sensing is shown in Figure 1.4. Also included in Figure 1.4 are example excitation light modulation and their corresponding emission waveforms. The sinusoidal excitation modulation waveform likely corresponds to a phase-based detection method, wherein the fluorescence lifetime affects the phase shift between excitation and emission sinusoids. Conversely, the square-wave excitation modulation waveform corresponds to a time-domain detection mechanism.
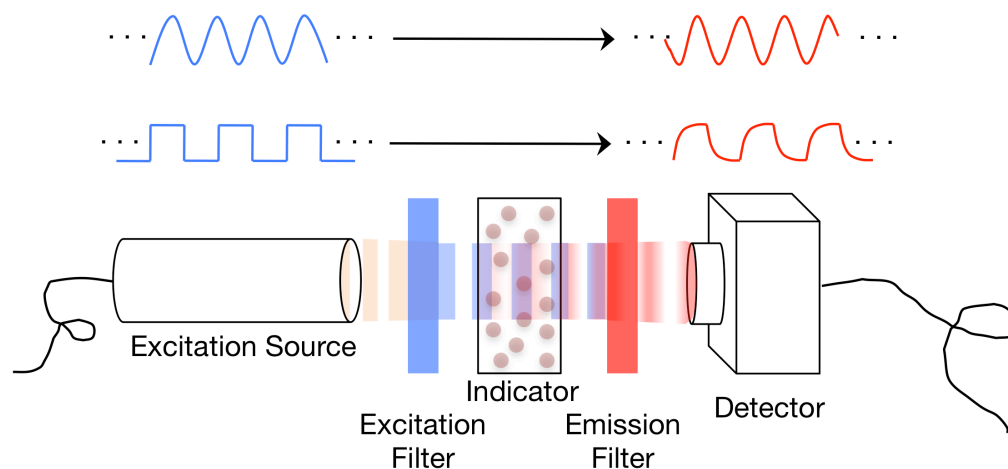
Figure 1.4. Simplified example setup for lifetime-based optical oxygen sensing. Example excitation modulation and emission waveforms are also shown. Figure previously published in [107].

The most common time-domain lifetime detection scheme is the "pulse-and-gate" method [141-148], as illustrated in Figure 1.5. In this method, the excitation light is modulated (generally by a square-wave pulse indicated by the thick blue line) and the detector is gated such that it acquires windows of emission intensity data (indicated by the coloured regions), generally during the luminescence decay period. The dashed red line represents the intensity of the emitted light.
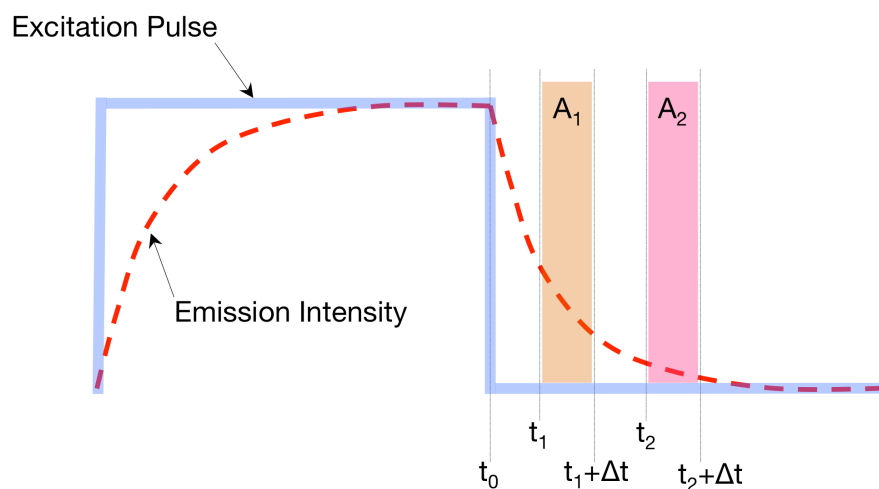
Figure 1.5. Illustration of "pulse-and-gate" time-domain luminescence lifetime detection. The transparent coloured boxes indicate the windows of data acquisition; the decay constant and luminescence lifetime can be determined from the data acquired in these windows (figure adapted from [141] and previously published in [107]).

Two acquisition windows are sufficient to characterize a monoexponential decay and are commonly used [141-143], although three-window and even five-window methods have been used for improved accuracy [127, 146]. The ratio of the integrated data collected during the two windows can be used to determine the decay constant of the signal and thus the luminescence lifetime of the indicator, via equation 3 [145]:

$$\tau = \frac{t_2 - t_1}{\ln \dfrac{A_1}{A_2}}$$ (3)

With the "pulse-and-gate" method, it is possible to remove the effects of short-lived background luminescence and any residual, decaying source light after the nominal shutoff time. This is usually accomplished by adding a short delay (~100-500 ns) between the end of the excitation pulse and the beginning of the first gated window [141, 143]. It is much more difficult to separate background luminescence with long lifetimes or similar lifetimes to that of the indicator of interest [127]. The "pulse-and-gate" method of lifetime detection has been successfully used with oxygen-sensitive indicators and gated detectors to obtain two-dimensional oxygen distribution images in micro-titer plates [141], engineered tissue, living cells, and *in vivo* samples [142, 146, 149, 150], coral sediment, lichen, and foraminifer samples [143], microfluidic bioreactors [150, 151], and biofilm growth flow chambers [152]. As long as the detector only detects the luminescence signal while the excitation lamp is not emitting and the effects of ambient light are insignificant, the emission filter shown in Figure 1.4 is not necessary for time-domain lifetime detection. For other methods such as phase-based lifetime detection, however, it is necessary to include the filter.

Another time-domain method of measuring luminescence lifetime involves taking the ratio of gated detection windows different from those illustrated in Figure 1.5 [117]. This method utilizes one window during the excitation pulse and another after the pulse, and the ratio of these windows (after subtracting any effects of dark current) may be used to determine the luminescence lifetime. This detection scheme has been compared to the "pulse-and-gate" method, and found to have a higher signal-to-noise ratio and faster calculation time [127] due to the longer windows and increased optical power during each window. Its disadvantages include its inability to separate out background luminescence and the need for an emission filter.

The frequency-domain method of determining luminescence lifetime (phase fluorometry or luminometry) measures the phase shift between the excitation light intensity and emitted light intensity waveforms. If the luminescence decay is modeled as single-exponential, the luminescence lifetime τ may be obtained from the phase shift φ using equation 4 [153]:

$$tan(\varphi) = \omega\tau,$$
(4)

where ω is the angular frequency of modulation. The optimal modulation frequency for frequency-domain lifetime measurements may be found from τ_1 and τ_2, the lifetimes (i.e. quenched and un-quenched) of interest, using equation 5 [138]:

$$\omega_{opt} = \frac{1}{\sqrt{\tau_1\tau_2}}.$$
(5)

Frequency-domain methods of lifetime detection require detection mechanisms capable of detecting phase differences, but separation of luminophores with close lifetimes is easier than with time-domain methods [127]. Phase fluorometry or luminometry was first used with simple point detectors such as photodiodes and photomultiplier tubes (PMTs) [154-156] but has also been expanded to use two-dimensional detectors to obtain two-dimensional images of oxygen distributions [157]. Phase-based optical oxygen sensing with photodiode detectors has also been successfully integrated into microfluidic channels and bioreactors [158-160] and even multi-chamber microfluidic cell culture analog systems [42].

Lifetime-based sensing is attractive due to its increased robustness; however, the requirement for specialized equipment limits its usability. It is for this reason that intensity-based sensing is so attractive, and there has been much effort developing intensity-based systems with improved robustness, as will be discussed in the next section.

1.3.2.3   Ratiometric Sensors

Intensity-based measurements are particularly attractive for microfluidic cell culture because of their inherent compatibility with standard fluorescence microscopy setups often already in place and because of the simplicity of the measurement method. Several methods have also been proposed to help overcome the disadvantages of intensity-based sensing, including the formulation of complex calibration functions incorporating photobleaching and leaching effects

and pixel-by-pixel calibration techniques [128] requiring no sample movement between calibration and sensor use. The best-investigated method has been ratiometric sensing [109, 118, 132, 161-163], wherein the sensing layer contains both the oxygen-sensitive dye and an oxygen-insensitive dye, with the two dyes having different emission spectra. Both dyes are excited by the excitation source and the sum of the two emission spectra is detected by a detector, but only the emission intensity of the oxygen-sensitive dye is quenched by the presence of oxygen. The oxygen levels are thus determined by measuring the ratio between the emission intensities of the two dyes (often carried out using different optical filters to separate the emissions of the two dyes by wavelength, or other methods of separation by wavelength). This method helps reduce the effect of excitation light, dye layer, detection optics, detector sensitivity, and sample inhomogeneities, as the emission intensity of the oxygen-insensitive dye is also affected by these factors.

Ungerböck *et al.* have presented a thin-film ratiometric sensor composed of platinum (II)-5,10,15,20-tetrakis-(2,3,4,5,6-pentafluorphenyl)-porphyrin (PtTFPP) and Macrolex Fluorescent Yellow (MFY), wherein the MFY acts as both the reference dye and an antenna dye (using light harvesting [164] to help excite the PtTFPP by transferring energy) [109, 163]. The luminescence of these films can be spectrally resolved using the colour channels of a colour camera, making them a convenient sensing platform offering improved robustness over intensity-based sensors with simple fluorescence microscope readout. These ratiometric sensors have been found to follow a simplified two-site quenching model:

$$\frac{R}{R_0} = \frac{f_1}{1 + k_{SV}pO_2} + f_2,$$

(6)

where R and R_0 are the ratiometric intensities (the ratio of the oxygen-sensitive channel's fluorescence intensity to that of the reference channel: $R = I_{sens}/I_{ref}$) in deoxygenated conditions and under oxygen partial pressure pO_2, respectively; k_{SV} is the Stern-Volmer quenching constant (a measure of the quenching efficiency); and f_1 and f_2 describe the fraction of the dye molecules that is quenched by oxygen with Stern-Volmer quenching constant equal to k_{SV}, and the fraction of dye molecules that are non-quenchable (Stern-Volmer quenching constant equal to 0), respectively [109]. A similar concept has since been expanded by the same group to perform ratiometric imaging of both oxygen and pH [165]. This method is very attractive because it

permits more robust measurements than intensity alone, while still requiring only standard fluorescence microscopy equipment.

1.3.3   Sensor Designs

There are a wide range of optical oxygen sensor designs, including various modalities (thin films, embedded microparticles, dissolved sensors, or sensor probes), various oxygen-sensitive indicator molecules, and various matrix materials. For microfluidic cell culture it is possible to use one of several oxygen sensor formats. Thin sensor films integrated into the cell culture device or substrate present perhaps the most obvious solution, but it may also be possible to integrate optical fibre-type sensors, micro/nanoparticle sensors, or even directly stain cells or the cell culture media with soluble oxygen-sensitive compounds. An illustrative overview of some of the sensor formats is presented in Figure 1.6. This section presents some of the previous work performed with these sensor formats and discusses how they may be applied to microfluidic cell culture.

Thin-film Sensors on Substrate: Thin-film type sensors are commonly used, and are generally fabricated by either pipetting or spinning solutions of the indicator and encapsulation medium onto a substrate of interest such as glass slides, polymers, or polyester foils. This type of sensor has been quite widely used as un-patterned films [117, 127, 128, 131, 141-143, 157, 166, 167]. A similar process has also been used to create patterned layers by pipetting only small areas or performing a pipetting and lift-off process [114, 135, 136, 140, 158, 168-170]. Fabricated thin layers have been lithographically patterned using poly (dimethylsiloxane) (PDMS) "stamps" as masks in a dry etch process [129, 171], and using a chromium mask layer [172]. Additionally, Ambekar *et al.* created photolithographically patterned thin-film oxygen sensors utilizing photopatternable silicone [173], however some difficulty was encountered with the use of a platinum porphyrin indicator, as it was highly absorbing at the wavelengths necessary to expose the photopatternable polymer.

Thin-film sensors are usually excited with either trans- or epi-illumination, but the excitation light has also been provided using optical fibre coupling [170] and evanescent fields from the glass substrate [131] or polymer waveguides [174].

Thin-film oxygen sensors have been integrated successfully with microfluidics [129, 158, 171] and used for microfluidic cell culture in order to monitor the dissolved oxygen concentrations during the culture of three types of bacteria requiring differing oxygen levels as well as mammalian cells [135, 136].

Optical Fibre Sensors: Oxygen-sensitive micro-optodes are another commonly used sensor format, wherein the oxygen-sensitive dye and encapsulation matrix are attached to the end of an optical fibre. The optical fibre can provide the excitation light, carry the emitted luminescence to the detector, or both [115, 118, 139, 175, 176]. Layers of black silicone have been used to optically isolate the sensor film from its surroundings, and arrays of the sensors have been used to obtain oxygen concentration gradients [138]. The optical fibre has been pulled to fabricate tip diameters as small as 5-10 μm, but larger (10-40 μm) diameters are usually used to increase signal strength [138, 175]. Other research has only used the optical fibres as a means of coupling the light to and from the sensor film, where the sensor layer is fabricated on a different substrate [170].

While the fibre optic platform presents a convenient method for coupling light to and from the sensor, integration with microfluidic devices is likely more difficult and inconvenient than that for the thin-film sensor platform. Nonetheless, there may be advantages to the fibre optic sensor platform, and integration with microfluidic cell culture should be possible. Similar to the fibre optic platform but possibly easier integrated with microfluidic cell culture, the ends of on-chip sol-gel waveguides have been coated with an oxygen-sensitive ruthenium compound encapsulated in sol-gel; this sensor platform was used to sense gaseous oxygen concentrations [177]. Although these waveguides are quite large (100 μm by 100 μm in cross-section), they lie parallel to the substrate and microfluidic cell culture environments could potentially be designed to incorporate them and bonded above them.
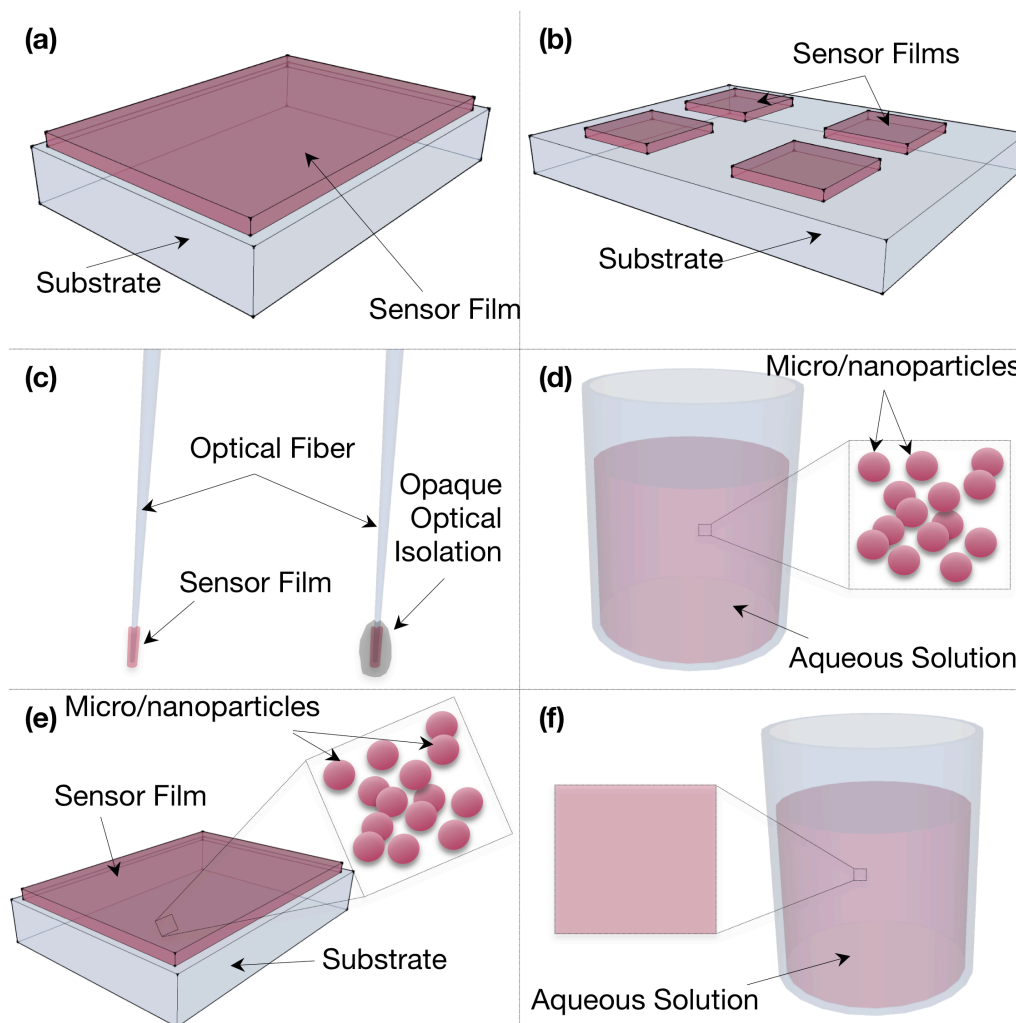
Figure 1.6. Illustration of example sensor formats. **(a)** Thin film sensor. **(b)** Patterned thin-film sensor. **(c)** Tapered optical fibre sensor without and with opaque polymer optical isolation (shown as partially transparent for figure clarity). **(d)** Micro/nanoparticle sensors suspended in aqueous media. **(e)** Micro/nanoparticle sensors suspended in a thin film. **(f)** Water-soluble sensor compound dissolved in aqueous media. Figure previously published in [107].

PEBBLE/Microparticles/Nanoparticle Sensors: The desire to create a versatile sensor platform with both the advantages of indicator encapsulation and the possibility of intracellular measurements led to the development of microparticle, nanoparticle, and "Probing Explorers for Bioanalysis with Biologically Localized Embedding" [161] or "Probes Encapsulated by Biologically Localized Embedding" (PEBBLE) [132] sensors. PEBBLE sensors are generally fabricated with the luminescent dye embedded in an ormosil matrix, and ratiometric, intensity-based measurements using these sensors have been used to map oxygen concentrations inside cells [132]. Other, poly (dimethylacrylamide) (PDMA)-based ratiometric PEBBLEs have been used to monitor oxygen concentrations in human plasma [161]. Reviews of the applications of

nano-sized PEBBLE sensors, including those for dissolved oxygen measurements, in biological and intracellular applications have been presented [178, 179], and another review of various sensor technologies for monitoring various indicators of metabolic activity (again including dissolved oxygen PEBBLEs) inside cells has been written [124].

Other microparticle and nanoparticle oxygen sensors have been fabricated by doping polymer or silica beads with luminescent indicator dye [128, 133, 162] or by grinding indicator-doped ormosil [180]. These microparticle and nanoparticle sensors have been used directly [133] or embedded in another material such as silicone [128] or hydrogel [180] to form thin-film sensors. Microparticle and nanoparticle sensors could be integrated in the cell culture area by adding the particles to silicone or hydrogel thin-films within the channels.

Water-Soluble Probes: The final general sensor platform is the dissolved, or macromolecular probe. This format uses water-soluble probes, which may be bound to albumin or other molecules to improve sensor characteristics. This probe format is versatile as it may be added to aqueous materials, including those for microfluidic cell culture. Water-soluble probes have been primarily used for *in vivo* biological imaging [130, 133, 181-187], but they could potentially be applied to other aqueous environments.

Water-soluble probes do suffer from several disadvantages. Because they are not encapsulated in a solid matrix, they are much more likely to interfere with their environment (e.g. binding to biological sample components or changing luminescence properties with changing sample chemical composition [133]) and it is more difficult to control the sensor parameters, such as its sensitivity and oxygen selectivity. As such, there has been effort to develop water-soluble probes that are encapsulated by or bound to other molecules to help overcome these disadvantages; dendritic encapsulation, whereby the luminophore is located inside a cage made up of repeatedly branched, large molecules (dendrimers) is one of the most promising of these methods [188].

Water-soluble probes could be used to monitor dissolved oxygen concentrations during microfluidic cell culture, as they could be added to the cell culture media to map oxygen concentrations in the entirety of the microfluidic channel. Using water-soluble probes could

allow techniques such as tomographic imaging to map 3-D images of oxygen concentrations within the cell culture area. However, it is likely that a greater amount of potentially expensive (e.g. ~$130/g for the water-soluble ruthenium oxygen indicator RTDP) probe molecules would be required for the water-soluble probe platform in comparison with the thin-film method, as the probes would need to be added to all of the cell culture solution and reuse may be impractical. Additionally, including the sensor molecules within the solution in which the cells grow increases the possibility of interactions between the cells and dye molecules. Nevertheless, as mentioned previously, water-soluble RTDP has been applied to dissolved oxygen monitoring in microfluidic channels [151, 189].

1.3.3.1   Oxygen-sensitive Indicator Materials

The sensitivity and other properties of optical oxygen sensors are dependent on a number of factors, most importantly the luminophore, or luminescent indicator. There are several properties to be considered when choosing the optimal indicator for a certain application. One of the most important properties of a luminescent indicator is how readily its emission is quenched by oxygen. This factor is dependent on the efficiency of the quenching process itself as well as the excited-state lifetime of the indicator, as the probability of the indicator interacting with oxygen increases when electrons are in the excited state for a longer time period [116]. For the sensor to be usable over long time periods and even be reusable, the indicator should be stable against photobleaching and leaching into the tested sample. The absorption and emission spectra of the dye are also often considered in the selection of luminescent indicators. It is often desirable for these spectra to be compatible with inexpensive and readily available excitation sources, detectors, and filters. Additionally, some materials (such as human plasma [161] and mammalian cells [190]) autofluoresce and this confounding signal can be removed either by the use of an emission filter or a lifetime detection method with good lifetime selectivity (such as frequency domain lifetime detection) after selection of materials/indicators with a sufficiently different emission spectrum or luminescence lifetime. Alternatively, materials with different excitation spectra from those of the autofluorescent materials may be selected to overcome this problem.

Various oxygen-sensitive indicators have been identified and used for various applications. Many of these indicator compounds fall into two main groups: ruthenium-based molecules or

metalloporphyrin-type molecules. Other, less commonly used, oxygen-sensitive compounds include fluorescein compounds [181], polycyclic aromatic hydrocarbons [120], and other organic compounds [122].

The following sections will introduce some of the most commonly used oxygen-sensing compounds and discuss their applicability to microfluidic cell culture. More general reviews of oxygen-sensing compounds may be found in [122], and a review of various phosphorescent metalloporphyrin complexes and their applications (not limited to oxygen sensing) is presented in [191].

Ruthenium-based: Several fluorescent, ruthenium-based compounds have been applied to optical oxygen sensing. Compounds of Ruthenium-tris-4,7-diphenyl-l,l0-phenanthroline ($[Ru(dpp)_3]^{2+}$) [42, 115, 119, 127, 138, 139, 143, 157, 170, 175, 176, 192-195] and Ruthenium(II)-tris(l,l0-phenanthroline) ($[Ru(phen)_3]^{2+}$) [117, 128, 141, 166] are commonly-used examples, and they have been modified to be soluble in silicone films for oxygen sensing [196]. Other Ruthenium compounds used in optical oxygen sensors include dichlorotris (1,10-phenanthroline) Ruthenium (II) hydrate [173] and Ruthenium tris(2,2′-dipyridyl dichloride) hexahydrate [131, 144, 146, 151, 174, 189].

Oxygen-sensitive, fluorescent ruthenium compounds have been used extensively in optical oxygen sensing and have even been previously integrated with microfluidic bioreactors and other devices [42, 151, 174]. While the ruthenium complexes have a high luminescence quantum yield and are very photostable, their short excited-state lifetimes (on the order of 100 ns – 1 μs [197]) lead to lower sensitivity to oxygen than is necessary in certain applications. These applications are in low-oxygen environments (e.g. modified-atmosphere food packaging with oxygen partial pressures of 0-2 kPa [170]), and culture of anaerobic bacteria with dissolved oxygen levels less than 12 ppm [136]), which necessitate highly sensitive oxygen sensors, and alternative oxygen-sensitive compounds such as some of the metalloporphyrin-type indicators fill this requirement. Most metalloporphyrin-type indicators phosphoresce rather than fluoresce, which leads to a lower luminescence quantum yield but a longer excited-state lifetime (on the order of 10 μs -1 ms [116]) and thus a higher sensitivity to oxygen.

Metalloporphyrin-based: Platinum(II)– and Palladium(II)– complexes of octaethyl–porphyrin (Pt- and Pd- OEP) [198, 199] have been used successfully in optical oxygen sensors for *in vivo* applications [166], engineered tissues [142], aquatic sediments [127, 138, 139, 176], microtiter plates [141], intracellular applications [132], and other biological applications [133]. They demonstrate a long luminescence lifetime and high quantum yield but relatively poor photostability, inhibiting their use in many applications.

Platinum(II)– and Palladium(II)– complexes of octaethyl–porphyrin ketone (Pt- and Pd- OEPK) [140] were introduced as another set of potential phosphorescent sensing dyes with improved properties over PtOEP and PdOEP including significantly improved photostability (in [140] the absorbance of Platinum(II) octaethylporphyrin ketone (PtOEPK) was found to decrease by only 12% after 18 hours of continuous ultraviolet (UV) illumination, while that of PtOEP was found to decrease by 90% under the same conditions), longwave emission, and good compatibility with Light-Emitting Diode (LED) excitation sources [200]. PtOEPK in particular has attracted much interest as an oxygen-sensitive probe. Its photostability has been found to be significantly (~10x) higher than that of PtOEP [132], making PtOEPK much more useful in intensity-based measurements and applications requiring long measurement times. Oxygen sensors using PtOEPK have been used in many applications, including glucose biosensors [168], microfluidics and microfluidic cell culture [129, 135, 136, 158, 171], inter- and intra-cellular measurements [118, 132], food packaging [114], and other biological applications [161].

Another category of oxygen-sensitive materials is the benzoporphyrins, which have been identified as highly promising due to their high luminescence brightness and photostability as well as the possibility of tuning their spectral properties for specific applications [201]. Vinogradov, Wilson, and colleagues have developed tetrabenzoporphyrin (TBP) compounds of several metals and found that water-soluble palladium (Pd) meso-tetra(sulfo-phenyl)tetra-benzoporphyrin [Pd(SO$_3$H)$_4$ Ph$_4$TBP] showed promise for oxygen sensing [202]; another TBP complex of Pd (Pd-meso-tetra-(4-carboxyphenyl) tetrabenzoporphyrin) has been commercialized into the water-soluble oxygen probe Oxyphor G2 [203]. Borisov, Klimant, and colleagues have subsequently developed platinum and palladium benzoporphyrin indicators encapsulated in

polystyrene films and poly(styrene-block-vinylpyrrolidone) and polysulfone nanoparticles, demonstrating high brightness and photostability as well as excitation in the red spectral range (desirable for biological applications such as subcutaneous measurements) [204]. Platinum(II) meso-tetra(4-fluorophenyl)tetrabenzoporphyrin (PtTPTBPF) showed good quenching characteristics over the range from 0-21% oxygen when embedded in polystyrene. More recent work by the same group has involved modifying platinum benzoporphyrin complexes to be bound to polymer matrices; covalent immobilization of these dyes into and onto polymer matrices including polystyrene was demonstrated to address the challenge of dye leaching and migration (that can be a particular issue for sensors with a high surface area to volume ratio) [205]. The same group has also recently demonstrated high-sensitivity sensors for trace oxygen applications based upon Pt and Pd benzoporphyrins covalently immobilized within highly oxygen-permeable silicone matrices [206]. The silicone-coupled Pt compound yielded a sensitivity ($Ksv = 0.082\text{-}0.141$ h Pa^{-1}) approximately 3.5 times higher than that reported for the polystyrene-bound Pt benzoporphyrin ($Ksv = 0.0298$ h Pa^{-1}) [205], while the silicone-coupled Pd compound yielded a sensitivity ($Ksv = 0.921$ h Pa^{-1}) approximately 31 times higher [206].

Most of the aforementioned metalloporphyrin compounds are generally encapsulated in a polymer or sol-gel matrix (section 1.3.3.2 discusses these matrices in more detail). Another class of commonly used metalloporphyrin compounds is water-soluble and generally bound to albumin compounds before use. These compounds include platinum (Pt) and palladium (Pd)-coproporphyrin [130, 181, 183, 207], palladium meso-tetra-(4-carboxyphenyl) porphine [149, 182, 183, 185, 208] and the polyglutamic phosphorescent "Oxyphor" probes [186, 187, 203, 209-220], all of which have mostly been used via intravenous injection for *in vivo* biological oxygen imaging. In addition to the water-soluble metalloporphyrins, there are also water-soluble ruthenium complexes, such as ruthenium tris(2,2' -dipyridyl) dichloride hexahydrate (RTDP) [151, 189].

Summary and Applicability to Microfluidic Cell Culture: During microfluidic cell culture, the cells may be in contact with the probe molecule and oxygen sensor as a whole for extended periods of time, extending from hours to days. It is important that these materials be biocompatible, without cytotoxic effects. O'Riordan *et al.* investigated indicator leaching into

various simulated food components and found that the leaching of PtOEPK and $[Ru(dpp)_3]^{2+}$ from polymer matrices into most aqueous solutions (with the exception of 95% ethanol) could not be detected [170]. No evidence of toxicity of the Oxyphor probes has been presented, with studies using Oxyphor R2 in rats at concentrations of up to 6.7 mg/kg body weight (~40 μM in blood) showing no evidence of toxicity up to ten days after injection [221]. Dobrucki [222] found that $[Ru(phen)_3]^{2+}$ can have phototoxic effects. When used as a dye, repeated illumination of a sample caused the plasma membranes of cells to rupture, and the dye was observed to enter the cell nuclei and cytoplasm. This toxicity may be due to the generation of singlet oxygen when the Ru(II) complex is illuminated. Phototoxic effects were not detected for $[Ru(bipy)_3]^{2+}$ in the concentration range of 2×10^{-4} M. Thomas *et al.* [223] observed phototoxicity of PtTFPP-PDMS sensors in close proximity to cell culture, and suggested that this effect could be due to the combination of reactive oxygen species generation and dye diffusion out of the PDMS. They mitigated this effect by incorporating a thin Teflon-AF$^{®}$ layer into their system to reduce dye diffusion into the cell culture.

Many of the oxygen-sensitive compounds are excitable with blue, green, yellow, or orange LEDs [139, 140], offering a great advantage for small, ideally low-cost applications such as microfluidics. The sensitivities of the various ruthenium or metalloporphyrin compounds dictate the oxygen levels at which they are best used (for example, different sensors should likely be used for studying anoxic environments than those used for normal cellular environments or atmospheric conditions).

The water-soluble compounds do not present the same advantages for microfluidic systems as they do for *in vivo* biological imaging, where the possibility of injection of water-based dye solution facilitates less invasive imaging and even imaging through skin. In microfluidics, it may be desirable to use the microfluidic channel and cell culture setup more than once. In this situation integrating the sensor into the channel allows the indicator to be reused as well, potentially lowering the cost of the testing setup. For microfluidic cell culture applications, incubation times can be on the order of hours or even days, often requiring the circulation of fresh culture media over this time period. This application would require significantly more water-soluble luminescent indicator than would be required for a device-integrated sensor if all

of the circulated solution is to be stained. Furthermore, encapsulating the sensor in a polymer or sol-gel matrix reduces the likelihood of unwanted interaction with the sample under test. Nevertheless, there are advantages (such as obtaining 3-D maps of oxygen distributions) to adding the indicator to the fluid in microfluidic channels, and this use has been previously demonstrated using RTDP [151, 189]. Table 1.1 presents a summary of indicators in various encapsulation materials along with some of their properties.

Table 1.1. Properties of luminescent oxygen indicator materials in various encapsulation matrices as previously reported.

Indicator	Encapsu-lation Matrix	Unquenched Lifetime (μs)	Quantum Yield	Reported Sensitivity [*]	Excitation Peaks (nm)	Emission Peaks (nm)	[Ref]
$[Ru(dpp)_3]^{2+}$	Polystyrene	5	NR	22% signal decrease from N_2 to air	450	600	[139]
$[Ru(dpp)_3]^{2+}$	Plasticized PVC	5	NR	50% signal decrease from N_2 to air	450	600	[139]
$[Ru(dpp)_3]^{2+}$	None	6.3 at 23°C (silicone-soluble ion pair in 2-butanone)	0.3 (in water/ ethanol) 0.35 (silicone-soluble ion pair in 2-butanone)	$k_Q = 2.5 \times 10^9$ $(dm^3 mol^{-1}s^{-1})$ (in methanol)	460	613, 627	[116, 196]
$[Ru(phen)_3]^{2+}$	None	0.74 at 23°C (silicone-soluble ion pair in 2-butanone)	0.08 (silicone-soluble ion pair in 2-butanone)	$k_Q = 4.2 \times 10^9$ $(dm^3 mol^{-1}s^{-1})$	447,421	605, 625	[116, 196]
$[Ru(Ph_2phen)_3]^{2+}$	Sol-gel silica	5.8	NR	$\tau_{N2}/\tau_{O2} = 5$	NR	NR	[224]
$[Ru(bpy)_3]^{2+}$	None	0.6	0.042	$k_Q = 3.3 \times 10^9$ $(dm^3 mol^{-1}s^{-1})$	423, 452	613, 627	[116, 181]
$[Ru(bpy)_3]^{2+}$	Sol-gel silica	1.26	NR	$\tau_{N2}/\tau_{O2} = 2$	NR	NR	[224]
PtOEPK	Polystyrene	61.4 at 22°C	0.12	$\tau_{N2}/\tau_{air} = 3.59$	398, 592	759	[140]
PtOEPK	PDMA	NR	NR	Q_{DO}=97.5%	NR	754	[161]
PdOEPK	Polystyrene	480 at 22°C	0.01	Very high	410, 602	790	[140]
PtOEP	Polystyrene	94.7 at 20°C	NR	τ_0/τ_{air}=3.60	383, 535	647	[139, 199]
PtTFPP	Polystyrene	$\tau_{0f} = 45.8$; $\tau_{0s} = 14.2$	NR	$I_0/I_{100} > 3$	305, 508, 541	650	[225, 226]

Indicator	Encapsu-lation Matrix	Unquenched Lifetime (µs)	Quantum Yield	Reported Sensitivity [*]	Excitation Peaks (nm)	Emission Peaks (nm)	[Ref]
PtTPTBPF	Polystyrene	52.6	NR	K_{SV} = 0.218 kPa^{-1}	431, 566, 617	777	[204]
PtTPTBPBr	Covalently grafted to polystyrene (0.41 wt%)	46 (in de-oxygenated toluene)	0.48 of that of platinum(II) tetraphenyl-tetrabenzo-porphyrin	K_{SV1} = 0.0298 h Pa^{-1}	616 (in de-oxygenated toluene)	774 (in de-oxygenated toluene)	[205]
Pd-coproporphyrin	None (aqueous solution)	530 (no BSA), 1200 (BSA)	0.2	k_Q = 195 mm Hg^{-1}s^{-1}	393. 545	667	[181, 227]
Pt-coproporphyrin	None (aqueous solution)	100	0.4	NR	380, 535	650	[227]
Pd-meso-tetra-(4-carboxy-phenyl) tetrabenzoporphyrin-dendrimer (Oxyphor G2)	None (BSA solution at pH 6.8, 23.5°C)	276	0.12	k_Q = 195 mm Hg^{-1}s^{-1}	442, 632	800	[203, 209]
Pd-meso-tetra-(4-carboxyphenyl) porphyrin-dendrimer (Oxyphor R2)	None (BSA solution at pH 6.8, 23.5°C)	738	0.1	k_Q = 270 mm Hg^{-1}s^{-1}	415, 524	700	[203]
Pd-meso-tetra (4-Carboxyphenyl) Porphine (Oxyphor R0)	None (albumin solution at pH 6.8, 23°C)	705	0.06	k_Q = 246 mm Hg^{-1}s^{-1}	416, 523	687	[209]

NR: Not Reported.

* Different measures of sensitivity were reported in different papers, and the values quoted in this table were those reported in the reference.

1.3.3.2 Matrix Materials

As mentioned previously, the luminescent indicator compound is often immobilized and encapsulated in a polymer or sol-gel matrix to improve sensor properties and reduce unwanted interaction with the sample under test. The encapsulation matrix can be patterned and holds the luminophore in place on the substrate. The encapsulation matrix has been found to greatly affect many of the properties of the oxygen sensor, such as its sensitivity and Stern-Volmer calibration function [169]. In particular, the oxygen diffusion constant of the polymer matrix is a very important parameter; it controls how easily the oxygen in the sample can migrate to the indicator

compound and as a result greatly affects the sensitivity and response time of the sensor [116]. This section introduces some of the commonly used immobilization matrices and discusses their applications and potential for use in microfluidic cell culture. Further detail on encapsulation matrices in general can be found in the literature [122, 169, 228, 229].

Polymers: Several criteria need to be taken into consideration when choosing a polymer matrix for a luminescent oxygen-sensitive indicator. Aside from the aforementioned permeability to oxygen, the matrix's mechanical stability is an important property in applications such as aquatic sediment mapping, however in microfluidic cell culture this property is often less important. If the sensor is patterned on the channel surface, the adhesion of the sensor and thus the polymer matrix to the channel should be sufficient such that microfluidic flow does not detach or damage the sensor. If the sensor is to be reused, the polymer matrix needs to be able to withstand whatever cleaning process is necessary. For microfluidic cell culture, the polymer matrix must be biocompatible. Finally, the chosen indicator needs to have good solubility in the matrix material in order to form homogeneous sensor films.

Commonly used polymers and corresponding references for their use in optical oxygen sensors include: polystyrene for $[Ru(dpp)_3]^{2+}$, PtOEPK, PdOEPK, PtTFPP, and PtOEP indicators [109, 114, 117, 127, 129, 133, 135, 136, 138-141, 158, 163, 166, 168-172, 225, 226, 230]; poly methyl methacrylate (PMMA) for PtOEP [139]; poly decyl methacrylate (PDMA) for PtOEPK [161], polyvinyl chloride (PVC) for PtOEPK, PdOEPK, and $[Ru(dpp)_3]^{2+}$ [118, 139, 169]; ethyl cellulose for $[Ru(dpp)_3]^{2+}$ [117]; and silicones for PtOEP, $[Ru(dpp)_3]^{2+}$, and to encapsulate dye-adsorbed silica beads [117, 128, 134, 142, 167]. Additionally, working sensors have been created using $[Ru(phen)_3]^{2+}$ in photopatternable silicone [173].

Although the addition of plasticizers to polymer matrices such as PVC allow sensor properties such as response time and sensitivity to be optimized for applications of interest, their use can lead to significant changes from the ideally linear Stern-Volmer calibration equation of the resultant oxygen sensors [169].

Silica, Ormosil, and Sol-gel: Indicators such as $[Ru(phen)_3]^{2+}$ have been adsorbed to silica microbeads [117, 128, 167] and then either used as-is or encapsulated in silicone films. Organically modified silica (ormosil) and sol-gel particles and layers have also been developed and optimized in an effort to improve the properties of optical oxygen sensors [228]. Ormosils and sol-gels are very promising as encapsulation matrices, showing excellent optical and physical properties and good porosity/permeability to oxygen as well as the ability for the layer properties to be customized to various sensor applications [228, 229]. Oxygen sensors using them have been developed [127, 157, 177, 193, 231, 232] and used in various applications, including aquatic sediments [119, 176].

Summary and Applicability to Microfluidic Cell Culture: Most of these commonly-used encapsulation media are applicable to microfluidic cell culture, and the best choice for a particular application depends on the indicator of interest, the desired level of sensitivity, and the desired sensor format. Previous applications in microfluidics have predominantly used polymer encapsulation matrices such as polystyrene [129, 135, 136, 158, 171] and poly(dimethylsiloxane) (PDMS) [134]. These polymer matrices tend to be easier to pattern and integrate with polymer microfluidic systems; however, there still exist issues with microfluidic integration, as discussed in the following section.

1.3.3.3 Thin-film Sensor Patterning

One often-used method for integrating optical oxygen sensors into microfluidic devices is incorporating thin sensor films within the microfluidic channels. This method is attractive for microfluidic cell culture applications because patterning the films offers the potential to isolate the sensors to specific parts of the channel, permitting unobstructed imaging of the cell cultures while also minimizing interaction of the sensor dyes with the cells. Luminescent sensing molecules can be encapsulated in polymer or sol-gel matrices [122] in order to form an oxygen-sensitive film that may be integrated with microfluidics. One commonly-used sensor film is platinum octaethylporphyrin ketone (PtOEPK) dye encapsulated in a polystyrene (PS) matrix [140]; this type of film has been found to have good oxygen sensitivity and photostability. A ratiometric alternative is the use of Platinum(II)-5,10,15,20-tetrakis-(2,3,4,5,6-pentafluorphenyl)-porphyrin (PtTFPP) along with Macrolex fluorescent yellow, also encapsulated within a PS film.

To make such films, the dye(s) and polystyrene can be dissolved in a solvent such as toluene or chloroform to yield sensor cocktails. The sensor cocktail can then be directly dispensed to form patches (via pipetting) [135, 136, 158] or spin- or knife-coated [109, 129] to form sensor films on glass substrates for integration with microfluidic devices. Because the measured luminescence intensity of the sensing film is dependent on film thickness, uniform spin- or knife-coated polymer sensor films are ideal for intensity-based or ratiometric sensing.

A complication of the spin-coating method is that for un-patterned films, non-standard bonding methods such as the use of silanes [233, 234] or carefully controlled air plasma parameters [235] must be used to facilitate the bonding of polystyrene with poly(dimethylsiloxane) (PDMS) microfluidic devices. Another issue is that polystyrene films adhere poorly to glass, greatly limiting the mechanical stability of the microfluidic device even if PS-PDMS bonding is achieved. Although the films are transparent, the presence of a sensor film at the bottom of the channel could affect sensitive imaging of other components of the microfluidic system (for example, slightly uneven sensor films could contribute to scattering effects degrading image quality during confocal microscopy). The bonding problem can be addressed by the use of a spin-coated PDMS film on top of the sensing layer [109], but patterning the films is necessary to address both issues with microfluidic integration.

While PtOEPK/PS films can be spin-cast onto glass substrates to form uniform sensor films with good intensity sensing characteristics, patterning of the films for subsequent integration into microfluidics can be difficult because common photoresist solvents and strippers attack the polystyrene matrix. Alternative sensor types involve hot embossing PtOEPK/PS films to generate microwells for cell culture [236], or incorporating oxygen-sensitive indicator molecules directly into photoresist or photopatternable PDMS matrices to form inherently photopatternable films [173, 237]. Although the photoresist-based films were tested for cell adherence and short-term culture, photoresists are often not biocompatible so these types of films may not be suitable for many lab-on-a-chip applications involving long-term cell culture. To pattern spin-coated PtOEPK-PS films, dry etching methods employing a pinhole-free metal etch mask [172, 238] and removable PDMS 'stamps' [129] have been proposed. We have found, however, that a residue exists after polystyrene dry etch processes that inhibits subsequent bonding of PDMS

microfluidic devices [239]. For this reason, the development of new fabrication processes for optical oxygen sensor patterning could aid in the applicability of these sensors to applications in microfluidic cell culture.

1.4 Microfluidic Systems for Oxygen Control and Measurement

Microfluidic devices are ideal for controlling oxygen levels within an environment for cell culture because their small size scales afford precise control and can mimic the kinds of gradients that can exist *in vivo* near blood vessels. A range of microfluidic devices have been previously developed to create and measure static oxygen levels, oxygen gradients, and time-varying oxygen profiles. These devices can offer fast switching times and excellent control to recreate the kinds of oxygen profiles that can exist *in vivo*. The integration of optical oxygen sensors into some of these microfluidic cell culture devices facilitated real-time and *in situ* oxygen concentration measurements within compact, controllable, and functional microfluidic cell culture setups, which would not otherwise have been possible.

1.4.1 Advantages of Microfluidic Devices for Oxygen Control and Measurement

Microfluidic systems present a number of advantages for studying the role that oxygen plays in biological systems, and can facilitate both oxygen control and measurement. Microfluidic integration of optical oxygen sensors in close proximity with single cell traps can facilitate the measurement of single cell oxygen consumption rates due to the small size scales of the microfluidic device. Cells trapped in microwell arrays [240] and in SU-8 negative epoxy photoresist micro-cups [241] have been studied using patterned sensor rings formed from PDMS-encapsulated oxygen-sensitive microspheres and photopatternable SU-8-encapsulated platinum porphyrin indicator, respectively. Combining single-cell isolation and analysis with oxygen sensing as was accomplished in these works could potentially provide a useful tool for researchers studying cell metabolism and other phenomena at a single-cell level. In collaboration with Microfluidic ChipShop, several interesting microfluidic systems in polymers [242] and in silicon-glass [243] that integrate lifetime-based optical oxygen sensors have been recently demonstrated, taking advantage of the small size scales of microfluidics to measure the oxygen consumption by cells and monitor oxygen levels in enzyme transformations (such as glucose oxidation by glucose oxidase).

Sin *et al.* reported a three-chamber microfluidic cell culture analog device employing an optical dissolved oxygen sensor [42]. The device was used to culture three types of mammalian cells in interconnected chambers, forming a compact platform simulating animal testing for chemicals and pharmaceuticals. The integrated dissolved oxygen sensor enabled real-time readout of the oxygen levels in the circulating culture media. The oxygen sensor used a compound of $Ru[dpp]_3^{2+}$ immobilized onto resin particles, encapsulated in thin-film PDMS sensor patches on the substrate. Frequency-domain lifetime sensing was used, employing LED excitation and photodiode detection. The device as presented in the original journal paper [42] is presented in Figure 1.7. This work highlights some of the advantages that microfluidic platforms can bring to cell culture systems. The design permitted the culture of cells in three interconnected chambers which represented the lung, liver, and other tissue compartments in a pharmacokinetic model. Flow characteristics, including liquid residence times and shear stress on cells, were controlled to be within physiological values. The ability to measure oxygen within the design allowed Sin *et al.* to monitor gas exchange. By providing more realistic models for drug adsorption, distribution, and metabolism kinetics in pharmacological testing, further development of such systems can contribute to reducing the need for animal testing.
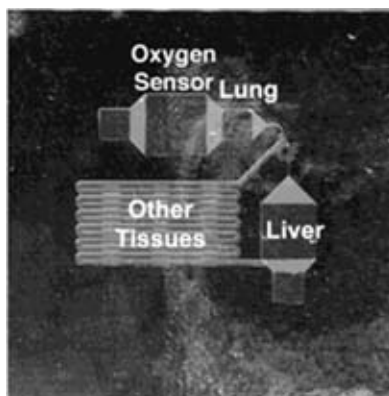
Figure 1.7. Photograph of Sin *et al.*'s fabricated three-chamber microfluidic cell culture analog device with integrated optical oxygen sensor. Reprinted from [42] with permission from John Wiley and Sons.

Microfluidic devices are also very attractive for oxygen control due to the level of spatial as well as temporal control that they can facilitate. The permeability of poly(dimethylsiloxane) (PDMS) microfluidic devices to oxygen is very high, which permits the use of separate channels (separated by thin PDMS membranes) to control the oxygen levels. The use of separated

channels presents an advantage over systems that provide gases in direct contact with the cell culture media because of the potential for sterility issues. Additionally, the diffusion distances between the channels in a microfluidic device can be very small. These small size scales combined with the commonly used low flow rates within the microfluidic devices can ensure that mass transport is diffusion-dominated. The short diffusion distances also lead to fast equilibration times, which facilitate the creation of time-varying oxygen profiles with fast switching times, recreating the kinds of switching times of several cycles per hour that have been seen in animal tumour models.

1.4.2   Oxygen Gradient Generators

One method that has been employed to create oxygen gradients is to use cellular oxygen consumption. In these devices, oxygenated media is input to the device, and oxygen is depleted from the fluid due to cellular respiration as it travels down the channel. Sud *et al.* integrated optical dissolved oxygen sensors into microfluidic channels containing C2C12 mouse myoblasts to monitor the oxygen levels as a function of space and of cell density [189]. From the same group, Mehta *et al.* integrated optical dissolved oxygen sensors into a microfluidic bioreactor and took measurements upstream and downstream of adherent cells cultured in the microchannel, finding that the downstream oxygen concentration was highly dependent on cell density and fluidic flow rate [151]. Both of these works used the water-soluble oxygen indicator RTDP dissolved in the fluid pumped through the channels. Both intensity-based measurements and RLD-based lifetime imaging modalities were used. Although they used a high concentration of 1 mg/mL (approximately 1.3 mM) RTDP in order to obtain useful fluorescence signal with low exposure time, the presence of this dye in the culture media contributed to less than 10% of the cell death over the course of 5 hours during this work. However, longer incubation periods exceeding 1 day in this concentrated dye did decrease cell viability, so it would not be suitable for the long-term studies required for many investigations of tumour hypoxia.

Mehta *et al.* [244] have also found that by using a combination of PDMS and rigid polymers in the construction of a perfusion cell culture system, lower oxygen tension can be achieved than in devices constructed entirely of PDMS. Using RTDP dissolved in solution, they verified that they could achieve oxygen concentrations as low as 1% using glycol-modified polyethylene

terephthalate (PETG) channels bonded to flexible PDMS membranes. The flexible PDMS bottom permitted the use of deformation-based on-chip valving and pumping, while the relatively oxygen-impermeable, rigid PETG material permitted them to reach the low oxygen conditions which are needed for studies of embryonic and stem cell differentiation, ischemia, and cancer. Lin *et al.* integrated several dissolved oxygen and glucose sensors along the length of a cell culture microchannel so as to quantify concentration gradients in the cells' environment along the channel [134]. The sensors were fabricated using a ruthenium dye embedded in PDMS, which was used to fill microtrenches in the PDMS microchannel walls, and intensity-based measurements were used. The work found that both the oxygen and glucose concentrations in the channel were dependent on the fluidic flow rate; this was expected because the cultured cells' oxygen and glucose consumption remained relatively constant while the supply of oxygen and glucose was altered by the change in flow rate. Although the cellular consumption method of oxygen gradient generation is simple and can model consumption-driven oxygen gradients *in vivo*, it is somewhat limited in the kinds of gradients that it is able to create.

A more flexible method is the use of separated control channels within the device to control the oxygen levels over a cell culture or chamber of interest. Lam, Kim, and Thorsen have created a microfluidic oxygenator with an array of channels of differing oxygen concentrations for cell culture, employing an optical dissolved oxygen sensor integrated at the end of each microchannel. The oxygen gradient generator, which was comprised of one inlet for O_2 and one for N_2 gas followed by a network of mixing channels leading to a number of parallel outlet channels, yielded different dissolved oxygen concentrations in each outlet microchannel. Integrated PtOEPK-polystyrene thin-film sensors permitted *in situ* measurement of these concentrations during cell culture. The device schematic diagram, fabricated device, and microscope image of the gradient generator are presented in Figure 1.8 [135]. Intensity-based imaging employing LED excitation and photodiode detection was used. This system has been used to culture mammalian cells as well as aerobic and anaerobic bacteria to investigate the effect of dissolved oxygen concentrations on the growth patterns of cells of differing oxygen requirements [135, 136].

Several other groups have presented devices to make spatial gradients in oxygen levels in a microfluidic device, using gases [245, 246], gas-equilibrated liquids [247, 248], and oxygen-generating and oxygen-scavenging chemicals and chemical reactions within control channels [249, 250]. The oxygen transport within a multilayer microfluidic oxygen control device using flowing gases has been modeled by Kim *et al.* and compared with measurements using a PtOEPK-polystyrene thin film optical oxygen sensor at the channel bottom [251]. Good agreement was found between the analytical model and experimental measurements.

One potential complication of the use of pressurized gases to control the oxygen levels is the tendency for bubbles to form in the cell culture channel, or for the media in the cell culture channel to evaporate through the thin PDMS membrane. A solution to this issue is the use of gas-equilibrated liquids as the control media; however, accurate control necessitates the use of very high flow rates that are impractical to provide via syringe pump. Additionally, the time necessary to oxygenate/deoxygenate these fluids adds to the equilibration time of the system, precluding the possibility of creating fast switching times within the device. As another solution to the problem of evaporation and bubble formation, Wood *et al.* have reported the use of a hydration layer between the gas-containing control layer and the sample [252]. A review on oxygen control using microfluidic platforms summarizes the various methods that have been employed [253].
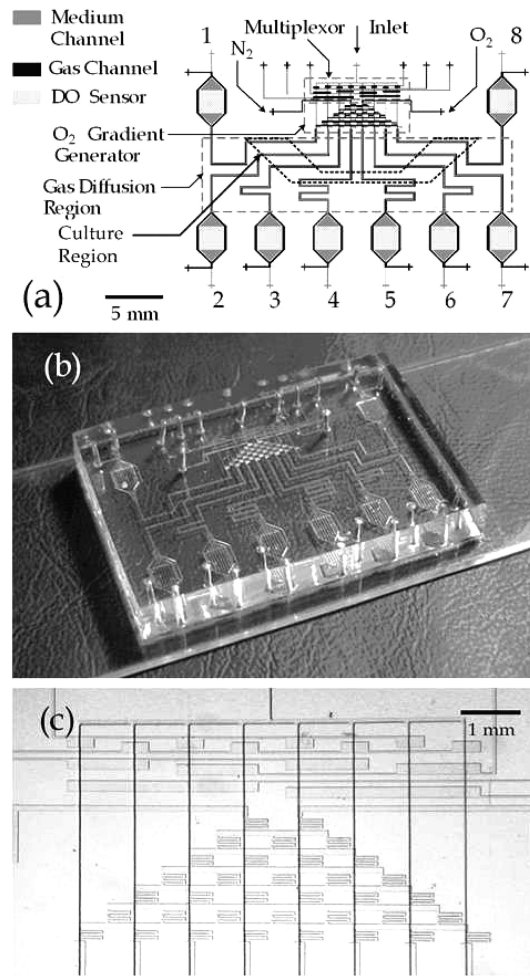
Figure 1.8. Lam *et al.*'s two-layer microfluidic oxygenator device permitting the on-chip study of several oxygen environments. (a) Schematic diagram of the microfluidic oxygenator with integrated oxygen sensors. (b) Photograph of the fabricated oxygenator device. (c) Microscope image of the microfluidic multiplexor and oxygen concentration gradient generator. Reprinted from [136] with permission from the American Chemical Society.

1.4.3   Microfluidic Devices for Intermittent Hypoxia

Microfluidic systems have also been used to create cyclic oxygen profiles. Groisman *et al.* presented a microfluidic device with integrated spatiotemporal control of oxygen levels, demonstrating oxygen switching times on the order of seconds within a thin, multilayer microfluidic device with a gas control layer [254]. Oppegard *et al.* presented a microfluidic insert containing control gas channels for a 6-well plate to modulate the oxygen levels over adherent cell cultures, demonstrating equilibration times on the order of minutes [255]; the same group used a similar device to control the oxygen levels within a Boyden chamber, showing equilibration times of approximately 20 minutes [256]. Both of these works showed impressive spatiotemporal control of the oxygen levels, stable oxygen levels over several days, as well as

47

biological validation of the devices. However, there remained potential for media evaporation through the PDMS membrane and into the flowing gas used to control the oxygen levels during multi-day culture in these devices (the authors took steps to pre-hydrate the PDMS to discourage evaporation through it, mitigating this effect for shorter term experiments). Oppegard *et al.* [256] used slides pre-coated with an oxygen-sensitive ruthenium complex (FOXY SGS; Ocean Optics) to study breast tumour cell migration. Fluorescence intensity measurements employing a fluorescence microscope and CCD detection were used to quantify the oxygen levels in the device in order to determine the effects of oxygen levels on tumour cell migration through a porous membrane. A parylene C coating on the highly oxygen-permeable PDMS was used to control the oxygen diffusion through the device, enabling the study of hypoxic oxygen levels. Their use of intensity-based optical oxygen sensors could induce instabilities over long-term experiments due to fluctuations in the fluorescence excitation intensity as well as due to the effects of photobleaching or dye leaching.

Similar oxygenators employing microfluidic gas control channels have also been applied to spatiotemporal control of oxygen over *ex vivo* pancreatic islets (1 minute cycles of 5% and 21% oxygen for one hour) [257] and brain slices (spatial oxygen control to expose part of the slice to hypoxia, as well as temporal oxygen control with equilibration times of ~10 minutes) [258]; both of these works used non-integrated commercial probes to measure the oxygen levels. Another work used a microfluidic device, again with gas control channels, to expose cardiomyocytes to different transient hypoxic profiles and measure the oxygen levels using a water-soluble optical ruthenium-based probe, showing a dependence of steady-state oxygen level on liquid flow rates [259]. Wood *et al.* used a three-layer microfluidic device to study the effects of deoxygenation on red blood cell velocity under constant pressure, using a hydration layer between the gas and liquid to prevent blood dehydration and using a commercial oxygen probe to measure oxygen levels in the gas phase during the experiment [252].

1.4.4   Integration of Oxygen Control and Measurement with 3-D Cell Cultures

There has also been recent work towards the integration of oxygen control and measurement with 3-D cell cultures over the past few years. Funamoto *et al.* [246] have recently demonstrated an oxygen control device which was used to study MDA-MB-231 breast tumour cell migration

within a chamber containing collagen I. This work used an oxygen control device with gas channels on either side of the cell culture and a polycarbonate film embedded in the PDMS above the cell culture to reduce diffusion of oxygen in the vertical direction. A commercial ruthenium-based thin-film sensor was used to quantify oxygen gradients within the device. Wang *et al.* [260] have used ratiometric oxygen-sensitive beads to quantify oxygen levels within human colon carcinoma cell line cultures on micropatterned collagen and PDMS surfaces. Jaeger *et al.* [261] have demonstrated an impressive multilayer bioreactor system that used oxygen-permeable silicone hydrogel micropillars extending into a cell culture chamber to control oxygen levels around ovarian carcinoma cells cultured in 3-D Matrigel®. The silicone hydrogel micropillars mimicked blood vessels in tissue, and the authors observed cell arrangement around the oxygen-source micropillars as well as hypoxic gradients extending outward from the pillars into the cells.

To study dynamic hypoxia on 3-D cultures, Mauleon *et al.* [258] have exposed brain slices to transient hypoxic profiles, while Lo *et al.* [257] have exposed pancreatic islets to cycling hypoxia. Although these systems are innovative, they do not contain integrated sensors, were not optimized for the culture of tumour cells, and were used for shorter-term studies (hours) than those required for the study of tumour hypoxia (days to weeks). The development of a system for 3-D tumour cell culture with integrated spatiotemporal oxygen control and measurement optimized for long-term studies could facilitate improved understanding of various factors associated with chronic and acute or cyclic tumour hypoxia. Such a system could also be used in future work to study the interaction of tumour cells within a microscale model of microvasculature to identify the factors which contribute to angiogenesis [262, 263] and further build upon the results of Ehsan and George, which suggested a dependence of blood vessel formation on the frequency of cycling hypoxia [103].

1.5 Research Question and Thesis Objectives

The ultimate goal of this work was to develop a platform to study the effects of various hypoxic regimes on tumour cells in 3-D culture. This platform needed to integrate the spatiotemporal control and measurement of oxygen into an environment for the *in vitro* testing of cancer treatments on 3-D cell cultures, in order to expose cells under test to chronic and transient hypoxic profiles. The purpose was to create a more physiologically relevant platform for

eventual use in the study of hypoxic tumour cell behaviour and the *in vitro* testing of cancer treatments. With this in mind, three main objectives of this platform were identified, and several challenges were addressed in order to meet these objectives:

1. Create a system for 2-D and 3-D cell culture and image-based analysis within a microfluidic device (Chapter 2). This system needed to address several challenges facing the use of 3-D culture and is composed of:

    a. 3-D cell cultures within a physiologically relevant environment suitable for long-term culture.

    b. A microfluidic device to immobilize 3-D cell cultures, permitting monitoring of their behaviour and growth. A new system was designed to monitor the device using both upright and inverted microscopes while keeping the microfluidic device immersed in liquid to prevent bubbles or osmolarity changes in the cell culture. Additionally, modified trapping structures were developed to improve 3-D culture retention in the traps during long-term culture.

    c. Improved methods for imaging 3-D cell cultures to permit image data acquisition from the heterogeneous tumour spheroid environment without dissociating the spheroid. Imaging problems due to light scattering are a known obstacle to the use of 3-D cultures, so a novel imaging protocol and on-chip tissue clearing methods were implemented to address this issue.

2. Measure the oxygen levels using sensors integrated into the microfluidic device (Chapter 3). As drug screening experiments often involve multi-day experiments, robust oxygen sensors are required to ensure that the oxygen profiles are stable for long time periods. The sensors also need to be capable of characterizing spatiotemporal changes in oxygen levels within the device and compatible with fluorescence microscope readout. Ratiometric thin-film optical oxygen sensors were chosen for this system to improve sensor response robustness, facilitate fluorescence microscope readout, and minimize interaction between the dye molecules and eventual cells under test. Novel patterning methods were developed to address challenges with PDMS bonding and permit integration within the microfluidic system.

3. Create spatially- and temporally-varying oxygen levels inside the microfluidic device, mimicking the kinds of oxygen profiles found inside breast tumours (Chapter 4). A testing system was also necessary to provide automated gas profiles to the microfluidic device. A novel microfluidic gas control device, compatible with the imaging and 3-D cultures described in (1), was developed and characterized to provide:

   a. Maintenance of cell culture conditions. Bubbles and pervaporation through the device were controlled using hydration channels in order to maintain fluid osmolarity in the cell culture.

   b. Precise oxygen control, capable of reaching severe hypoxic regimes (0.1% or lower). A design surrounding the cell culture channel with gas control channels on three sides was simulated, implemented, and characterized to meet these criteria.

   c. Fast oxygen equilibration times, in order to reproduce the kinds of transient oxygen profiles that can exist in tumours (a few cycles per hour). The design implemented to address (b) also facilitated fast oxygen equilibration.

The resulting platform should permit the quantitative study of the effects of oxygen on cancer cells and cancer treatments while mimicking the oxygen gradients in time and space naturally found in human tissue. As a biological proof-of-concept, we aimed to demonstrate (primarily in Chapter 5):

1. Cell proliferation within the microfluidic device, demonstrating compatibility of the system.
2. The ability to monitor 2-D and 3-D cell cultures inside the device.
3. The ability of the system to monitor cells' response to hypoxic conditions and intermittent hypoxia.
4. The ability of the system to monitor cells' response to cancer treatments while exposed to hypoxic conditions and intermittent hypoxia.

Chapter 2 Microfluidic Cell Culture System and Image-Based Analysis

The first component of the platform to expose 2-D and 3-D cell cultures to chronic and transient hypoxic profiles was a system for microfluidic cell culture; the goals for this system are presented in section 2.1. First, it was necessary to develop a device in which to grow and monitor the cells in 3-D during long-term cultures. A brief overview of the cell-laden hydrogel beads developed by other members of our research group and used to maintain the cells in 3-D culture is presented in section 2.2, and an overview of the microfluidic chips for immobilizing the beads is presented in section 2.3. As highlighted in section 1.1.2.1, data readout from 3-D cell cultures is very challenging due to optical scattering effects caused by refractive index discontinuities between the media, lipid membranes, and cytoplasm of the cells. This scattering precludes imaging of the cores of tumour spheroids using standard confocal microscopy, causing low fluorescence image intensities as well as blurred images at depths deeper than ~50 μm into the spheroid. This is problematic because, as discussed in section 1.1.2 the cells within a spheroid are exposed to heterogeneous conditions from the exterior to the core, and many of the more interesting effects that spheroids can model (diffusion gradients of oxygen, nutrients, and drugs as well as cell-cell interactions, hypoxic and necrotic regions) are more apparent near the core of the spheroid (with hypoxic cores forming in ~100 μm spheroids [15] and necrotic cores in ~600 μm spheroids [16]).

For this reason, before the system could be used for quantitative biological experiments it is necessary to improve data readout capabilities. As a result, several investigations into improving imaging of 3-D cell cultures were conducted and are described in section 2.5. The first of these was two-photon imaging of live cells, which improves optical penetration into spheroids due to the less scattering-susceptible longer-wavelength excitation of two-photon imaging. This long-wavelength excitation also reduces photodamage to cells, facilitating 3-D monitoring of tumour spheroids. This first investigation of two-photon imaging is presented in section 2.5.1. Although two-photon microscopy improved optical imaging of spheroids compared to standard confocal microscopy, imaging was still limited to depths of ~80 μm. To improve image intensity deeper in the spheroid, laser intensity modulation was investigated, wherein the power of the excitation laser was increased with depth into the spheroid in order to compensate for light lost to

absorption and scattering; this method could be used on either live or fixed spheroids, and the results of this study are presented in section 2.5.2. Although intensity modulation increases the fluorescence intensity, facilitating imaging deeper in the spheroid, it does not address the blurring also induced by scattering effects (described and shown in Figure 1.1). To address both of these issues, previously-demonstrated tissue clearing methods were adapted for 3-D cell cultures and implemented in the same microfluidic devices used for 3-D cell culture, offering improved imaging characterization at the endpoint of 3-D culture studies; this study is presented in section 2.5.3.

2.1   Goals

The purpose of the microfluidic 3-D cell culture system was to create a controlled environment in which to study the tumour cells and their interaction with their surroundings, as well as the imaging tools necessary to extract data from the 3-D cell cultures. To fulfill this purpose, the following goals were identified for the microfluidic 3-D cell culture system:

1. The capability to grow and optically monitor an array of individual 3-D cell cultures in a manner that could potentially be scaled to future drug screening applications.
2. Compatibility with on-chip oxygen control as well as the integration of optical oxygen sensors.
3. Compatibility with 3-D monitoring of the cultures using confocal or two-photon microscopy.
4. The ability to permit staining of the spheroids and 3-D imaging at the study endpoint. As an initial goal we aimed to visualize from the spheroid periphery to its centre. The initial spheroid/3-D culture size chosen for this study was 300 μm in diameter.

2.2   Microfluidic 3-D Cell Cultures
2.2.1   Maintenance Cultures

For all cell-based experiments, cells were grown in 2-D in standard T25 and T75 polystyrene cell culture flasks (Corning, Falcon) prior to use. Four different cell lines were used over the course of this work. Normal Murine Mammary Gland (NMuMG) cells were kindly donated by Dr. Christopher Maxwell and cultured in Dulbecco's Modified Eagle's Medium (DMEM) completed with 10% Fetal Bovine Serum (FBS), 10 μg/mL insulin, and 1% penicillin-streptomycin.

Parental Michigan Cancer Foundation (MCF)-7 human breast cancer cells were kindly donated by the group of Dr. Calvin Roskelley and cultured in Dulbecco's Modified Eagle's Medium F-12-HAM (DMEM/F-12-HAM) completed with 5% FBS (Invitrogen), 2.5 mM L-Glutamine (Invitrogen), and 0.05 mg/mL gentamicin sulphate (Bio Basic). In case of contamination risk, 1X anti-anti (Gibco, antibiotic-antimycotic composed of 100 units/mL penicillin, 100 μg/mL streptomycin, and 0.25 μg/mL Fungizone® amphotericin B antimycotic) was used in place of the gentamicin. Some of these parental MCF-7 cells were also stably transfected to express the FUCCI cell cycle indicator by Soroush Nasseri and Tak Poon and maintained in the same media as the parental MCF-7 cells. Finally, GFP-LC3-expressing MCF-7 cells were kindly donated by the group of Dr. Marcel Bally, and maintained in Roswell Park Memorial Institute (RPMI) cell culture medium completed with 10% FBS and 0.05 mg/mL gentamicin sulphate or 1X anti-anti as described above. All cells were kept in a standard cell culture incubator at 37°C with 5% CO_2 and passaged every 3-7 days at a split ratio of 1:10-1:20, as they grew to confluence.

2.2.2 3-D Cell Culture Formation

The initial implementation of microfluidic 3-D cell culture integrated with the oxygen control and measurement platform used a 3-D, alginate-based cell culture platform [46, 264] that involved forming a hydrogel matrix with entrapped cells in part of a microfluidic channel and flowing nutrient-replenishing cell culture media containing the treatments to be tested through the remainder of the channel. The hydrogel-based platform mimics the extracellular matrix, allowing the formation of multicellular tumour spheroids and the transport of nutrients, treatments, and waste products to and from the cells. Compared with standard spheroid culture platforms such as hanging drop, low attachment plates, and spinner culture, this platform offered the advantage of constant media perfusion to replenish nutrients and mimic physiologic perfusion. The disadvantage of this platform was that it did not facilitate the integration of components of the natural extracellular matrix such as collagen. Additionally, the size of the tumour spheroids that formed within this platform could not be well controlled, as the hydrogel was formed within a large portion of the microchannel and multiple spheroids formed within the same bar of alginate.

To address these limitations, our group has developed cell cultures based on alginate microbeads. By microfluidically-generating beads using droplet generation and subsequent alginate gelation, cell-laden beads of relatively uniform size can be formed. Over a period of ~6 days, the dispersed cells in these beads will proliferate into tumour spheroids, and the uniformly-sized beads lead to reasonably uniform cell numbers in each bead [44]. This uniformity makes the system relevant for array-based high throughput drug screening assays.

In order to further improve the bead-based cultures, beads with a core-shell structure were created in order to reduce cell proliferation out of the bead. These beads are generated using microfluidic flow focusing prior to droplet generation [265] or a two-step process in which cell-laden beads are first generated and then subsequently suspended in alginate solution and input to another droplet-generation chip [266], and the formed beads are composed of a core containing dispersed cells and a shell with no cells. This structure allows the beads to prolong 3-D culture, as the cells can form 3-D spheroids and grow for a longer period of time before proliferating out of the bead and growing in monolayer. As evidence for this effect, our tests of cancer drugs on these cell-laden beads demonstrate multicellular resistance; the half-maximal inhibitory concentration (IC_{50}, or the drug concentration at which half the cell growth is inhibited) of the cells in bead-based 3-D cultures exposed to tamoxifen was 6-9 times greater than that for monolayer culture [265, 266]. The core-shell structure also facilitates the generation of beads that contain components of the extracellular matrix (collagen I and Matrigel[®]) in the core with an alginate shell. Incorporating these components provides a more physiological environment in which the tumour spheroids can grow, and it also helps form more round, uniform spheroids within the core of the bead [265].

Figure 2.1 (a) presents the flow-focusing process used to generate the alginate beads, detailed by our group in [265]. Briefly, the first part of the chip flow-focuses the core solution containing dispersed cells, 2% alginate in PBS (Manucol LKX, FMC Biopolymer), Collagen I, and Matrigel[®] (supplied through a chilled tube to prevent gelation of the Collagen I and Matrigel[®]) between streams of alginate containing 60 mM insoluble $CaCO_3$ particles (J.T. Baker@1301-01). The resulting flow is then input to a device that generates droplets of this aqueous phase in mineral oil (Sigma Aldrich) using microfluidic shear forces. The oil is acidified using 1 μL/mL

acetic acid, and the acid releases Ca^{2+} from the $CaCO_3$ particles, internally gelling the alginate beads. The oil also contains 1% SPAN80® (sorbitane mono-oleate nonionic surfactant, Sigma Aldrich) in order to stabilize the hydrogel droplets and prevent their coalescence. Batches of beads were collected in a bath of medium and centrifuged to remove residual oil before being resuspended in the same medium as used for the maintenance cultures and cultured in the same polystyrene cell culture flasks before imaging. Figure 2.1 (b) shows a bead containing FUCCI-expressing cells immediately after bead formation and 27 days after bead formation; the initially dispersed cells have proliferated to form a large cluster of cells within the bead.
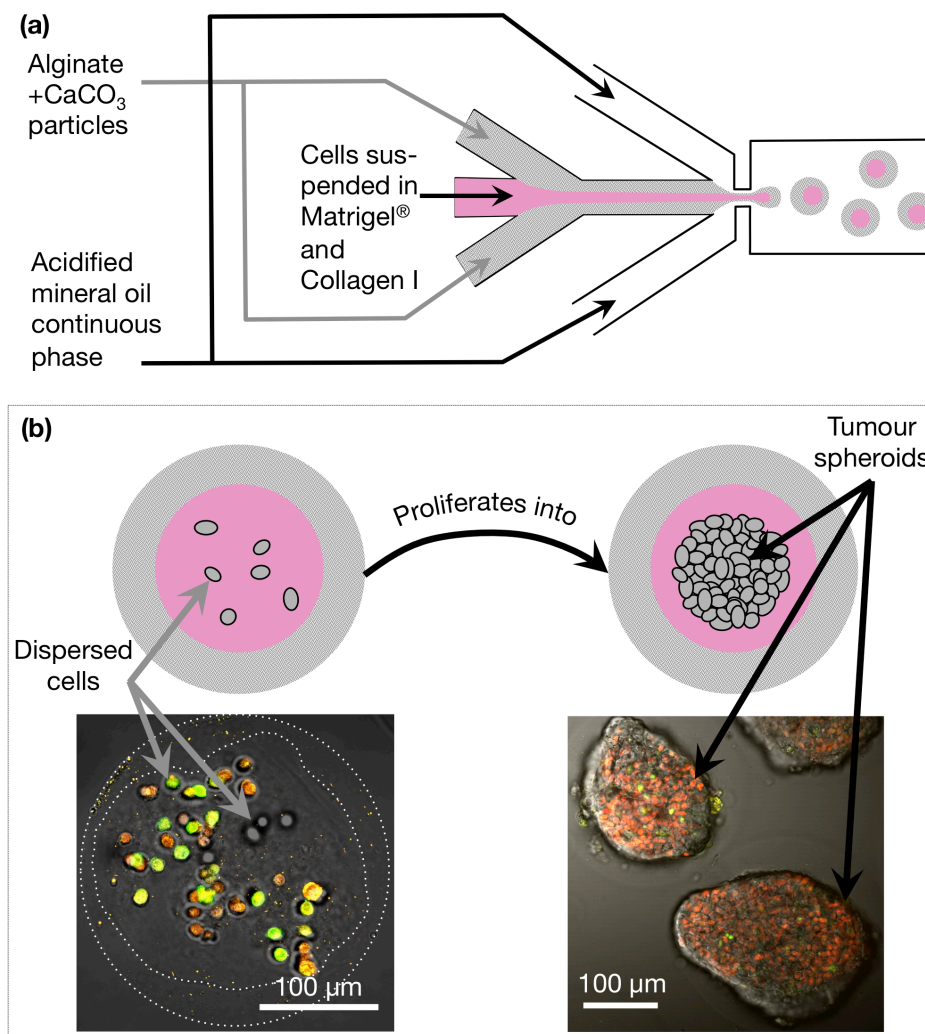
Figure 2.1. 3-D culture in alginate microbeads. **(a)** shows the flow-focusing process used to generate the cell-laden alginate beads, and **(b)** depicts beads containing MCF-7 human breast cancer cells soon after bead formation (with the bead core and shell outlined) and after the dispersed cells had proliferated into tumour spheroids (27 days after formation). Cells express the FUCCI cell cycle indicator.

2.3 Microfluidic Chips for Immobilizing 3-D Cultures

In order to monitor individual 3-D cell cultures in an array-based format, a microfluidic device containing an array of hydrodynamic trapping structures was designed and implemented. This implementation contained an array of 12 hydrodynamic traps, each 300 μm in diameter. The traps contained a small channel to permit fluid flow to facilitate trapping, and the opening of the trap was partly obscured by a small PDMS flap near the top of each trap to reduce bead migration due to small amounts of backflow. The flap does not extend down to the bottom of the channel, permitting the bead to enter the trap. Additional flaps are also integrated into the other pathways of the device to improve trap yield (ensuring that the cultures need to pass by flaps whether they enter the traps or continue down the channel). A schematic illustration of this microfluidic cell culture device is presented in Figure 2.2.
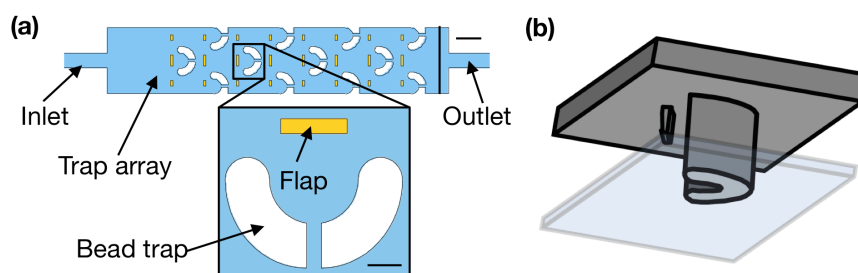
Figure 2.2. Microfluidic device for monitoring 3-D cell cultures. **(a)** shows the full chip schematic, while **(b)** depicts a 3-D view of a single trap, showing the small flap structure that extends partway from the channel top to improve bead retention. The gap in the trap that permits fluid perfusion is 50 μm in width, while the flap width on the mask is 45 μm. Scale bar represents 100 μm. Figure previously published in [267].

The microfluidic trapping device was fabricated in Sylgard 184 PDMS (Paisley Products of Canada) using standard soft lithography with an SU-8 3050 (Microchem Corporation) on silicon (University Wafer) master. The master was formed using a single transparency mask (Infinite Graphics Inc.) and single layer of 300 μm-thick photoresist, and the flap was formed by choosing a flap width less than that resolvable by the slightly overexposed resist process. This resulted in an incompletely developed hole in the resist for the flap, and thus a flap that did not reach the bottom of the 300-μm-height channel. After demolding the PDMS devices and punching the 0.5 mm input and output holes using a biopsy punch (Harris UniCore, Ted Pella, no longer

available), the bead trap devices were bonded to #1.5 coverslips (0.17 mm thickness) using a 75s air plasma exposure prior to bringing the PDMS and glass surfaces together.

For long-term cell culture experiments, a custom chamber for the microfluidic system was designed to: (1) keep the chip immersed in saline buffer, preserving physiological osmolarity and discouraging pervaporation through the PDMS while (2) permitting flipping of the device to be observed on either upright or inverted microscopes and (3) maintaining an aseptic saline immersion to prevent potential cross-contamination. First, a rectangular PDMS ring with 50x75 mm outer dimension and 7 mm wall thickness was created using a 3-D printed mould master. The top and bottom of the ring were then flattened by adding uncured PDMS and re-curing between two glass slides. Next, the chamber ring and microfluidic device were both air plasma bonded to a 75x75mm #1.5 cover glass (Nexterion). Fluidic connections from the chip were routed through the PDMS ring using Tygon microbore tubing (Cole Parmer) and 22G stainless steel tubing (EFD), which was friction-fit through the 0.5 mm holes punched in the microfluidic device and the ring. Additional inputs were inserted through the ring to permit filling of the chamber, and a 50x75x1 mm thick glass slide was plasma bonded to the ring top to seal the device. This setup is presented in Figure 2.3.

After fabrication, we used a degassing and pre-hydration procedure to reduce bubble formation in the channels and preserve osmolarity. The device was degassed in water under vacuum desiccation both at room temperature and 40°C, and left overnight in water at 70°C between the two vacuum desiccations. The water-immersed device was then sterilized by autoclave and the fluid in the chamber and chip switched to Dulbecco's Phosphate Buffered Saline (DPBS) containing calcium and magnesium ions to prevent alginate dissolution before loading in the spheroid-containing beads (loaded 8 days after bead formation). The setup was transferred to a standard incubator, kept at 37°C with 5% CO_2, and perfused with HEPES-buffered completed DMEM/F12-HAM media at a rate of 1 μL/min by syringe pump.
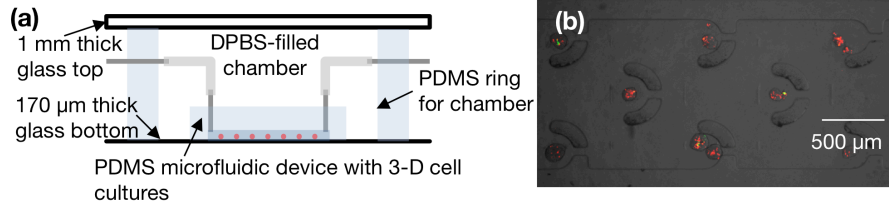
Figure 2.3. On-chip long-term cell culture system permitting high-resolution microscopy. **(a)** system schematic. **(b)** brightfield/fluorescence overlay image showing 3-D cell cultures trapped on chip for observation. Figure previously published in [267].

2.4 On-Chip Cell Proliferation in 3-D with Two-Photon Monitoring

The goal of this experiment was to demonstrate feasibility of the use of 3-D cultures within our microfluidic system. We wanted to demonstrate (1) that 3-D cell cultures could survive and proliferate within the microfluidic cell culture devices, and (2) that it is feasible to image the cultures to monitor their growth. As it is preferable to obtain confocal-like images of 3-D cultures (so that images from various z-depths into the spheroid can be analyzed), and two-photon (2-P) imaging offers both improved image quality and reduced likelihood of sample damage in comparison with standard confocal (as will be discussed in section 2.5.1), 2-P imaging was chosen for this study.

2.4.1 Experimental

As described in section 2.2, we generated cell-laden core-shell hydrogel beads using microfluidic flow focusing [265]. We used MCF-7 breast cancer cells expressing the FUCCI cell cycle indicator [268], which labels nuclei in the $S/G_2/M$ stages of their cycle green, and nuclei in the G_1 stage orange. FUCCI uses two fluorescent proteins: a green and an orange, linked with different cell cycle regulators. Monomeric Azami Green (mAG) is fused to Gemenin, labeling the nuclei of cells in the S, G_2, and M phases green, while monomeric Kusabira Orange 2 (mKO2) is fused to Cdt1, labeling the nuclei of cells in the G_1 phase orange [268, 269]. Figure 2.4 (from [268]) presents the expected cell fluorescence colours at different stages of the cell cycle as well as a time-lapse image of HeLa cells expressing the FUCCI indicator.

The cells in the core-shell beads proliferate to form spheroids in the bead cores which incorporate extracellular matrix elements such as collagen and Matrigel® [265], while the alginate shell maintains the spheroids in 3-D culture [266]. The spheroids were

59

hydrodynamically trapped within the microfluidic device in custom chamber described in section 2.3 (Figure 2.2 and Figure 2.3), permitting optical monitoring with 2-P at multiple points during their culture to observe their growth and proliferation status.
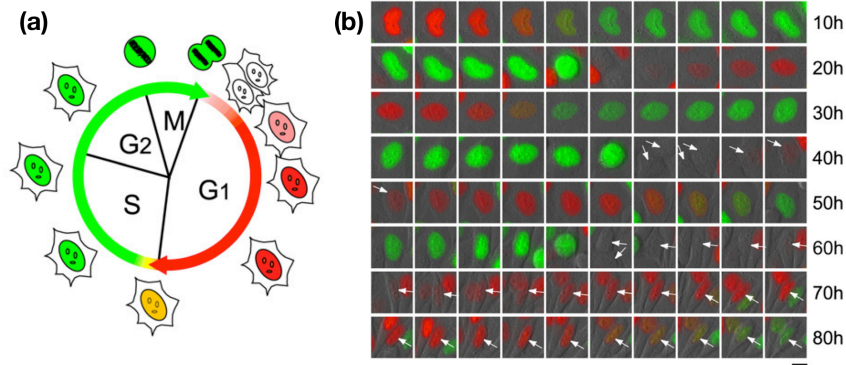
Figure 2.4. FUCCI cell cycle indicator. Image reproduced with permission from [268]. **(a)** depicts the expected fluorescent colours of FUCCI-expressing cells in different stages of the cell cycle, while **(b)** depicts a time-lapse DIC and fluorescence overlay image of FUCCI-expressing HeLa cells as they go through their cell cycle. The scale bar represents 10 μm.

The beads on chip were imaged on the day they were loaded (8 days after formation) as well as 5 and 9 days after loading (13 and 17 days after formation) using an upright Olympus FV1000 MPE BX61WI microscope at the UBC Bioimaging Facility with a MaiTai DeepSee Ti:Sapphire excitation laser at 880 nm (yielding diffraction-limited x-y and z-resolutions of $\omega_{xy} = 0.19$ μm and $\omega_{z} = 0.64$ μm, respectively, via equation 1). An XLPN25XWMP 25X water dipping objective lens designed for two-photon microscopy with a numerical aperture (NA) of 1.05 and a working distance of 2 mm was used for all measurements. The objective lens was used as a water immersion lens, with its correction factor set for the 170 μm expected thickness of the #1.5 glass coverslip between it and the specimen. The emitted green and orange FUCCI fluorescence passed through 495-540 nm and 576-630 nm bandpass filters before being detected by Hamamatsu R3896 PMTs. Z-stack images of the spheroids were acquired using the Olympus FV10-ASW software package (Ver.03.01) with 5 μm objective z-spacing, taking approximately 15 minutes for each z-stack. Between imaging cycles, the chip was maintained in a standard cell culture incubator with a humidified environment containing air supplemented with 5% CO_2.

At the study endpoint, the spheroids on chip were stained with eFluor® 450 fixable viability stain, which labels dead cell nuclei blue. Dulbecco's Phosphate Buffered Saline (DPBS) containing calcium and magnesium ions was flowed through the chip to rinse away the serum-containing media before flowing in a solution of 1 μL/mL fixable viability stain in DPBS and incubating for 60 minutes at approximately 4°C. Excess stain was then rinsed away with DPBS before imaging. After rinsing, the stain remained in the spheroid; however, the stain does not penetrate into live nuclei. Viability was assessed by counting the live nuclei (holes in the staining) and total nuclei (holes plus nuclei into which the stain had penetrated) using ImageJ (NIH, http://imagej.nih.gov/ij/).

2.4.2   Results and Discussion

We observed that the spheroids proliferated within the microfluidic device as they were monitored with two-photon microscopy over the 9 days of culture. Figure 2.5 presents on-chip proliferation data. Figure 2.5 (a), (b), and (c) depict z-intensity projection images of the same spheroid at day 8, 13, and 17 after bead generation. The spheroid grew noticeably between each imaging time point. Figure 2.5 (d) presents a comparison of spheroid proliferation (average diameter) on-chip with that in a standard culture flask; on-chip proliferation closely followed that in the flask.
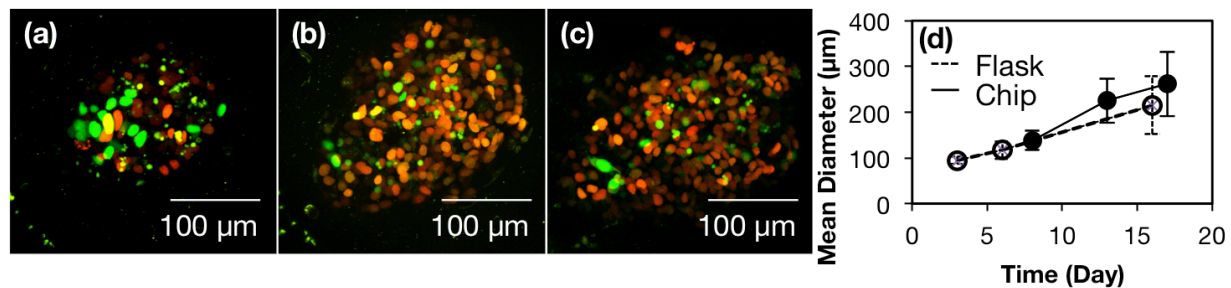
Figure 2.5. On-chip tracking of MCF-7 breast cancer cell spheroid proliferation. **(a-c)** z-intensity projection images of the growing spheroid, at day 8 (a), 13 (b), and 17 (c) after bead generation. **(d)** average spheroid diameter on chip (n = 5, except n=4 at day 17 as one spheroid was lost) compared with that in a cell culture flask (n = 7). The spheroid diameter after 17 days of on-chip culture was not found to be significantly different from that after 16 days of flask culture by a student's two-sided t-test (p=0.29). Error bars depict 1 S.D. Figure previously published in [267].

Figure 2.6 presents a comparison of images of a different on-chip spheroid acquired at day 13 (a,b) and 17 (c,d) after spheroid formation; the spheroid grew noticeably between the two

imaging time points. At the endpoint of the study, eFluor® 450 fixable viability staining confirmed 89±5% viability after 9 days of on-chip culture, not significantly different from the viability of live control spheroids grown in the cell culture flask with no imaging (93±2%). Viability values were calculated from 2-P slice images. Viability staining results of the on-chip spheroid (a,b), live control spheroid (c), and dead control spheroid (d) are depicted in Figure 2.7. It is evident from the control images that although the stain remains in the live spheroid material after rinsing, live cells exhibit holes in the staining for their nuclei, while no such holes are visible in the dead control spheroid.
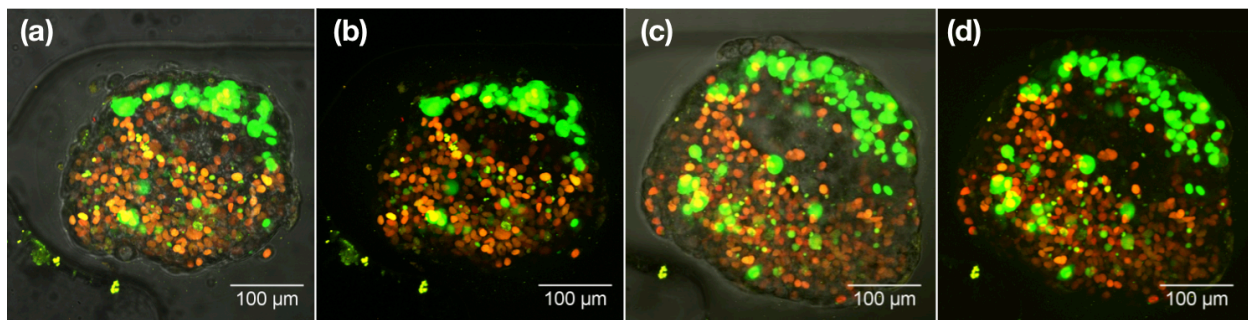
Figure 2.6. Spheroid proliferation within the microfluidic device. Comparison of growing MCF-7 spheroid at day 13 **(a, b)** and day 17 **(c, d)**, with (a,c) and without (b,d) the overlay of the transmitted light image. 2-P images show z-intensity projections. Figure previously published in [267].
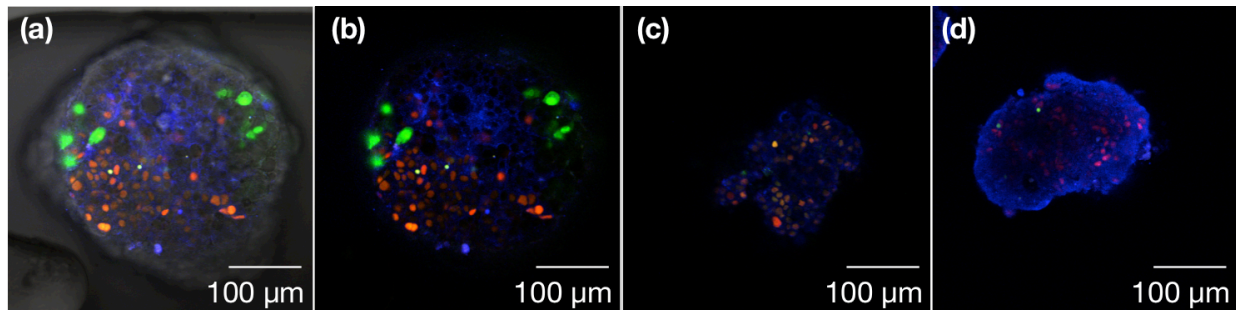
Figure 2.7. Viability staining of tumour spheroid culture. **(a, b)** show a 2-P image slice at 45 μm spheroid depth, depicting the eFluor® 450 (blue) and FUCCI fluorescence (orange and green) of the spheroid shown in **Figure 2.6** with (a) and without (b) transmitted light overlay, while **(c, d)** show the live (c) and dead (d) control spheroids. Live spheroids show holes in the blue stain for live nuclei, while dead cells exhibit blue nuclei. Figure previously published in [267].

The good viability observed after on-chip culture with 2-P monitoring demonstrates the feasibility of our microfluidic cell culture system for long-term studies. This demonstration of the compatibility of these techniques with long-term monitoring of spheroids verifies the utility

of the 3-D microfluidic cell culture system and opens the door for studies involving oxygen control and drug screening.

2.5   Imaging and Data Readout Methods for 3-D Cultures

2.5.1   Comparison of Confocal and Two-Photon Imaging

In this section, the imaging results yielded by confocal and two-photon imaging of cell spheroid cultures are compared. Two-photon imaging is an attractive imaging option due to its long-wavelength excitation, which uses a laser of twice the fluorophore excitation wavelength to excite the sample fluorescence. This long-wavelength excitation results in effective single-point excitation due to the high photon flux required for excitation; this in turn results in less photodamage to the sample. In addition, the long-wavelength excitation is less susceptible to scattering effects within the spheroid, and thus offers the potential to achieve improved imaging quality.

2.5.1.1   Methods

2.5.1.1.1   Cell Culture and Bead Generation

As described in section 1.1.2.1, 3-D cultures can be difficult to analyze both because of issues with dye penetration into the cell mass and because of light penetration issues. In order to separate the effects of the imaging process from those of staining processes, Normal Murine Mammary Gland (NMuMG) cells expressing the fluorescence ubiquitination cell cycle indicator (FUCCI) were chosen for this project. Although NMuMG cells are not tumour cells, they have been observed to form spheroids with lumina and acini-like structures in 3-D culture [270, 271]. As fluorescent stains can be subject to diffusion limitations when penetrating into tumour spheroids, by using the intrinsically fluorescent NMuMG-FUCCI cells we hoped to remove any potential dye penetration limitations (which could also impact fluorescence images) and study only the effects of light scattering and absorption.

NMuMG-FUCCI cells were kindly donated by Christopher Maxwell from the Child and Family Research Institute. The cells were kept in maintenance 2-D culture for several weeks prior to bead formation. To create the 3-D cultures, the cells were suspended at a concentration of 2.8×10^7 cells/mL in a mixture of 50 μL PBS, 100 μL 9.2 mg/mL collagen I, 200 μL Matrigel®,

and 5 μL NaHCO$_3$, and the beads were generated as described in section 2.2.2. The resulting beads of approximately 300 μm diameter were imaged 11 and 25 days after bead formation, in order to allow the cells to grow into 3-D spheroid structures.

2.5.1.1.2   Sample Mounting

The beads were imaged in custom chambers made from microscope slides, prepared at the UBC Bioimaging Facility. Three layers of electrical tape (SA LR203233 no. 810) were applied to cleaned standard 25x75x1 mm microscope slides and an approximately 6x6 mm square reservoir was cut out of the tape using a razor blade and removed with tweezers. The slide was cleaned with ethanol and dried thoroughly before pipetting approximately 40 μL of bead solution (in the same completed culture medium used for their culture) into the reservoir. Care was taken not to introduce bubbles into the solution when pipetting. The chamber was then closed by placing an ethanol-cleaned and dried standard 22x22 mm #1.5 coverslip on top of the chamber while taking care not to introduce bubbles into the chamber and sealing with paraffin. Prepared slides were kept in a cell culture incubator for no longer than 30 minutes prior to starting imaging.

2.5.1.1.3   Two-Photon and Confocal Imaging

Both the two-photon and confocal imaging were conducted using the same Olympus FV1000 MPE BX61WI microscope system with the same 25X objective described in section 2.4.1. The two-photon excitation source was a MaiTai DeepSee ultrafast pulsed Ti:Sapphire tunable laser. A wavelength of 950 nm was chosen for this study upon the recommendation of Kevin Hodgson from the UBC Bioimaging Facility to excite the two FUCCI fluorescent proteins simultaneously, as half of this wavelength overlapped with the excitation spectra of both the mAg and mKO2 fluorescent proteins, as depicted in Figure 2.8(a). This wavelength yielded diffraction-limited x-y and z-resolutions of $\omega_{xy} = 0.21$ μm and $\omega_{z} = 0.70$ μm, respectively, via equation 1. The emitted light was separated from the excitation by RDM690 dichroic mirror before being separated into the red and green components using an SDM570 dichroic mirror. The green channel passed through a DM485 dichroic mirror and 495-540 nm bandpass filter before reaching the channel 2 detector, while the red channel passed through a DM570 dichroic mirror and 576-630 nm bandpass filter before reaching the channel 4 detector. The overlap of the emission filters with the spectra of the two fluorescent proteins is also depicted in Figure 2.8(a).
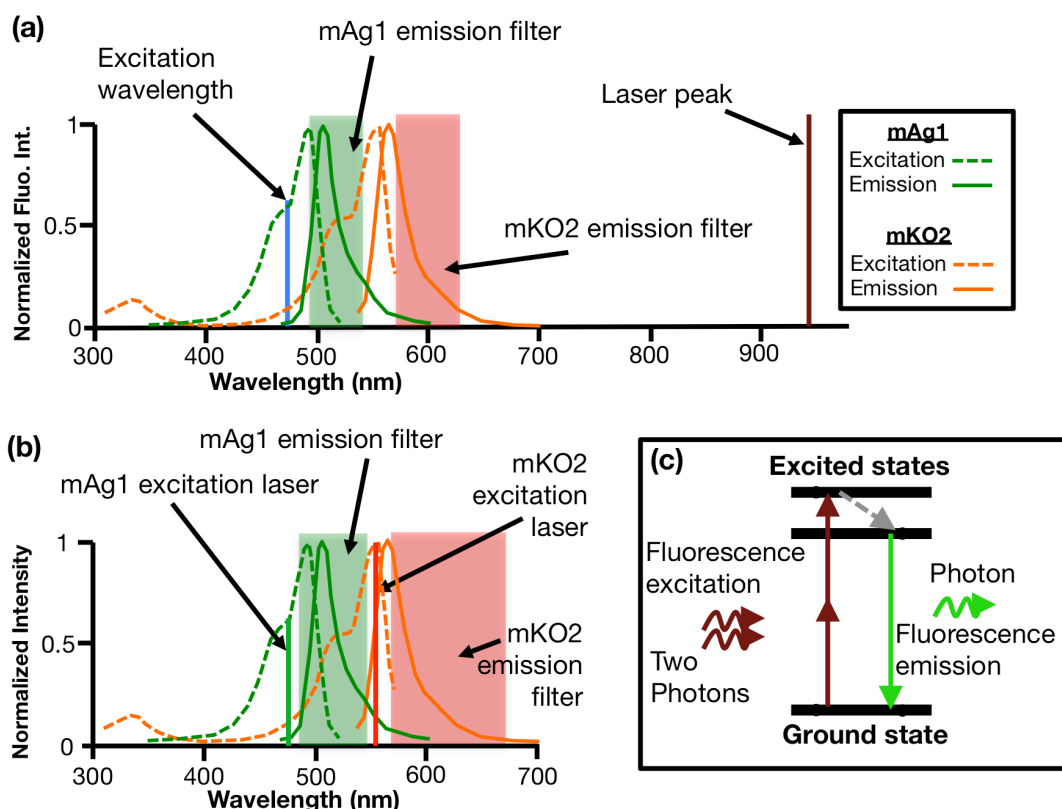
Figure 2.8. Optical imaging spectra for FUCCI proteins. **(a-b)** Annotated excitation and Emission spectra of FUCCI proteins (spectra redrawn from [272]), along with excitation and emission wavelengths and filter ranges for (a) two-photon imaging, where a single laser is used to excite both mAg1 and mKO2 and (b) confocal imaging, where two lasers are used. **(c)** depicts the Jablonski diagram for two-photon excitation, where two photons, each with half the energy needed to excite an electron in the fluorophore to the excited state, simultaneously interact with the fluorophore, exciting it to the excited state. A photon of the normal fluorophore emission wavelength is released as the electron returns to the ground state.

Confocal measurements were acquired using the same microscope system, objective lens, and detector described above. Excitation lasers of 473 and 559 nm wavelength were scanned sequentially to excite the mAg and mKO2 fluorescent proteins, respectively. The emitted light was separated from the excitation by a DM405/473/559 dichroic mirror before being split into two channels by an SDM560 dichroic mirror. The dyes of interest were set in the FV10-ASW software to be EGFP (channel 1, for the mAg) and RFP (channel 2, for the mKO2), which the software used to automatically select a 485-545 nm bandpass emission filter for the mAg and a 570-670 nm bandpass filter for the mKO2. The overlap of the confocal excitation wavelengths and emission filters with the excitation and emission spectra of the two fluorescent proteins is depicted in Figure 2.8(b). For the confocal imaging, the transmitted 473 nm laser intensity was

also collected using another detector below the specimen. This intensity image gave a shadow-like transmitted light differential interference contrast image of the sample, permitting the observation of the general shape and absorption of the bead and spheroid alongside the emitted fluorescence.

In order to obtain good imaging quality, a mid-range PMT voltage of 700 V and dwell time of 4 μs was used for all images. For confocal imaging a pinhole diameter of 60 μm was used to obtain thin optical section thickness. Three line Kalman integration was set in the FV10-ASW software to reduce imaging noise. For all spheroid-containing samples, z-stacks with 2-5 μm objective z-steps were acquired for the full z-range in which fluorescence was observed. For the control samples, a single frame was acquired near the approximate center of the bead (found using the brightfield imaging mode of the microscope) using the same imaging parameters as those used for the spheroids, as no fluorescence was observed.

All images were acquired with the two-photon laser intensity set to 7-8%, the 473 nm confocal laser intensity set to 2-3%, and the 559 nm confocal laser intensity set to 0.5%. Two-photon and confocal images were acquired of the same spheroids in all cases in order to compare the two modalities. Because two-photon imaging is expected to result in reduced photobleaching and photodamage of the sample, two-photon imaging was conducted before confocal imaging in all cases.

2.5.1.1.4   Data Analysis

Images were brightness and contrast adjusted in ImageJ by setting the maximum and minimum display values to fit the image histogram. The maximum and minimum display values are the values for which the image brightness is shown as saturated and black, respectively (set by default to 255 and 0 for 8-bit images and 4095 and 0 for 12-bit images). For the purpose of comparing images, the same adjustment was made to all compared images.

A MATLAB® script was used to find and plot the average image intensities with depth for the z-stacks as a preliminary quantitative means of comparing the confocal and two-photon data. In this script, the raw 12-bit Tagged Image File Format (TIFF) images in the image stack were read

in. The images were then segmented by thresholding in an effort to isolate only regions of the image containing fluorescent signal. The resulting binary image mask (white for regions with fluorescence and black for regions without) was denoised with erosion and dilation operations using a 2-pixel radius disk-shaped structuring element before the pixel intensity values of the original image in the white binary image regions (the regions of the image most likely to contain fluorescence intensity) were averaged to produce an average intensity value. The average intensity values in these segmented regions for each colour channel were then plotted versus z-depth in order to obtain a measure of image degradation with depth and compare the confocal and two-photon images. The red channel data was used for all measurements because the majority of the FUCCI-labelled cells were in the orange-labelled (G$_1$) stage of their cell cycle.

2.5.1.2 Results and Discussion

Figure 2.9 presents a comparison of confocal and two-photon images from z-stacks acquired of the same spheroids. Figure 2.9 (a) presents the two-photon image from the 11-day old spheroid at depth 150 µm, while Figure 2.9 (b) presents the corresponding confocal image. The confocal image appears less uniform in intensity at this depth, with very dark regions in the centres of the smaller spheroids. The enhanced penetration of two-photon imaging is even more apparent when examining the un-modulated data from deeper in the larger 25-day old spheroid. Figure 2.9 (c) depicts the two-photon image from the 25-day old spheroid at depth 240 µm, and Figure 2.9 (d) depicts the corresponding confocal image (both images were acquired without laser intensity modulation). In this larger spheroid, the deeper penetration of the two-photon imaging is clearly visible, with more features visible in the two-photon image than in the confocal. Figure 2.9 (e) presents a two-photon image of the same spheroid as Figure 2.9 (c-d), at depth 123 µm, acquired with a higher excitation intensity (8.25%) to better visualize the features deep in the spheroid, and Figure 2.9 (f) the corresponding confocal image at higher laser intensity (7.75% for the blue laser, 2% for the green laser).
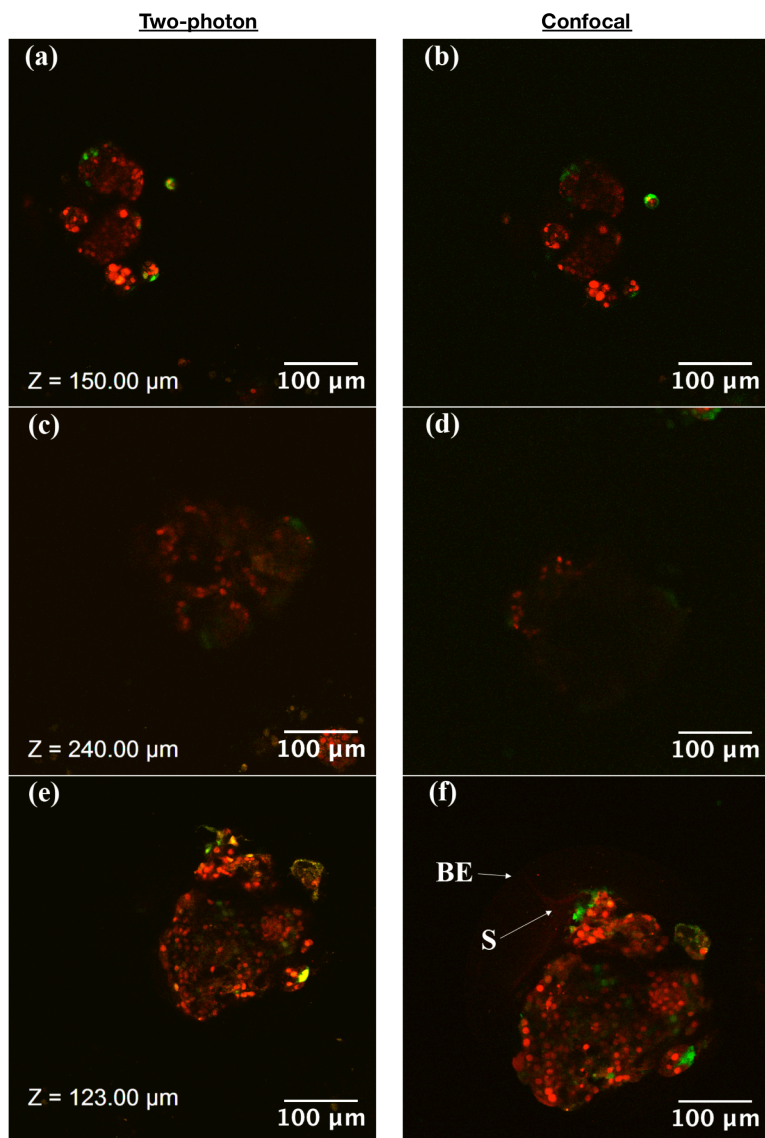
Figure 2.9. Comparison of confocal and two-photon images from z-stacks acquired of the same spheroids. **(a)** presents the two-photon image from an 11-day old spheroid at depth 150 μm, while **(b)** presents the corresponding confocal image. Both images have been brightness and contrast adjusted in ImageJ by setting the maximum values to 41 as described in section 2.5.1.1.4. The confocal image appears less uniform in intensity at this depth, with very dark regions in the centres of the smaller spheroids. **(c)** depicts the two-photon image from a 25-day old spheroid at depth 240 μm, and **(d)** depicts the corresponding confocal image. Both images have been brightness and contrast adjusted in ImageJ by setting the maximum values to 34. In this larger spheroid, the deeper penetration of the two-photon imaging is clearly visible, with more features visible in the two-photon image than in the confocal. **(e)** presents a two-photon image of the same spheroid as (c-d), at depth 123 μm acquired with higher excitation laser intensity (8.25%) to better visualize the features at this depth, and **(f)** the corresponding confocal image at higher excitation intensity (7.75% for the blue laser, 2% for the green laser). Both images have been brightness and contrast adjusted in ImageJ by setting the maximum values to 44. The reduced noise and background fluorescence in the two-photon image compared to the confocal is evident in (e-f), with the outline of the bead edge (BE) as well as structure within the bead (S) visible in the confocal image but not the two-photon; these features are likely artifacts caused by light excited elsewhere in the z-direction being scattered into the focal plane.

The reduced noise and background fluorescence in the two-photon image compared to the confocal is evident in Figure 2.9 (e-f), with the outline of the bead edge (B) as well as structure within the bead (S) visible in the confocal image but not the two-photon; these features are likely artifacts caused by light excited elsewhere in the z-direction being scattered into the focal plane. This scattered light is more visible near refractive index contrast regions such as the bead edge as well as features inside the bead that could be due to nonuniform collagen/Matrigel® distribution. Because two-photon imaging results in effective single-point excitation (due to the extremely low likelihood of simultaneous absorption of two photons elsewhere in the sample), these artifacts are not present in the two-photon images.

In addition to this qualitative analysis, quantitative analysis of the average red channel fluorescence intensity of the cell-containing spheroid regions is presented in Figure 2.10.
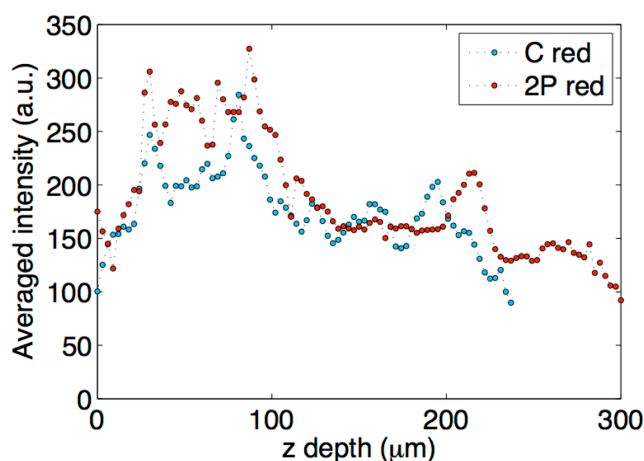
Figure 2.10. Comparison of average fluorescence intensity in two-photon and standard confocal z-stacks. The plot shows the average intensity in spheroid-containing region at different depths into the spheroid, comparing the red channels of confocal ('C red', blue markers) and two-photon ('2P red', red markers) images from z-stacks acquired of the same spheroids.

Figure 2.10 presents the averaged image pixel intensities in the cell-containing regions plotted against depth in the spheroid, for both confocal (C) and two-photon (2-P). For both confocal and 2-P, the acquisition settings were adjusted such that saturated pixels just started to become visible at the beginning of the spheroid. This equality at the beginning of the z-stack permits some measure of comparison of the two sets of intensities. At objective z-step depths of 50-100 μm into the spheroid, the two-photon intensity appears to be higher (both in Figure 2.10 and in Figure 2.9 (a-b)). At depths greater than 240 μm, the confocal fluorescence intensity had

degraded such that the segmentation script picked up no fluorescent regions, whereas the two-photon intensity was still present.

These results demonstrate that two-photon microscopy yields notably better sample penetration than standard confocal microscopy. Two-photon microscopy also yielded less noisy images with less background fluorescence, which is likely due to the unique single-point excitation provided by two-photon microscopy.

The depths reported above as well as in the following sections of this thesis denote the distance that the objective lens was stepped towards the sample, and would also be the distance imaged into the sample if the full sample had a refractive index matching that of the water immersion media of the objective lens (RI = ~1.33). Because the spheroid has a higher refractive index, the actual depths imaged will be deeper than the reported objective z-depth (approximately 1.1 times greater if the sample had a homogeneous refractive index of 1.38, which was reported as a measured refractive index for bovine muscle tissue [273]).

2.5.2   Modulated 2-Photon Imaging for Improved Light Penetration in Spheroids

In section 2.5.1, it was apparent that two-photon imaging yielded improved spheroid penetration compared with confocal imaging; however, the imaging depth was still limited. This limitation, likely caused by scattering of the excited and emitted light, resulted in darkened images deep in the z-stack. In this section, we investigate increasing the excitation laser power to compensate for light lost to absorption and scattering within the spheroid.

2.5.2.1   Methods

Similar cell culture and imaging methods were performed as for the two-photon imaging described in section 2.5.1. NMuMG cells expressing the FUCCI cell cycle indicator [268] were microfluidically encapsulated in alginate beads containing Type I collagen and Matrigel® using a method described in section 2.2 [265]. To demonstrate microfluidic compatibility, the beads were imaged in the PDMS microfluidic bead trapping chips presented in section 2.3.

Imaging was conducted using the same setup as that described for two-photon imaging in section 2.5.1.1.3. The excitation laser intensity was modulated using the two different modulation schemes illustrated in Figure 2.11. In the linear scheme, the intensity was increased linearly from 8% to 50% (of approximately 140 mW at 100% intensity) between 50-300 μm sample depth. In the adaptive nonlinear scheme, the sample was pre-imaged at 50 μm objective z-step depth intervals and the laser intensity was increased at each until saturated pixels were visible; linear interpolation of the power was used between these 50 μm intervals.
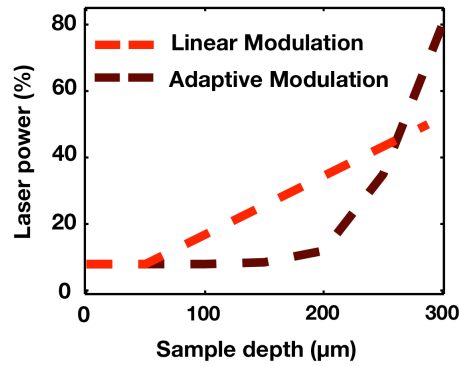
Figure 2.11. Laser intensity modulation profiles for the linear (red) and adaptive (brown) schemes. Figure previously published in [274].

Image z-stacks were analyzed by comparing slice images and 3-D renderings, and the average image intensities with depth into the spheroid were obtained and compared using the MATLAB script described in section 2.5.1.1.4.

2.5.2.2   Results and Discussion

The laser intensity modulation process results in improved image intensity, facilitating imaging deeper into the spheroids. Figure 2.12 (a) depicts an overlay image of the orange and green 2-P FUCCI fluorescence (z-projection) atop a transmitted light image of a bead immobilized within the PDMS bead-trapping chip of Figure 2.2. The light collected after passing through the sample during a 2-P scan generates a transmitted light differential interference contrast image showing the outline of the bead (1) with encapsulated spheroids (2) as well as the trap (3) and flap (4) PDMS structures. Figure 2.12 (b-c) presents maximum intensity projection (MIP) 3-D renderings of 2-P z-stacks acquired with (c) and without (b) linear laser power modulation. In the

unmodulated z-stack, a decrease in fluorescence intensity with sample depth is visible, with few features discernible beyond 200 μm in depth. In contrast, the fluorescence intensity of the linearly modulated z-stack appears much more constant with sample depth compared with the rendering of (b).
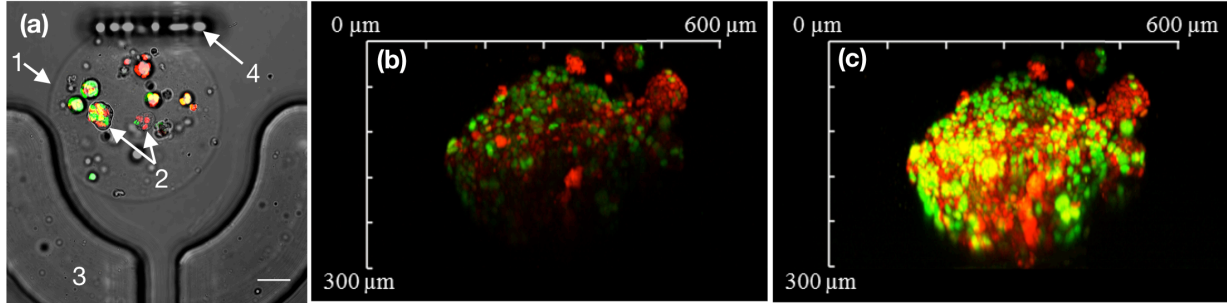
Figure 2.12. Two photon images of spheroids with and without laser-intensity modulation. **(a)** Top view showing a z-projection image of the orange and green FUCCI fluorescence overlaid upon a transmitted light image of the bead (4 days post-formation) and microfluidic bead trap. The bead outline (1), small spheroid clusters (2), bead trap (3), and flap (4) are all visible in the transmitted light image. Scale bar represents 50 μm. **(b-c)** MIP 3-D renderings of 2-P z-stacks acquired with and without laser power modulation, showing spheroid width versus objective z-step depth into the sample. Both images depict the same spheroid that had been cultured for 25 days. **(b)** z-stack acquired under constant laser power. **(c)** z-stack acquired using linear laser intensity modulation. Figure previously published in [274].

This difference is further apparent when the average fluorescence intensity from the red channel was plotted to compare the results of the unmodulated 2-P imaging with the linearly and adaptively modulated 2-P imaging methods. Linear laser modulation significantly improves the sample penetration of the 2-P imaging, maintaining the average image intensity at depths up to approximately 250 μm. In contrast, the adaptive modulation shows limited efficacy in improving imaging outcome, as the spheroid edges are more likely to saturate due to the shortened optical path through the scattering cell material while the centre remains dim. Thus, there is a tradeoff between saturated spheroid edges and signal-to-noise ratio at the spheroid centre; it may be possible to develop an improved adaptive method to balance these effects. This more relevant adaptive method could potentially be based upon choosing the laser intensity at several depths into the spheroid that caused saturated pixels to start to be visible in the centre of the spheroid, rather than at any point in the image.
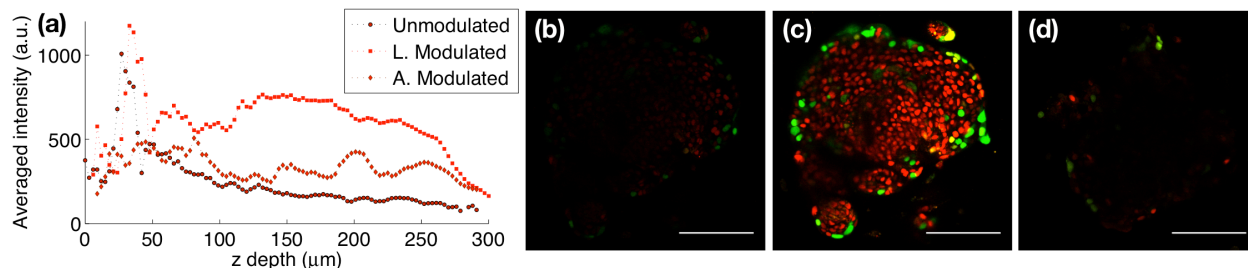
Figure 2.13. Comparison of modulated and un-modulated 2-P intensities. **(a)** Average fluorescence intensity vs. objective z-step depth from the red channel for 2-P (Unmodulated; dark red circles) and linearly intensity-modulated 2-P (L. Modulated; bright red squares) imaging, compared with the adaptive modulation scheme (A. Modulated; brown diamonds. (b-d) 2-P images acquired at 150 µm depth. **(b)** no laser intensity modulation; **(c)** linear modulation; **(d)** adaptive nonlinear modulation. (b,c) were the same bead; (d) was an equivalent bead. Scale bar represents 100 µm. Figure previously published in [274].

Figure 2.12 and Figure 2.13 demonstrate that the linear laser modulation profile improves the signal-to-noise ratio for z-slices at depths up to 250 µm into the bead; this will allow image processing such as segmentation of the cell nuclei to be performed more reliably than with an un-modulated imaging modality. The use of 2-P imaging in contrast with the confocal imaging of [26] reduces photodamage and photobleaching of the sample to offset the increased laser powers used with modulation. The linear modulation technique shown in Fig. 3 (c) allows us to visualize the spheroid centre and note that most of the dividing cells (green) are located near the perimeter of the spheroid. This suggests the development of a quiescent core in the spheroid surrounded by a periphery of proliferating cells, in agreement with previous findings [13, 275].

The improved imaging results facilitated by 2-P laser modulation greatly improve the capability of optical sectioning to analyze 3-D cell cultures. This proof-of-concept demonstrates the compatibility of this live-cell imaging technique with microfluidic devices, thus opening the door for *in situ* monitoring of the growing spheroids within a microfluidic continuous-perfusion drug screening system.

The primary artifact observed in the laser-modulated imaging was blurring and z-direction stretching of the images deep in the image stack (indicative of changes in the optical section thickness, or of changes in refractive index leading to changes in the z-plane spacing); we believe that these artifacts are due to the scattering nature of the spheroid sample. It may be possible to reduce the artifacts by using tissue clearing methods like SeeDB [32] to reduce

scattering and make the tissue optically transparent; however, these need to be performed on fixed samples and as such would not permit monitoring of the cells' proliferation in the spheroid or other time studies. The adaptation of tissue clearing to microfluidic 3-D cell cultures is described in section 2.5.3.

2.5.3   Tissue Clearing for Improved Spheroid Imaging

In order to address both the intensity gradient and blurring issues caused by optical scattering within 3-D cell cultures, we have created an on-chip implementation of tissue clearing protocols developed for larger-scale tissues (discussed in section 1.1.2.2). Although Boutin *et al.* have studied optical clearing in neural stem cell spheroids and gliomas [37], to the best of our knowledge, optical clearing of ECM-containing tumour spheroids has not yet been studied. Most of the clearing protocols were developed for millimetre-scale tissue samples and require successive incubations in different solutions; this can be difficult to implement, requiring centrifugation for solution exchange around tumour spheroid samples. Centrifugation can damage the spheroid structure, and for some protocols such as SeeDB can actually be impossible to implement due to solution density matching that of the micro-tissue or 3-D culture, resulting in the loss of spheroid samples during the clearing process. Additionally, it is difficult to compare the same spheroid samples before and after clearing, or to image samples that had been monitored during microfluidic on-chip cell culture.

This section demonstrates a rapid and high-throughput system for on-chip optical clearing of arrays of tumour spheroids. We have adapted the SeeDB and Clear^{T2} tissue clearing techniques for application in a microfluidic environment (hereafter called μSeeDB and μClear^{T2}, respectively). Of the clearing techniques summarized in section 1.1.2.2 of the Introduction, SeeDB and Clear^{T2} were the first ones compatible with visualizing both intrinsically expressed fluorescent proteins and lipophilic dyes [276], two types of fluorophores with wide applicability in phenotypic drug screening research. We use two-photon microscopy to assess the methods' clearing efficacy in multicellular tumour spheroids of fluorescent protein expressing human cancer cells, as two-photon presents the best-case imaging results (as demonstrated in section 2.5.1).

2.5.3.1   Methods

2.5.3.1.1   Cell Culture and Spheroid Preparation

Cancer Cell Culture MCF-7 breast cancer cells were transfected with the FUCCI cell cycle indicator [268] using Lypofectamine 3000 (Invitrogen, Carlsbad, CA) reagent, following the product guidelines. The transfected cells express mKO2 (ex/em:551/565 nm) during the G_1 phase, while expressing mAG1 (ex/em:492/505 nm) during the $S/G_2/M$ phases as described in section 2.4.1 [268]. The cells were cultured in DMEM/F-12-HAM (Sigma-Aldrich, St. Louis, USA) supplied with 5% fetal bovine serum (Invitrogen, Carlsbad, USA), 2.5 mM L-glutamine and 0.05 mg/mL gentamicin sulphate (Bio Basic, Markham, Canada) at 37˚C and 5% CO_2. Cells were detached using 0.25% Trypsin/EDTA (Invitrogen) and centrifuged to be resuspended to the desired concentration.

Tumour Spheroid Formation MCF-7 breast cancer tumour spheroids were formed within hydrogel beads formed using a microfluidic flow-focusing method (depicted in Figure 2.1 and described in section 2.2.2) [265]. The cell-laden beads were cultured in hydrophobic cell culture flasks (Sarstedt, Nümbrecht, Germany) with other culture conditions similar to the previously described adherent cell culture.

Spheroid Fixation The alginate shells around the spheroids were removed by suspending the beads in Ca^{2+}/Mg^{2+}-free phosphate buffered saline (PBS; Invitrogen). Because the PBS does not contain calcium ions, the calcium-cross-linked alginate dissolves within 5 minutes as the calcium ions diffuse out of the gel; this does not occur in cell culture media as it contains calcium ions. Subsequently, the spheroids were fixed using 2% electron microscopy-grade formaldehyde (Ted Pella, Redding, USA) in PBS at room temperature overnight.

2.5.3.1.2   Clearing Solution Preparation

SeeDB Tissue Clearing As described by Ke *et al.* [32], solutions of 20%, 40%, 60%, 80%, 100% and 115% wt/vol fructose were dissolved in ultrapure H_2O at room temperature, except the latter two at 65˚C. α-thioglycerol was added after cooling to reach a final concentration of 0.5%.

Clear^{T2} Tissue Clearing As described by Kuwajima *et al.* [33], a 40% polyethylene glycol (PEG) solution in ultrapure H_2O was prepared by dissolving PEG 8000 (Sigma-Aldrich) in warm water. A 50% formamide/20% PEG solution was made by mixing formamide with 40% PEG/H_2O in equal amounts. A 25% formamide/10% PEG solution was prepared by the dilution of the 50% formamide/20% PEG solution in an equal amount of ultrapure H_2O.

2.5.3.1.3   Microfluidic Chip Design and Experimental Setup

The experimental setup during tissue clearing is depicted in Figure 2.14 (a). The tumour spheroids, trapped inside the microfluidic device described in section 2.3, were imaged through a #1.5 (0.17 mm thick) glass coverslip (Fisher Scientific, Pittsburgh, USA). The microfluidic spheroid trap device used for tissue clearing was prepared as described in section 2.3. During imaging, the device was loaded upside-down into the upright microscope so that it could be imaged through the cover glass at the device base. The microscope was located in a dark enclosure; the chip output tubing was connected to a waste tube inside this enclosure, and the chip input was routed outside the enclosure to permit fluid supply during imaging.
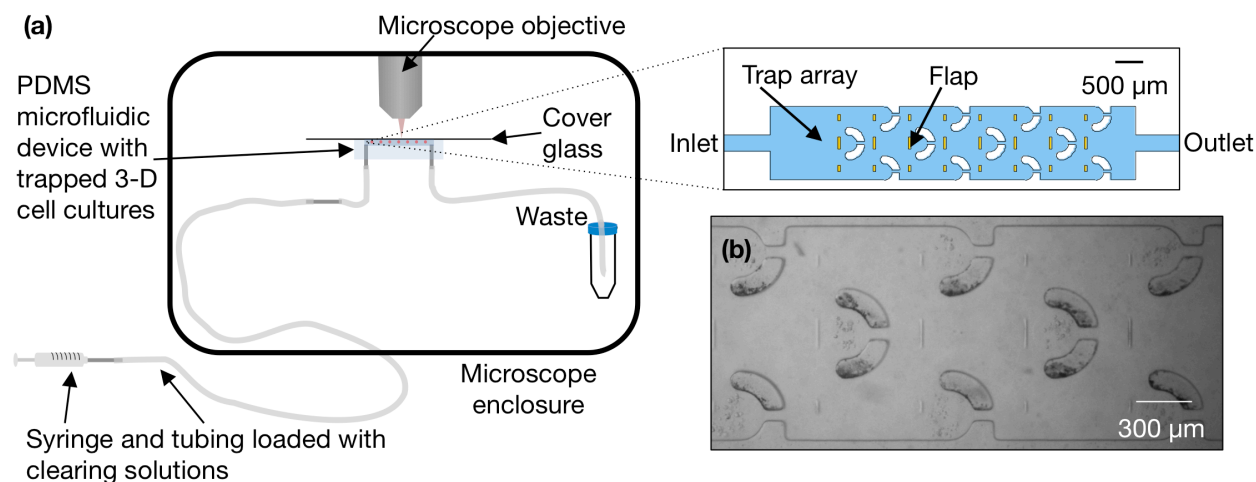
Figure 2.14. Experimental setup during on-chip tissue clearing. **(a)** clearing setup on the stage of the two-photon microscope used to monitor the clearing process. Inset shows the schematic of the microfluidic trapping chip, including the small flap structures used to help make the traps more resilient to small amounts of backflow. **(b)** phase contrast microscope image of the trapping chip with immobilized hydrogel beads containing dispersed cells.

The design of the microfluidic device, the same as that detailed in section 2.3, is shown in the inset of Figure 2.14 (a). The device consists of a large channel (1.35 mm × 7 mm) containing 12

C-shaped hydrodynamic trapping structures to immobilize 3-D cell cultures. A phase contrast microscope image of the microfluidic device is shown in Figure 2.14 (b).

2.5.3.1.4 Tissue Clearing Setup and Procedure

After fixation, spheroids in PBS were loaded into the microfluidic trapping devices using a syringe under positive manual pressure. A 3 mL plastic syringe (BD, Mississauga, Canada) outfitted with a 22G blunt needle tip (Nordson EFD, East Providence, USA) was connected to the microfluidic device friction-fit with another 22G blunt needle via Tygon microbore tubing (Cole-Parmer, Montreal, Canada). Tubing pinch-clamps (Cole-Parmer, Montreal, Canada) were used to stop the flow while the syringe was changed to a PBS-containing syringe to prevent bubble introduction into the channel. After rinsing un-trapped spheroids away using PBS, the tubing was clamped and syringe disconnected. A long tube, pre-filled with clearing solution and connected to a syringe filled with the final clearing solution was then connected to the device input for both clearing methods. Care was taken during tube filling and connection to ensure that bubbles were not introduced to the tubing.

SeeDB Tissue Clearing We developed an accelerated SeeDB process to expose the spheroids to the increasing concentrations of fructose more rapidly than perfusing each solution sequentially through the long tube. The long tube was pre-loaded with 10 cm lengths of 20%, 40%, 60%, 80%, 100% and 115% fructose in water. The beads were imaged prior to clearing. Then, the tubing was un-clamped and the solutions were slowly perfused into the device at a rate of approximately 300 μL/min by applying positive pressure to the syringe. The clearing result should not depend strongly on flow rate, as long as fresh solution is continually supplied to the device. As the purpose of the increasing concentrations of solutions is to gradually expose the micro-tissues to the clearing solution, any mixing of the solutions within the tube due to diffusion or solution flow was not deemed problematic. The solution was continuously perfused during clearing, and the tubing was re-clamped after the spheroid was judged to be sufficiently cleared using the two-photon fluorescence and transmitted light images acquired during clearing (which took approximately 20 minutes for the imaged samples).

Clear^{T2} Tissue Clearing The long tube was pre-loaded with a 10 cm length of PBS, 40 cm length of 25% formamide and 10% PEG (Clear^{T2}-1), and a 10 cm length of 50% formamide and 20% PEG (Clear^{T2}-2), with the syringe of Clear^{T2}-2 left attached to the inlet. After imaging the beads before clearing, the tubing was un-clamped and the solutions were slowly perfused into the device at a rate of approximately 300 μL/min; again the clearing result should not depend strongly on flow rate as long as fresh clearing solution is continuously supplied to the device. Again, the solution was continuously perfused during the clearing process and the tubing was re-clamped after the monitored spheroid was judged to be sufficiently cleared.

2.5.3.1.5   Imaging

The orange and green FUCCI expression of the tumour spheroids was imaged both before and after clearing using 2-P microscopy to assess the clearing performance. All imaging was performed using the same Olympus FV1000 MPE upright microscope setup described in section 2.4.1. The microscope permitted the acquisition of an image representing the transmitted laser intensity using the microscope's condenser setup below the microfluidic device. This transmitted laser intensity yielded a differential interference contrast (DIC)-like image of the scanned area that allowed us to analyze spheroid size changes in response to the clearing protocols.

A two-photon z-stack of each spheroid (with red, green, and transmitted light colour channels) was acquired before and after clearing with a 5 μm objective z-step slice spacing. Additionally, a time series x-y image of one spheroid per chip, at a z-depth where light attenuation was present, was acquired during clearing to monitor the process. This time series was used to discern the endpoint of our clearing process (the point at which the spheroid was judged to be sufficiently cleared and tubing re-clamped).

2.5.3.1.6   Compatibility of On-Chip Cell Culture with On-Chip Clearing

The microfluidic devices used for our implementation of on-chip clearing may also be used for on-chip cell culture. We have demonstrated the on-chip culture of arrays of tumour spheroids in such a device, using two-photon imaging to monitor the spheroids' proliferation in 3-D while maintaining good spheroid viability [267]; this study is presented in section 2.4. For this work, the custom chamber described in section 2.3 was used to keep the microfluidic device immersed

in Dulbecco's PBS containing calcium and magnesium to maintain channel osmolality while also permitting flipping the device upside-down to be observed with the upright microscope. The enclosed chamber permitted monitoring with both an inverted brightfield microscope and the upright 2-P.

After degassing the chip and sterilizing the channel by flowing 70% ethanol, water, PBS, and cell culture media sequentially through the channels, the hydrogel bead-based cell cultures containing small MCF-7 tumour spheroids were loaded into the chip 8 days after bead formation. The chamber was filled with Dulbecco's PBS and the channel was perfused with cell culture media at a rate of 1 μL/min as described in section 2.4.1. The spheroids were cultured on-chip for 9 days and then fixed on-chip using 4% paraformaldehyde in PBS. After fixation, the spheroids were rinsed with PBS and cleared using a single-step SeeDB-like process [277], in which the channel was immediately perfused with the 115% fructose in water solution while monitoring using two-photon microscopy.

2.5.3.1.7   Image Processing

Images were histogram-adjusted in ImageJ (NIH, http://imagej.nih.gov/ij/) as described in section 2.5.1.1.4 to ensure visibility in print. For the purposes of comparing images, the same histogram adjustment was made to each image. Maximum intensity 3-D renderings were created from the z-stack data using BioView3D (from the Center for Bio-Image Informatics, UCSB). Again, each z-stack and rendering was made using the same process for the purposes of comparison. Image measurements were made either manually in ImageJ or using custom scripts written using MATLAB® (Mathworks, Natick, USA) where indicated. For calculations of spheroid size change after treatment, the area change was calculated as A_{post}/A_{pre}, where A_{post} and A_{pre} are the spheroid areas after and before treatment, respectively, calculated using manual segmentation in ImageJ.

2.5.3.2   Results and Discussion

2.5.3.2.1   Clearing Increases Fluorescence Imaging Penetration Depth

Figure 2.15 presents a comparison of images acquired before and after clearing using the μSeeDB and μClear^{T2} clearing methods.
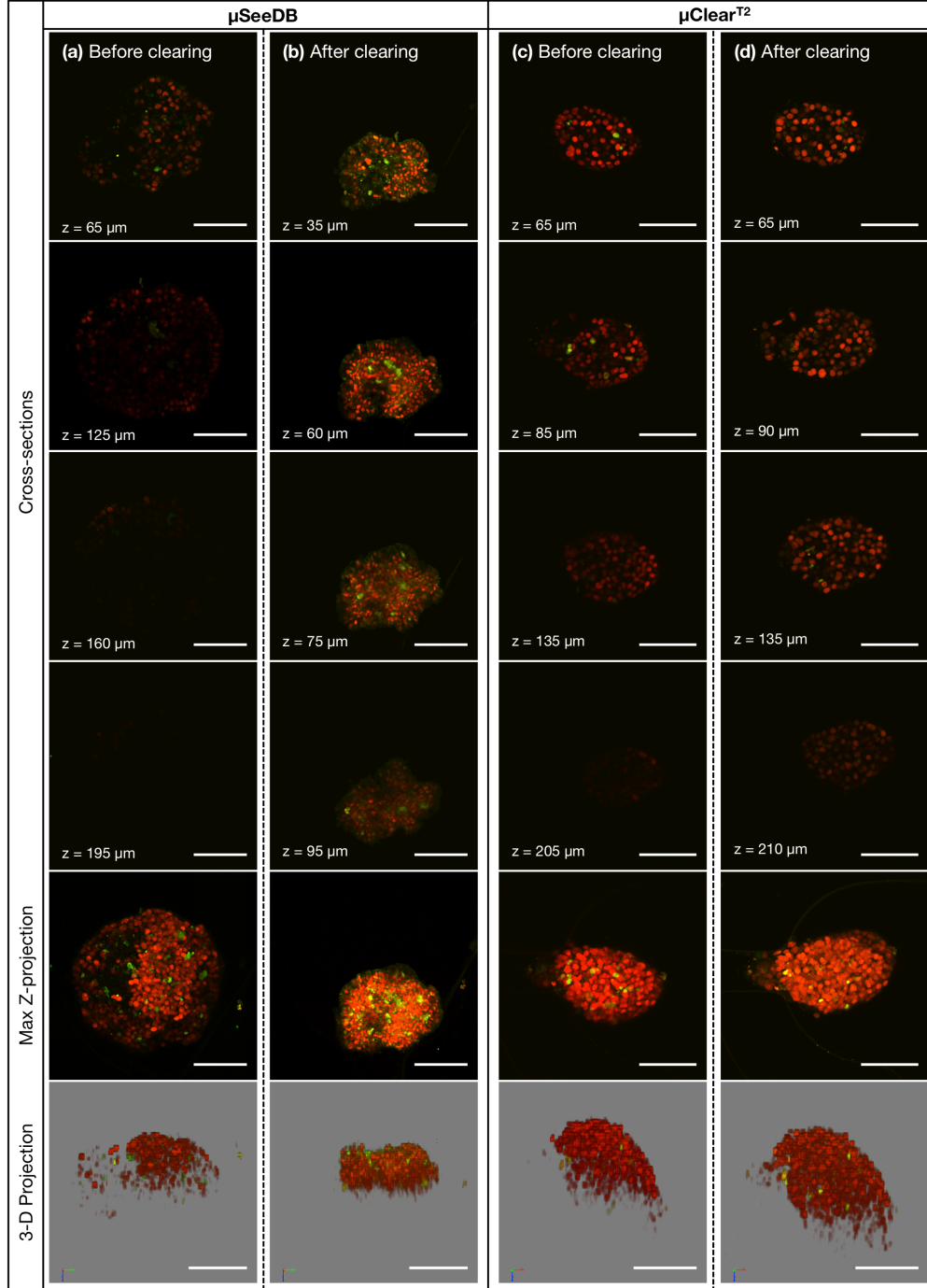
Figure 2.15. Results of on-chip tissue clearing of tumour spheroid cultures. Results using SeeDB **(a-b)** and Clear^{T2} **(c-d)** are presented. Cross-sectional image slices at various objective z-step depths into the spheroids, maximum z-intensity projection images, and 3-D renderings reconstructed from the two-photon z-stack are presented for each clearing type before (left - a,c) and after (right – b,c) the clearing process. Slice images were chosen to show approximately the same sample position before and after clearing (the SeeDB depths are smaller primarily due to the large sample shrinkage during the clearing process). Both clearing processes appear to improve imaging quality deep into the spheroid, with enhanced light penetration and sharper images visible after clearing. The SeeDB process induces significant shrinkage in the sample (spheroid slices shrink to approximately 60% of their initial area for this sample) and also induces green autofluorescence. The Clear^{T2} process offers a more moderate improvement in brightness while appearing to better maintain sample size and fluorescence. All scale bars represent 100 μm.

Figure 2.15 (a-b) shows images of a spheroid prior to (a) and after (b) clearing with μSeeDB, while Figure 2.15 (c-d) shows images of a spheroid prior to (c) and after (d) clearing with μClear^{T2}. Figure 2.15 (a-d) each show 2-P slice images at four z-depths (with images of the same spheroid matched to best show approximately the same spheroid position), as well as a maximum z-intensity projection image and a maximum intensity projection 3-D rendering of the spheroid. Both clearing methods improve visibility of deeper parts of the spheroid, increasing light penetration as well as reducing blurring of the nuclei deep into the spheroid. We find, however, that μSeeDB induces significant shrinkage of the tumour spheroids (A_{post}/A_{pre} = 0.48±0.13, N=4) as well as some green autofluorescence, while μClear^{T2} yields cleared images of a spheroid more closely resembling the original spheroid structure with slight swelling (A_{post}/A_{pre} = 1.16±0.09, N=5, for the same batch of spheroids as that reported for μSeeDB above).

We compared our accelerated μSeeDB process (involving perfusion through tubing pre-loaded with 10 cm lengths of the sequential solutions) with a single-step process (perfusing the spheroids immediately with 115% fructose in water solution) and a more traditional multi-step process (in which the spheroids were perfused sequentially with each solution while imaging, allowing equilibration in each solution in a longer, ~1 hour total, process). Example images for a representative spheroid treated with each of these procedures are presented in Figure 2.16 (a-c). Fructose is a reducing sugar, and can induce autofluorescence of tissue samples via Maillard reactions [32]. We found that the sample became more autofluorescent in the green channel after longer times in the fructose solutions, making the original multi-step process with sequential perfusions less useful, although the sample shrinkage was reduced (A_{post}/A_{pre} = 0.85±0.04, N=3). We observed reduced sample shrinkage in the accelerated multi-step process in comparison with the single-step process on the same batch of spheroids (single-step: A_{post}/A_{pre} = 0.54±0.09, N=3; multi-step: A_{post}/A_{pre} = 0.78±0.09, N=3), so the accelerated multi-step μSeeDB process appeared to be the best option for SeeDB treatment of our tumour spheroid samples.
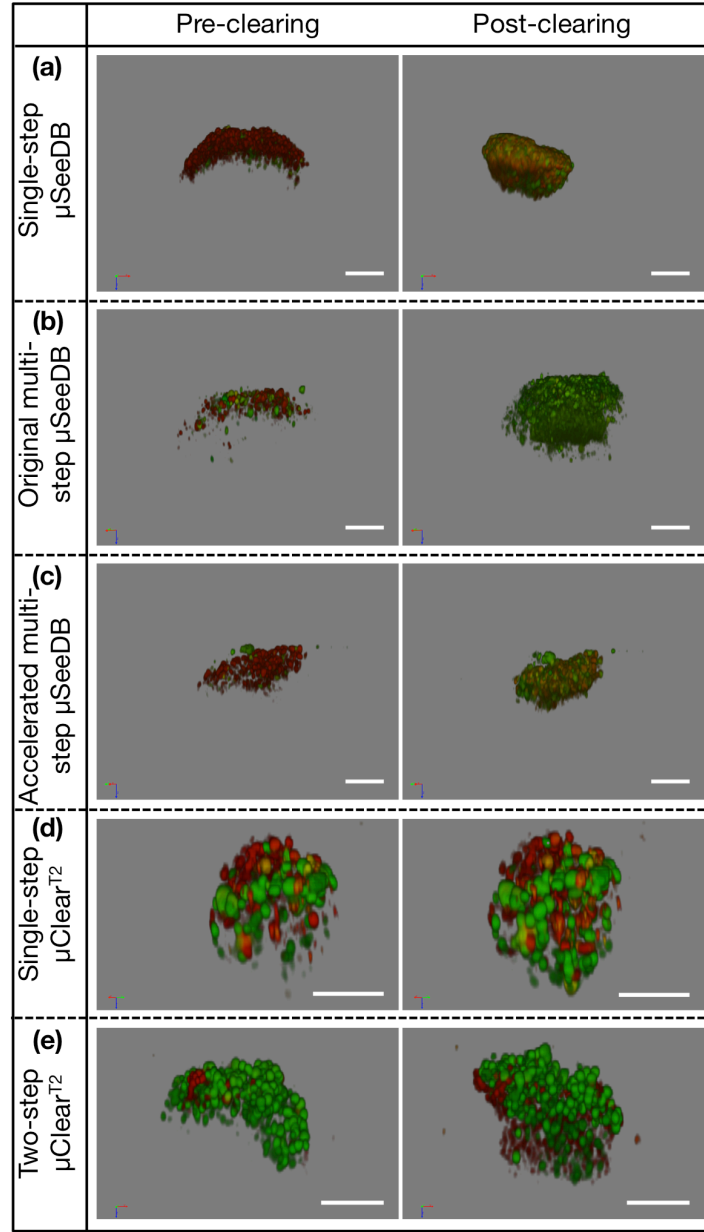
Figure 2.16. Comparison of single-step and multi-step clearing. Comparison of maximum intensity projection 3-D renderings of tumour spheroid samples before and after clearing with **(a)** single-step μSeeDB (in which the sample is directly perfused with the final 115% fructose solution), **(b)** original multi-step μSeeDB (involving sequential incubations and equilibrations in each solution in a longer, ~1h process), **(c)** accelerated μSeeDB (using tubing pre-loaded with 10 cm lengths of each solution in a shorter process exposing the samples to the sequential concentrations of fructose solutions), **(d)** single-step μClear^{T2} (in which the sample is directly immersed in the final 50% formamide/20% PEG clearing solution), and **(e)** the original two-step μClear^{T2} (in which the sample is perfused first with 25% formamide/10% PEG and then with 50% formamide/20% PEG). We observed that longer incubations in the fructose solution induced increasing amounts of green autofluorescence in the sample after clearing (visible in comparing the images of the longer process of (b) to those of (a) and (c) – (b) results in images after clearing with much stronger green channel fluorescence). The accelerated μSeeDB process was thus judged to be the best SeeDB-based option for clearing our samples. There was no apparent difference between the results of single and two-step Clear^{T2} for our samples. Scale bar in all images represents 100 μm.

We also compared a single-step μClear^{T2} process (perfusing directly with the 50% formamide/20% PEG solution) with the standard process (25% formamide/10% PEG followed by 50% formamide/20% PEG), and observed similar clearing and spheroid behaviour (example images for a representative spheroid presented in Figure 2.16 (d-e)). For the single-step process, A_{post}/A_{pre} = 1.16±0.10, N=3.

As a measure of clearing efficacy, we quantified spheroid fluorescence intensity in the red channel as a function of depth into the sample, before and after treatment, for three spheroids cleared with μSeeDB and three spheroids cleared with μClear^{T2}. The fluorescent regions in a denoised red channel two photon fluorescence image at each depth were first segmented using a custom MATLAB$^{®}$ script using a low intensity threshold of 0.004. This threshold was chosen by running the segmentation using several thresholds and comparing the segmentations' ability to separate the cell-containing spheroid region from the background. Otsu's method of choosing the segmentation threshold [278] was also attempted; however, it was not found to be more effective (potentially due to the large variance in nucleus intensities present within the spheroid regions).

These segmented regions were then dilated and eroded (morphological close operation), and subsequently eroded and then dilated (morphological open operation) using a disk-shaped structuring element with 50 pixel radius to fill in the spheroid regions and remove segmented non-spheroid regions. Holes in the segmented regions were filled, and isolated segmented regions of size less than 300 pixels were removed. The intensities of the final segmented regions in the original (not denoised) fluorescence image were then averaged (yielding the mean μ), and the variance $\left(\frac{1}{n}\sum_{i=1}^{n}(x_i - \mu)^2\right)$ in these pixel intensities was also calculated as a measure of image contrast in the spheroid-containing region. Slices deep in the uncleared spheroids tend to exhibit blurriness of the fluorescent nuclei due to scattering effects, which reduces image contrast in this region. Both average spheroid intensity and spheroid intensity variance were plotted versus depth into the spheroid, and the plots from before and after clearing of each spheroid were plotted on the same axes. The results of this process are plotted in Figure 2.17.
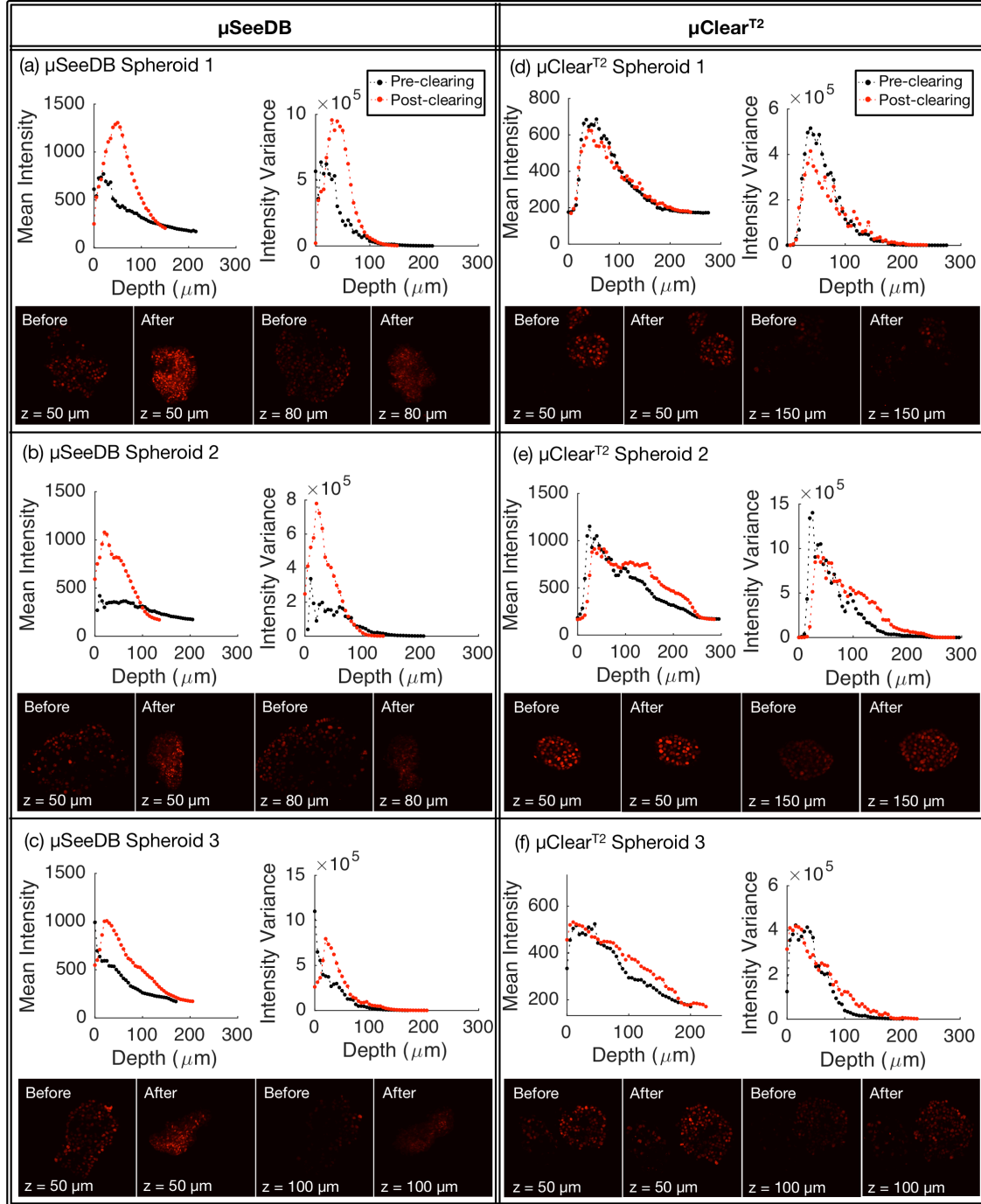
Figure 2.17. Quantitative analysis of spheroid clearing efficacy. Analysis of average red fluorescence intensity in the spheroid regions before (black) and after (red) clearing, for three spheroid samples of each clearing type, plotted vs. objective z-step depth. Each sub-image presents the average spheroid fluorescence intensity, its intensity variance, and slice images at two depths into the sample, both before and after clearing. μSeeDB **(a-c)** results in a marked improvement in intensity with depth, which is likely attributable to sample shrinkage (and thus concentration of sample fluorescence) as well as clearing ability. μClear^{T2} **(d-f)** results in a moderate improvement in intensity and variance in (e) and (f) and much better-resolved nuclei at deep imaging depths in all three cleared samples. The spheroid depicted in (d) was less dense and showed reasonable intensities in the images acquired prior to clearing. All slice images were acquired using the same imaging parameters and no postprocessing was conducted.

Figure 2.17 (a)-(c) present these results for three separate spheroids cleared with μSeeDB, while Figure 2.17 (d)-(f) present these results for three separate spheroids cleared with μClear^{T2}. For each spheroid, we present a plot of the average spheroid red 2-P fluorescence intensity vs. objective z-step depth, a plot of the spheroid intensity variance, and z-slice images at two different depths; all plots and images show both before and after clearing.

For each of the three μSeeDB-cleared spheroids, the post-clearing plots showed a very large increase in intensity in comparison with the pre-clearing plots, while the slice images showed a large increase in brightness. This drastic change could have been induced in part by the large (almost 50% area) shrinkage observed in the samples during the μSeeDB treatment. The shrinkage concentrates the fluorescence into a smaller volume, greatly increasing the average fluorescence intensity, as well as the range of intensity values (and thus the intensity variance) in that region. We observe an increase in penetration depth, and the spheroid also shrinks in the z-direction. Additionally, the nuclei become better resolved and images become clearer deep into the spheroid after treatment.

Although the difference in the plots for the μClear^{T2}-treated samples is less immediately apparent, the intensity and intensity variance of the spheroids in Figure 2.17 (d) and (f) are noticeably higher after clearing. When examining the slice images, the nuclei in the centre of the spheroid are much brighter and much better resolved after the clearing process, resulting in clearer, sharper images. The images of the μClear^{T2}-treated samples are clearer and sharper than those of the μSeeDB-treated samples, and less spheroid and nucleus distortion is present due to the reduced sample shrinkage. The spheroid presented in Figure 2.17 (d) was less dense and already reasonably clear prior to clearing; however, deep into the spheroid such as at the 150 μm slices shown, the nuclei are much better resolved after the clearing process.

2.5.3.2.2   On-Chip Clearing is Compatible with Microfluidic Devices Used for On-Chip Culture and Monitoring

The results of our on-chip culture and clearing within the same microfluidic device are presented in Figure 4. All images depict the same spheroid at different points in the experiment. Figure

2.18 (a) and (b) present maximum z-intensity projection images of the spheroid 13 days (a) and 17 days (b) after hydrogel bead formation, showing the increase in spheroid size between these two imaging points. Figure 2.18 (c) presents a single two-photon fluorescence z-slice image overlaid upon a transmitted light image at day 17. Figure 2.18 (d) presents a two-photon fluorescence z-slice image overlaid upon a transmitted light image of the same spheroid after fixation, conducted immediately after imaging at day 17. Both the fluorescence intensity and the transmitted light intensity decreased after paraformaldehyde fixation, consistent with findings reported in the previous work on SeeDB [32]. Fixation also resulted in spheroid shrinkage and deformation into a curved shape, potentially due to the initial concave morphology of this spheroid. Finally, Figure 2.18 (e) presents a two-photon fluorescence z-slice image overlaid upon a transmitted light image of the same spheroid after a single-step μSeeDB process, in which the spheroid was immediately perfused with the 115% fructose solution while monitoring with two-photon microscopy. Some green autofluorescence induced by the SeeDB process is visible, while both the orange and green nuclei in the spheroid centre are much more visible and better resolved after clearing. Figure 2.18 (c), (d), and (e) present 2-P slice images taken at approximately the same position in the sample overlaid upon transmitted light images of the sample.
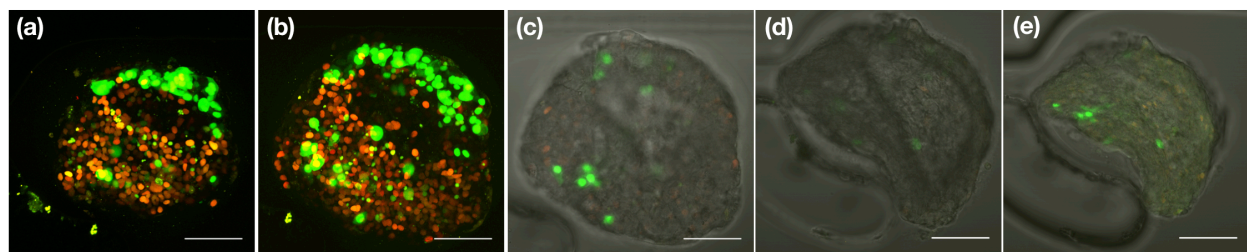
Figure 2.18. Demonstration of the compatibility of the μSeeDB clearing process with microfluidic devices used for on-chip cell culture. **(a-b)** maximum z-intensity projection images of the spheroid 13 days **(a)** and 17 days **(b)** after hydrogel bead formation, showing the increase in spheroid size between these two imaging points. **(c-e)** two-photon fluorescence z-slice images overlaid upon transmitted light images of the same spheroid at different points during the clearing process. **(c)** prior to fixation, during imaging at day 17. A slice approximately 175 μm into the spheroid is shown. **(d)** after on-chip fixation in 4% paraformaldehyde, conducted immediately after imaging at day 17 (approximately the same sample position as in (c) is depicted). Both the fluorescence intensity and the transmitted light intensity decreased after paraformaldehyde fixation, and fixation also induced sample shrinkage and deformation. **(e)** after a single-step μSeeDB process, in which the spheroid was immediately perfused with the 115% fructose solution while monitoring with two-photon microscopy. Both fixation and clearing were performed in the same chip as the spheroid culture. Many more fluorescent nuclei are visible in the spheroid core after clearing (e) than in the un-cleared live (c) or fixed (d) spheroid images. All scale bars represent 100 μm.

This work demonstrates the compatibility of the on-chip clearing implementation with microfluidic on-chip cell culture. Since the same microfluidic devices were used for all of our

on-chip clearing studies (both the μSeeDB and the μClear^{T2}), it follows that all of the investigated clearing protocols could be applied directly after on-chip culture and fixation. This compatibility is highly beneficial because it permits tracking of the same 3-D cultures during culture, test conditions such as drug treatment, staining, fixation, and clearing. This compatibility could be particularly useful in studies where spheroids at different positions in the device are exposed to gradients in oxygen or chemical concentrations; tracking the same spheroids over time is essential in this case. This kind of implementation could permit a study where two-photon microscopy is used to monitor the experiment and tissue clearing used at the study endpoint to better acquire data from the full z-depth of the same spheroids studied through the course of the experiment.

2.5.3.2.3 On-Chip Clearing is Rapid and Permits Monitoring of the 3-D Cultures During the Clearing Process

All clearing experiments performed on-chip were conducted in less than 1 hour, which is a significant improvement over the multi-day original SeeDB process. We believe that the combination of smaller diffusion distances (tumour spheroids are at least an order of magnitude smaller than brain tissues) and the constant supply of fresh clearing solution to the sample expedite this rapid clearing.

Another advantage of the on-chip clearing method is that it permits monitoring of the clearing process. This monitoring is advantageous as it allows the endpoint of clearing to be more accurately discerned, permitting more expedient imaging. The prolonged exposure to SeeDB reagents can increase sample autofluorescence over time, and the formamide in Clear^{T2} is not suitable for long-term sample storage [33]; as such, expedient imaging could be advantageous. Monitoring also allows us to visualize the same spheroid at different stages of the clearing process, facilitating the optimization of clearing protocols as it can permit the visualization of sample changes in response to the clearing assays that could induce artifacts.

Examples of this *in situ* monitoring capability are presented in Figure 2.19. We acquired both a 2-P fluorescence at a single z-plane and a transmitted light intensity projection image during the processes, acquiring one frame every ~11s.
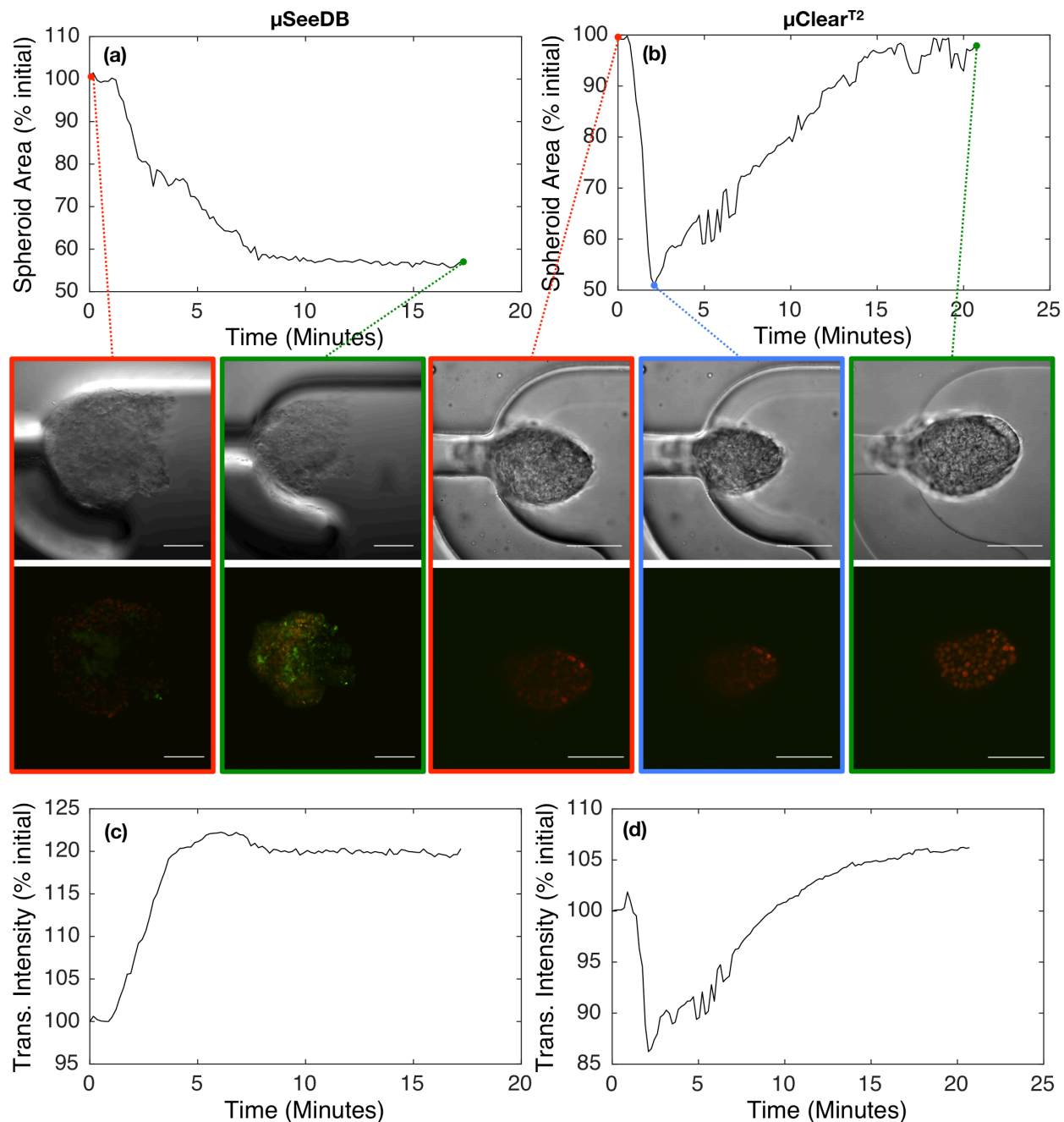
Figure 2.19. Monitoring of spheroid size and transmitted light intensity. Monitoring results are shown for μSeeDB (left) and μClear^{T2} (right) clearing processes. **(a-b)** Segmented spheroid area is plotted vs. time in the μSeeDB **(a)** and μClear^{T2} **(b)** clearing processes, with the transmitted light (top) and two-photon fluorescence (bottom) slice images of the spheroid at different points on the graph also shown as colour-coded insets. Both clearing protocols induce spheroid shrinkage; however, the μClear^{T2} process results in the sample recovering to close to its initial size. Both solutions improve fluorescence brightness and image sharpness at the spheroid core during the clearing process. **(c-d)** Monitoring of transmitted light intensity through the spheroid during the μSeeDB **(c)** and μClear^{T2} **(d)** clearing processes. μSeeDB results in a near-immediate improvement in transmitted light intensity, while μClear^{T2} results in an initial drop in intensity coincident with the spheroid shrinkage, followed by a recovery and slight improvement in intensity. All scale bars represent 100 μm.

88

We segmented the spheroid from the transmitted light intensity images and plotted the spheroid size (a-b) and average transmitted light intensity (c-d) during μSeeDB (a,c) and μClear^{T2} (b,d). We found that the SeeDB process caused the sample to shrink to approximately 60% of its initial area, likely due to osmotic pressure from the concentrated fructose solutions leading to osmosis out of the cells. As a further demonstration of the utility of the ability to monitor the sample during clearing, we found that during the Clear^{T2} process our spheroid samples first shrunk to approximately 50% of their original area, and then expanded back to close to their initial size (Figure 2.19 (b) and inset images). Clear^{T2} was previously reported (with only endpoint analysis) to not cause significant sample volume change [33, 37]. Formamide-based clearing has been hypothesized to operate by a similar mechanism as urea-based clearing processes, which penetrate into and partially denature hydrophobic proteins, causing hyperhydration and swelling; this in turn lowers the refractive index of the sample [279]. It is possible that the shrinking-swelling behaviour we observe in the Clear^{T2}-treated samples could be due to the sample first shrinking due to osmotic pressure and subsequently swelling as the formamide penetrates into the sample and promotes hydration. Awareness of responses like this could be important to users of this clearing method as the shrinkage-expansion process has the potential to induce imaging artifacts. The microfluidic implementation of tissue clearing facilitates the monitoring required to discover these types of effects.

2.5.3.2.4   Summary of On-Chip Tissue Clearing

We have demonstrated on-chip clearing of arrays of tumour spheroid cultures using both the SeeDB fructose-based tissue clearing process and the Clear^{T2} formamide-PEG clearing process. The on-chip tissue clearing protocol yields rapid (< 1 hour) clearing of arrays of 3-D cultures using both methods. The unique microfluidic implementation reduces spheroid loss during clearing and allows 3-D cultures to be monitored during the clearing process. Additionally, the same spheroid can be easily imaged at different stages of clearing. The monitoring facilitated by our microfluidic process allowed us to observe a spheroid shrinkage-expansion process during Clear^{T2} treatment that, to our knowledge, had not been previously reported as previous work (finding minimal sample volume changes) used endpoint analysis alone. This type of shrinkage and expansion could lead to sample changes and imaging artifacts, so the awareness of these effects enabled by monitoring could be beneficial to researchers developing clearing assays.

Although we demonstrate the procedure using the SeeDB and Clear^{T2} clearing solutions, the versatile on-chip implementation is also compatible with other clearing protocols. For example, FRUIT [36] or Clear^{T} [33] could also be implemented in this on-chip manner and may offer improved results for different types of 3-D cultures while retaining the advantages offered by the microfluidic implementation. This increases the versatility of the clearing system, as different types of 3-D cultures and micro-tissues could respond differently to different clearing protocols and the system could aid in the protocol optimization for different tissue types.

We also demonstrated a proof-of-concept on-chip study, in which tumour spheroids grown and monitored on-chip were fixed and cleared in the same microfluidic device, permitting monitoring of the same spheroids throughout the process. We anticipate that this capability will aid in the development of on-chip array-based drug screening assays, in which arrays of 3-D cell cultures can be monitored in 3-D throughout their culture, drug treatment, staining, fixation, and clearing. Additionally, the process will be compatible with microfluidic devices that we have developed for microenvironment control [280], further increasing the scope of these results. Future work could involve increasing the microfluidic array size to simultaneously clear larger arrays of tissues, optimizing the process for other types of micro-tissues, and applying this on-chip clearing implementation to drug screening or other 3-D culture assays.

2.6   Summary

This chapter has demonstrated several key contributions to the use of 3-D cell cultures undertaken as a part of this thesis project. We have created a microfluidic system that permits the monitoring of the interaction of tumour cells with their surroundings using microscopy and demonstrated a novel study in which the on-chip culture of 3-D tumour spheroids is monitored at several points during their culture, showing excellent viability at the study endpoint. This microfluidic culture system permits the study of an array of spheroids, and is compatible with on-chip oxygen control (which will be discussed in Chapter 4) as well as on-chip fixation and clearing at the study endpoint.

We have also presented several methods by which the imaging of 3-D cultures was improved to permit better analysis of 3-D culture experiments at the study endpoint. These imaging methods utilized a high-NA objective lens, which permits the resolution of collagen fibres by second harmonic generation imaging [281], or other small features, in future studies. If this high resolution is not required, imaging depth could be further improved by using a lower-NA objective lens, which would likely be less susceptible to scattering. We demonstrated a novel modulation of laser intensity with depth into the spheroid, as well as the novel adaptation of two different tissue clearing protocols for on-chip clearing. Our on-chip implementation of tissue clearing facilitated the monitoring of the clearing process and allowed us to observe dynamic changes in the spheroid as a result of exposure to the clearing reagents, observing for the first time shrinkage followed by expansion to close to the initial tissue volume during exposure to the formamide-based Clear^{T2} clearing reagents. Finally, we have demonstrated a novel integration of these methods, with on-chip culture, staining, fixation, tissue clearing, and two-photon imaging within the same microfluidic device. These studies build a foundation for the additional oxygen control and measurement functionality that will be discussed in Chapter 3 and Chapter 4, and also facilitate the cell-based studies presented in Chapter 5 and open the door for future studies that could use 3-D cultures with controlled micro-environmental changes for drug screening studies.

Chapter 3 Optical Oxygen Sensor Fabrication and Integration

In order to characterize and validate the oxygen profiles created within the microfluidic oxygen control device that will be presented in Chapter 4, optical oxygen sensors were developed and integrated into the microfluidic channels. This chapter presents the fabrication, integration, and characterization of these optical sensors. The goals for the sensors are presented in section 3.1 and the methods used to fabricate the sensors presented in section 3.2. An overview of the setup with which the sensors were calibrated and measured, developed in collaboration with several other students, is presented in section 3.3. Over the course of developing this platform, we moved from intensity-based sensors to ratiometric sensors in order to improve the robustness and consistency of the sensor response. A comparison of intensity-based to ratiometric sensors is presented in section 3.4, the calibration process and characterization of the ratiometric sensors presented in section 3.5, and the process by which the sensors were measured is presented in section 3.6.

3.1   Goals

The purpose of the oxygen sensors within the microfluidic environment was to:

1. Verify that the oxygen control system was able to create the spatiotemporally-varying oxygen profiles of interest within the cell culture chamber.
2. Be usable during future cell studies as needed, for example permitting future studies where the cellular oxygen consumption could be measured.

The goal of the oxygen sensors was to be usable both in the studies that are presented as a part of this thesis, as well as in more sophisticated future studies, wherein cell-induced oxygen gradients or other deviations in the oxygen levels due to cells or chemical reagents could be quantified during cell culture experiments. To fulfill this purpose, the oxygen sensing implementation needed to:

1. Provide 2-D maps of the oxygen levels.
2. Be stable over long periods of time.
3. Permit high-resolution and fluorescence imaging of the cells (unobstructed by sensors in the optical path).

4. Minimally interact with the cells.

For initial cell studies, we needed to compare standard normoxic culture (commonly performed at 20-21% oxygen) with hypoxic and even anoxic culture (down to 0% oxygen); the sensors thus needed to have a sensing range of at least 0-21% with good sensitivity.

In order to be compatible with monitoring of cell cultures using microscopy, intensity and ratiometric sensing implementations were investigated (described in section 1.3.2). Both of these permitted microscopic monitoring of both the oxygen sensors and cells using only a standard fluorescence microscope. The dyes were encapsulated within a polystyrene film in order to minimize the interaction between the sensor dye molecules and the cells (as discussed in section 1.3.3.1). To make the sensors viable for long-term studies, dyes with good photostability were chosen and additional measures were taken to improve stability. Intensity-based sensors were first implemented, and fabrication processes were developed for these films. In order to improve stability, ratiometric sensors using the same polystyrene matrix were then implemented and could be fabricated using the same patterning methods developed for the intensity sensors.

3.2 Fabrication Methods

Over the course of this work, several sensor fabrication methods were investigated. Patterned spin-coated thin-film sensors were chosen as they afforded the best sensor film uniformity (important for intensity and ratiometric sensing implementations) while also allowing isolation of the sensor regions so that cell cultures could be imaged without obstruction. Patterning these spin-coated films proved to be challenging, as polystyrene is readily attacked by many photoresist solvents and strippers. Previously-demonstrated dry etching methods employing a pinhole-free metal etch mask [172, 238] and removable PDMS 'stamps' [129] were first implemented; however, neither of these methods were found to be ideal for this thesis project. It was found that generating a sufficiently pinhole-free etch mask on top of the sensor film using the available thermal evaporation or sputter-coating equipment was very difficult and resulted in a low yield, as even small pinholes resulted in sensor film destruction during photoresist spin or removal. The metal etch mask method also necessitated a multi-step fabrication process which was not ideal for this application as the microfluidic devices with integrated sensors needed to be

single-use. Although the PDMS stamp method is a single-step process employing a reusable stamp, fidelity of pattern transfer was highly dependent on the type of plasma etcher and etch parameters used; reliable pattern transfer was not achievable using etch equipment available at UBC or the SFU 4D Labs. For this reason, two novel, maskless fabrication processes were developed with which to pattern the oxygen sensor films: a water-soluble polyvinyl alcohol (PVA) dry etch mask process, and a novel laser-cutting process.

3.2.1   Sensor Fabrication using a Water-Soluble PVA Etch Mask

A simple, alternative fabrication method employing a PVA etch mask was developed to pattern solvent-incompatible materials. PVA has been previously demonstrated as a masking layer used while patterning biomolecules using photolithography to prevent the photoresist from coming into direct contact with the biomolecules [282]. Similarly, a lift-off process using a PVA/SU-8 bilayer has been demonstrated for the fabrication of organic thin-film transistors [283], and PVA has also been demonstrated as an SU-8 structure release layer for microelectromechanical systems (MEMS) applications [284]. While these methods are capable of very high resolution features, they require photolithographic processing of each substrate. Because many of the applications of microfluidic and lab-on-a-chip devices necessitate inexpensive single-use devices, minimal processing to fabricate each sample is an advantage. Our method is faster, easier, and less expensive than the photolithographic methods, and presents a promising alternative for applications where the resolution is less important than the speed and cost.

3.2.1.1   Methods

Figure 3.1 presents the fabrication process flow for the process applied to the fabrication of optical oxygen sensors. We chose PVA for the etch mask material because it is water-soluble (and thus can be dissolved without damaging the sensor) and can be patterned in sufficiently thick films to serve as an etch mask. We demonstrate a manual dispensing method, using a syringe and micromanipulator stage; however, the PVA could also be deposited using a 3-D or multi-layer inkjet printer.
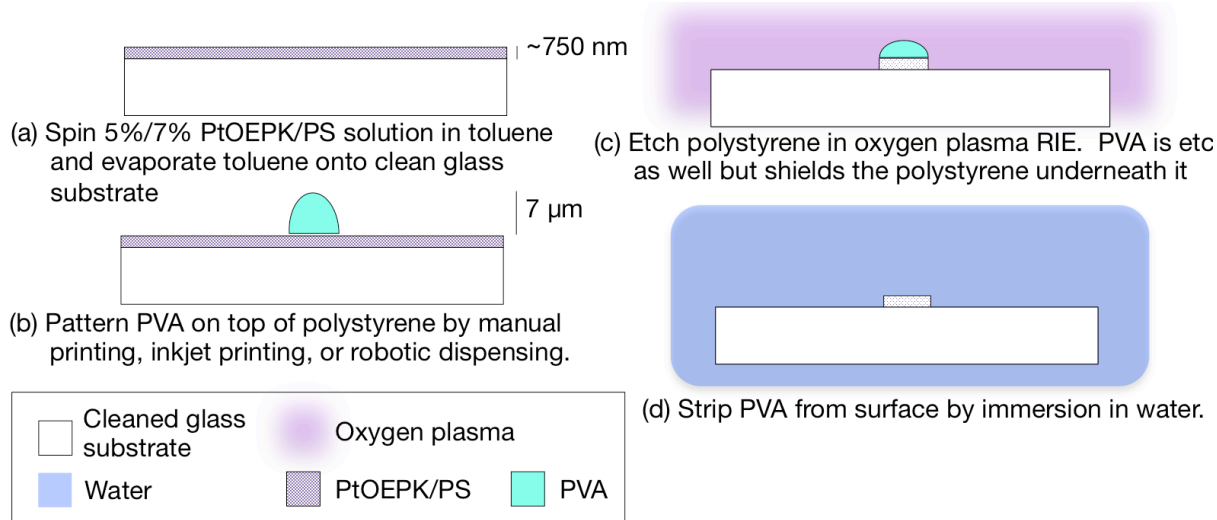
Figure 3.1. Oxygen sensor fabrication process using a PVA etch mask. **(a)** Sensor film spin. **(b)** Patterning of 10% (w/w) solution of PVA in water. **(c)** Exposure to oxygen plasma (Technics Planar Etcher II, P=400 mTorr and P=160W, t=12 minutes). We measure average etch rates of 90 nm/min for the PVA and 86 nm/min for the polystyrene. **(d)** PVA strip. Figure previously published in [285].

Etch completion was verified with profilometry using a Dektak 150 profilometer and fluorescence microscopy using a Nikon TE-2000-U fluorescence microscope system. A filter set for measuring the phosphorescence of the PtOEPK dye (Omega Optical 400AF30 bandpass excitation filter, 475DCLP longpass dichroic mirror, and 700ALP longpass emission filter) was used for the fluorescence microscopy characterization. Oxygen sensor function after patterning using PVA etch masks was verified by calibration using three gaseous oxygen concentrations (0 atm, 0.21 atm, and 1 atm). Briefly, the sensors were exposed to pure gaseous nitrogen, air, and oxygen, and the sensors' phosphorescence intensities were measured at each of these known oxygen concentrations. The quenching characteristics of four separate oxygen patches were determined and averaged, with each patch being calculated on an average of 25 000 pixels.

3.2.1.2   Results and Discussion

We observed good pattern transfer using the PVA etch mask method, demonstrating large patterns of ~300-500 μm linewidths (limited by the resolution of our manual PVA dispensing method). Figure 3.2 and Figure 3.3 present the phosphorescence sensor images and the profilometry results of the patterned sensors, respectively. The thickness uniformity of the PVA film does not have an effect on the patterning results, as long as the film had a minimum thickness large enough to withstand the oxygen plasma etching time required to etch the oxygen

sensor film. For our sensor film thickness of approximately 750 nm, we found that 5 μm of PVA was sufficient.
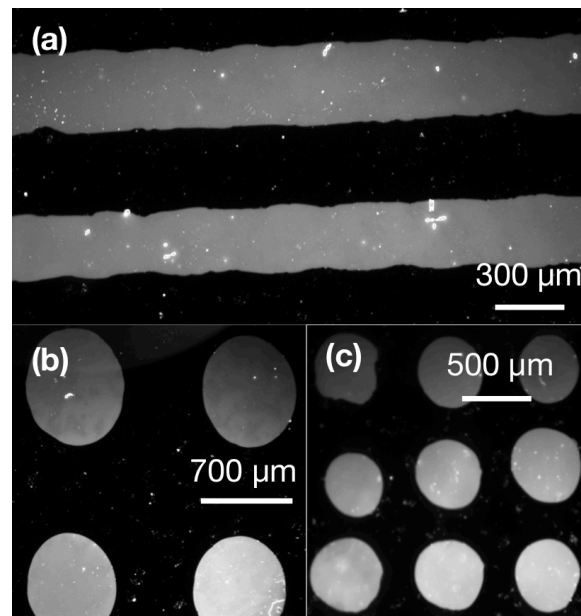
Figure 3.2. Fluorescence microscope characterization of PVA-patterned oxygen sensor film. Phosphorescence images of patterned oxygen sensor **(a)** lines, **(b)** larger patches, and **(c)** smaller patches. Figure previously published in [285].
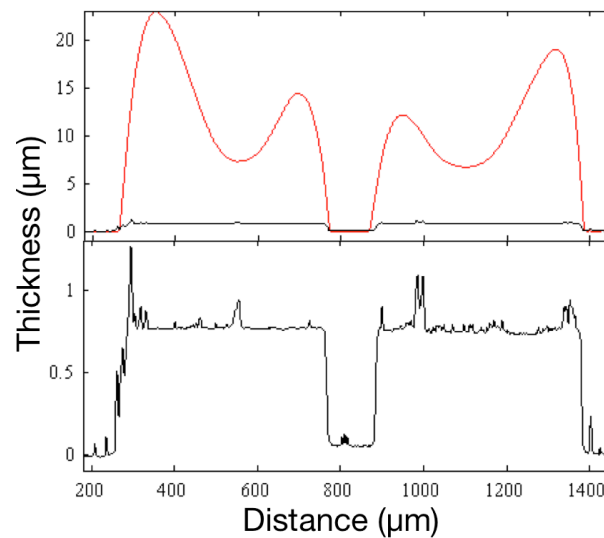
Figure 3.3. Profilometry characterization of PVA sensor fabrication process. Profilometry measurements of (top) PVA film before etching (red) and patterned sensor film after PVA strip (black), and (bottom) close-up of patterned sensor film after PVA strip, acquired using a Dektak 150 profilometer. Figure previously published in [285].

The sensor calibration conducted after patterning verified that the oxygen sensors remained functional. The sensor performance (shown in Figure 3.4) was found to demonstrate a linear Stern-Volmer quenching relationship, as was expected from equation 2 on page 21 and observed in the sensor films before the patterning process.
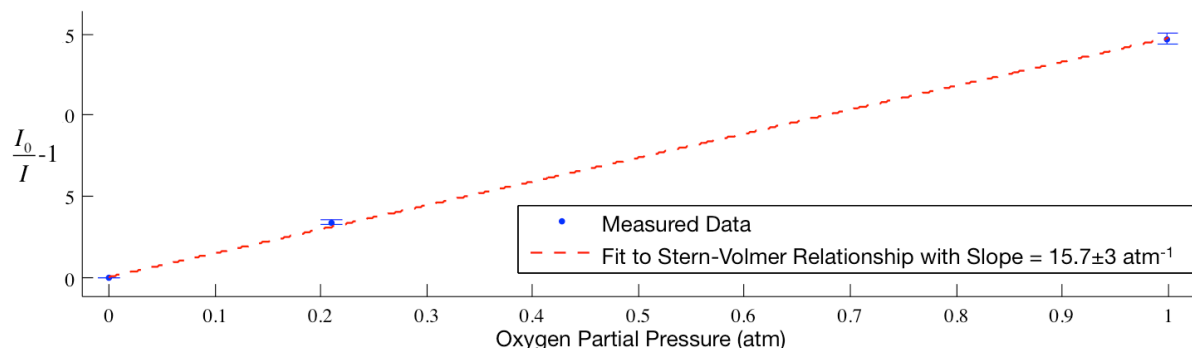
Figure 3.4. Demonstration of optical oxygen sensor functionality after PVA patterning. Measured phosphorescence quenching behaviour of patterned optical oxygen sensors (blue datapoints), fit to the Stern-Volmer relationship shown in equation **2** (red dotted line). The patterned sensors exhibited linear quenching behaviour with an unquenched intensity (I_0) of 157 and a quenching constant (K_{SV}) of 15.7±3 atm^{-1}. Error bars represent the standard deviation of the measurements of 3 sensor patches. Figure previously published in [285].

3.2.2   Sensor Fabrication using a Laser-Cutting Process

In testing previously-demonstrated dry etching methods employing metal etch masks [172, 238] and removable PDMS 'stamps' [129], as well as our non-photolithographic dry etch method utilizing the PVA etch mask [285] (described in section 3.2.1), we have found that residue on the glass slides after dry etching of the polystyrene inhibits subsequent plasma bonding of PDMS, which complicates the patterned sensors' use in microfluidics. We tried various models of oxygen plasma etchers (Technics PE-II, Trion PECVD, and Sentech Etchlab 200 RIE) but were unable to reliably bond PDMS to previously-etched substrates in all cases. To overcome this challenge, we devised a simple and mask-less method for the patterning of polystyrene optical oxygen sensor films in which the bulk film is peeled/lifted off rather than etched. This process is facilitated by the poor adhesion between the glass and spin-coated PtOEPK/PS film.

Our method patterns the polystyrene film containing the oxygen-sensitive dye using a commercial laser cutter system. Laser ablation of polystyrene has been previously found to be a

thermal and photothermal dissociative process that 'unzips' the polymers into monomer styrene [286, 287]. We use laser ablation to selectively remove polystyrene from pattern edges, separating desired patterns from the film bulk. Because the laser is only used in small regions compared to the large substrate areas affected by plasma etch processes, any residue left behind after laser ablation does not impact subsequent PDMS bonding.

This section presents our novel sensor patterning fabrication process, as well as the sensing performance and characterization of the patterned sensors. We characterized the physical structure of the patterned sensor films using brightfield, fluorescence, and atomic force microscopy (AFM). We also investigated the chemical residues left on the glass after laser-cutting, oxygen plasma dry etching, and bulk film lift-off/peeling in order to understand the mechanism by which this method operates as well as to understand why polystyrene dry etch processes inhibit subsequent PDMS bonding. Finally, we demonstrate the compatibility of our fabrication process with PDMS microfluidic devices by integrating the patterned sensors with a microfluidic oxygen gradient generator device and measuring *in situ* oxygen gradients.

3.2.2.1   Methods

The phosphorescent oxygen sensor films were fabricated by spin coating, patterned by mask-less laser ablation, and integrated with a microfluidic device patterned with standard soft lithography. This section details the methods used to fabricate the sensors, as well as the methods by which they were tested and characterized, including their microfluidic integration.

3.2.2.1.1   Materials

Platinum (II) octaethylporphyrin ketone (PtOEPK) (Frontier Scientific), polystyrene pellets (MW 280 000, Sigma Aldrich) and toluene (CHROMASOLV® 99.9%, Sigma Aldrich) were used to fabricate the sensor films. Soda-lime glass slides of size 50 x 75 x 1 mm (Fisher Scientific) were used as the glass substrates. Dow Corning Sylgard 184 PDMS was used for the microfluidic devices (Paisley Products of Canada).

3.2.2.1.2   Sensor Fabrication

The fabrication process flow diagram is presented in Figure 3.5. PtOEPK (1 mg/mL) dissolved in a solution of polystyrene (PS) in toluene (5% w/w) is first spin cast onto a soda-lime glass substrate after preparing the substrate with a 5 minute oxygen plasma exposure (Technics Planar Etch II, at a pressure of 400 mTorr and a power of 180 W) to improve polystyrene adhesion (Figure 3.5 (a)). The films were measured (after solvent evaporation and a 5 minute bake at 100°C) to be approximately 650 nm in thickness using non-contact AFM measurements (Nanosurf easyScan 2). A Quiklaze-50 ST2 Nd:YAG laser system (ESI, Portland, Oregon) outfitted with a 50x magnification objective and x-y translation stage (maximum translation distance of 50 mm in each direction, precision of 1 μm [288], variable laser aperture size of 2-50 μm) is then used to trace around the edges of final patterns and ablate the polystyrene film (b). The sample was placed on a silicon wafer during patterning to act as a non-transparent substrate. It is important to completely cut through the polymer film to separate the desired patterns from the bulk in order to prevent patterned structures from lifting off with the bulk film.

We found that the UV3 (355 nm) high power setting (5.1 W/um^2) [289] at a 50 Hz frequency with a 40 μm/s scan speed yielded excellent results after two passes for our 650 nm film thickness. Although most of the film was ablated after a single pass, residue was visible in some regions that connected the patterns and the bulk film; two passes were used in order to ensure that the patterns were completely separated from the bulk. After two passes, the patterns were completely separated from the bulk but slight residue remains in the laser cut regions, as shown in the AFM measurements and images of section 3.2.2.2. A 5 μm x 5 μm square aperture was used for the patterned sensor films presented in this work.

After completion of the laser tracing, the bulk film around the patterns is removed by aqueous lift-off/peeling; a water bath aids in this process (depicted in Figure 3.5 (c-d)). We find that tracing around the edge of the glass slide with a scalpel to penetrate the film and start the lift-off process prior to placing the sample in the water bath helps ensure good results. We find that the scalpel tugs at the film during cutting, locally delaminating it near the cut and allowing the water to start penetrating under the film (whereas the laser tends to seal the cut edges to the substrate).

~650 nm

(a) Spin 5% PtOEPK/PS solution in toluene onto oxygen plasma treated clean glass substrate and evaporate toluene.

(b) Laser-cut the outlines of small structures in the PtOEPK/PS film.

(c) Cut around edges of slide with scalpel to pierce the film and initiate liftoff.

(*)

(d) Peel/lift off bulk film using a water bath and tweezers to aid in film removal. If high density patterns have been cut it may be necessary to gently pull the film edge to remove the bulk film from the patterned area as the laser cutting process slightly improves film adhesion in ablated areas (*).

(e) Peel off any remaining pieces at the outside of the slide in the water bath and dry the substrate.

| Cleaned glass substrate | UV Laser |
| PtOEPK/PS | Water |

Figure 3.5. Fabrication process flow diagram for the laser cutting sensor patterning process. **(a)** dissolved sensing dye and PS in toluene are spin-coated onto a clean and plasma-treated glass surface, and toluene is evaporated. **(b)** outlines of sensor structures are traced with a Quiklaze-50 ST2 Nd:YAG laser cutter. **(c)** bulk liftoff process is initiated by piercing the film at the edge of the slide with a scalpel. **(d)** bulk film is lifted off using a water bath and tweezers to aid in film removal. Figure previously published in [239].

During the peeling/lift-off process we find that the film is easy to remove in one or two large pieces, leaving behind the isolated patterns and removing the need to touch the film or substrate in areas close to the patterns of interest. To lift off the film, the glass slide is first placed on the water surface; the polystyrene-coated 1 mm thick soda-lime glass slides will sit atop the water surface. The slide corners are then very gently pushed down; if the slide is pushed very slowly to the point where the water meets the scalpel-cut interface, the water slowly seeps underneath the

100

scalpel-cut film, peeling off the film bulk as the sample sinks. The bulk film is often left floating atop the water bath after the sample sinks to the bottom. If the sample stops sinking or pulls the film below the surface, we find that the film edge (already lifted by the water) may be gently pulled with tweezers to lift it from the substrate without touching the substrate near the patterns. We have found this necessary when patterning high-density patterns, indicating a small improvement in film adhesion at the patterned interfaces. This process is depicted in Figure 3.5 (d)(*). After removal of the bulk of the film close to the sensors, the edges of the film outside of the scalpel line may be removed by pulling with tweezers in the water bath.

After the bulk film has been removed, the patterned sensors are gently dried with a nitrogen gun, baked on a hotplate for 10 minutes at 100°C, and cooled prior to storage or microfluidic integration.

3.2.2.1.3   Microfluidic Fabrication and Sensor Integration

To demonstrate compatibility with PDMS microfluidics, we integrated the patterned sensors into a microfluidic device. The device we chose for this purpose was an oxygen gradient generator with a large central chamber and parallel separated 400 μm gas control channels, similar to previously demonstrated oxygen control microfluidic devices [247, 249, 250]. Fluid is supplied to the 3 mm central chamber at a slow flow rate (0.5-1 μL/min, velocity of 9-18 μm/s) while the gas control side channels control the oxygen levels in the central chamber. Because one potential disadvantage of gradient generator designs employing pressurized gas control channels is the possibility for bubbles to develop inside the fluid channels due to the high gas permeability of PDMS [247], we also integrate narrow (100 μm) fluid channels perfused with fluid at a rate of 0.25 μL/min between the gas control channels and microfluidic chamber in an effort to remove any bubbles. This use of fluidic side channels is similar to one previously used for a multilayer oxygenator system [252].

The microfluidic channels were patterned in PDMS by standard soft lithography using an intermediate polyurethane replicate of the original wafer of SU-8 3050 photoresist on silicon (photolithographically patterned to form channels 360 μm in height). Inlets and outlets are bored

using a 0.5 mm punch (Harris Uni-Core through Ted Pella, no longer available) before bonding with the glass substrate containing the patterned sensors.

Permanent plasma bonding was used to enclose the microfluidic channels; the PDMS microfluidic channels and glass substrate around the patterned polystyrene sensors were exposed to air plasma for one minute and then brought into contact. Devices were left overnight in a 65°C oven to complete the bonding between the PDMS and lifted-off glass regions. Final devices were connected to Tygon® microbore tubing (Cole-Parmer) with blunt 22 gauge needles (Nordson EFD) after sensor integration.

3.2.2.1.4   Sensor Characterization

Microscopy After patterning, the sensors were characterized under brightfield and fluorescence microscopy to verify the lift-off fidelity. To obtain these microscope images, a Nikon TE-2000-U microscope was equipped with a bandpass excitation filter (Omega Optical 400AF30), long-pass dichroic mirror (Omega Optical 475DCLP), and long-pass emission filter (Omega Optical 700ALP), mercury arc fluorescence excitation lamp (Nikon Intensilight® C-HGFI) and colour camera (Qimaging Retiga EXi). The fluorescence microscopy filters were chosen to provide and measure PtOEPK dye excitation and emission wavelengths of 398 nm and 759 nm [140], respectively. The 3-D pattern geometries and the morphology of the laser cut interface were characterized with an AFM (Nanosurf easyScan 2) operating in non-contact mode.

Test structures were also patterned to investigate the limitations on the patterning process in terms of pattern spacing aspect ratio (the maximum length/width ratio facilitating lift-off, where the length was ablated with the laser to separate the pattern and the width was connected to the bulk film). We have observed slightly improved film adhesion near laser cut regions of the film, as evidenced by the need to use tweezers to lift off the bulk film near high density patterns as illustrated in Figure 3.5 (d)(*); we anticipated that at some aspect ratio (the length of ablated lines divided by the spacing between them) the improvement in adhesion provided by the laser cutting process would cause the film between the cut lines to tear, remaining attached to the substrate and causing the patterning process to fail.

To find the maximum aspect ratio resolvable with this patterning process, we patterned U-shaped 'flap' structures (rectangles with only three sides cut) of varying aspect ratios (the length of the long side of the rectangles divided by the length of the shorter side containing the un-cut edge). These flap structures are presented in Figure 3.6, and could simulate complex structures spaced closely together; in order to adequately resolve closely spaced structures, we need to ensure that the bulk film between them will lift off with the rest of the bulk film rather than tearing and remaining attached to substrate. We patterned various aspect ratios (the ratio of the rectangle length to its width, with the shorter width containing the un-cut side and the longer length having been traced by the laser), and then examined the sample after liftoff to determine whether the flaps had lifted off or torn at their tops. Because we have observed slightly improved film adhesion at laser cut edges (as evidenced by the film bulk requiring gentle pulling with tweezers for removal/liftoff near densely-spaced structures, depicted in (*) of Figure 3.5(d)), we anticipated that at some aspect ratio (dependent on film thickness as well as bulk film adhesion to the substrate) the film would tear and the patterned structures would no longer be resolved.
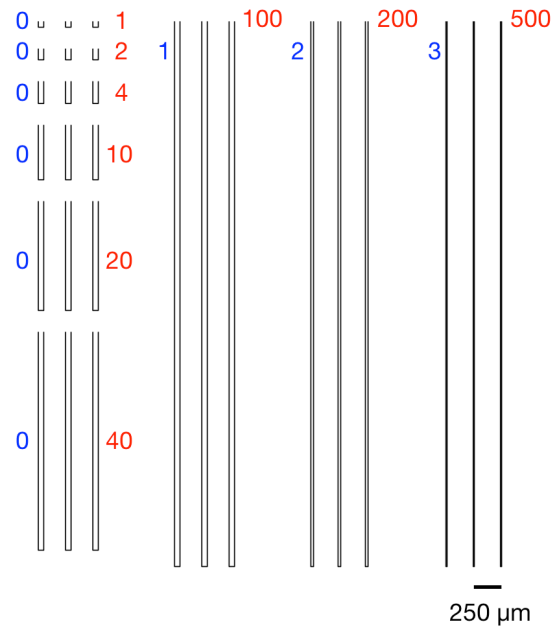
Figure 3.6. Flap designs used to investigate the laser-cutting process limitations. Laser cut lines are shown in black, the pattern aspect ratio is shown in red, and the number of patterns in each set of three remaining after bulk film removal is shown in blue. Figure previously published in [239].

Flaps with aspect ratios of 1, 2, 4, 10, 20, 40, 100, 200, and 500 were patterned, subjected to the lift-off process, and examined after lift-off to determine whether the flap had lifted off with the bulk or if it had torn at the un-cut edge, leaving behind a rectangle. The flap widths (short side) for the aspect ratios of 1, 2, 4, 10, 20, 40, and 100 were 50 μm, while those for the aspect ratios of 200 and 500 were 25 μm and 10 μm, respectively. The average film thickness was approximately 650 nm. After the liftoff process, the samples were analysed to determine which flaps remained attached to the slide. Figure 3.6 presents the flap designs used in the minimum spacing investigation, along with their aspect ratios (in red, on the right side of each pattern set) and the number of flaps in each set remaining after liftoff (in blue, on the left side of each pattern set).

ToF-SIMS In order to understand why the patterned structures do not lift off with the bulk film as well as to investigate why PDMS bonding is inhibited by dry etch processes of polystyrene, Time-of-Flight Secondary Ion Mass Spectrometry (ToF-SIMS) analysis was performed using a PHI TRIFT V nanoTOF-SIMS spectrometer (Physical Electronics PHI, Inc.). A pulsed primary 30 keV Au^+ ion beam was raster scanned over a 400 μm × 400 μm area. To ensure static analysis conditions, the total ion dose per spectrum was controlled to <$1.3x10^{12}$ ions/cm^2. For one sample (the laser cut patterned sample), a mosaic ion image was acquired, wherein the stage was moved and the raster scanned sub-areas were stitched together to examine a larger, approximately 3.2 mm x 3.2 mm area.

A control sample as well as laser-cut and plasma etched polystyrene samples were prepared using processing steps similar to those used to pattern the sensor films, except the oxygen-sensitive dye was not added to the film. For a 'degreased glass' control as well as a first step for all other samples, soda-lime glass slides were degreased with solvent rinses (acetone, isopropanol, and deionized water) and dehydration baked for 10 minutes at 100°C.

For the polystyrene samples, the soda-lime substrates were first degreased as above and then oxygen plasma-etched in a Technics Planar Etch II system at a pressure of 400 mTorr and a power of 180 W, for 5 minutes. Immediately following this plasma etch step, a 2% (w/w) solution of polystyrene in toluene (using the same constituents as used for the oxygen-sensitive

films above, except without the PtOEPK) was pipetted onto the glass substrates and allowed to evaporate for approximately 10 minutes before baking at 100°C again for 10 minutes. Profilometry (Dektak 150) measurements indicated that this deposition yielded a film approximately 1.2 μm in thickness.

One of the polystyrene-coated samples was then oxygen plasma etched (Technics Planar Etch II) at a pressure of 400 mTorr and a power of 180 W for 10 minutes to mimic the removal of the polystyrene film in standard dry etch patterning processes. Another polystyrene-coated sample was patterned using our laser cutting patterning process (laser ablation with the Quiklaze-50 ST2 followed by aqueous lift-off of the bulk film and drying with nitrogen) to generate a 1 mm x 1 mm polystyrene square. The 355 nm UV3 beam at 100% power intensity with two passes at a scan speed of 40 μm/s was again used for this pattern; however, the full beam aperture (50 μm x 50 μm) was used to yield more laser-cut surface area per pass for ease of analysis. The lifted off, polystyrene-coated, and laser ablated areas of this sample were all analysed separately and compared.

3.2.2.1.5   Sensor Calibration

To ensure that the sensor patterning process did not damage the sensors' sensing abilities, we calibrated the sensors to measure both gaseous and dissolved oxygen levels. For the gaseous sensor calibration, patterned sensors with bonded microfluidic devices were enclosed in a stage-top incubator chamber (Live Cell Instrument Chamlide) atop the same microscope setup used to acquire the fluorescence microscope images of the patterned sensors. A custom gas mixing system employing a commercial reference oxygen sensor (Presens) supplied 0%, 10%, and 20% oxygen to the setup. The chamber, gas control, and central microfluidic chamber were flushed with these gases for 15 minutes prior to acquiring fluorescence images of the three sensor patches in the field of view. The experiment was repeated three times for a total N=9, and the averaged intensities of the sensor patches were then fitted to the Stern-Volmer equation (equation 2) to obtain the sensors' calibration constants.

To obtain the fluidic sensor calibration constants, the patterned sensors and integrated microfluidics were enclosed in the same chamber as used for the gaseous calibration. To obtain

the deoxygenated sensor intensities I_0, the oxygen control channels and chamber were flushed with 0% oxygen for 3 hours prior to acquiring images to ensure complete deoxygenation. The oxygen control channels and chamber were then flushed with 10% and 20% oxygen for 30 minutes each prior to acquiring fluorescence images of the sensor patches. Additionally, distilled water bubbled with nitrogen, air, and oxygen was supplied to the central microfluidic chamber. Fluid flow in this central chamber was maintained at a rate of 10 (for the first two experiments) and 100 µL/min (for the final experiment), withdrawn with a syringe pump (kdScientific).

3.2.2.1.6   Demonstration of Microfluidic Compatibility

As a final test, we integrated the sensors into a microfluidic oxygen gradient generator device and measured oxygen gradients in a fluidic environment in order to demonstrate the patterning process's compatibility with microfluidic integration. To do this, the sensors and integrated microfluidics were again enclosed in the same chamber as used for the sensor calibration. Gaseous nitrogen was supplied to the ambient environment in the chamber, while gaseous oxygen and nitrogen were supplied to the microfluidic gas control channels. Oxygen and nitrogen were chosen as the control gases in order to demonstrate the full range of the sensor response. Ultrapure water flow in the innermost, main channel was maintained with a syringe pump at a rate of 0.5 µL/min, while that in the middle, red bubble removal channels was maintained at 0.25 µL/min.

Fluorescence microscope images were acquired and the fluidic calibration data were used to convert the image phosphorescence intensities into a map of the oxygen gradient in the device by the Stern Volmer equation (equation 2). The device was immersed in fluid and left for three days with constant gas and fluid perfusion to the microfluidic channels in order to investigate the stability of the sensor adhesion to the glass substrate as well as the PDMS-glass bonding stability.

3.2.2.2 Results and Discussion

3.2.2.2.1 Laser Ablation and Liftoff Gives High Pattern Fidelity and Integrability with PDMS Devices

Microscopy Characterization The patterned sensors were characterized with fluorescence and bright-field microscopy to verify pattern fidelity after lift-off; these results are presented in Figure 3.7.
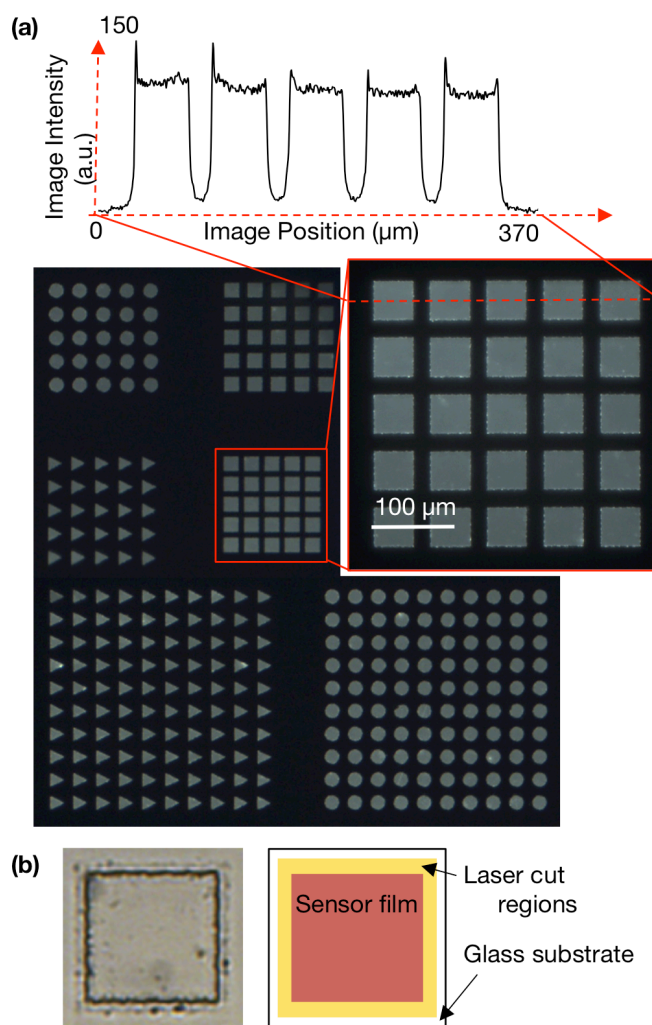
Figure 3.7. Fluorescence microscopy characterization of the laser-patterned sensor films. **(a)** Phosphorescence intensity images of the patterned sensor films, showing arrays of 50 μm squares, circles, and triangles on a pitch of 75 μm (except the lower array of squares and inset, on a pitch of 65 μm). An intensity cross-section of the array of squares is also presented. The peaks at pattern edges are likely due to redeposition during the laser ablation. As this effect is confined to the pattern edges we have eliminated any effects on the measurements by using a slightly smaller region of the sensor image for oxygen calculations. **(b)** Brightfield image of one of the squares in the patterned array, as well as a diagram indicating the different regions (sensor film, laser ablation line showing the residue remaining after laser cutting, and glass substrate) within it. Figure previously published in [239].

Phosphorescence intensity images of the patterned sensor films are presented in Figure 3.7 (a); we successfully demonstrated the patterning of 5x5 and 10x10 arrays of 50 μm squares, circles, and triangles on pitches of 65 and 75 μm. An intensity cross-section of the patterned square sensor array shows fairly uniform intensity characteristics across sensors along with evidence of redeposition (intensity peaks) at pattern edges from the laser ablation process. These intensity peaks at pattern edges were removed from our measurements by choosing a sensor sub-region slightly smaller than the full sensor size during our image analysis. Figure 3.7 (b) presents a bright-field image of a patterned sensor film along with a diagram indicating the different regions shown (sensor film, laser ablation line showing the residue remaining after laser cutting, and glass substrate). Figure 3.7 (b) shows that visible residue remains on the substrate in the laser ablated regions, although the patterned portions of the film were completely separated from the bulk to facilitate lift-off.

Although this new fabrication method can only be used to form simple patterns (all of the polystyrene areas to be removed must be connected), these types of patterns are sufficient for most lab on a chip oxygen sensing applications.

AFM images of patterned sensing squares as well as the flap structures are presented in Figure 3.8. We observe residue in the laser-cut areas both before and after lift-off, as well as a small increase in thickness of the polystyrene film around the structure edges, which could be evidence of redeposition. These data show a steady decrease in thickness near the laser-cut lines. Cross-sectional profiles (depicted in Figure 3.9) were taken of the edge of a structure patterned with the laser cutting method followed by liftoff (a) as well as the edge of a film scratched with a scalpel to compare the two interfaces (b). In doing this analysis we aimed to understand why water is able to easily penetrate under scalpel cut interfaces to lift off the film, while it does not appear to have the same effect on laser cut interfaces. It is evident in Figure 3.9 (a) that the laser ablation process results in significant redeposition on the film surface as well as at the interface, and that the thickness profile decreases at an angle of approximately 51° at the film edge. The interface of Figure 3.9 (b), however, shows a peak at the interface (likely where the film has folded back or folded under itself) and a steeper interface angle of 40°.

This data supports our theory that the scalpel cutting process slightly delaminates the polystyrene film near the cut interface. Conversely, we believe that the thermal and photothermal ablation processes induced by the laser are able to separate the patterns from the bulk polystyrene film without delaminating it from the surface. In fact, slight redeposition or thermal melting processes could potentially help the film better conform to the glass surface at the interface, slightly improving the film adhesion at the laser-ablated edges. The slight delamination caused by the scalpel cutting process likely permits the water to penetrate under the film, lifting it off of the substrate. In contrast, there is no such delamination at the laser cut interface, allowing the laser cut structures to remain attached to the substrate and facilitating the patterning process.
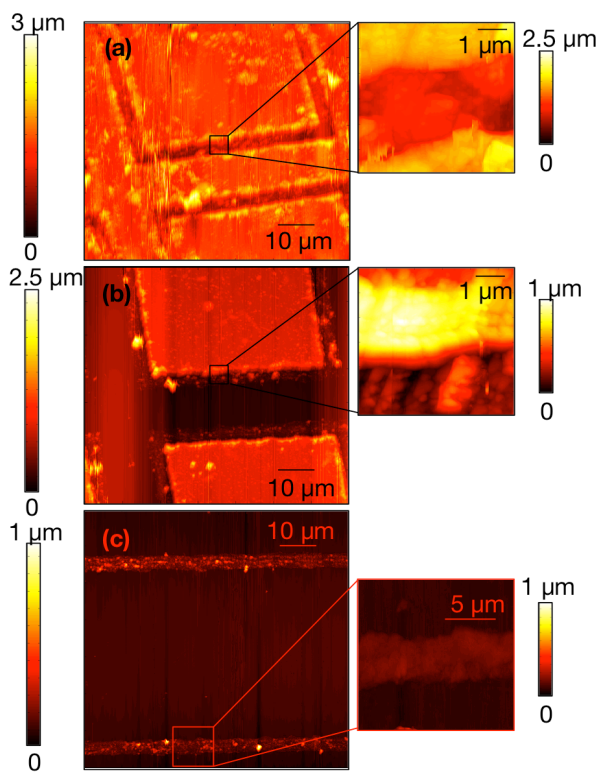
Figure 3.8. AFM characterization of laser-patterned sensor films. Non-contact AFM images of patterned sensing squares before **(a)** and after **(b)** bulk film removal, showing overall morphology as well as edge detail. **(c)** depicts the laser cut area alone after bulk film removal of the incompletely outlined flap structures (no patterned film remaining). Figure previously published in [239].
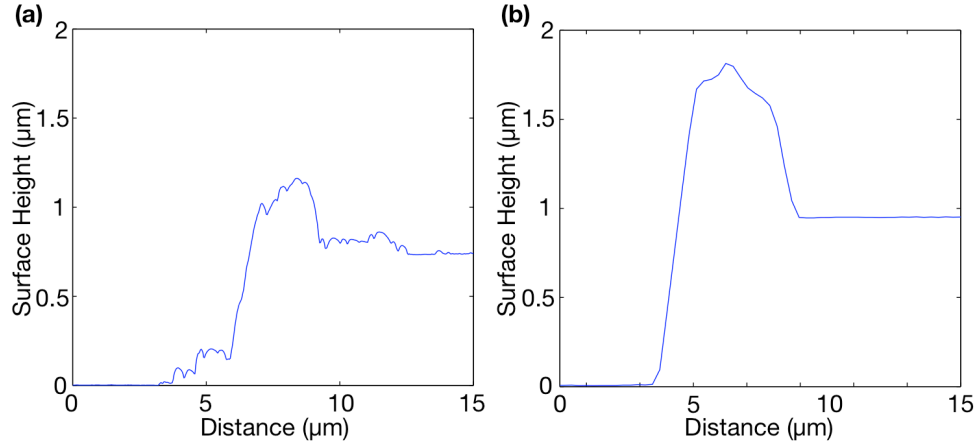
Figure 3.9. Comparison of laser-cut and scalpel-cut sensor interfaces. Cross-sectional profilometry measurements of the edge of **(a)** laser cut patterned sensor film structures and **(b)** scalpel-cut sensor film structures. The film thickness steadily changes in the laser-cut interface of (a), with an angle of approximately 51° at the film edge. In contrast, the thickness changes more sharply in the scalpel-cut interface, with a peak at the interface (likely where the film has folded back or folded under itself) and a steeper interface angle of 40°. Figure previously published in [239].

The AFM data were analysed to yield roughness as well as mean film thickness information about the patterned polystyrene sensor film, the glass (where the film bulk had been lifted/peeled off), and the laser cut areas. Additionally, AFM measurements were acquired of an oxygen plasma etched sensor film (again using the Nanosurf easyScan 2 in non-contact mode) as a point of comparison. Figure 3.10 presents the regions of the AFM images analysed to yield this information, as well as the mean thicknesses (μ) and arithmetic average of the absolute values of the thickness deviation from the mean (R_a). (a) depicts the AFM image of incompletely etched structures, showing laser cut lines and lifted off film. The area analysed to yield the roughness of the laser cut lines is outlined by the solid rectangle, while the area analysed to yield the roughness of the substrate after film liftoff is outlined with the dashed rectangle. (b) depicts the AFM image of the substrate after oxygen plasma etching of the sensor film. The area analysed to yield the roughness of this area is outlined by the dashed rectangle. Finally, (c) depicts the AFM image of patterned square structures after bulk film liftoff. The area analysed to yield the roughness of the polystyrene film is outlined by the dashed rectangle.

Figure 3.10 (b) shows that significant roughness and surface residue remains on the substrate even after dry etching the polystyrene sensor film (μ=69 nm, R_a=25 nm); this likely contributes to the PDMS bonding problems observed after dry etch processes. Although residue also remains

in the laser cut areas of Figure 3.10 (a) and (c) (μ=96 nm, R_a=51 nm), this does not impact PDMS bonding because the laser cut lines are small in comparison to the substrate area.
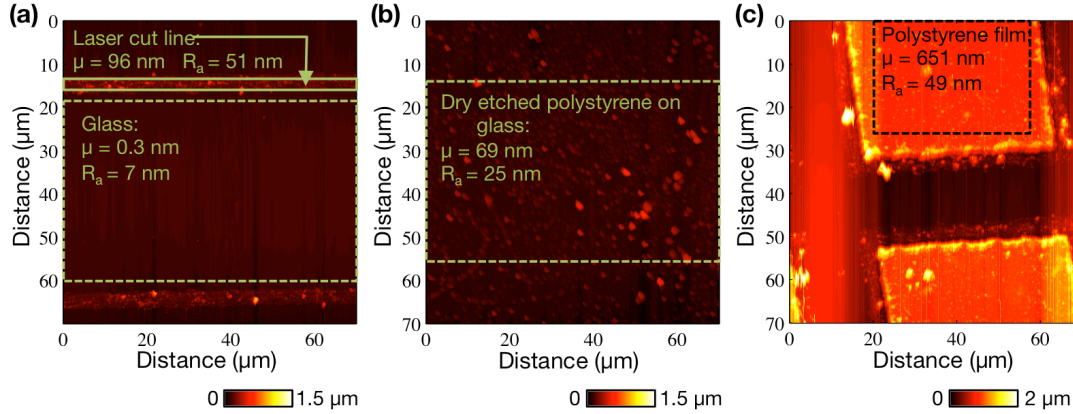
Figure 3.10. Mean thickness and roughness AFM characterization of laser-cutting process. Non-contact AFM images of: **(a)** incompletely cut structures after sensor film liftoff, showing laser cut areas (solid line rectangle) and lifted off areas (dashed rectangle) used for roughness analysis; **(b)** plasma etched sensor film, showing area used for roughness analysis (dashed rectangle); **(c)** patterned sensor film after bulk film liftoff, showing polystyrene sensor film area used for roughness analysis (dashed rectangle). Images are annotated to label the regions analysed as well as the mean thicknesses (μ) and arithmetic roughness averages (R_a). Figure previously published in [239].

After bulk film lift-off, we examined the area containing the flap structures for the minimum spacing analysis using brightfield and fluorescence microscopy. The aspect ratio of the structure needed to be very high (>100) in order for the flap to tear across the un-cut edge and remain on the substrate; this indicates that very high aspect ratios of pattern spacing can be successfully patterned and lifted off with this process. It also indicates that the improvement in film adhesion provided by the laser cut process, although sufficient for patterning and microfluidic integration, is small in comparison to the strength of the 650 nm thick film. Full results of the minimum spacing investigation as well as the details regarding the flap designs patterned are presented in Figure 3.6.

ToF-SIMS characterization Analysis of the laser-cut and plasma etched polystyrene samples and comparison with the degreased glass control showed that three main chemical species were formed in these processes that could contribute to the results we observed. It was found that plasma etched polystyrene films left residual chemical species giving the fragment $[C_8H_{18}O]^+$, which covered almost half of the glass surface in the interrogated regions and would be expected to block the glass substrate during the subsequent PDMS plasma bonding step.

Figure 3.11 presents SIMS images of the plasma etched polystyrene sample as well as the degreased glass control sample as a comparison. The $[C_8H_{18}O]^+$ residue after plasma etching appears to cover nearly half of the glass substrate in the plasma etched polystyrene sample, while it does not appear to be present in the glass control. The signal from the silicon is much lower in the regions of the plasma etched sample containing the $[C_8H_{18}O]^+$ while its intensity is fairly uniform in the control sample, further supporting the conclusion that the $[C_8H_{18}O]^+$ could be blocking the glass surface and preventing subsequent PDMS bonding.
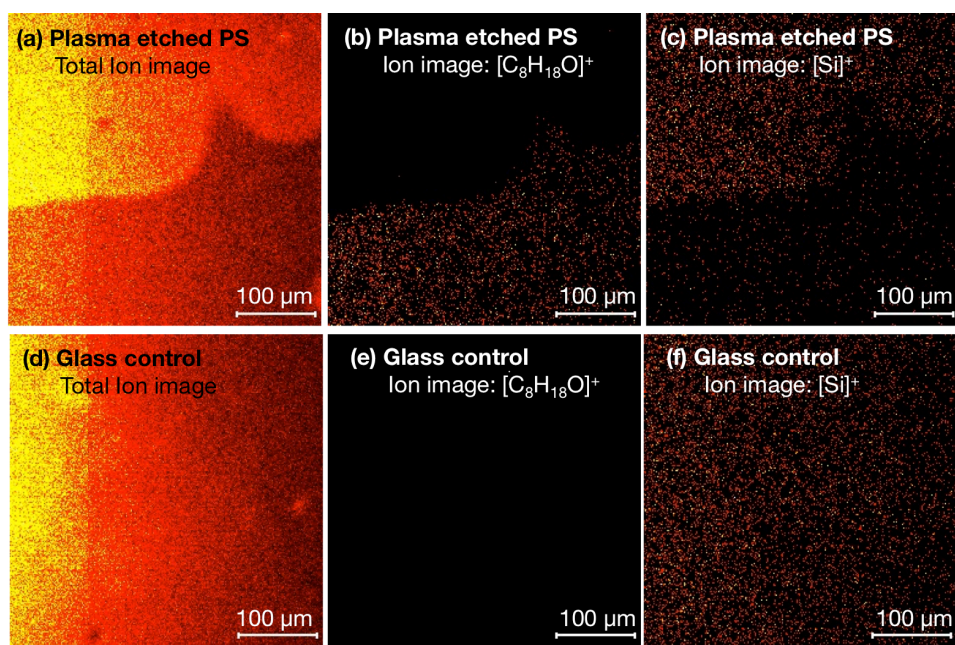
Figure 3.11. ToF-SIMS characterization of plasma-etched PS on glass and clean glass control. ToF-SIMS images of oxygen plasma etched polystyrene sample **(a-c)** and degreased glass control sample **(d-f)**. **(a)** and **(d)** show the total ion images; **(b)** and **(e)** show the $[C_8H_{18}O]^+$ ion images, and **(c)** and **(f)** show the $[Si]^+$ ion images. It is observed that approximately half of the glass substrate (and silicon contained in it) is covered by $[C_8H_{18}O]^+$ in the plasma etched polystyrene sample, while this ion fragment does not appear to be present in the degreased glass control. Figure previously published in [239].

Oxygen plasma bonding of PDMS to glass relies on the formation of OH^- groups on both surfaces; when the surfaces are brought together, the OH^- groups condense, forming the permanent Si-O-Si (siloxane) bond [290]. As such, permanent oxygen plasma bonding of PDMS is not feasible without reliable formation of OH^- groups on the glass surface. As the heavy alkoxyalkane-like residual chemical species formed during the plasma treatment (evidenced by the detection of the $[C_8H_{18}O]^+$) would block the surface during the plasma treatment and thus

inhibit formation of the OH$^-$ groups, it is likely that it may be the chemical species responsible for the poor bonding performance of glass surfaces after polystyrene plasma etch processes.

Although small amounts of [C$_8$H$_{18}$O]$^+$ were also found on the laser cut sample after bulk film lift-off, it covered less of the surface, which enables more interfacial bonding between these regions and PDMS. Furthermore, the SIMS image reveals that two new chemical species were formed near the laser cut regions of the laser-cut polystyrene-on-glass sample, which is evidenced by the observation of the fragments [C$_7$H$_6$O$_2$Al]$^+$ and [SnCH$_3$]$^+$. It is believed that the heat from the laser treatment causes Sn and Al to segregate from the bulk to the glass surface and then subsequently react with the polystyrene, as evidenced by the detection of [C$_7$H$_6$O$_2$Al]$^+$ and [SnCH$_3$]$^+$ peaks. Heightened levels of Sn and Al were also found on the surface of a bare glass sample that had been treated with the laser solely as compared to a degreased glass control. As these new chemical species incorporate elements from both the glass substrate and the polystyrene film, they could further improve the adhesion of the polystyrene film near the pattern edges.

Figure 3.12 presents SIMS images of the laser ablated polystyrene sample after partial bulk film liftoff. We tore the film during bulk film liftoff in this case, so the bulk film, patterned film, laser ablated, and glass substrate regions after liftoff are all present in this mosaic SIMS image. The sample regions are labelled in Figure 3.12 (a), while (b)-(e) present SIMS ion images of various ions detected ([Si]$^+$ and [B]$^+$ from the glass substrate as well as [C$_7$H$_6$O$_2$Al]$^+$ and [SnCH$_3$]$^+$ formed near the laser cut lines), while (f) presents an ion overlay image, clearly showing the contributions of the fragments [C$_7$H$_6$O$_2$Al]$^+$ and [SnCH$_3$]$^+$ in the laser ablated polystyrene regions. These two new fragments contain components originating from the glass (Al and Sn) as well as from the polystyrene, melded together with energy from the laser and oxygen from the laser ablation environment.

ToF-SIMS analysis of the peeled-off region of the laser cut sample immediately after a 1 minute 20 second exposure to air plasma to simulate a plasma bonding process showed evidence of heightened levels of [SiOH]$^+$ and [SiOH$_2$]$^+$ on the surface; this result is similar to that observed for the degreased glass control after the same plasma exposure. As these groups could be

involved in the formation of plasma bonds with silanol groups on the PDMS surface, the presence of these ions supports our observation that the peeled off region demonstrates good ability to bond with PDMS. Figure 3.12 (g), (h), and (i) present a selected region of the SIMS spectra for the degreased glass control (g), the same control after a 1 minute 20 second air plasma exposure mimicking the procedure used for permanent PDMS plasma bonding (h), and the peeled-off region of the laser cut polystyrene sample (exposing the glass underneath) after the same plasma exposure (i). This region of the SIMS spectra contains characteristic peaks of $[SiOH]^+$, and $[SiOH_2]^+$, which are expected to aid the permanent plasma bonding of PDMS to glass; $[SiOH]^+$ and $[SiOH_2]^+$ peaks are labelled in part (g) of Figure 3.12. The other peaks in the spectrum are mainly due to organic compounds. By comparing the relative sizes of the $[SiOH]^+$ peak and the nearby large organic peak (approximately 0.06 m/z higher than the $[SiOH]^+$ peak), it is evident that the plasma treatment enhances relative levels of $[SiOH]^+$ on the degreased glass surface. This enhancement is also evident in the peeled-off polystyrene region after the laser treatment, indicating that the peeled-off surface should behave similarly to the degreased glass surface during PDMS plasma bonding; this is consistent with our observation of strong PDMS bonding to this surface. A similar enhancement of the relative levels of $[SiOH_2]^+$ after the plasma treatment further supports this observation.

The results obtained from the ToF-SIMS analysis indicate that although oxygen plasma dry etch processes can remove the polystyrene films, they leave behind a glass surface that is contaminated with chemical species giving $[C_8H_{18}O]^+$. The laser ablation process locally changes the glass surface composition, as was evidenced by the detection of tin in these regions. The focused UV laser not only ablated the polystyrene film, separating patterned structures from the bulk, but also melded the polystyrene with elements from the glass substrate to form potentially useful adhesion components.
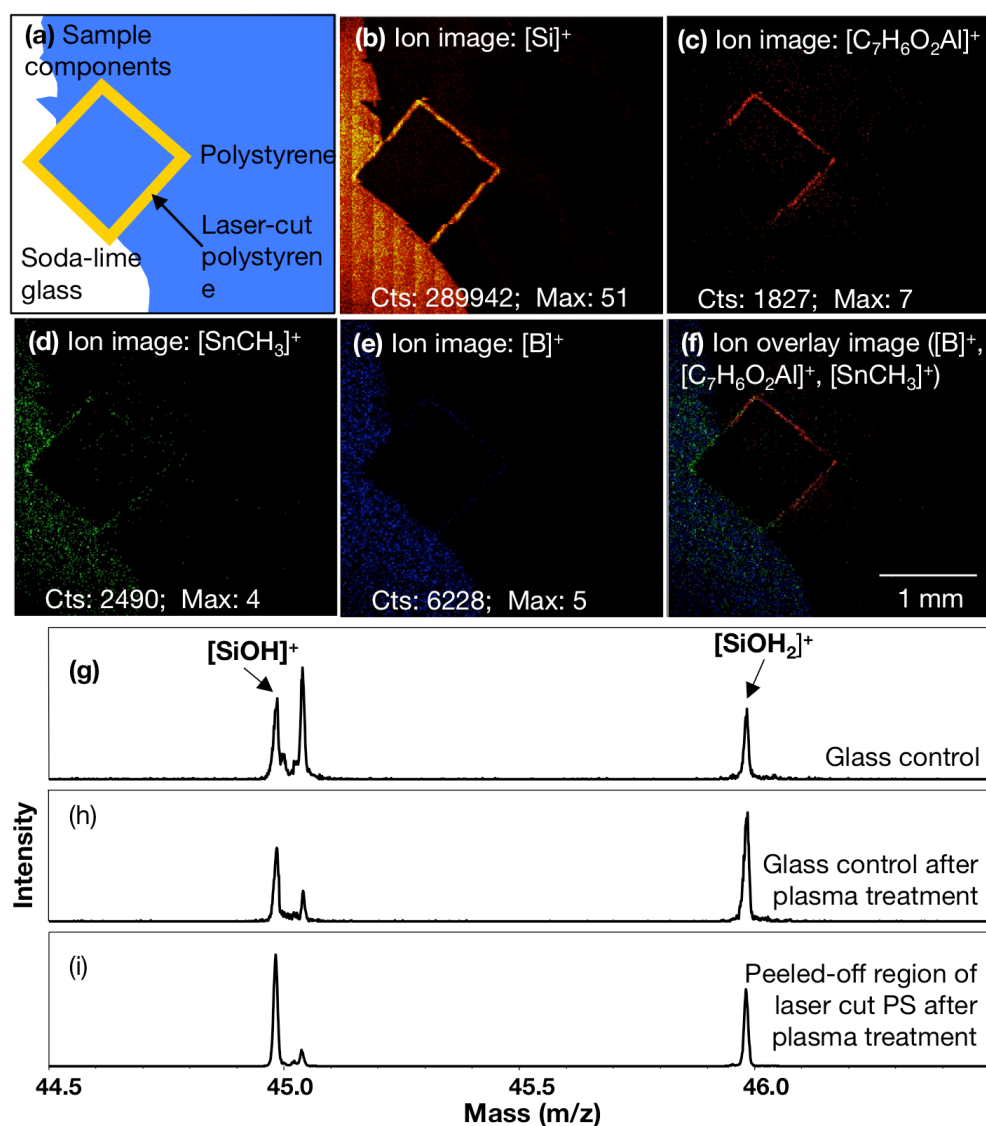
Figure 3.12. ToF-SIMS images of laser cut polystyrene sample. The sample regions are labelled in **(a)**. Chemical contributions from silicon **(b)** and boron **(e)** from the glass substrate are mapped, as well as those of the fragments $[C_7H_6O_2Al]^+$ **(c)** and $[SnCH_3]^+$ **(d)** from the new chemical species formed during the laser ablation process. **(f)** presents an ion overlay image of the $[C_7H_6O_2Al]^+$, $[SnCH_3]^+$, and $[B]^+$ (another element present in soda-lime glass) using the same colour channels as in (c-e). **(g)**,**(h)**, and **(i)** present ToF-SIMS spectra showing the characteristic peaks of $[SiOH]^+$, and $[SiOH_2]^+$, for the degreased glass control **(g)**, the degreased glass control after a 1 minute 20 second air plasma treatment mimicking the PDMS plasma bonding procedure **(h)**, and the peeled-off region of the laser-cut polystyrene sample after the same one minute 20 second plasma treatment **(i)**. The relative levels of $[SiOH]^+$ and $[SiOH_2]^+$ increase after plasma exposure in the glass control sample as is expected to facilitate PDMS-glass bonding. These increased levels of $[SiOH]^+$ and $[SiOH_2]^+$ are also present in the peeled-off region of the laser-cut polystyrene sample, supporting our observation of the ability of this surface to support PDMS bonding. Figure previously published in [239].

3.2.2.2.2 Laser-Patterned Films Function as Oxygen Sensors

Figure 3.13 (a) and (b) present the gaseous and fluidic calibration of the oxygen sensors, respectively.
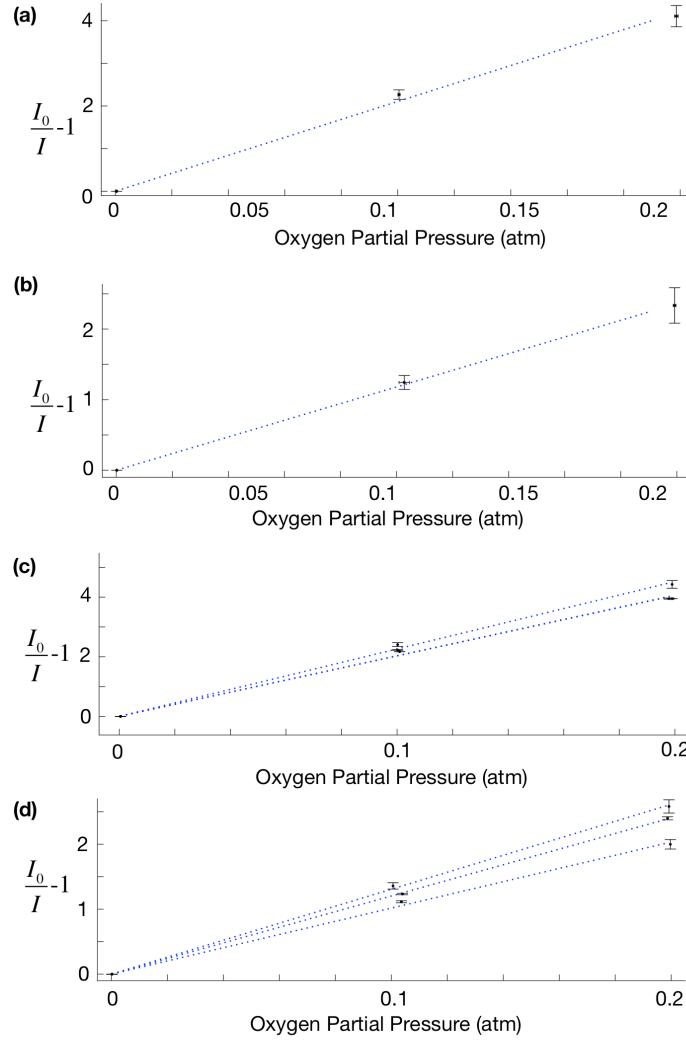
Figure 3.13. Demonstration of oxygen sensor functionality after laser-patterning process. Results of **(a)** gaseous and **(b)** fluidic calibration of patterned oxygen sensors, along with a fit to the Stern-Volmer relationship. **(a-b)** Error bars indicate one standard deviation bounds for the N=9 averaged datasets (3 sensor patches, each calibrated 3 times). Fit results yielded I_0=830±100 (gaseous) and 610±140 (fluidic), and k_{SV}=21±2 atm^{-1} (gaseous) and 11.8±0.4 atm^{-1} (fluidic). **(c-d)** depict the same gaseous **(c)** and fluidic **(d)** calibration results as those shown in (a-b), with the different repetitions of the calibration plotted as separate lines. Error bars depict one standard deviation bounds for the N=3 averaged sensors for each line. Fit results to the three separate calibration datasets yielded I_0=890±120, 820±100, 800±100 (gaseous) and 770±120, 500±60, 570±70 (fluidic), and k_{SV}=23±2 atm^{-1}, 20±3 atm^{-1}, 20.3±1.9 atm^{-1} (gaseous) and k_{SV}=13.1±0.7 atm^{-1}, 10.2±0.9 atm^{-1}, 12.0±0.3 atm^{-1} (fluidic). (a-b) previously published in [239].

The x-axis of Figure 3.13 (b) represents the oxygen partial pressure in equilibrium with the fluidic environment inside the chip, as the sensor itself was inside a channel filled with water.

The Stern-Volmer constants obtained by fitting the calibration data to the Stern-Volmer relationship (21 atm^{-1} and 11.8 atm^{-1}, for the gaseous and fluidic calibration, respectively) are in line with those previously measured by our group for un-patterned films. No significant difference was found between the datasets acquired at the lower flow rate compared to those acquired at the higher flow rate. Analysis of the images was performed in the same manner as for the gaseous calibration. The errors on the datasets are largely due to temporal variations in excitation source intensity; the use of ratiometric sensors instead of the simple intensity-based sensors used here would address this issue as well as sensor-to-sensor variations caused by film thickness nonuniformities.

3.2.2.2.3 Laser-Patterned Sensors Function During Long-Term Perfusion Flow

We did not observe sensor delamination within the device or bubble generation in the fluid channels after the 3-day experiment with the device immersed in fluid and with constant gas and fluid perfusion. In separate tests, we tested the devices with microfluidic flows resulting in shear rates of 7.6 s^{-1} up to 15 000 s^{-1}, for periods of several hours to 3 days, and found the sensors remained attached to the substrate. These results indicate that the sensor patterning process yields sensors with film adhesion compatible with multi-day microfluidic experiments. It also affirms that the glass-PDMS bond strength after our patterning method is sufficiently high for reliable microfluidic integration.

Figure 3.14 presents the results of an oxygen gradient measurement within a microfluidic oxygen gradient generator device.
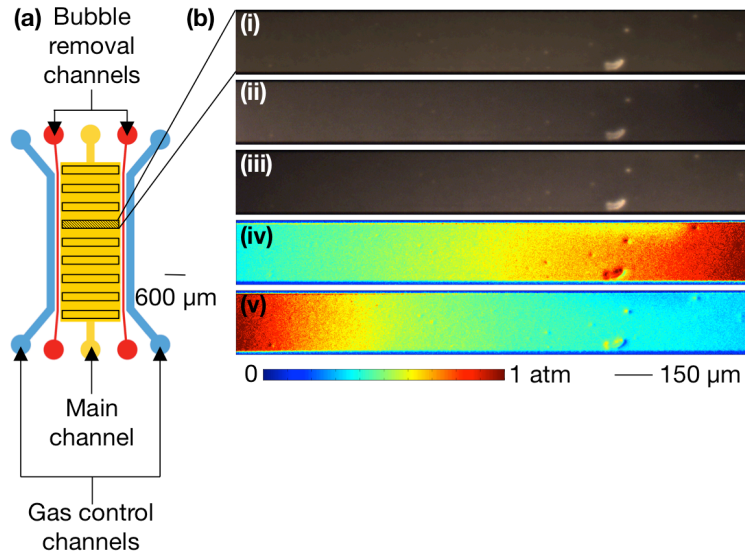
Figure 3.14. Demonstration of laser-patterned sensor microfluidic compatibility. Dissolved oxygen measurements inside the gradient generator microfluidic device. **(a)** depicts the channel geometry of the microfluidic gradient generator, along with the positions of the patterned sensors integrated within it (shown by the black rectangles). **(b)** shows various sensor images and fluidic oxygen gradient measurements taken from the fourth sensor from the gradient generator device inlet. **(i)** shows the original image taken with the channel filled with deoxygenated fluid, yielding the reference I_0. **(ii)** shows the original sensor images taken with nitrogen supplied to the left gas control channel and oxygen supplied to the right. **(iii)** shows the original sensor image taken with oxygen supplied to the left gas control channel and nitrogen supplied to the right. **(iv)** and **(v)** show the oxygen levels obtained by analysing the intensities of (ii) and (iii), respectively. Figure previously published in [239].

Figure 3.14 (a) shows the schematic of the gradient generator device along with the locations of the patterned sensors integrated within it, while (b) shows various sensor images and oxygen gradient maps taken using the fourth sensor from the device inlet (i-v). (i) shows the original phosphorescence intensity image taken during the calibration, with the channel filled with deoxygenated fluid. (ii) and (iii) show similar images of the sensor but under oxygen gradient conditions within the device, with oxygen and nitrogen supplied to the two gas control channels of the gradient generator device. In (ii), nitrogen was supplied to the left gas control channel and oxygen supplied to the right, while the gas inputs were switched for (iii). Finally, (iv) and (v) show a map of the dissolved oxygen levels obtained using the sensor intensities from (ii) and (iii), respectively, and the calibration data from Figure 3.13 (b). As the sensor was in a fluidic environment, the oxygen scale again represents the partial pressure of oxygen in a gaseous state that would be in equilibrium with the fluid.

These results demonstrate that the patterned sensors fabricated using the laser cutting method can be integrated into PDMS microfluidic devices using standard plasma bonding and exhibit

sufficient adhesion to the glass substrate to be compatible with many lab on a chip applications with incubation periods of days.

3.3 Gas Supply System

Because the goal of the oxygen control and measurement system was to spatiotemporally control and measure the oxygen levels within the cell culture environment, a system needed to be created to supply gas of known oxygen level to the microfluidic oxygen control device as well as optically measure the optical oxygen sensors. This system was used both for sensor calibration and for the oxygen control and measurement during experiments using the microfluidic device. It was composed of a gas control system, implemented using an Arduino microcontroller, and a microscope automation software GUI, implemented in C# using the .NET framework. The purpose of the system was to: (a) supply the microfluidic device with known gases; (b) supply a time-varying profile of gases to the device to create time-varying oxygen profiles; (c) image the oxygen sensors as well as any cell cultures in an automated fashion, using both fluorescence and brightfield microscopy and an automated microscope stage. The system was completed by (in chronological order) Jimmy Hsin-Chia Chao, Brian Terry, Ta Shun (Michael) Chien, Nora Bishop, Jake Davis, Selim Gawad, Damandeep Dhillon, Reily Blackner, Jackie (Shi Shu) Chen, Trace Wu, and Jonathan Schmok, who were supervised by the author between 2012 and 2015.

The gas control system was completed as part of the Masters project of Mr. Selim Gawad, whose project was technically supervised by the author in 2013 and built upon work by undergraduate students: Mr. Jimmy Hsin-Chia Chao, Mr. Brian Terry, Mr. Ta Shun (Michael) Chien, Ms. Nora Bishop, and Mr. Jake Davis. The system will only be briefly discussed in this thesis; details of the specifics of the system can be found in Mr. Gawad's Masters thesis [291]. The gas control system was developed using an Arduino microcontroller controlling solenoid valves and reference oxygen (Presens, Germany) and carbon dioxide (co2meter.com) sensors to mix user-specified concentrations of air, nitrogen, and carbon dioxide, store them in small tanks, and supply them to the device in a programmable fashion. The commercial oxygen and carbon dioxide sensors verify that the gas levels in the mixed gas tanks are within tolerance (0.5%) of the user-specified value; this tolerance could be improved in future work to permit more precise gas mixtures using the automated system, but in the meantime the system could also be used

with premixed gas cylinders formulated with higher precision. To provide gases to the microfluidic device, the Arduino controls another array of solenoid valves that are able to route the outputs of any of the three mixed gas tanks to any or all of three system outputs. The system automatically refills the tanks as they are emptied, and the tanks can be refilled while they are in use (although this does generate some instability – typically up to 1% in 10% oxygen - in the composition of the gas supplied to the output). The system is also able to switch the tank supplied to each output in a user-programmable, automated fashion, and the delay between sending the tank switch command and measuring the changed oxygen level at the microfluidic device is approximately 1 minute.

The software GUI of the system allows the user to set up automated imaging of their sample; the GUI was first developed by Mr. Jimmy Hsin-Chia Chao. It interacts with the microscope camera (Qimaging Retiga EXi) and automated stage controller (Prior ProScan II) to move the stage to a set of defined locations and acquire images at each location. The user can set up as many imaging locations as needed, and define how often each location should be imaged with brightfield and fluorescence microscopy. Mr. Selim Gawad worked with Mr. Damandeep Dhillon to integrate communication with the gas control system into the software GUI. Since the completion of Mr. Gawad's Masters project, the software GUI has been significantly improved by undergraduate students: Mr. Reily Blackner, Mr. Jackie (Shi Shu) Chen, Mr. Trace Wu and Mr. Jonathan Schmok. The GUI also creates a file to log the last known oxygen levels supplied to each output as well as the gas supply protocol at each imaging time point; this functionality was implemented by Mr. Jonathan Schmok, and it is extremely useful for subsequent analysis of experimental data.

The final portion of the measurement system was a shutter system, designed and completed by Mr. Gawad based on preliminary work by Mr. Brian Terry and Mr. Ta Shun (Michael) Chien, and documented in Mr. Gawad's thesis [291]. The Nikon TE-2000-U microscope used for our studies did not have built-in shutters, so they had to be built in order to complete automated measurements without causing excessive photodamage to the sample. Two shutters were fabricated (to block the brightfield and fluorescence sources), and the shutters were implemented using an Arduino Nano microcontroller and servo motors, as well as machined aluminum parts.

3.4 Ratiometric Sensing for Improved Sensor Stability

Although the microfabrication methods described in section 3.2 were developed for intensity-based PtOEPK/polystyrene sensors and preliminary work was completed using these sensors, it became apparent that the stability of the intensity-based sensing modality was insufficient for long-term experiments using our fluorescence microscope setup. The Nikon TE-2000-U microscope used for our experiments uses a Nikon Intensilight mercury arc fluorescence excitation source, and the temporal homogeneity of the intensity of this source, as well as the spatial homogeneity offered by the microscope system, were far insufficient for the required precision in oxygen measurements. Spatial fluctuations in intensity meant that movements in the position of the sensors within the image over time caused fluctuations in the apparent oxygen level (requiring the sensors to remain stationary between calibration and measurement), and temporal fluctuations in intensity resulted in apparent fluctuations in oxygen levels over time. In an effort to improve sensor stability, we also investigated the use of ratiometric sensors and found a significant improvement in the sensing results.

3.4.1 Comparison of Intensity and Ratiometric Sensors

This section presents our implementation of ratiometric sensors. We chose to implement ratiometric sensors based upon the excellent work of Ungerböck *et al.* [109], employing Platinum(II)-5,10,15,20-tetrakis-(2,3,4,5,6-pentafluorphenyl)-porphyrin (PtTFPP) as the oxygen-sensitive dye, and Macrolex Fluorescent Yellow (MFY) as the oxygen-insensitive dye; both dyes are contained within the same polystyrene film. The PtTFPP emits in the red channel of a colour CCD while MFY emits in the green channel, which allows a colour camera to be used to separate the oxygen-dependent from the oxygen-independent luminescence. We chose this sensor type because of its ease of implementation (requiring only a colour camera to separate the two types of luminescence), the good photostability of PtTFPP and MFY, and its compatibility with our existing sensor fabrication processes.

3.4.1.1 Methods

3.4.1.1.1 Ratiometric Sensor Fabrication

Ratiometric optical oxygen sensors were fabricated using the laser-cutting process detailed in section 3.2.2. Briefly, polystyrene films containing 1% w/w PtTFPP (Frontier Scientific) and 2% w/w MFY (LANXESS) films were formed. The dyes were first dissolved in a 5% solution of polystyrene in toluene, and the solution was mixed using a magnetic spin bar for 1-2 hours as well as sonicated for >30 seconds in an effort to ensure dye distribution uniformity within the solution. After mixing, the solution was spin-coated (2000 RPM, 1 minute) on glass microscope slides that had been dehydration-baked at 125ºC and pre-treated with a 5-minute exposure to oxygen plasma (400 mTorr, 160 W in a Technics PE-II). The toluene was then left to evaporate for 5-10 minutes before the sensors were baked on a hotplate for 5 minutes at 125ºC. A laser cutter was then used to cut around the edges of the sensor patches, and the film bulk was lifted off with the aid of a water bath (taking advantage of the relatively poor adhesion of polystyrene films to glass surfaces), leaving behind the isolated sensor patches as described in the sensor fabrication process of section 3.2.2. Sensors were then again baked on a hotplate for 5 minutes at 115ºC after liftoff but before integration with the microfluidic device. The optical oxygen sensors were integrated with the microfluidic oxygen control device via irreversible plasma bonding with the glass substrate.

3.4.1.1.2 Comparison Measurements of Intensity and Ratiometric Sensors

To test the stability of the oxygen sensors under a time-varying gas profile, gases were supplied directly to the microfluidic channel enclosing ratiometric optical oxygen sensors and the gaseous oxygen levels were sensed using the gaseous calibration data for the same sensors. We ran a 12-hour experiment where the following demonstrative time-varying gas profile was repeated every 140 minutes: 2% oxygen was supplied for 35 minutes, followed by 0% for 30 minutes, 0.5% for 35 minutes, 0% for 20 minutes, and 0.5% for 20 minutes. The chip was temperature controlled to 37°C during the experiment using a microscope stage-top incubator (Live Cell Instrument Chamlide), in order to minimize any temperature-related signal drift. As a worst-case demonstration, this experiment was completed with the microscope fluorescence excitation shutter left open for the entirety of the experiment.

In order to compare the stability of the intensity-based sensors with that of the ratiometric sensors under exactly the same conditions, the response of the PtTFPP dye alone (red image channel, represents the intensity-based sensor response) was compared with the ratiometric response (using both the red and green image channels) from the same sensors.

3.4.1.2   Results: Ratiometric Sensing Improves Measurement Stability

The comparison of the intensity-based sensor response to ratiometric sensor response is depicted in Figure 3.15 (a). It is evident that the ratiometric intensity (shown in black) yields a much more stable sensor response than the intensity-based response alone (shown in red). The majority of the non-oxygen-dependent fluctuations in the intensity-based sensor response are also reflected in the MFY fluorescence intensity (shown in green), and as such are able to be removed by the ratiometric measurement. We believe that the upward slope at the beginning of the experiment could be due to mercury arc lamp warm-up; this is removed by the ratiometric measurement.
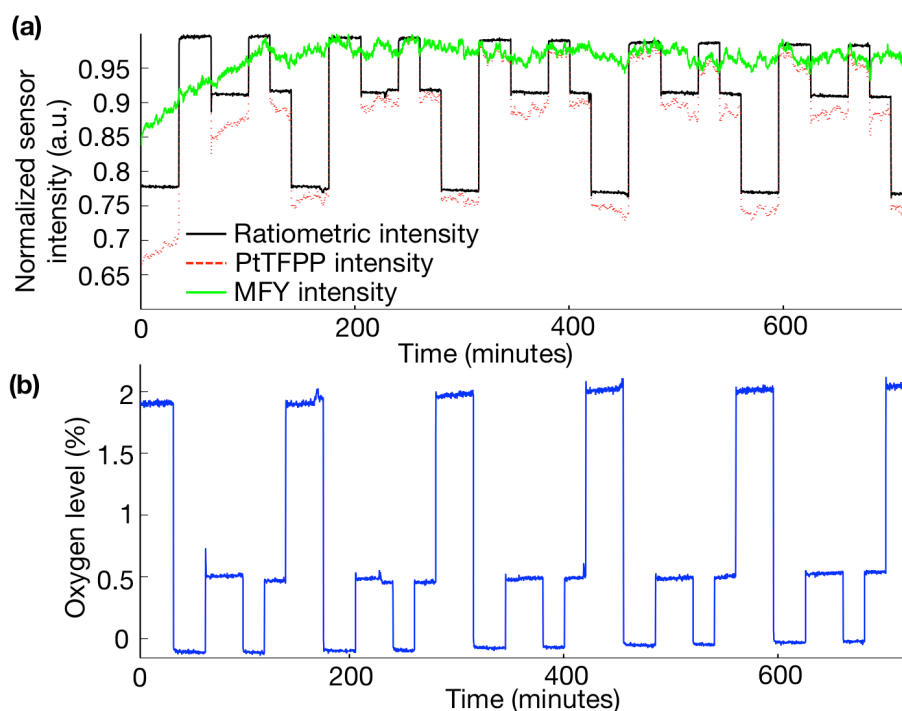
Figure 3.15. Stability of ratiometric oxygen sensor response during a 12-hour experiment. **(a)** Comparison between the normalized intensities of the ratiometric intensity (black), the red channel (PtTFPP phosphorescence intensity alone, representing an intensity-based sensor response, red), and the green channel (Macrolex Fluorescent Yellow (MFY) fluorescence intensity alone, green). **(b)** Measured gaseous oxygen levels obtained from the ratiometric intensity shown in (a). Figure previously published in [292].

The stability of the ratiometric response is very good, and results in a fairly robust oxygen measurement over the 12-hour experiment (shown in Figure 3.15 (b)). The slight upward drift in the measured oxygen levels is likely due to unequal photobleaching rates of the two dyes, and the shutter system significantly improves this. Additional strategies that were implemented to address this issue are presented in section 3.5.3.

3.5   Sensor Calibration

After fabrication and integration with the microfluidic device, the oxygen sensors were calibrated for both gaseous and fluidic oxygen measurements using microscope imaging and image processing methods described in section 3.5.1.1. The gaseous calibration was performed by flowing gases of known oxygen level through a microfluidic channel immediately on top of the sensors. The gaseous calibration methods are discussed in section 3.5.1.2, and the results in section 3.5.2.1. To perform the fluidic calibration, it was necessary to measure the oxygen sensors while exposed to aqueous solutions of known oxygen level. This fluidic calibration was performed using the oxygen control microfluidic device that will be detailed in Chapter 4. The methods for this fluidic calibration are discussed in section 3.5.1.3, and the results in section 3.5.2.2. Finally, to validate that the fluidic oxygen levels obtained by the control device were the expected values used to calibrate the sensors, an oxygen-scavenging solution was used to ensure that 0% oxygen was reached in the fluid during control with the microfluidic oxygen control system. The methods of this study are presented in section 3.5.1.4, and the results presented in section 3.5.2.4.

3.5.1   Sensor Calibration Methods

3.5.1.1   Image Processing

For both gaseous and fluidic calibration as well as subsequent measurements, 3 images at each datapoint were acquired and averaged. The ratiometric intensity R was calculated from the ratio of the red to the green colour channels of the colour camera (as the PtTFPP emits in the red channel while MFY emits in the green). The averaged R_0/R result for all pixels in each sensor patch at each gas level was plotted versus the oxygen level and fitted to the simplified two-site quenching model (equation 6). For the purposes of showing the calibration plots, the responses from four sensor patches were averaged. For subsequent measurements using the sensors, each

sensor was measured using its own calibration parameters (i.e., sensor-by-sensor calibration was performed and used). All calibrations were performed using a custom MATLAB image processing script.

3.5.1.2   Gaseous Sensor Calibration

Microfluidics were used to provide known gaseous oxygen levels to the sensors to complete the gaseous sensor calibration. The microfluidic oxygen control device that will be detailed in Chapter 4 was bonded to the glass slide containing the patterned oxygen sensors. This device contains 6 channels; however, only one channel was used for the gaseous sensor calibration. Gas containing known oxygen levels (measured with a commercial oxygen sensor: Presens Fibox 2) was flowed through a large central microfluidic channel, directly over top of the sensors, at a gas flow rate of approximately 10 mL/min. The temperature around the chip was controlled to 37ºC using a microscope stage-top incubator (Live Cell Instrument Chamlide).

3.5.1.3   Fluidic Sensor Calibration using Microfluidic Gas Control Device

The microfluidic oxygen control device that will be detailed in Chapter 4 (device schematic from Figure 4.1 is reproduced here for convenience as Figure 3.17) was also used for fluidic calibration of the optical oxygen sensors. Briefly, this device contains a central channel designed for cell culture, in direct contact with the optical oxygen sensors on the glass substrate. This cell culture channel (C) is surrounded on three sides by three gas control channels (L3G, L1GR, L1GL), through which gas can flow to control the oxygen levels in the cell culture channel. The device is fabricated from oxygen-permeable PDMS, so oxygen can move between the various channels of the oxygen control device. Additional straight channels are integrated between the cell culture channel and gas control channels to mediate any evaporation of fluid through the PDMS, as well as the formation of gas bubbles within the cell culture channel. As such, these channels were named hydration channels, and these two channels (L1H, L2H) lie between the cell culture channel and the three gas control channels.
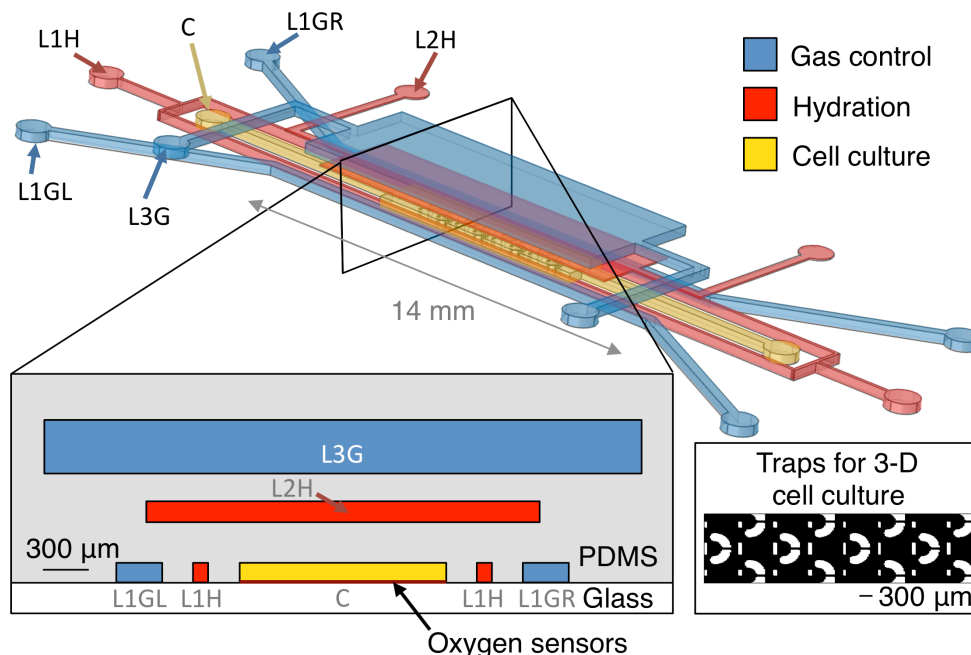
Figure 3.16. Oxygen control microfluidic device layout. Reproduced here from its full description in **Figure 4.1** for convenience. 3-D and cross-sectional views of the device as well as the position of the integrated optical oxygen sensors within the cell culture channel are shown. The cell culture channel (C) is surrounded on three sides by gas control channels (L1GL, L1GR, and L3G), with hydration/bubble removal channels (L1H, L2H) between each of the gas channels and the centre channel. Inset shows trapping structures for 3-D cell cultures within the cell culture channel. Please note that the 3-D view is not to scale (microfluidic layers are spaced farther apart in the illustration than in the device to permit visualization of the three layers). Cross-sectional view is to scale. Figure previously published in [280].

For fluidic calibration, the device was immersed in water and again maintained at 37ºC using a microscope stage-top incubator system. The cell culture and hydration channels (C, L1H, L2H) were filled with water, and gas was supplied to the gas control channels (L1GR, L1GL, L3G) as well as the environment around the chip. Fluid flow in the liquid-filled channels was stopped using pinch clamps (Cole-Parmer) on the micro-bore tubing inlets, and all calibration points were acquired after equilibrium was reached (images were acquired every 30 seconds after gas supply began, and this image series was used to determine equilibration).

3.5.1.4   Fluidic Sensor Calibration using Microfluidics and Oxygen Scavenger

One potential concern with the use of the microfluidic gas control device to calibrate the optical oxygen sensors is whether the fluid in contact with the sensors was able to completely equilibrate with the gas flowing through the gas control channels. To ensure that the microfluidic gas control device was able to accurately calibrate the sensors, a test was conducted using an oxygen scavenger solution. The question addressed by this test was whether the microfluidic gas control

system was able to create a truly anoxic fluidic environment around the sensors (to the extent of the limit of detection of the sensors), or whether the fluid oxygenation was partly influenced by the environment outside the chip.

Sodium sulphite (Na_2SO_3) is an oxygen scavenger which is commonly used in water treatment to remove oxygen from water to prevent corrosion. The reaction between sodium sulphite and oxygen produces sodium sulphate, as shown in equation 7 [293, 294]:

$$2Na_2SO_3 + O_2 \rightarrow 2Na_2SO_4. \tag{7}$$

Within a microfluidic system, 4 g/L (0.4 wt%) sodium sulphite has been used as a scavenger to create oxygen gradients [250], and a 10 wt% solution of sodium sulphite has been used to calibrate optical oxygen sensors [246]. For our tests, we first calibrated the optical oxygen sensors with the microfluidic oxygen control device using the methods described in section 3.5.1.3. A freshly-prepared 10 wt% solution of sodium sulphite was subsequently supplied to the main cell culture channel of the device at a flow rate of 10 μL/min, in direct contact with the optical oxygen sensors. The oxygen levels were measured while the scavenger solution was flowing, both with and without supplying 0% oxygen to the gas control channels as described in the fluidic calibration section 3.5.1.3. If the measured oxygen level became negative during these measurements, it followed that the microfluidic calibration of the sensors was insufficient (the fluid in contact with the sensors was not completely equilibrating with the gas supplied to the chip). In contrast, if the measured oxygen level remained at 0%, the oxygen scavenger test would have demonstrated that the microfluidic calibration was accurate.

3.5.2   Sensor Calibration Results

3.5.2.1   Gaseous Sensor Calibration

The results of the gaseous calibration of the sensors are presented in Figure 3.17. Fit parameters for the gaseous calibration were calculated (the average and one standard deviation error of three repeats of the calibration, each on the averaged response from four sensor patches) as $k_{sv} = 0.151 \pm 0.004$ %atm^{-1}; $f_1 = 0.756 \pm 0.007$; $f_2 = 0.243 \pm 0.007$.
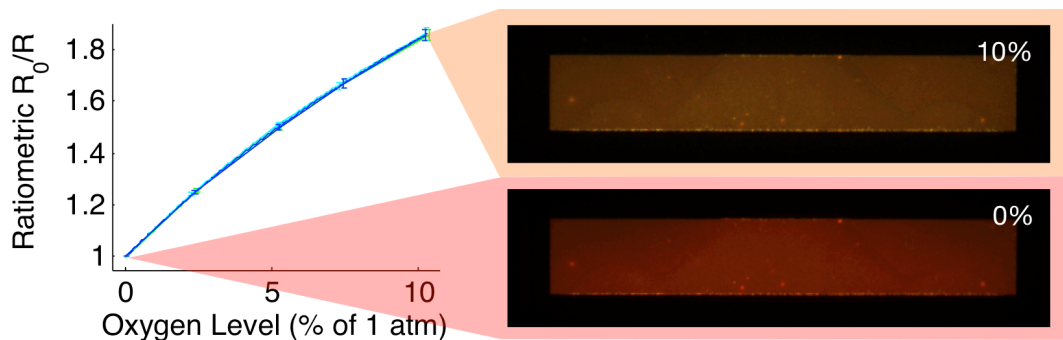
Figure 3.17. Gaseous calibration plots for optical oxygen sensors with fit to the simplified two-site quenching model (equation **6**). Fit parameters were: $k_{sv} = 0.151\pm0.004$ %atm^{-1}; $f_1 = 0.756\pm0.007$; $f_2 = 0.243\pm0.007$. Error bars represent the standard deviation in ratiometric intensity between four different sensor patches. Line colours represent the calibration curves for three different repetitions of the calibration; the resulting curves are very similar. Insets show fluorescence microscope images of a sensor patch exposed to 10% (top) and 0% (bottom) of 1 atm gaseous oxygen used in the calibration, demonstrating the colour change induced by changing oxygen levels.

3.5.2.2   Fluidic Sensor Calibration using Microfluidic Gas Control Device

The results of the fluidic calibration of the sensors are presented in Figure 3.18. Fit parameters for the fluidic calibration were calculated (three repeats of the calibration on the averaged response from four sensor patches) as $k_{sv} = 0.152\pm0.006$ %atm^{-1}; $f_1 = 0.755\pm0.016$; $f_2 = 0.243\pm0.015$. These constants are similar to those previously reported by Ungerböck *et al.* [109] ($k_{sv} = 11.5\times10^{-3}$ hPa^{-1} = 0.1165 %atm^{-1}; $f_1 = 0.785$; $f_2 = 0.215$).
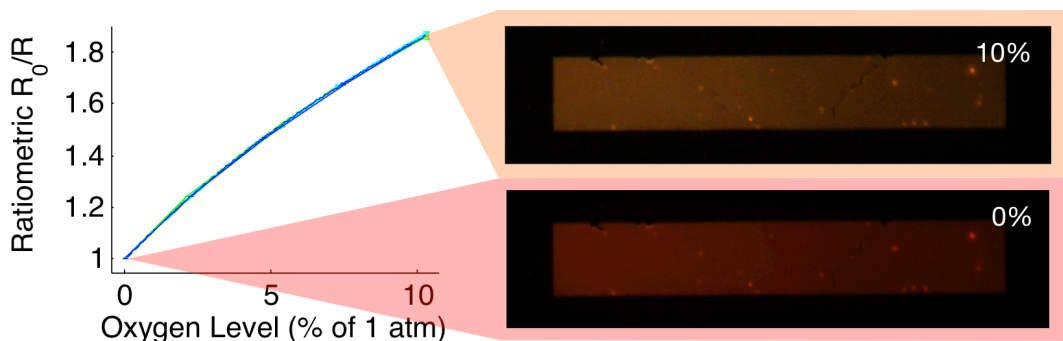
Figure 3.18. Fluidic calibration plot for optical oxygen sensors with fit to the simplified two-site quenching model (equation **6**). Fit parameters were: $k_{sv} = 0.152\pm0.006$ %atm^{-1}; $f_1 = 0.755\pm0.016$; $f_2 = 0.243\pm0.015$. Oxygen level is reported as the level of the gas in equilibrium with the liquid. Error bars represent the standard deviation in ratiometric intensity between four different sensor patches. Line colours represent the calibration curves for three different repetitions of the calibration; the resulting curves are very similar. Insets show fluorescence microscope images of a sensor patch exposed to 10% (top) and 0% (bottom) of 1 atm fluidic oxygen used in the calibration, demonstrating the colour change induced by changing oxygen levels.

3.5.2.3   Sensor Limit of Detection

The Limit of Detection (LoD) for the sensors was calculated based on the methods described by Armbruster and Pry [295]. First, the Limit of Blank (LoB) was determined; the LoB is defined as the highest oxygen level expected to be measured by the system when zero oxygen is present [295]. It was calculated by exposing the sensors to zero oxygen (directly to gas for the gaseous LoDs, and via the microfluidic oxygen control chip for fluidic calibration) and acquiring >5 readings from the integrated sensors. The LoB was then calculated as 95% of these measured values assuming a Gaussian distribution [295]: $LoB = mean_{blank} + 1.645(SD_{blank})$.

This process was repeated for a sample containing 2% oxygen in order to find the LoD, which is defined as the lowest oxygen level that can be measured by the system and discerned from the LoB [295]. The LoD was calculated from the LoB and the standard deviation of the measurements taken as 2% oxygen was supplied to the system, again assuming a Gaussian distribution and finding a 95% confidence interval [295]: $LoD = LoB + 1.645(SD_{sample})$. All datapoints were acquired after equilibrium was reached, and LoDs reflect the stability of the full system (gas supply system, microfluidic oxygen control device, and sensors). Each LoD was calculated by averaging the LoDs of four sensor patches and two sets of measurements (N=8), each calculated from >5 measurements. The calculated LoD was 0.06% for the gaseous oxygen levels and 0.08% for fluidic oxygen levels. These LoDs are sufficiently precise to distinguish between modest (2.5%), moderate (0.5%), and severe (0.1%) hypoxia. In order to improve the sensor LoD, and particularly for studies at very low oxygen levels below 0.1%, future work could include the investigation of different oxygen-sensitive indicators with higher sensitivities; either PdTFPP, which has approximately twice the sensitivity of PtTFPP [296, 297], or other ultra-sensitive sensors [298], could be employed.

3.5.2.4   Fluidic Sensor Calibration using Microfluidics and Oxygen Scavenger

The results of the calibration tests using the oxygen scavenger solution are presented in Figure 3.19. The deoxygenated measurement using only the microfluidic oxygen control (Figure 3.19 (a)) is very close to zero after the system equilibrated (approximately 9 minutes after the gas was switched). The deoxygenated measurement using only the 10 wt% sodium sulphite oxygen scavenger solution (Figure 3.19 (b)) equilibrated much faster; however, it was not able to

completely deoxygenate the channel, particularly regions close to the PDMS structures where there is little to no flow (as evidenced by the false-colour 2-D oxygen plot in the inset of Figure 3.19 (b)). The deoxygenated measurement using the combination of the microfluidic oxygen control and the oxygen scavenger (Figure 3.19 (c)) equilibrates very fast and also yields oxygen measurements very close to zero.
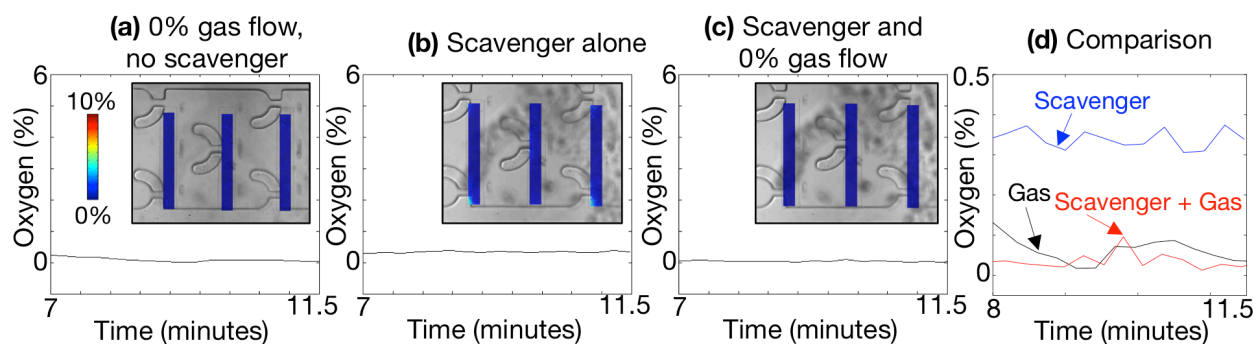
Figure 3.19. Validation of fluidic calibration protocol using an oxygen-scavenging solution. **(a-c)** depict the measured oxygen levels over time under three different conditions providing 0% oxygen: **(a)** using only the 0% gas flow in the microfluidic oxygen control chip to deoxygenate the fluid in the channel; **(b)** using only a 10 wt% solution of sodium sulphite oxygen scavenger flowed through the channel immediately atop the sensors at a rate of 10 μL/min; and **(c)** using both the microfluidic gas control and the oxygen scavenger solution flowed in direct contact with the sensors at a rate of 10 μL/min. All three plots show the measured oxygen levels over time (averaged readings from all of the pixels in the three sensor regions) as well as a false-colour image of the oxygen levels in the channel. **(d)** presents a comparison of the three methods in a narrow oxygen range (0-0.5%). It is evident that the scavenger alone is not able to completely deoxygenate the sensor regions, particularly those near the PDMS structures. The results from the microfluidic gas control and the combination of the microfluidic gas control and the scavenger are not significantly different, suggesting that microfluidic gas control alone is sufficient for sensor calibration within the limits of these oxygen sensors.

Figure 3.19 (d) shows that the zero-oxygen measurement using the microfluidic gas control chip is not significantly different from that using both the gas control and the oxygen scavenger solution. From gas equilibration (9 minutes after gas switch) until 14 minutes after gas switch (18 measurements), the average sensor reading in the gas control-only measurement was 0.03±0.03%, whereas that for the gas control plus oxygen scavenger measurement was 0.04±0.02% (uncertainties represent one standard deviation of the 18 measurements). These values are not significantly different from each other and also below the limit of detection for our system described in section 3.5.2.3, validating our use of microfluidic oxygen control during the sensor calibration process.

3.5.3   Improvement of Ratiometric Oxygen Sensor Stability by Pre-Bleaching

To test the sensors' stability during long-term experiments, an analysis of the ratiometric intensity over time was performed. First, the oxygen levels measured with the ratiometric method were compared to those obtained from the intensity alone during a fluidic experiment. After fluidic calibration, the oxygen levels supplied to the gas control channels were switched between 0%, 2%, and 7% oxygen over a period of 2 hours while the cell culture channel was perfused with water at a rate of 0.5 μL/min. The device was imaged every 60 seconds during the course of this experiment using an excitation shutter (providing approximately 3 seconds of exposure every 60 seconds) and the oxygen levels were calculated from both the ratiometric signal and the intensity signal alone, and compared.

During long experiments where an excitation shutter was not used, we observed that measured oxygen levels drifted upwards over time, indicating that the ratiometric intensity decreased over time. This observation was consistent with sample photobleaching, with the PtTFPP bleaching at a faster rate than the MFY. Indeed, the measured intensities of the red and green channels of the sensor images showed that the luminescence intensities of both dyes decreased over time under continuous exposure. This effect was observed during both gaseous and fluidic oxygen measurements, suggesting that photobleaching, rather than dye leaching, was the dominant effect. We have investigated two methods of improving the sensor stability over time: the use of the excitation shutter to limit sensor exposure to the excitation light (which will also be necessary for subsequent cell-based studies using the system) and pre-bleaching of the sensor films to decrease the rate of ratiometric intensity decrease over time. To test the pre-bleaching procedure, sensors, within the microscope stage top incubator controlled to 37ºC and exposed to air (21% O_2), were imaged every 10 minutes over time periods greater than 12 hours. Sensors were imaged using the microscope shutter (yielding approximately 3 seconds of exposure every 10 minutes), as well as without the shutter (yielding constant exposure).

A summary of the results of the ratiometric stability experiments is presented in Figure 3.20. Figure 3.20 (a) presents a comparison between the oxygen levels measured by the ratiometric method to those measured by intensity alone from the same sensor (PtTFPP channel only), during the fluidic oxygen switching experiment. The ratiometric measurements show a much

more stable profile, consistent with previous literature on ratiometric sensors. We believe that the dominant cause for the observed intensity fluctuations is the mercury arc lamp excitation source used in many fluorescence microscopes. Consistent with the results presented in the comparison of intensity-based to ratiometric sensors (section 3.4.1), these results suggest that ratiometric sensors are far better suited to long-term experiments than the intensity-based sensors employed in some of the previous demonstrations of microfluidic cyclic hypoxia.

Figure 3.20 (b-d) present the stability over time of the ratiometric intensity (R), normalized to its value at the start of the experiment, as the sensor was left exposed to 21% O_2 atmospheric conditions and controlled to 37°C. Figure 3.20 (b) presents the observed decrease in normalized R during an experiment in which the sensor film was left constantly exposed to the mercury arc lamp excitation source. The curve sharply decreases over the first 24 hours and approaches a stable value close to 60% of its initial ratiometric intensity, levelling off after approximately 48 hours.

(a) Comparison of ratiometric to intensity-only (PtTFPP) sensing

(b) Bleaching: R decrease under continuous excitation exposure

(c) Pre-prebleaching: R stability under shuttered exposure

(d) Post-prebleaching: R stability under shuttered exposure
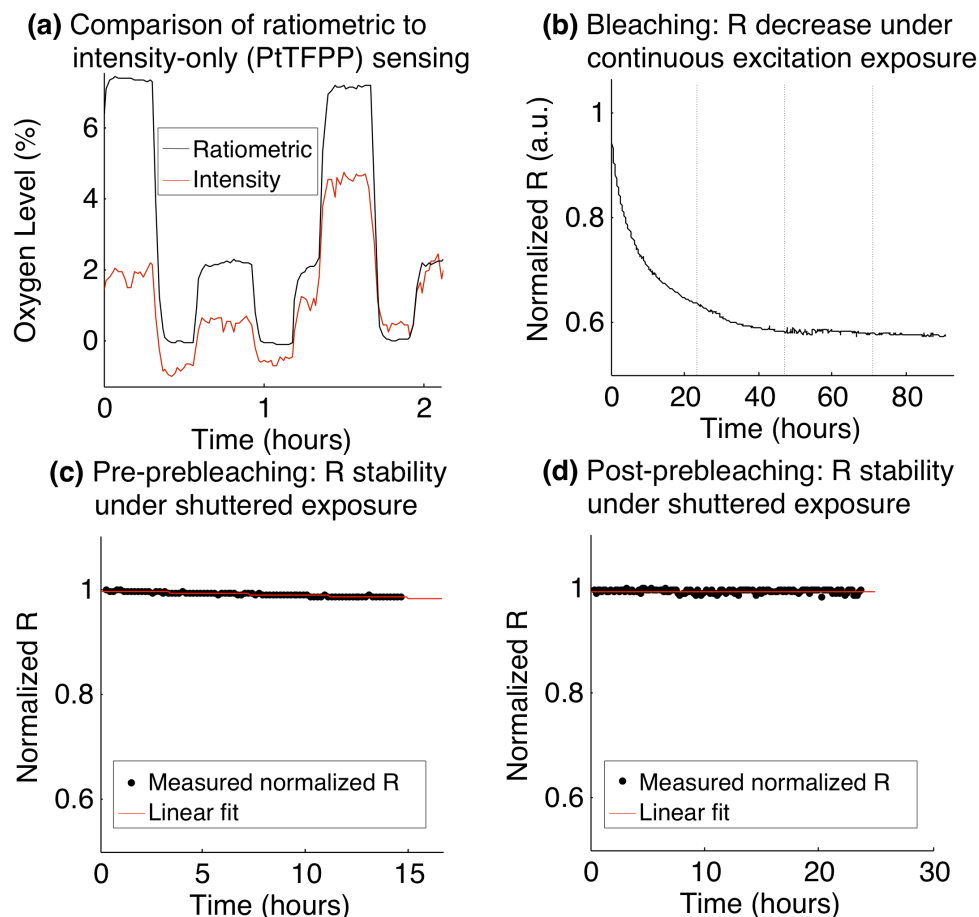
Figure 3.20. Stability of ratiometric sensors over time. **(a)** Comparison of ratiometric stability with the stability of the PtTFPP channel alone during a fluidic oxygen switching experiment; **(b)** Ratiometric intensity decrease over time while being constantly exposed to the fluorescence excitation source (dotted vertical lines denote increments of days); **(c)** Stability of the ratiometric intensity (black), before pre-bleaching. The standard deviation of the normalized ratiometric intensity over the 14.5 hour time course was 0.0038, and a linear fit to the normalized ratiometric intensity (red) shows a slope of -1.5×10^{-5} min^{-1}; **(d)** Stability of the ratiometric intensity (black), after a 61-hour pre-bleaching process. The standard deviation of the normalized ratiometric intensity over the 23.5 hour time course was 0.0035, and a linear fit to the normalized ratiometric intensity (red) shows a slope of -1.4×10^{-6} min^{-1}. Figure previously published in [280].

With this behaviour in mind, we tested a prebleaching process in which the ratiometric stability was analyzed both before and after 61 hours of constant exposure to the excitation source (prebleaching). In each test, the sensor was imaged with the use of the fluorescence excitation shutter (which yielded approximately 3 seconds of exposure every 10 minute imaging cycle) for periods >12 hours. Figure 3.20 (c-d) present the results of this study, with (c) depicting the ratiometric stability before the pre-bleaching process, and (d) depicting the stability after pre-bleaching. The data were fitted to a line to analyze the rate of decrease of the ratiometric

intensity in each case, and the standard deviation of all of the measurements in the time series was taken as a measure of the stability in each case.

The slopes before and after the pre-bleaching process were found to be $-1.5\text{x}10^{-5}$ min^{-1} and $-1.4\text{x}10^{-6}$ min^{-1}, respectively, showing a decrease of over an order of magnitude in the rate of ratiometric intensity attenuation after the pre-bleaching process. The disadvantage of the pre-bleaching process is the overall luminescence intensity degradation that it induces, which leads to noisier signals after the bleaching process. For long experiments, however, this additional noise will be counteracted by the decrease in the downward slope of R over time. In our study, we found that the standard deviation of the normalized ratiometric intensity measurements over the 14.5 hour time course of the experiment before pre-bleaching was 0.0038, and that over the 23.5 hour time course of the experiment after the pre-bleaching was 0.0035. The stability of the measurements was thus greater over the longer experiment after pre-bleaching than that during the shorter experiment before, even with the increased noise induced by the lower intensities after bleaching. The effect of the slope in the ratiometric intensity would only become more pronounced during longer experiments, while the noise induced after pre-bleaching could be reduced at oxygen levels of physiologic relevance (less than the 21% used in this experiment), due to the reduction in quenching of the PtTFPP luminescence.

3.6   Sensor Measurement

The microfabricated ratiometric optical oxygen sensors, integrated into the microfluidic oxygen control device, were used to characterize the capabilities of the oxygen control system, as will be presented in Chapter 4. In acquiring all of these measurements, the same sensor measurement process was used. The sensor measurement methods are described in section 3.6.1, while the specifics of the image processing techniques used are presented in section 3.6.2.

3.6.1   Sensor Measurement Methods

During all oxygen measurement experiments presented in Chapter 4, the sensors were integrated within the microfluidic oxygen control device and maintained in a microscope stage-top incubator (Live Cell Instrument Chamlide) in a humidified environment at 37°C. The sensors were calibrated either before or after the experiment using the methods described in section

3.5.1.3, and this calibration was used to interpret the ratiometric intensities acquired using fluorescence microscopy. A fluorescence microscope (Nikon TE-2000-U) with mercury arc fluorescence excitation source (Nikon Intensilight) and fluorescence filter block (Omega Optics XF115-2) was used to measure the sensor films. The measurement system described in section 3.3 was used to provide gaseous oxygen to the microfluidic oxygen control device as well as to image multiple stage locations and multiple sensors in an automated fashion. The microscope shutter system was used in all cases to limit sensor film exposure to the excitation light.

3.6.2 Image Processing

After acquisition, the oxygen sensor images were used to compute the oxygen levels within the microfluidic device using the calibration data for the same sensors. Sensor-by-sensor calibration was used in all cases. A custom MATLAB$^{®}$ script was used to compute the oxygen levels from the sensor images. For each image to be measured, the image was read in and a dark image (with no excitation light) was subtracted to remove any background. The sensor regions were found either by manual input or automatic thresholding using the green (oxygen-independent) channel, and sensor edges were removed as the edge region intensity tends to be less uniform than the rest of the sensor. For every pixel location within each sensor, the red channel intensity was divided by the green channel intensity at that point to yield the ratiometric intensity R. The two-site quenching oxygen calibration function of equation 6 with the calibration constants (e.g. those found in Figure 3.18) was then used to compute the oxygen levels from R. If a single, average, oxygen level was being computed for the sensor, the averaged R_0 value for that sensor, along with the values for the averaged Stern-Volmer bimolecular quenching constant (k_{SV}), and quenched and unquenched dye fractions $(f_1,$ and $f_2)$, were used in the computation. If a 1-D or 2-D map of the oxygen levels was being computed, the full R_0 matrix for that sensor was used instead, for semi-point-by-point calibration, as this yielded more uniform oxygen measurement results. Moving to full pixel-by-pixel calibration could yield further improved measurement results for the 2-D sensor maps.

2-D plots of oxygen levels were created by first computing the 2-D oxygen map as described above, and subsequently plotting it using the 'jet' colourmap. These coloured image plots could

then be overlaid upon brightfield images of the device by inserting the coloured oxygen plot at the correct location within a grayscale brightfield image by script in MATLAB®.

3.7   Summary

In Chapter 3, we have demonstrated several contributions to the sensing of oxygen within microfluidic systems. To address the problems with integrating patterned thin-film sensors into microfluidic devices, we have developed two novel maskless fabrication processes for patterning polymer thin-films. In particular, the unique laser cutting fabrication process permits the integration of patterned sensors with PDMS microfluidic devices using standard irreversible plasma bonding techniques, which was not possible using dry-etch methods. We have investigated the chemical methods by which the laser cutting method is effective and demonstrated the integrability of the sensors with microfluidic systems. Due to its ease of use and excellent patterning results, the laser cutting method was used to fabricate the sensors used in both Chapter 4 and Chapter 5.

We have chosen and characterized sensors based on their suitability for long-term cell culture experiments and we have showed that moving to the ratiometric sensors developed by Ungerböck *et al.* [109] from intensity-based methods improves the measurement robustness for long-term measurements. We calculated a limit of detection of 0.08% for fluidic oxygen levels for the oxygen sensors; we believe this is sufficient to distinguish severe hypoxia (0.1%) from anoxia (0%), but one possible avenue for future work includes moving to higher-sensitivity sensor dyes in order to improve this limit of detection. We also discussed a gas supply system that has been developed, permitting the supply of controlled gases to the microfluidic device during these long-term experiments. Finally, we have presented calibration and measurement methods that permit the characterization of the microfluidic gas control device that will be presented in Chapter 4.

Chapter 4 Design, Fabrication, and Validation of a Multilayer Microfluidic Oxygen Control System

The final component of the oxygen control test platform was the device used to control the oxygen levels over the cell cultures under test. In order to achieve the fast oxygen switching times necessary to recreate the cycling oxygen profiles that can exist in tumours, a microfluidic device was chosen due to the capability for excellent oxygen control and fast oxygen equilibration facilitated by its short diffusion distances (discussed in section 1.4.1). The device was designed to offer spatiotemporal oxygen control compatible with long-term cell culture, and the optical oxygen sensors described in Chapter 3 were integrated into the device to characterize its oxygen control capabilities and compare with simulation. This chapter presents the design, fabrication, and validation of this microfluidic oxygen control system. The detailed design requirements for the system are presented in section 4.1, the final design for the device is presented in section 4.2, the simulation parameters for the device presented in section 4.3, the fabrication process for the device as well as its integration with the optical oxygen sensors are presented in section 4.4, and the characterization of the oxygen profiles obtainable with the device are presented in section 4.5. Section 4.5 also contains a comparison of the simulated oxygen control and equilibration times to those measured by the integrated sensors within the device.

4.1   Goals

The design goal for the microfluidic oxygen control system was to create a device compatible with long-term 2-D or 3-D cell culture that was able to recreate the kinds of chronic and time-varying, as well as static and spatially-varying, oxygen profiles that can exist in tumours. The device needed to facilitate precise control of the oxygen levels within the cell culture, in order to differentiate between different degrees of hypoxia. The system also needed to permit monitoring of the sensors and cell cultures with fluorescence, confocal, and two-photon microscopy and allow perfusion of the cultures with media, drugs, and stain solutions. These goals led to 6 major requirements, for which a novel design was required:

1. Address the challenge of stability over long-term culture without fluid evaporation from or bubble formation within the cell culture.

2. Precise oxygen control, independent from the environment outside the chip and able to create and differentiate physiologic normoxia (~10% oxygen) from modest hypoxia (2.5%), moderate hypoxia (0.5%), severe hypoxia (0.1%), and anoxia (0%) [79]. Previous work on oxygen control within microfluidic devices had not, to our knowledge, designed devices with these criteria in mind.

3. Oxygen switching/equilibration times within the cell culture compatible with physiological rates of cycling hypoxia, which can range from several cycles per hour to cycles in days [97].

4. Spatiotemporal oxygen control: the ability to create oxygen gradients within the device to potentially recreate oxygen gradients like those measured in tumours [89, 90] over 2-D cell cultures.

5. Compatibility with 3-D as well as 2-D cell culture with constant slow perfusion of media, drugs, and other solutions.

6. Optical access for high-resolution imaging: glass bottom compatible with standard imaging coverslip thicknesses (0.17 mm #1.5 glass).

4.2 Final Design

In order to meet the system design requirements, several design iterations of the microfluidic oxygen control device were simulated, fabricated, and tested. This section presents the final design for the oxygen control device, which is a multilayer device containing on-chip oxygen control channels. The device is fabricated from highly oxygen-permeable PDMS, which permits oxygen diffusion between the channels of the device and facilitates the on-chip oxygen control. The oxygen control microfluidic device is designed to support either 2-D or 3-D cell culture in its centre channel. The glass bottom of the device can be fabricated with either 1 mm thick glass for improved structural stability, or 0.17 mm (#1.5) glass coverslips to permit high-resolution confocal or two-photon microscopy with short working distance objectives. Other glass thicknesses would also be compatible. Both glass substrates support monolayer cell culture, and the device also contains 300 μm hydrodynamic trapping structures (with a small flap in front of the trap opening to aid in trap retention under small amounts of backflow [274]) to immobilize tumour spheroids or hydrogel bead 3-D cell cultures [265] (described in section 2.2) in the device for monitoring. The cell culture channel (1.35 mm x 7 mm) within the tested device

contains 12 trapping structures as depicted in the inset of Figure 4.1, which permit the immobilization of 12 spheroids or cell-laden hydrogel beads for 3-D cell culture, each of 300 μm diameter; the size and design of the cell culture channel could also be tailored to permit the culture of different sized 3-D spheroids or more cells in 3-D or monolayer culture. The multilayer microfluidic oxygen control device is depicted in Figure 4.1.
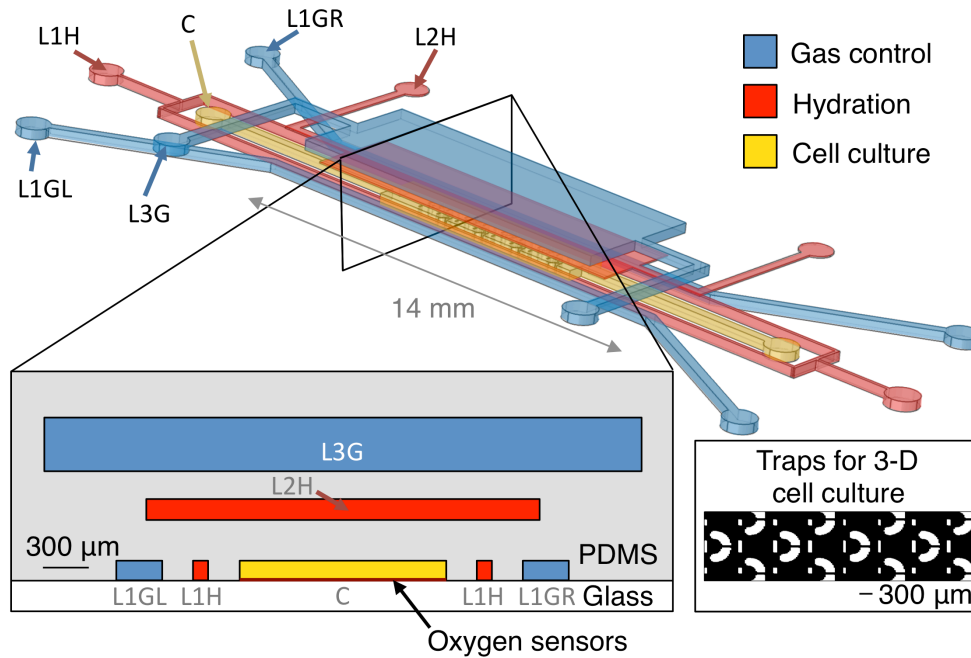
Figure 4.1. Oxygen control microfluidic device layout. 3-D and cross-sectional views of the device as well as the position of the integrated optical oxygen sensors within the cell culture channel are shown. The cell culture channel (C) is surrounded on three sides by gas control channels (L1GL, L1GR, and L3G), with hydration/bubble removal channels (L1H, L2H) between each of the gas channels and the centre channel. Inset shows trapping structures for 3-D cell cultures within the cell culture channel. Please note that the 3-D view is not to scale (microfluidic layers are spaced farther apart in the illustration than in the device to permit visualization of the three layers). Cross-sectional view is to scale. Figure previously published in [280].

The device consists of three layers of channels in PDMS on a glass substrate. A centre channel for cell culture on the first layer of the device (C), is surrounded on three sides by oxygen control gas channels (L1GL and L1GR on the left and right, respectively, of the cell culture channel on layer 1, and L3G on layer 3). There is a 1.3 mm entrance region at the start of the cell culture chamber before trapping structures begin to permit gas equilibration with the fluid before it reaches the cell cultures; the size of this region was estimated based on oxygen gradient measurements from previous design iterations of the oxygen control device. Gas channels are individually addressable to permit the creation of oxygen gradients within the device. Additional

139

fluid-containing channels similar to the hydration layer previously presented by Wood *et al.* [252] (L1H on layer 1 and L2H on layer 2) are integrated between the cell culture channel and the gas channels to discourage sample evaporation from and bubble formation within the cell culture channel, which are potential disadvantages of the use of pressurized gases for oxygen control [247].

4.3   Finite-Element Modeling of Oxygen Control Device

The oxygen control microfluidic device was simulated using COMSOL® Multiphysics. The Navier-Stokes equations were solved to find the fluid velocities in the gas and liquid phase channels. For the gas phase channels (L1GR, L1GL, L3G in Figure 4.1), compressible turbulent flow was simulated, based on the approximated Reynolds Number (5700). The gas inlet relative pressure boundary conditions were defined as 1000 Pa, based on measurements of the pressure at the chip inlet by a pressure sensor (First Sensor HDI) and the outlet pressure boundary conditions defined at 0 Pa (with an absolute pressure of 101 325 Pa). Wall boundaries were defined as wall functions with no wall roughness.

For the liquid phase channels (C, L1H, L2H in Figure 4.1), incompressible laminar flow was simulated. The inlets were defined as velocity-based boundary conditions based on the volumetric flow Q ($v = Q/A$, where A is the cross-sectional area of the channel inlet). Various liquid flow rates were simulated. The outlets were defined as pressure boundary conditions (0 Pa), and all other walls defined as no-slip boundaries.

 To simulate the oxygen levels within the device, three instances of the convection-diffusion equation [299] were solved (one for the oxygen concentration in the gas phase, one for that dissolved in PDMS, and one for that dissolved in media/water):

$$\frac{\partial c}{\partial t} = D\nabla^2 c - \boldsymbol{u} \cdot \nabla c \, , \tag{8}$$

where c is the concentration of oxygen, D is the diffusivity of oxygen in the various media in the device, and $\boldsymbol{u}$ is the fluid velocity field. Oxygen consumption or generation by the media were taken to be zero for these simulations (cellular oxygen consumption was not taken into account,

140

but could in future be measured by using the integrated sensors to determine the oxygen levels with and without cells in the channel and comparing the results with simulated oxygen profiles, or by using 3-D oxygen sensors (water-soluble or microparticle) to measure the oxygen levels within spheroids). The velocity fields in the gas and liquid phases were taken as the results of the flow modeling described above. Boundary conditions and values for the diffusivity (D) and solubility (S) of oxygen in PDMS and cell culture media (water) were based upon Kim *et al.*'s previous work on mathematical modeling of oxygen transport in microfluidic devices (D_{PDMS} = 7.88x10^{-5} cm^2/s; D_{H2O} = 2.8x10^{-5} cm^2/s; S_{PDMS} = 1.25 mM/atm; S_{H2O} = 0.218 mM/atm) [251]. Although these constants provide an estimate, it is worth noting that the oxygen diffusion in PDMS can vary depending on curing conditions, hydration, and time since plasma treatment [300, 301]. A schematic showing the simulation boundary types and locations in the device layout is presented in Figure 4.2.
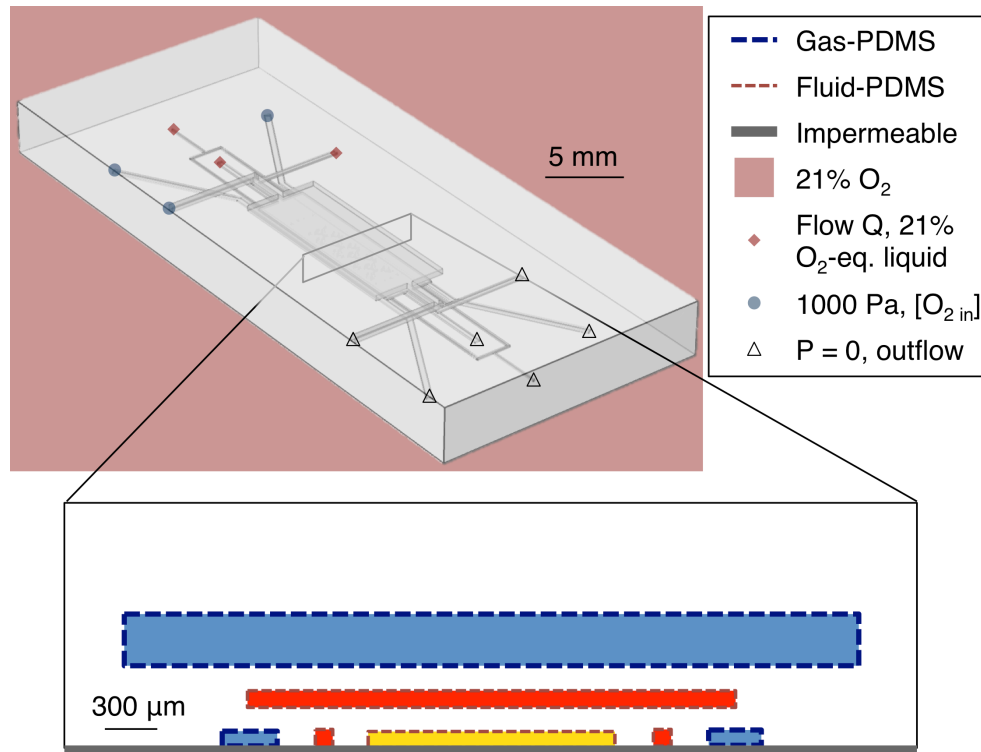
Figure 4.2. Simulation geometry and boundary types. Simulated channel heights were 100 μm for layers 1 and 2 (C, L1H, L1GL, L1GR, L2H), and 300 μm for layer 3 (L3G). Simulated PDMS membrane thicknesses were 100 μm both between layers 1 and 2 and between layers 2 and 3. Figure previously published in [280].

The boundaries at the bottom surface of layer 1 (in contact with the glass in the fabricated device) were simulated as oxygen-impermeable. At the gas-PDMS boundaries within the device,

Henry's Law was used to relate the concentrations of oxygen in the gas phase and in the PDMS (c_g and c_{PDMS}, respectively):

$$c_{PDMS} = S_{PDMS} \cdot pO_2 \approx S_{PDMS} \cdot c_g \cdot R \cdot T, \tag{9}$$

where pO_2 represents the partial pressure of oxygen, R the ideal gas constant, and T the temperature. At the PDMS-water boundaries, pO_2 was taken to be constant and Henry's Law again applied:

$$\frac{c_{PDMS}}{S_{PDMS}} = \frac{c_{H2O}}{S_{H2O}}. \tag{10}$$

Gas inlet oxygen concentrations were simulated based on experimental conditions; boundary values ranged from 0-10% oxygen and are noted in the results section for each simulation. All channel outlets were set to outflow boundary conditions. For all simulations, the exterior of the PDMS chip as well as the fluid at each liquid inlet was simulated as exposed to air (21% oxygen).

The independence of the oxygen levels in the device from the atmospheric condition, and from the oxygenation of the input fluid, was simulated at steady-state using a stationary solver. Additionally, the equilibration times in the device after changing the gas control input were simulated by running a time-dependent solver. The mesh on which the simulations were computed was created by using free tetrahedral meshing optimized for fluid dynamics and specifying maximum mesh sizes for the different domains within the device (the five channel regions and the PDMS bulk). Maximum and minimum mesh cell sizes ranging from minimum 1.34 μm and maximum 20 μm in the hydration channels to minimum 27 μm to maximum 250 μm in the PDMS bulk were specified. A total of 1.3×10^7 domain mesh elements, 5.3×10^5 boundary mesh elements, and 2.4×10^4 edge mesh elements were used in all final simulations. We found that increasing the domain mesh elements to 2.2×10^7, the boundary mesh elements to 8.2×10^5, and the edge mesh elements to 3.1×10^4 resulted in a change in the simulated average oxygen level in the cell-containing channel region of less than 1% of the average value, suggesting that our simulations were acceptably mesh independent.

The results of the simulations of oxygen control within the device and the oxygen equilibration times were compared with measured results and presented in sections 4.5.2 and 4.5.4, respectively.

4.4   Fabrication

4.4.1   Microfluidics Fabrication

The 3-layer device was fabricated by standard multilayer soft lithography using SU-8 3050 photoresist (Microchem) on silicon masters, with an intermediate polyurethane mould for the thick PDMS (layer 3) portion. Layers were bonded by air plasma bonding; layers were exposed to air plasma (Harrick plasma cleaner) for 75 seconds before bringing the layers into contact, pressing gently, and leaving the device in an oven at 70ºC for 30 minutes. After demolding, inlets and outlets were punched and the piece was bonded to the next layer or integrated with the sensor-containing substrate. After bonding the PDMS layers but before integrating with the glass substrate, several devices from the same fabrication batch as the tested samples were sacrificed, diced near the centre and end of their channels, and examined using microscopy to measure channel and membrane heights. The layer 1 channel height was measured to be 130±6 μm, the PDMS membrane between layers 1 and 2 was measured to be 260±30 μm, the layer 2 channel height was 137±7 μm, the membrane between layers 2 and 3 was 174±50 μm, and the layer 3 channel height was 350±30 μm.

4.4.2   Integration with Optical Oxygen Sensors

The ratiometric optical oxygen sensors described in Chapter 3 were fabricated with the laser-cutting patterning method presented in section 3.2.2 prior to integration with the oxygen control device. Sensors were then baked on a hotplate for 5 minutes at 115ºC after liftoff but before integration with the microfluidic device. The optical oxygen sensors were integrated with the microfluidic oxygen control device via irreversible plasma bonding with the glass substrate; layers were exposed to air plasma (Harrick plasma cleaner) for 75 seconds before bringing the layers into contact and pressing gently to ensure all channel regions made contact with the substrate. Bonded devices were left in an oven at 70ºC overnight to ensure bonding was complete before use.

Although the sensor adhesion was maintained during channel flow and desiccation, we did encounter issues with the sensor adhesion in certain use cases. For long cell culture experiments, an intensive PDMS pre-hydration process was used in order to minimize gas dissolved in the PDMS (and thus further discourage bubble formation during culture). This process entailed filling the channels with ethanol using a syringe (as ethanol better wets the hydrophobic channel features than does water), flushing well with water, degassing the chips in a beaker of water within a vacuum desiccator for >30 minutes, placing the chip in the beaker of water in an oven at 70°C overnight, adding cool water to bring the temperature down to ~40-50°C, and degassing again in the vacuum desiccator for >30 minutes. When bubbles had formed on the PDMS surface between any of these steps, a brief (~15s) sonication treatment (Branson Ultrasonic Corporation 8510-DTH) was used to dislodge them. The 70°C treatment was used to bring the temperature significantly above that used during cell culture, as bubbles are more likely to come out of fluid and PDMS at higher temperatures. By pre-treating at a temperature above the cell culture temperature, we reduce the chance of bubbles emerging during culture. Although this process appeared to be effective in reducing bubble formation during long cell cultures, it unfortunately negatively affected the sensor adhesion to the glass bottom of the microfluidic channel. It is believed that this could be due to the difference in thermal expansion coefficients of polystyrene (70×10^{-6} m/(m K) [274]) and glass (9×10^{-6} m/(m K) [302]), which could cause the sensors to start to lift off from the surface and allow the water to penetrate underneath, completing the liftoff process.

Because sensor adhesion was maintained during temperature cycling in the absence of water, to resolve this issue a thin PDMS film was spun on top of the patterned sensors to eliminate direct contact between the sensors and the water. After sensor patterning, Sylgard 184 PDMS was spun on the glass substrate at 3000 RPM for 5 minutes (550 RPM/s acceleration), using an intermediate spin of 500 RPM for 30s (110 RPM/s acceleration). This spin speed should result in a PDMS thickness of approximately 10 μm [303]. After curing overnight, the PDMS-coated sensors were integrated with the microfluidic oxygenator device using the same process as that described above for the un-coated sensors.

4.5   Results: Oxygen Measurements

4.5.1   Measurement Setup

The oxygen control system was characterized using the integrated optical oxygen sensors within a setup composed of a custom gas mixing and supply system and a fluorescence microscope (Nikon TE-2000-U). A mercury arc fluorescence excitation source (Nikon Intensilight) passed through a fluorescence filter block (Omega Optics XF115-2) to excite the sensor films. A custom software graphical user interface (GUI) written in C# using the .NET framework communicated with the camera (Qimaging Retiga EXi), microscope stage controller (Prior ProScan II), and custom-built shutters. The shutters were fitted onto the microscope to selectively block the fluorescence and brightfield light sources, permitting long-term automated imaging of the samples. This software GUI also communicated with a microcontroller (Arduino Mega) controlling an array of solenoid valves to mix known proportions of air, nitrogen, and carbon dioxide, store the mixed gases in small storage tanks, and supply them to the microfluidic system (switching between them in an automated fashion to create automated time-varying oxygen profiles within the device). More information regarding the oxygen control system and automated microscope system is presented in section 3.3, and more information regarding specific sensor measurement protocols is presented in section 3.6.

The device, immersed in water during all fluidic oxygen measurements, remained in a microscope stage-top incubator controlled to 37ºC for all calibrations and measurements. All connections from the chip to the inlet and outlet tubes (Tygon micro-bore tubing, Cole-Parmer) were made via friction fitting of 22 gauge blunt needles (EFD) into holes cored into the PDMS using a 0.5 mm biopsy punch (Harris Uni-Core). A syringe pump (Chemyx) was used to control the flow rate in all liquid-containing channels.

4.5.2   Oxygen Control

Finite-element modeling was used to validate the ability of the oxygen control channels to control the oxygen levels within the cell culture channel, independent of the environment outside of the chip and the oxygenation of the liquid supplied to the cell culture and hydration channels. In all simulations, the environment outside of the chip and the liquid entering the channels were taken to be equilibrated with 21% oxygen. Liquid flow rates of 0, 0.5, 1, 10, and 15 µL/min were

simulated and compared, and the oxygen levels near the bottom of the cell culture channel, in the part of the channel designed to contain the cell cultures (the 'cell-containing channel region', after the entrance/equilibration length), were extracted. The average velocity in this same region of the chip, but at the channel middle rather than channel bottom, was also extracted. Experimental measurements using the device and integrated sensors were conducted to compare with the simulated results. Figure 4.3 presents the simulation geometry showing the region of the cell culture channel analyzed (the 'cell-containing channel region') (a), the results of these simulations (b-f), and the measurements (g).

The data extracted from these simulations is summarized in Table 4.1. The average velocity $\bar{u}$, and average ($\bar{O}_2$) and maximum ($O_{2\,max}$) oxygen levels in the cell-containing channel region were extracted from the simulations and plotted. The Reynolds number (Re) was calculated from $\bar{u}$ (Re = $\bar{u} D_h \rho / \mu$, with D_h indicating the channel hydraulic diameter (for the full 1.35 mm width of the cell culture channel neglecting the impact of the trapping structures) and ρ and μ denoting the density and viscosity of the fluid, respectively). A Péclet number Pe was also defined for the system and calculated from $\bar{u}$, representing the ratio between the diffusion time (1-D simplification) across the channel height (100 µm in the simulation geometry) and the convection time for the fluid to travel the length of the equilibration region at the beginning of the channel, before the cell-containing region begins (1.3 mm):

$$\mathrm{Pe} = \frac{h^2/2D}{L_{eq}/\bar{u}} = \frac{h^2 \bar{u}}{2 L_{eq} D}, \tag{11}$$

where h is the channel height, L_{eq} is the equilibration length at the start of the channel before the cell traps begin, and D is the diffusion coefficient of oxygen in water.
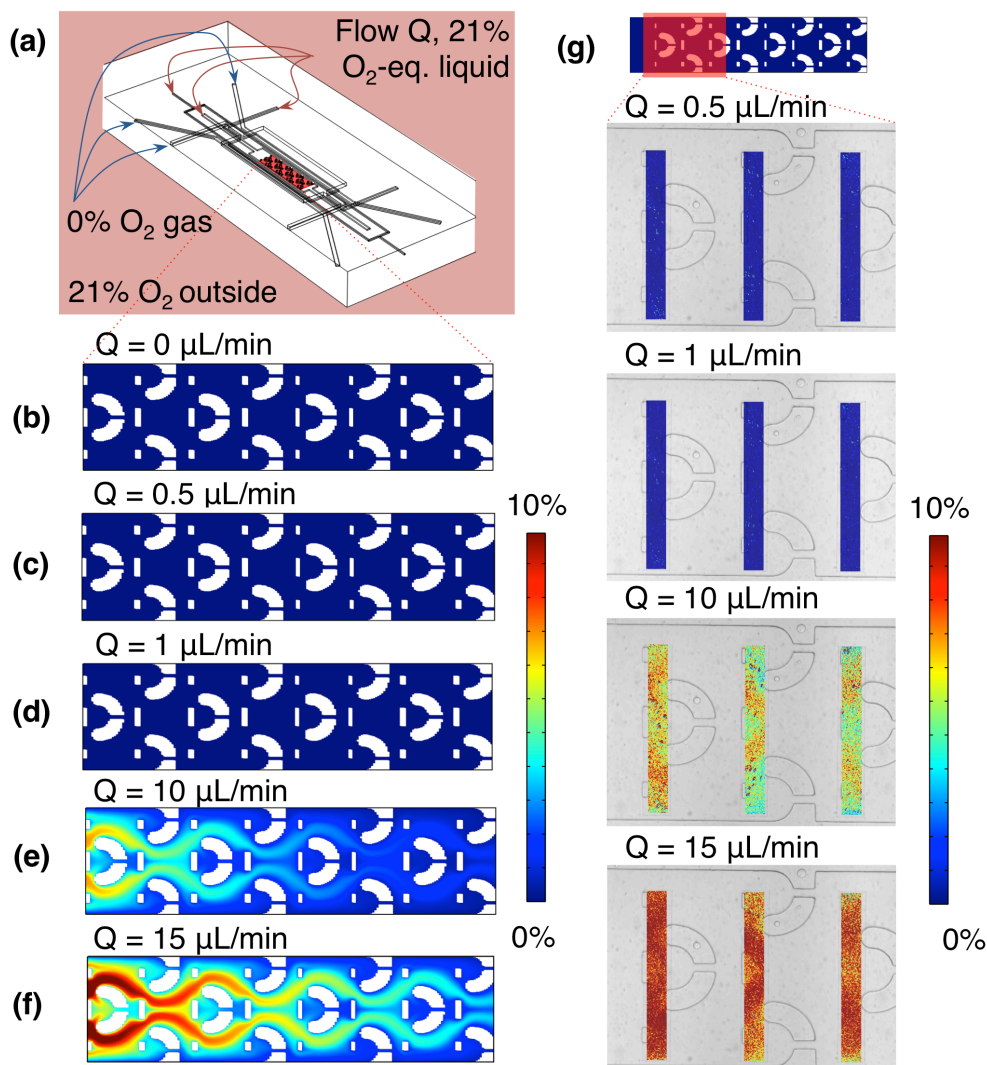
Figure 4.3. Validation of oxygen control within the microfluidic oxygen control system. Simulated and experimental oxygen levels within the microfluidic device, at various rates of fluid flow in the cell culture channel and bubble removal/hydration channels (the same rate supplied to all three channels); **(a)** Simulation geometry, showing the region analyzed (a 2-D slice near the channel bottom, through the region of the channel designed to contain cell cultures: the 'cell-containing channel region'), as well as the input oxygen conditions; **(b)** Simulated oxygen levels within the channel at 0 µL/min fluid flow. Average oxygen level in this region was 0.03%, while the maximum was 0.06%; **(c)** Simulated oxygen levels within the channel at 0.5 µL/min fluid flow. Average oxygen level in this region was 0.03%, while the maximum was 0.05%; **(d)** Simulated oxygen levels within the channel at 1 µL/min fluid flow. Average oxygen level in this region was 0.03%, while the maximum was 0.05%; **(e)** Simulated oxygen levels within the channel at 10 µL/min fluid flow. Average oxygen level in this region was 2.01%, while the maximum was 7.33%; **(f)** Simulated oxygen levels within the channel at 15 µL/min fluid flow. Average oxygen level in this region was 3.86%, while the maximum was 11.2%; **(g)** False-colour images of measured 2-D oxygen profiles near the chip inlet, at 0.5, 1, 10, and 15 µL/min fluid flow, overlaid upon a brightfield microscope image of the channel. Average oxygen levels in the sensor patch regions were 0.01%, 0.009%, 6.5%, and 9.9% at 0.5, 1, 10, and 15 µL/min fluid flow, respectively. Figure previously published in [280].

Table 4.1. Simulated flow rate-dependent properties of microfluidic oxygen control system. Simulated average velocity ū in the channel middle, Reynolds number Re, Péclet number Pe, and the average ($\bar{O}_2$) and maximum ($O_{2\,max}$) oxygen level in the bottom of the cell-containing channel region for different volumetric liquid flow rates Q. All values determined from the results of the simulations presented in **Figure 4.3**.

Q [μL/min]	ū [m/s]	Re	Pe	$\bar{O}_2$ [%]	$O_{2\,max}$ [%]
0	0	0	0	3.46×10^{-2}	5.75×10^{-2}
0.5	1.10×10^{-4}	2.97×10^{-5}	0.150	3.41×10^{-2}	5.10×10^{-2}
1	2.19×10^{-4}	5.94×10^{-5}	0.301	3.46×10^{-2}	4.90×10^{-2}
3	6.57×10^{-4}	1.78×10^{-4}	0.903	8.96×10^{-2}	0.503
5	1.10×10^{-3}	2.97×10^{-4}	1.50	0.382	2.12
10	2.19×10^{-3}	5.94×10^{-4}	3.01	2.01	7.33
15	3.29×10^{-3}	8.91×10^{-4}	4.51	3.86	11.2

The laminar Reynolds numbers remain much less than 1 for the extent of the flow rates tested. As the calculated Péclet numbers are for the cell culture channel only, and do not take into account the full system, the simulation results ($\bar{O}_2$, $O_{2\,max}$ as well as the plots of the oxygen levels in the cell-containing channel region shown in Figure 4.3(b-f)) better reflect the experimental system. The simulation results indicate that accurate control of the channel oxygen levels is achievable using the gas control channels for flow rates ≤ 1 μL/min (the operating regime of the device); these results are validated by the experimental findings. The transition point appears to be near 3 μL/min, where the maximum oxygen level in the cell-containing region is approximately 0.5%. After this point at higher flow rates (5, 10 and 15 μL/min), the faster liquid flow brings higher oxygen levels with it into the cell-containing channel region. These results also fit with our expectation of diffusion-based control over mass transport from the Péclet numbers calculated at flow rates ≤ 1 μL/min, given our entrance/equilibration length at the beginning of the cell culture channel. This control and isolation from the environment is essential for creating time-varying oxygen profiles with fast switching times, as if it is not achieved, the diffusion times through the PDMS bulk (~7 mm in thickness, leading to much longer time scales on the order of 1 hour by a 1-D diffusion calculation) will begin to have an effect. Isolation from the input liquid oxygen level is also important, as it impacts the levels of hypoxia achievable using the device without pre-equilibrating the cell culture media perfused to the chip (which could also impact the equilibration times for the system).

The oxygen simulations and measurements in this section have analyzed the oxygen levels at the bottom of the cell culture channel, where cells would grow in monolayer on the oxygen-impermeable glass surface. The 3-D modeling of the oxygen levels within the microfluidic device also allows us to visualize whether there exists an oxygen gradient in the z-direction, which could be relevant for studies involving dispersed cell cultures in 3-D hydrogel beads (tumour spheroids generate their own oxygen gradients due to cellular consumption of oxygen, which were not modelled in this evaluation of the microfluidic device). An example of these modeling results, showing the oxygen levels in the PDMS (a) and in the fluid (b) at steady-state with a fluid flow rate Q of 0.5 µL/min is presented in Figure 4.4. An oxygen gradient is visible in the PDMS bulk around the gas control channels extending towards the chip edge; however, the oxygen levels in the fluid channels show good uniformity in the z-direction.
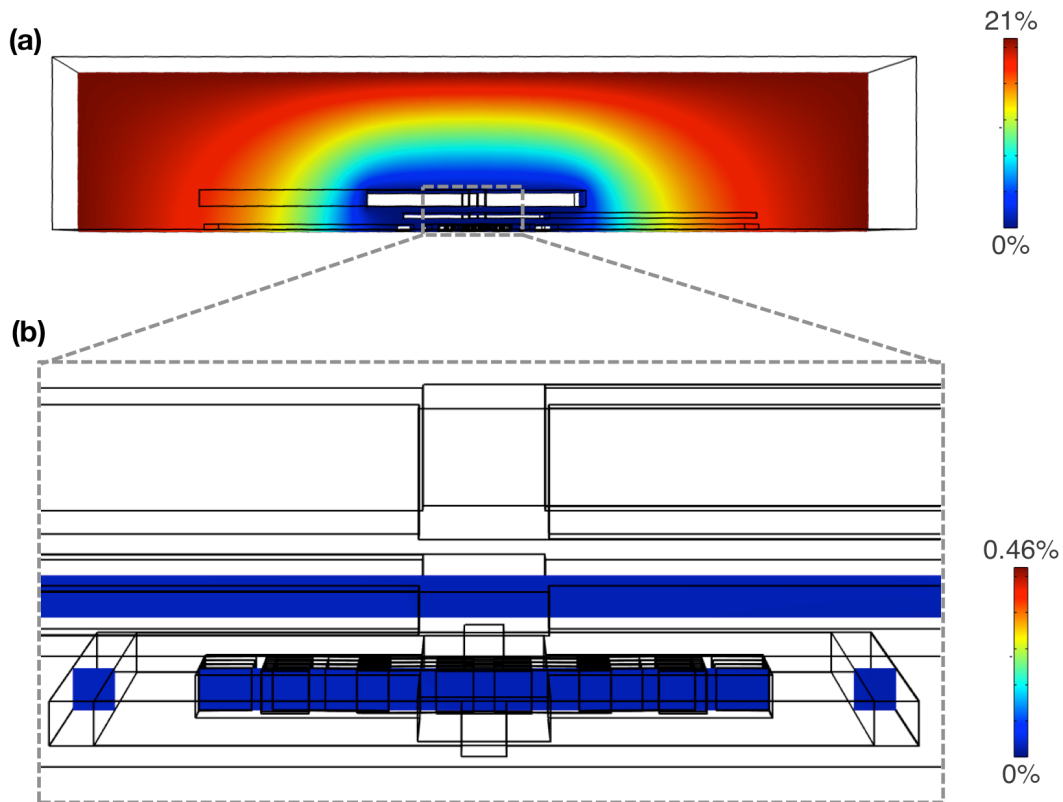
Figure 4.4. Simulated oxygen control in the z-direction within the microfluidic oxygen control device. For this simulation, the fluid flow rate was 0.5 µL/min in the cell culture channel and bubble removal/hydration channels (the same rate supplied to all three channels). **(a)** Simulated oxygen levels in the PDMS bulk of the chip cross-section (looking down the direction of flow). **(b)** Simulated oxygen levels in the fluid, showing good uniformity in the z-direction.

149

4.5.3   Oxygen Gradients

The individually-addressable gas control channels within the microfluidic device offer the opportunity to create spatial oxygen gradients across the cell culture channel. An example oxygen gradient measurement within the microfluidic oxygen control device is presented in Figure 4.5. A stable gradient across the width of the cell culture channel is formed after equilibrating for approximately 10 minutes.

(a) Gradient channel setup   **(b)** Measured oxygen gradient
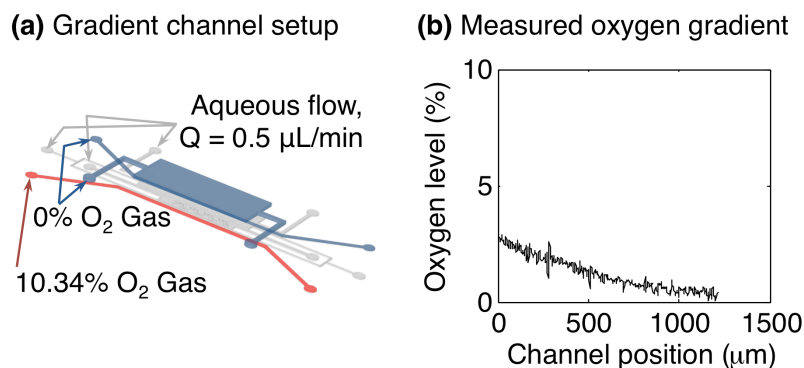
Figure 4.5. Oxygen gradient formation within the microfluidic oxygen control device. **(a)** Microfluidic channel setup for gradient measurement. L1GL was supplied with 10.34% oxygen, while L1GR and L3G were supplied with 0%; **(b)** Oxygen gradient measured inside the cell culture channel by the *in situ* sensors, after ~10 minutes equilibration. The plot shows the oxygen level versus the position across the width of the cell culture channel (i.e., in the direction between L1GL and L1GR). Figure previously published in [280].

4.5.4   Time-Varying Oxygen Levels

The equilibration time within the gas control device (after switching the gas control inlets from 7.33% oxygen to 0% oxygen) was simulated to stabilize to less than 0.5% of the initial oxygen value within 530 seconds. Equilibration curves for starting oxygen levels ($O_{2\ start}$) of 7.33%, 10%, and 21% and flow rates (Q) of 0, 0.5, and 1 µL/min were simuluated. Due to the dominant control of the channel oxygen by the control channels at the flow rates simulated, neither the $O_{2\ start}$ nor Q significantly affected the equilibration curves within the simulated range. This finding further demonstrates the control over the oxygen levels achieved by the gas control channels and is consistent with the Péclet number calculation of Table 4.1 and simulation results of Figure 4.3. The oxygen level at time 530 seconds only varied by 0.3% of the starting value between all of the simulations, with the flow rate showing no effect on the curves, and the curves for $O_{2\ start}$ = 7.33% and 21% reaching 0.5% and 0.2% of $O_{2\ start}$, respectively at t = 530 seconds.

This simulated switching time was also verified experimentally by changing the gas level supplied to the gas control channels from 7.33% to 0% and monitoring the oxygen levels in the cell culture channel using the integrated sensors during the equilibration period. Figure 4.6 presents the simulated equilibration curves, normalized to $O_{2\,start}$, for three values of $O_{2\,start}$ and Q, as well as the oxygen levels measured by the integrated sensors during an oxygen switching experiment with a fluid flow rate of 0.5 µL/min overlaid upon the simulated values (also using $O_{2\,start} = 7.33\%$ using $Q = 0.5$ µL/min), showing excellent agreement.

(a) Simulated equilibration for various starting oxygen levels and flow rate
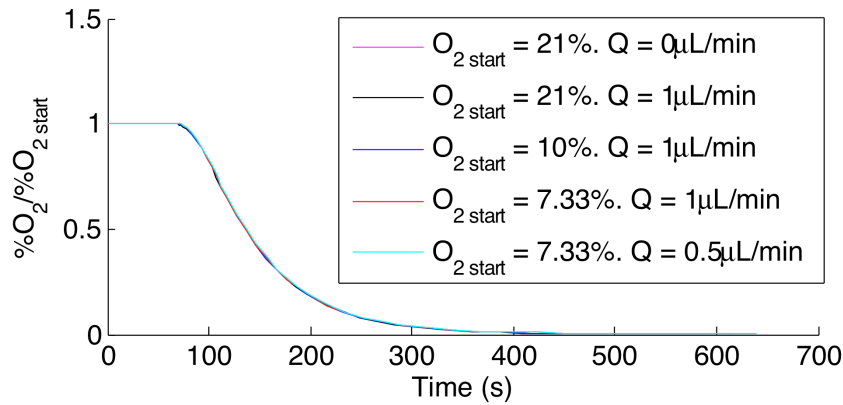
(b) Simulated and measured equilibration times
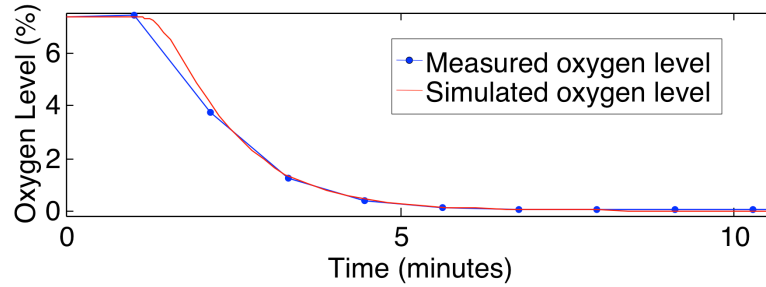
Figure 4.6. Simulated and experimental oxygen equilibration times within the multilayer microfluidic device. **(a)** Time-dependent simulation results, showing the oxygen level at the centre of the cell culture channel after the oxygen level supplied to the gas control channels L1GL, L1GR, and L3G was switched from $O_{2\,start}$ to 0% at time 60 s, for values of $O_{2\,start}$ ranging from 7.33% to 21%, and flow rates Q ranging from 0-1 µL/min. Neither the $O_{2\,start}$ nor Q significantly affected the equilibration curves (e.g. the oxygen level at time 530 seconds only varied by 0.3% of $O_{2\,start}$ between all of the simulations, with the flow rate showing no effect on the curves, and the curves for $O_{2\,start} = 7.33\%$ and 21% reaching 0.5% and 0.2% of $O_{2\,start}$, respectively at t = 530 seconds); **(b)** Simulation and measurement of the oxygen levels within the oxygen control device, after the input gas level changed from 7.33% to 0% oxygen at time 1 minute. System shows equilibration to less than 0.5% of the initial oxygen level within 530 seconds. Figure previously published in [280].

We believe that the slight discrepancy between the measured and simulated curves just after the switch in gas level is due to the sampling rate used in the measurement (1 minute between imaging cycles, with a line used to connect the data points for visualization). The oxygen levels equilibrated to within 0.5% of the initial value after 530 seconds. As the equilibration time is very consistent between the experimental results and the model, we do not believe that the sensor response time has a significant impact on the measured equilibration.

The switching times of 530 seconds achievable with the multilayer device permit the formation of complex, cyclic oxygen profiles within the cell culture channel. An example measurement of this kind of profile is presented in Figure 4.7. For this measurement, a cyclic profile repeating the following oxygen levels was supplied to all three gas control channels: 10% oxygen was supplied for 800 seconds, followed by 0% for 700 seconds, 5% for 1200 seconds, 0% for 1000 seconds, and 5% for 750 seconds. This profile was repeated for 31 hours and monitored with the integrated sensors in the cell culture channel by imaging every 60 seconds. Water was perfused into the cell culture and hydration channels at a rate of 0.5 µL/min throughout the course of the experiment using a syringe pump to simulate the perfusion of fresh media to cells in culture. Slight variations in the 5% and 10% readings are likely due to the mixing error of the gas system (which had a tolerance of 0.5%). The measured oxygen levels appear to be stable over the course of the experiment, demonstrating the suitability of the system for applications in long-term cell culture.
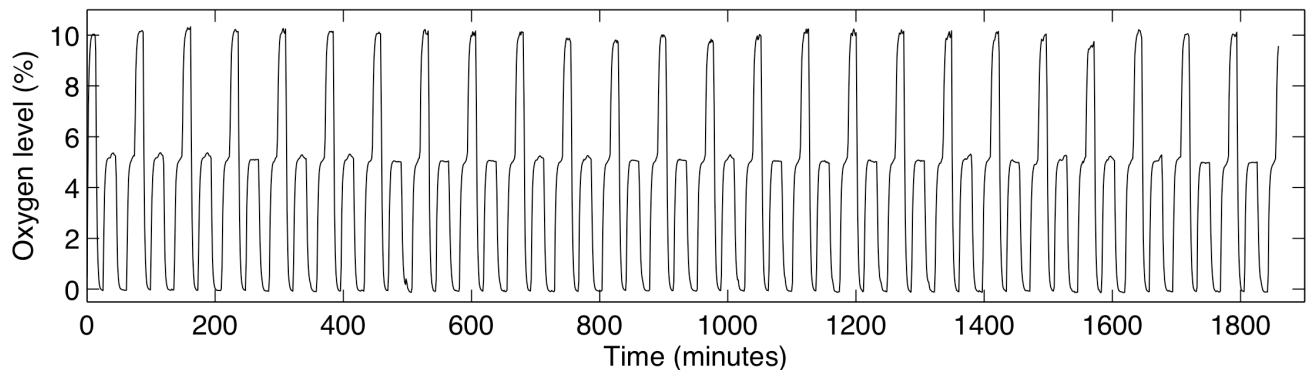
Figure 4.7. Long-term stability of oxygen control system. Measured oxygen levels within the cell culture channel during a cyclic, time-varying oxygen profile in the device, lasting 31 hours. Figure previously published in [280].

4.6   Summary

In this chapter, we have presented a new microfluidic device designed to control oxygen levels around either 2-D or 3-D cell cultures like the cell-laden hydrogel beads presented in section 2.2. The three-layer microfluidic device contains hydrodynamic trapping structures for the beads and surrounds the cell culture by gas control channels on three sides, separated by thin, oxygen-permeable PDMS membranes. Hydration channels are integrated between the cell culture and gas control channels in order to discourage evaporation through the PDMS into the flowing gas. We have characterized the system using both finite-element modeling and the integrated ratiometric optical oxygen sensors described in Chapter 3, and demonstrated excellent oxygen control down to 0.05% oxygen. We characterize the oxygen switching time and find that the oxygen levels equilibrate in less than 10 minutes, showing good agreement between simulation and experimental measurements. Finally, we demonstrate that both physiologically-relevant time-varying oxygen profiles and spatial oxygen gradients can be formed in the device using the three individually addressable gas control channels, and that these profiles show good stability during long-term studies. This characterization validates the ability of the microfluidic device to expose cells to chronic and time-varying hypoxic profiles and forms the basis for the cell-based studies that will be presented in Chapter 5.

Chapter 5 Demonstration of System Utility for Cell-Based Studies

As the goal for this thesis was to create a platform with which to study the response of 2-D and 3-D cell cultures to chronic and time-varying oxygen profiles, several proof-of-concept biological experiments were carried out to validate the platform. The goals of these experiments were to demonstrate:

1. That cells in 2-D and 3-D culture can survive and proliferate within the device.
2. That the device can be used to expose cell cultures to varying oxygen profiles and monitor their response.
3. Whether changes in oxygen level have an observable effect on human breast cancer cells in 2-D or 3-D culture.
4. Whether the device is suitable for cancer drug screening studies.

The experiments conducted include preliminary tests in which 2-D and 3-D cell cultures were grown within the microfluidic device, as well as tests investigating the effects of changing oxygen levels on 2-D and 3-D cell cultures. This chapter presents the results of these investigations; the 2-D cell culture studies are outlined in section 5.1, and the 3-D cell culture studies are outlined in section 5.2.

5.1   2-D Cell Studies

Although the ultimate goal of the system was to study the effects of chronic and transient hypoxic profiles on 3-D cultures, it was important to also demonstrate compatibility with 2-D cell cultures as a proof of concept. Compatibility with both 2-D and 3-D cell cultures is useful for future studies that could compare the effects of anticancer agents on 2-D and 3-D cultures under different oxygen profiles, and potentially observe effects such as multicellular resistance in the 3-D cultures. This section presents the results of these proof-of-concept 2-D cell studies.

5.1.1   Fluorescence Inhibition at Low Oxygen

The first 2-D cell culture study investigated the effects of changing oxygen levels on a human breast cancer cell line that had been genetically modified to express green fluorescent protein (GFP). GFP has been extensively used for a number of applications including studying gene expression and live-cell imaging [304-306]. GFP produces a strong green fluorescence, and cells modified to express GFP can be studied using fluorescence microscopy; however, the intensity

of the GFP fluorescence has been found to depend on oxygen, with very low oxygen levels resulting in decreased fluorescence [307]. For this reason, GFP fluorescence is one potential indicator of changing oxygen levels around cells.

In this study, we exposed a GFP-expressing cell line to a cycling oxygen profile and monitored the cell culture with fluorescence microscopy. We aimed to investigate the effects of the cycling oxygen profiles on the GFP fluorescence intensity as a biological proof-of-concept of the system. We use MCF-7-GFP-LC3 cells, which express diffuse GFP fluorescence under normal conditions, and concentrate the GFP into small fluorescent 'puncta' that are indicative of autophagosomes as the cell undergoes autophagy [308]. For this study, primarily the diffuse fluorescence was studied. Oxygen sensors were not used for this study as the capabilities of the oxygen control microfluidic device had been demonstrated in Chapter 4, and to avoid confounding the fluorescent signal from the cells with the fluorescent signal from the sensors.

Cellular oxygen consumption likely slightly reduces the oxygen levels within the microfluidic channel (compared to the system without cells), so future work could include evaluating the effects of this cellular consumption on the oxygen profiles. Kim *et al.* have measured the oxygen pressure drop (the difference between the cellular and gaseous oxygen levels divided by the gaseous oxygen level) in a simpler 2-layer PDMS microfluidic oxygenator system using human umbilical vein endothelial cells (HUVECs) and found that the cellular oxygen levels could deviate from the gaseous ones by ~2-17% of the gaseous value depending on the monolayer cell density [251]. This previous work found that the use of a thin PDMS membrane between the gas control and cell culture channels (reducing the diffusion time) as well as a PDMS substrate minimized the oxygen pressure drop by permitting expedient gas exchange. In our initial demonstrations of system utility for cell-based studies the integrated sensors were not used; however, they could be used to offer additional insight into the effects of cells on the fluidic oxygen levels in future work.

5.1.1.1   Experimental

The multi-layer PDMS microfluidic gas control device described in Chapter 4, with channel heights of approximately 100 μm for layer 1, 100 μm for layer 2, and 300 μm for layer 3, was

used for this study. The microfluidic device was degassed by first flowing ethanol (as ethanol better wets the hydrophobic PDMS structures) and then ultrapure water through each of its channels and subsequently immersing in ultrapure water and desiccating under vacuum for >1h. The device in water was then placed in an oven at 65°C for >12h, and the water was then changed to bring the temperature down to ~40-50°C before desiccating under vacuum again for >1h. After degassing was complete, the Tygon® microbore tubing (Cole-Parmer) inlets and outlets were then connected to the device's punched inlet and outlet holes using blunt needles (Nordson EFD). Fluidic inlet tubing was filled with fluid prior to connecting with the device to avoid the introduction of bubbles into the system.

The device's cell culture channel was rinsed with > 1 mL ethanol through its inlet tubing prior to use in order to reduce likelihood of contamination, followed by rinsing with sterile PBS to remove the ethanol from the system. After this pre-treatment, the cell culture channel was coated with rat tail collagen I solution (3.78 mg/mL, Corning) to improve cell attachment to the glass channel bottom. This dilute collagen solution was flowed into the cell culture channel and incubated for 1.5h at 37°C before rinsing again with PBS to remove the excess collagen solution. MCF-7-GFP-LC3 cells kindly provided by the group of Dr. Marcel Bally were suspended at a concentration of approximately 1.67×10^6 cells/mL in cell culture media and flowed through the cell culture channel. After cell loading, the cell culture channel inlet was blocked using a tubing flow control pinch clamp (Cole-Parmer) to stop flow in the device and permit cell attachment to the glass bottom of the channel. The device was incubated for 24h in a microscope stage-top incubator (Live Cell Instrument Chamlide) at 37°C while imaging every 30 minutes in order to allow the cells to attach to the channel bottom. During all fluid supply steps, care was taken not to introduce bubbles into the system.

After 24 hours, the cells had formed a confluent monolayer. A syringe pump was then used to provide RPMI media completed with 10% Fetal Bovine Serum and 0.05 mg/mL gentamicin sulphate (to reduce contamination risk) at a rate of 0.5 μL/min after initially flushing the channel at 10 μL/min until detached cells (from the loading tubing) were no longer visible in the cell culture channel. Several stage locations within the cell culture channel were imaged using brightfield and fluorescence microscopy every 10 minutes to monitor the GFP fluorescence

during the study. A mercury arc lamp (Nikon Intensilight) was used as the excitation source, and the fluorescence microscopy filter block (Chroma, 49002-ET-GFP) contained a 40 nm bandpass excitation filter centred at 470 nm, a dichroic mirror with 495 nm cutoff wavelength, and a 50 nm bandpass emission filter centred at 525 nm. The hydration channels were perfused with PBS at a rate of 0.5 μL/min while a cycling gas profile was supplied to the gas control channels. 0% oxygen was supplied to the device for 2h, then 3% oxygen was supplied for 2h, and 10% oxygen was supplied for 2h before looping back to the 0%; all gases contained 5% carbon dioxide. The device remained in the microscope stage-top incubator controlled between 36.5°C and 37°C for the extent of the experiment.

The acquired fluorescence images were analyzed using a custom MATLAB script to segment and find the average intensity in the cell-containing regions. Thresholding segmentation was used, employing a threshold determined by Otsu's method and scaled by 0.7 to ensure all cell-covered regions were included. To obtain the average GFP fluorescence intensity, the intensity value of all pixels in the green channel of the segmented region were averaged.

5.1.1.2   Results and Discussion

During the course of the experiment, effects of the oxygen levels on the cells were visible in both the brightfield and fluorescence images of the cell culture (Figure 5.1). The fluorescence intensity tended to be higher when the cells were exposed to 3% and 10% oxygen, and lower when the cells were exposed to 0% oxygen. This effect is consistent with previous findings that GFP fluorescence is dependent on oxygen levels, with the fluorescence intensity at oxygen levels of 1%-5% actually higher than that in normoxia, and a decrease in fluorescence intensity at oxygen levels below 0.02% [307]; this has been corroborated by another study, which found that GFP fluorescence intensities were unaffected until oxygen levels dropped below 0.02% [309]. A third, microbial, study found that GFP fluorescence in a biofilm decreased to near zero during exposure to very low oxygen levels, but fluorescence could be detected 4 minutes after reoxygenation and reached a maximum after 16 minutes of reoxygenation [310].

Interestingly, it also appeared that when the cells were exposed to 0% oxygen, the cell boundaries were less visible in brightfield than when they were exposed to higher oxygen levels.

Contrast in brightfield images can stem from either sample absorption (which should be minimal in this case) or from phase differences generated by defocusing the microscope [311]. It is possible that the changing oxygen levels could result in position, shape, or refractive index changes within the cells that could produce this observed effect. A summary of the results of this experiment is presented in Figure 5.1.
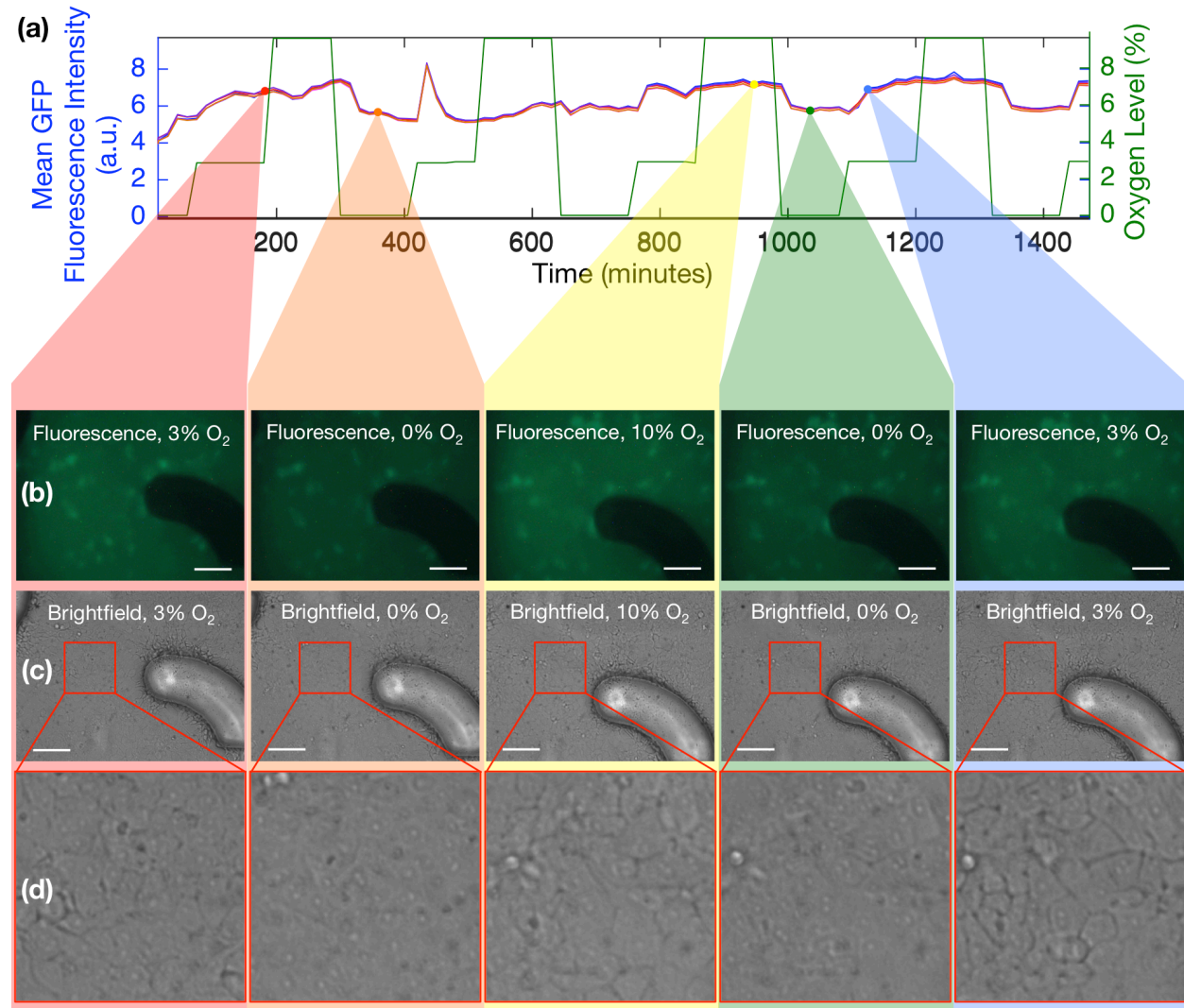
Figure 5.1. GFP fluorescence and brightfield imaging of MCF-7-GFP-LC3 cells during a cycling oxygen profile. **(a)** Average GFP fluorescence intensity in the cell-containing region over time as the oxygen levels were changed. The green line depicts the gaseous oxygen levels supplied to the gas control channels of the device, while the red, orange, purple, blue, and pink lines depict the average fluorescence intensity of 5 different fields of view within the same microfluidic device. Fluorescence intensity tends to be lower at 0% oxygen than at 3% and 10% oxygen, in a cycling fashion. **(b)** Fluorescence images of the same stage location at several different times and oxygen levels within the experiment (coloured overlays depict the time at which the image was acquired in the plot of (a)). Scale bars represent 100 μm. **(c)** Brightfield images at the same stage location and times as those shown in (b). Scale bars represent 100 μm. **(d)** Magnified portions of the brightfield images of (c), showing the change in image contrast observed during the experiment. At 0% oxygen, the cell boundaries tended to be less visible than at 3% and 10% oxygen.

Figure 5.1 (a) shows the average GFP fluorescence intensity over time at 5 different channel locations (orange, red, purple, pink, blue lines on the plot), along with the oxygen levels (green line) during the experiment. Although these fluorescence intensity measurements can be confounded by excitation source or other system nonuniformities (as was discussed in the context of the optical oxygen sensors in section 3.4) and are likely exacerbated by the low overall diffuse GFP fluorescence intensities, we can observe a trend in the average GFP fluorescence intensity related to the oxygen level. It appears that the GFP fluorescence intensity changes over time in a pattern consistent with fluorescence inhibition at low oxygen levels; the intensity decreased when the cells were exposed to 0% oxygen and increased at 3% and 10% oxygen. Although some portions of the plot (particularly the peak near t=430 minutes, which could be due to the mercury arc lamp excitation intensity or due to ambient background light) do not follow this pattern, the measurements before that as well as after approximately t=700 minutes appear to show a trend of fluorescence intensity changing with the oxygen level. In each of these three cycles, the fluorescence intensity sharply decreases 1-2 imaging iterations (15-30 minutes) after the gaseous oxygen input to the device changes from 10% to 0% oxygen, while the intensity increases again 1-2 iterations after the gas input changes from 0% to 3% oxygen.

Figure 5.1 (b) shows the fluorescence images of the same stage location of the sample at various times during the experiment (coloured overlays show the time at which each image was taken). The decrease in intensity at 0% oxygen compared to 3% and 10% is also visible in these images. Figure 5.1 (c) shows brightfield images acquired at the same time points as the fluorescence images of (b), while Figure 5.1 (d) presents magnified regions of the brightfield images of (c). Lines showing the boundaries between cells are evident at 3% and 10% oxygen, but were much less visible at 0% oxygen, potentially due to changes within the cells induced by the changing oxygen levels.

Although we used MCF-7-GFP-LC3 cells that concentrate the diffuse GFP into small fluorescent 'puncta' indicating autophagosomes when the cells undergo autophagy [308], we do not see any evidence of puncta formation in Figure 5.1. This could be due to the image resolution (which is

159

likely not sufficient to clearly separate individual puncta), or because the 2-hour period at 0%
oxygen did not induce significant changes in the formation of autophagosomes. In another
experiment, the same MCF-7-GFP-LC3 cells were exposed to an 8-hour treatment at 0% oxygen
followed by a 2-hour treatment at 10% oxygen, and at one of the imaging locations several bright
spots that could be indicative of one or more puncta were visible upon reoxygenation. In this
experiment, the same 20X objective lens was used for imaging and cells were imaged every 4
minutes. The bright spots appeared approximately 12 minutes (3 iterations) after reoxygenation,
coincident with higher average GFP fluorescence intensity. The results of this experiment are
presented in Figure 5.2.
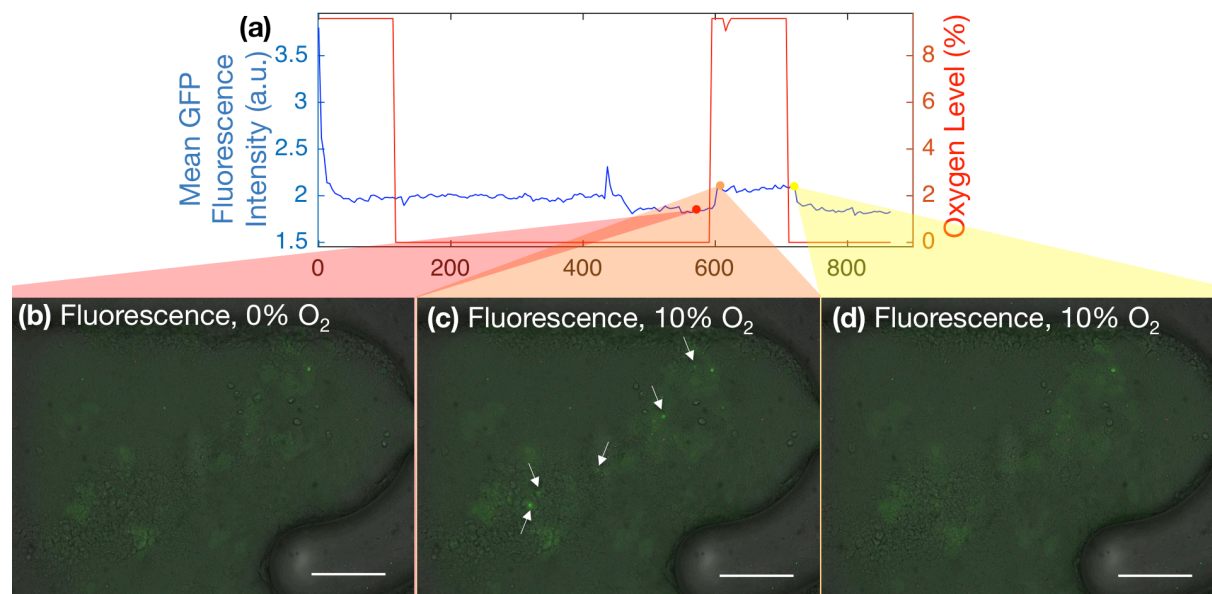
Figure 5.2. GFP fluorescence of MCF-7-GFP-LC3 cells during a cycling oxygen profile with 8 hours at 0% oxygen
and 2 hours at 10% oxygen. **(a)** Average GFP fluorescence intensity in the cell-containing region over time as the
oxygen levels were changed. The red line depicts the gaseous oxygen levels supplied to the gas control channels of
the device, while the blue lines depicts the average fluorescence intensity. After t=450 minutes, the average
fluorescence intensity increases when the cells were exposed to 10% oxygen and decreases when exposed to 0%
oxygen. **(b-d)** Fluorescence images of the same stage location at three different times during the experiment,
showing bright spot formation upon reoxygenation (coloured overlays depict the time at which the image was
acquired in the plot of (a)). **(b)** shows the cells near the end of the 8-hour treatment with 0% oxygen. **(c)** shows the
cells 12 minutes after the gas input was switched from 0% to 10% oxygen, when the bright spots (highlighted by
white arrows) became visible. **(d)** shows the cells at the end of the treatment with 10% oxygen; the bright spots have
faded although average fluorescence intensity remains high. Scale bars represent 100 μm.

Figure 5.2 (a) depicts the average GFP fluorescence intensity in the cell-containing region over
time, showing an increase in intensity approximately 12 minutes after switching to 10% oxygen
near t=600 minutes, and a decrease in intensity after switching back to 0% near t=800 minutes.

Earlier in the experiment a dependence of average GFP intensity on oxygen level is not visible, again perhaps due to the limitations of the fluorescence intensity-based measurements. Figure 5.2 (b-d) depict brightfield-fluorescence overlay images of the cells in the microfluidic channel at three times during the experiment indicated by the coloured overlays. Figure 5.2 (b) shows the cells just before reoxygenation, with the bright spots not yet visible. Figure 5.2 (c) shows the cells approximately 12 minutes after reoxygenation, with the bright spots visible (highlighted by white arrows on the figure). Figure 5.2 (d) shows the cells 2 hours later, at the end of the 2-hour exposure to 10% oxygen. By this point most of the bright spots had faded away, which could perhaps be due to a reduction in autophagy after normoxic exposure, although higher-resolution imaging and a far more rigorous analysis would be necessary to draw any conclusions about the level of autophagy in the cells. Although hypoxia can induce autophagy [312], autophagy in GFP-LC3 cells needs to be quantified by determining the number of cells containing greater than a threshold number of puncta (e.g. >5 puncta per cell [308]), and typically needs to be combined with another stain to ensure accurate results as GFP-LC3 staining alone is subject to several issues [313]. If the bright spots visible in Figure 5.2 (c) are indeed autophagosomes, it is possible that the autophagosomes could be forming during the exposure to 0% oxygen, but the GFP only becomes visibly fluorescent after reoxygenation. Future work could include inducing autophagy (using an autophagy-inducing drug such as rapamycin or tamoxifen) as a positive control, in order to compare with the fluorescence measurements using cyclic hypoxic treatment alone. Hansen *et al.* [310] found that GFP fluorescence in microbial biofilms increased to a maximum intensity approximately 16 minutes after reoxygenation, which is consistent with the time scales that we observe.

GFP fluorescence in cells is affected by a number of steps which can be affected by the oxygen levels, including transcription, translation, and post-translational modifications to the protein (with a final chromophore oxidation step) [307]. This, combined with the different GFP constructs used, could explain the different time scales that have been observed using different cells and different GFP constructs, ranging from 16 minutes in microbial biofilms [310] to hours in mammalian cells [307, 309]. Vordermark *et al.* found that in HT1080 fibrosarcoma cells with a hypoxia-responsive GFP construct the fluorescence increase in the first 2 hours after reoxygenation was primarily due to increased chromophore oxidation, while that between 2-6

hours was due to increased protein levels [309]. It is likely that the relatively fast return of GFP fluorescence that we observe indicates that we are primarily observing chromophore oxidation after reoxygenating the cells, rather than changes in protein levels.

5.1.2   Effects of Doxorubicin under Varying Oxygen Conditions

Cells within our microfluidic system were exposed to doxorubicin, a chemotherapeutic treatment for cancer, as a proof-of-concept demonstration of the microfluidic system as a platform for the cell-based screening of cancer treatments. Doxorubicin is an anthracycline antibiotic anticancer drug that intercalates DNA and binds to DNA-associated enzymes to cause cytotoxic damage to cells. It preferentially affects dividing cells but can also affect interphase cells [314]. Doxorubicin has been used in the treatment of many types of cancer, including breast cancer, since its development in the 1960s, and it has been identified as one of the most effective anticancer drugs [315].

Doxorubicin was identified as an interesting drug to study using MCF-7 breast cancer cells under different oxygen conditions in our platform because it has been found to have different half-maximal inhibitory concentrations (IC_{50}s, or the drug concentration at which half the cell growth is inhibited) under different oxygen conditions, as was discussed in section 1.2.1. Using standard 96-well plates and hypoxic incubators, Strese *et al.* [74] found that the doxorubicin IC_{50} of MCF-7 cells in hypoxia (1% oxygen) was 0.59 times that of cells in normoxic (20-21% oxygen) conditions (i.e., the drug became more effective in hypoxia). Conversely, they found that the IC_{50} of cells in anoxia (0.1% oxygen) was greater than 2.1 times that of cells in normoxia (i.e., the drug became less effective in anoxic conditions) [74]. In another study, Doublier *et al.* [316] found that hypoxic exposure (3% oxygen) led to significantly less drug accumulation in MCF-7 cells after an 18-hour treatment with 3 μM doxorubicin (indicative of doxorubicin resistance at 3% oxygen, in contrast to the doxorubicin sensitivity at 1% oxygen reported by Strese *et al.* on the same cell line). The authors also showed less drug accumulation in tumour spheroids, and attributed this doxorubicin resistance in part to the activation of HIF-1α, which can occur at 3% oxygen. The early work by Teicher *et al.* [71, 72] also characterized doxorubicin on tumour cells. On EMT6 mouse mammary tumour cells *in vitro* [71], they found that flushing the cell culture flasks with gaseous 0% oxygen for 4 hours before and during the 1-hour treatment

162

(leading to hypoxia sufficient to cause radiobiological resistance) increased the cells' sensitivity to doxorubicin by nearly 10 times at high concentrations. In the subsequent *in vivo* study on the FSaIIC murine fibrosarcoma, they found that the least-Hoechst-stained (indicating poor diffusion of the stain from the blood vessels and taken to be hypoxic) tumour regions were 2.2 times less sensitive to doxorubicin than the brightest regions. There could be a great many reasons for the discrepancy between these results, including availability of the drug *in vivo,* the use of a different tumour type, and different oxygenation status of the cells.

The goal of our study was to determine whether an effect of hypoxia could be observed in our microfluidic system, as well as what the effect of the drug would be on cells exposed to a cycling hypoxic profile, which would be much more difficult or impossible to achieve using the standard methods used by Strese *et al.* because of the long system equilibration times in the static 96-well plates used that study. 2-D (monolayer-based) cell culture was used for this preliminary study due to the ease of data analysis as well as the comparison to the monolayer-based study of Strese *et al.* [74].

5.1.2.1   Experimental

The doxorubicin experiment was conducted in two phases. As the reported normoxic IC_{50}s of doxorubicin on MCF-7 breast cancer cells (which were used for this study) have been found to vary from 0.012 μM [317] to 29 μM [74], a normoxic cell-based study was first conducted using several doxorubicin concentrations to determine the appropriate doxorubicin concentration to use in our system for the oxygen-dependent study. For both studies, the cells were grown in monolayer perfusion culture, exposed to the drug for 3 days, and stained with the Live/Dead$^{®}$ cell viability assay to determine cell viability on-chip.

5.1.2.1.1   Determination of Relevant Doxorubicin Concentration

Cell Culture Device Preparation: The aim of this experiment was to find a concentration at which the cell viability was close to 50% under normoxic conditions, so that it would be possible to measure deviations from this viability caused by changes in oxygenation. The microfluidic cell culture device described in section 2.3 with no perfusion in gas or hydration channels and a channel height of approximately 308 μm was used to determine the relevant doxorubicin

concentration for further study. 5 single-layer devices were fabricated using single-layer PDMS soft lithography, punched using a 0.5 mm coring tool (Harris Uni-Core through Ted Pella, no longer available), and bonded to the same 50 mm x 75 mm #2 glass coverslip (Nexterion) using a 75 second exposure to air plasma. Inlet and outlet Tygon® microbore tubing (Cole-Parmer) was connected to the chip via 22G blunt needles (Nordson EFD). The rectangular PDMS chamber described in section 2.3 was used to keep the chips immersed in PBS throughout the duration of the experiment to minimize pervaporation or bubbles as the single-layer device does not have hydration channels.

Before using the chips, they were degassed and coated with collagen using a process similar to that described in section 5.1.1.1. During the chip treatment and cell loading, a short (~30 cm) loading inlet tube connected to a syringe was used to treat the chip and load the cells, in order to minimize the solution used during these steps (long tubing would require larger solution volumes during solution changes). 2 mL of ethanol was flowed through the chip prior to use to sterilize it, and 2 mL sterile PBS was flowed immediately thereafter to rinse the chip. The tubing of each chip was then blocked using a pinch clamp (Cole-Parmer) for ~30 minutes while the other chips were rinsed and collagen solutions were prepared. The channels were then treated with collagen solution to promote cell attachment. Before treatment, an additional 0.5 mL PBS was flowed through the channels. The syringes were then switched to those containing rat tail collagen I solutions (3.78 mg/mL, Corning), and the collagen solution was flowed into the channel and incubated 1.5h at 37°C with the tubing inlets blocked with the same pinch clamps. After collagen treatment, the channel was again rinsed with PBS prior to cell loading. Similar to the procedure used in section 5.1.1.1, care was taken not to introduce bubbles into the system during all fluid handling steps.

Microfluidic Cell Loading: Parental MCF-7 human breast cancer cells were kindly donated by the group of Dr. Calvin Roskelley and suspended in Dulbecco's Modified Eagle's Medium F-12-HAM (DMEM/F-12-HAM) completed with 5% FBS (Invitrogen), 2.5 mM L-Glutamine (Invitrogen), and 1X anti-anti (Gibco, antibiotic-antimycotic composed of 100 units/mL penicillin, 100 µg/mL streptomycin, and 0.25 µg/mL Fungizone® amphotericin B antimycotic) at

a concentration of approximately 8.4×10^6 cells/mL. This cell solution was flowed into the devices and the tubing inlets clamped for 20h while the cells attached.

On-Chip Cell Culture: After attachment, a long tube was connected to each loading tube to perfuse the chips with degassed, conditioned media by syringe pump. The conditioned media was a 2:1 mixture of fresh completed DMEM/F-12-HAM and completed DMEM/F-12-HAM that had been used by the cells in monolayer flask culture for 7 days prior to loading on chip. The media was degassed by bringing it to 50°C for 15 minutes and subsequent desiccation for 60 minutes. Media was supplied at a rate of 10 µL/min for 20 minutes to rinse away loose cells from the tubing before switching to 0.5 µL/min perfusion. Throughout the cell loading and remainder of the experiment, the chips were kept in a microscope stage-top incubator at 37°C supplied with humidified air containing 5% CO_2.

Drug Treatment: After approximately 24 hours of media perfusion, the syringes were switched to media containing various concentrations of doxorubicin. A stock solution of 50 mg/mL doxorubicin hydrochloride (Sigma-Aldrich) in dimethyl sulfoxide (DMSO), (Sigma-Aldrich) was first prepared by adding 200 µL sterile DMSO to the manufacturer's vial containing 10 mg doxorubicin hydrochloride. The doxorubicin vial was kept tightly closed at all times except when transferring solutions to minimize exposure to atmospheric humidity. 3 mL of each drug-containing solution in completed DMEM/F-12-HAM was prepared, and extra DMSO was added to each solution to equalize the concentration of DMSO. The composition of each media solution is presented in Table 5.1.

The doxorubicin-containing media solutions were prepared by first adding the DMSO to the media volume, bringing the solutions to 50°C for approximately 10 minutes, and desiccating for 45 minutes. After this degassing process, the doxorubicin stock was added and mixed by trituration while minimizing air introduced into the solution. The solutions were then slowly withdrawn into 3 mL syringes without air bubbles in preparation for connection with the microfluidic devices. Bubble-free connection was made by blocking the inlet tubing, slowly removing the 21G fluid dispensing tips (Nordson EFD) from the media syringes while applying pressure to the syringe so as to completely fill the tip with liquid and not introduce bubbles,

165

ensuring that the doxorubicin solutions were at the tip of the new syringe (no bubble was present), and then connecting the new, drug-containing, syringe to the fluid-dispensing tip. The syringes were then loaded into the syringe pump, tubing unblocked, and perfusion started at 10 µL/min for approximately 20 minutes to ensure the doxorubicin had reached the chips before switching to 0.5 µL/min for the remainder of the 3-day treatment. Throughout the treatment process, one stage location per device was imaged with low-intensity brightfield illumination every 30 minutes to monitor the cells' response to the drug.

Table 5.1. Composition of doxorubicin solutions used to test cell viability when exposed to various concentrations of doxorubicin.

Sample	Doxorubicin Concentration	Media	Doxorubicin Stock (Drug+DMSO)	100 µM Stock	Additional DMSO
1	0 µM	2.985 mL	0 µL	0 µL	15.1 µL
2	1 µM	2.955 mL	0 µL	30 µL	15 µL
3	10 µM	2.686 mL	0 µL	300 µL	13.6 µL
4	50 µM	2.985 mL	1.74 µL	0 µL	13.6 µL
5	100 µM	2.984 mL	3.48 µL	0 µL	12.1 µL

Viability Staining and Data Analysis: At the end of the 3-day treatment, a solution of 10 µM Live/Dead® stain (Thermo Fisher Scientific) in Hank's Balanced Salt Solution (HBSS) was prepared and perfused to the microfluidic devices to assess the viability. Live/Dead® consists of two stains: Calcein-AM, which interacts with live cells to label them fluorescently green, and ethidium homodimer-1 (EthD-1), which penetrates into compromised cell membranes to label dead cell nuclei fluorescently red. To prepare this solution, 25 µL Calcein-AM and 12.5 µL EthD-1 stock solutions were added to 5 mL HBSS.

Prior to introducing the stain to the devices, five stage locations in each device were imaged using fluorescence microscopy to determine the background fluorescence because doxorubicin is itself a fluorescent molecule. A Nikon Intensilight mercury arc excitation source and triple-band

DAPI/FITC/TRITC RGB filter (Chroma 61000v2), with excitation bands centred near 400 nm, 483 nm, and 554 nm and emission bands centred near 453 nm, 516 nm, and 605 nm, was used to observe the fluorescence. The Live/Dead® stain solution was then supplied to each chip through its inlet via syringe pump by flowing for 30 minutes at 10 µL/min and then blocked and incubated for an additional 30 minutes before imaging the same stage locations using the same excitation source and filter set. As the Live/Dead® stains are not fluorescent except after interaction with cells (at which point the fluorescent molecules remain within the cells), it was not necessary to rinse the stain away before imaging.

The viability was assessed by manually counting live and dead cells in the images from three stage locations for each chip using the ImageJ CellCounter plugin. In cases where cells appeared to have significant portions of both red and green, the cell was counted as alive because the doxorubicin fluorescence emission was an orange-red colour. Stage locations in each device were chosen to be representative of the results in the full device. The full device was inspected using brightfield microscopy and representative stage locations chosen to depict the variation in cell appearances present within each chip.

5.1.2.1.2   Effects of Doxorubicin on Cells Under Varying Oxygen Conditions

As a preliminary demonstration of the system's utility to assess the oxygen dependence of drug efficacy, cell viability was assessed after doxorubicin treatment under three different oxygen profiles: normoxia (air containing 5% CO_2), anoxia as defined by Strese *et al.* [74] (0.1% O_2, 5% CO_2), and a cycling hypoxic profile (3 hours at 0% O_2 followed by 1 hour at 10% O_2). The microfluidic oxygen control device described in Chapter 4 was used to create all oxygen profiles, and all oxygen test conditions were run in parallel using the same cells and reagents.

Cell Culture Device Preparation: The microfluidic cell culture and oxygen control device described in section 4.2 with hydration and gas control channels, and a cell culture channel height of approximately 308 µm was used for this study. Four multilayer microfluidic devices were fabricated using the fabrication process described in section 4.4.1, punched using a 0.5 mm coring tool (Harris Uni-Core through Ted Pella, no longer available), and bonded to the same 76 mm x 89 mm #2 glass coverslip (Ted Pella) using a 75 second exposure to air plasma. Inlet

and outlet Tygon® microbore tubing (Cole-Parmer) was connected to the chip via 22G blunt needles (Nordson EFD). Immersion of the chip in PBS during the experiment was not necessary due to the on-chip hydration channels, which were perfused with PBS throughout the experiment.

Before using the chips, they were degassed and prepared using the same process as that used for the preliminary doxorubicin experiment with single-layer microfluidic chips (described in section 5.1.2.1.1). Like the cell culture inlets, the inlets and outlets of the hydration channels were also connected while the chips were immersed in water, and after filling the hydration channel inlet with PBS.

The chip was treated with collagen solution as described in section 5.1.2.1.1 to promote cell attachment. For this experiment, a sterile dilute solution of 0.1% (V/V) acetic acid in water (with a pH of 4.5, like that of the collagen solution) was used before and after treatment with 3.78 mg/mL collagen to avoid collagen gelation as it came into contact with the neutral pH of the PBS rinse at the 37°C incubation temperature. At least 2 mL of cell culture media was flowed through the cell culture channel of each chip after the dilute acid rinse to ensure that the acid did not remain in the chip during cell loading.

Microfluidic Cell Loading: Cells were loaded into the cell culture channels of the devices using the same protocol as that described in section 5.1.2.1.1, and the cells were left to attach for approximately 15 hours before starting the flow of media. During cell attachment, the on-chip gas channels were not used, and the microfluidic devices were maintained at 37°C within a microscope stage-top incubator supplied with a humidified mixture of air containing 5% CO_2 at a rate of approximately 60 mL/min. The hydration channels were perfused with degassed PBS at a rate of 0.5 μL/min during cell loading as well as the remainder of the experiment. The cells were imaged with low-intensity brightfield illumination every 30 minutes to monitor their attachment. Fields of view were chosen to be representative of the cell density in the channel; however, aggregates of cells (which can be trapped by the trapping structures and should be removed by cell straining in future monolayer experiments) were avoided when selecting stage locations.

On-Chip Cell Culture: After attachment, a long tube was connected to each loading tube to perfuse the chips with degassed, conditioned media by syringe pump. The conditioned media was a 2:1 mixture of fresh completed DMEM/F-12-HAM and completed DMEM/F-12-HAM that had been used by the cells in monolayer flask culture for 5 days prior to loading on chip. The media was degassed and supplied to the cell culture channels as described in section 5.1.2.1.1. The cells were cultured on chip for 3 days in normoxic conditions without on-chip oxygen control prior to exposing the cells to different oxygen conditions using the on-chip control. The on-chip hydration channels continued to be perfused with PBS during the on-chip cell culture.

After 3 days of on-chip culture in the 4 separate microfluidic devices, the cells had proliferated such that they had become 60-80% confluent. At this point, the gas flows were started, with two chips perfused with air containing 5% CO_2 (one control chip and one drug-treated chip), one chip perfused with 0.1% O_2 and 5% CO_2, and one chip perfused with a demonstrative cycling gas profile of 3 hours at 0% O_2 and 5% CO_2, followed by 1 hour at 10% O_2 and 5% CO_2. All three gas control channels in each microfluidic device were perfused with the same gas mixture. The cells were exposed to the gas profiles for 9.5 hours prior to doxorubicin treatment.

Drug Treatment: 1 μM doxorubicin was used as the drug treatment concentration, and 3 mL of drug and control solutions in completed DMEM/F-12-HAM were prepared. Solutions were prepared to match the doxorubicin and DMSO concentrations present in the 0 μM and 1 μM samples of Table 5.1. A mixture of 0.5% (V/V) DMSO in completed media was degassed by first heating to 50°C for 20 minutes and subsequently desiccating for 30 minutes. This DMSO in media mixture was used as the vehicle control, and 0.229 μL 86.2 mM doxorubicin stock solution in DMSO was added to 20.1 mL of vehicle to form a 1 μM doxorubicin drug solution. The doxorubicin solution was mixed by trituration while minimizing air introduced into the solution. The drug and vehicle solutions were then slowly withdrawn into 3 mL syringes without air bubbles in preparation for connection with the microfluidic devices.

Bubble-free connection of the new syringes was made by blocking the inlet tubing, slowly removing the 21G fluid dispensing tips (Nordson EFD) from the media syringes while applying pressure to the syringe so as to completely fill the tip with liquid and not introduce bubbles,

ensuring that the doxorubicin solutions were at the tip of the new syringe (no bubble was present), and then connecting the new, drug-containing, syringe to the fluid-dispensing tip. The syringes were then loaded into the syringe pump, tubing unblocked, and perfusion started at 10 µL/min for approximately 25 minutes to ensure the doxorubicin had reached the chips before switching to 0.5 µL/min for the remainder of the 3-day treatment. Throughout the treatment process, one stage location per device was imaged with low-intensity brightfield illumination every 30 minutes to monitor the cells' response to the drug.

Viability Staining and Data Analysis: As described in section 5.1.2.1.1, the cells in all four microfluidic devices were stained for viability at the end of the 3-day treatment using a solution of 10 µM Live/Dead® stain (Thermo Fisher Scientific) in Hank's Balanced Salt Solution (HBSS) after imaging the doxorubicin fluorescence. Images were acquired and analyzed at multiple stage locations within the device as described in section 5.1.2.1.1.

5.1.2.2   Results and Discussion

5.1.2.2.1   Determination of Relevant Doxorubicin Concentration

The results of the doxorubicin experiment showed a relationship between cell viability and doxorubicin concentration. Prior to introducing the doxorubicin solutions, the cells in all 5 tested devices had attached to the glass surface of the microchannel and were proliferating. Almost immediately after the introduction of the doxorubicin solutions, the cells exposed to the 10 µM, 50 µM, and 100 µM solutions began to detach and clump together showing immediate evidence of doxorubicin toxicity. Over the course of the treatment, some of the cells exposed to the 1 µM solution gradually detached as well. Brightfield images of the same stage location in each of the 5 chips just prior to introducing the doxorubicin, and 24h, 48h, and 60h after doxorubicin introduction, are presented in Figure 5.3 (a,b,c,d), respectively.

The doxorubicin fluorescence images, overlaid upon the brightfield images and presented in Figure 5.3 (e), showed that the drug was taken up by the cells over the course of the experiment, as the cell fluorescence was significantly brighter than that of the background. This is consistent with previously-reported data, which indicates that doxorubicin accumulates in the cell, with intracellular concentrations 10 to 500 times greater than those outside the cell, and

concentrations in the nucleus up to 50 times greater than those in the cytoplasm (up to a saturation level of 340 μM) [314].

It is also interesting to note from the doxorubicin fluorescence images that the PDMS structures do not appear to have become significantly fluorescent over the course of the experiment for any of the tested concentrations. This indicates that the PDMS did not take up significant amounts of doxorubicin from the solution, which was a potential concern regarding the use of PDMS devices as PDMS can take up small hydrophobic molecules [318] and doxorubicin is known to adsorb to container surfaces such as polystyrene and polypropylene [319].

The Live/Dead® fluorescence images, overlaid upon the brightfield images and presented in Figure 5.3 (f), show a clear decrease in cell viability with increasing doxorubicin concentration. The calculated viabilities are plotted against the doxorubicin concentration in Figure 5.3 (g). From this viability data, a doxorubicin concentration of 1 μM was chosen for subsequent experiments, as it resulted in a viability of 44±4%. This viability is sufficiently close to 50% so as to permit the observation of changes in viability in either direction induced by changes in oxygen level. Although the 10 μM concentration yielded a similar measured viability as that for 1 μM, the cells exposed to 10 μM started to detach from the surface very quickly after introduction of the doxorubicin solution. This faster detachment is likely evidence of much higher toxicity, which is not reflected in the viability measurement.

It is worth noting that the calculated viabilities are likely overestimated, particularly for the higher concentrations, because some of the cells that detach from the glass surface (cells that are likely dying) may be carried away by the perfusion flow in the channel. Although this issue will be resolved with the eventual use of 3-D cultures, even with this potential overestimation in 2-D culture the concentration of 1 μM will likely permit the observation of changes in doxorubicin response caused by changes in oxygenation. For future experiments using 2-D cultures, a design such as that demonstrated by Lecault *et al.* could be implemented, which uses perfusion flow over top of suspension cell cultures confined within chambers below the flowing liquid [320]. This design permits perfusion of fresh media to the cells without having the cells directly within the flow path, potentially solving the problem of viability overestimation due to cell detachment.
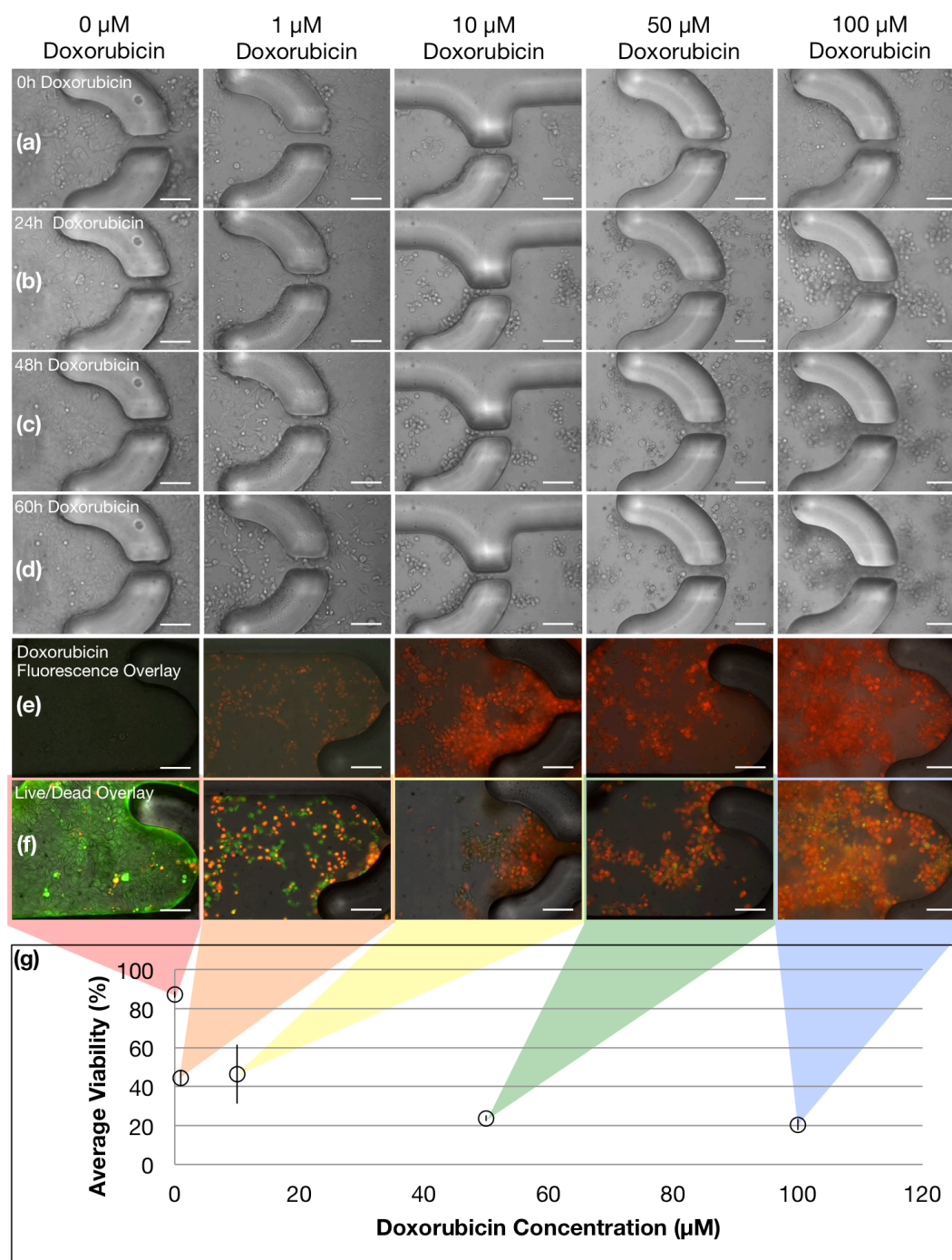
Figure 5.3. Results of on-chip 2-D monolayer study investigating the dose response of MCF-7 breast cancer cells to doxorubicin under normoxia. Image columns indicate different doxorubicin concentrations. **(a-d)** Brightfield images of 5 different microchannels exposed to 5 different doxorubicin concentrations, at different times after doxorubicin was introduced to the system: **(a)** prior to doxorubicin loading; **(b)** 24h after doxorubicin introduction; **(c)** 48h after doxorubicin introduction; **(d)** 60h after doxorubicin introduction. **(e)** Overlay images of brightfield and doxorubicin fluorescence, after 3-day doxorubicin treatment. **(f)** Overlay images of brightfield and Live/Dead® staining fluorescence, after 3-day doxorubicin treatment. Live cells are stained green with Calcein, while dead cells are stained red with Ethidium Homodimer-1. **(g)** Average cell viability, calculated from the Live/Dead® staining images, plotted against doxorubicin concentration. Error bars represent one standard deviation calculated from measurements of 3 representative locations within the channel.

5.1.2.2.2   Effects of Doxorubicin on Cells under Varying Oxygen Conditions

The results of the preliminary experiment to investigate the effects of varying oxygen profiles on MCF-7 cell viability after doxorubicin treatment are presented in Figure 5.4. The results depicted in Figure 5.4 show a possible dependence of cell viability after doxorubicin treatment on oxygen level; however, the results are not statistically significant and further experiments will be necessary to validate this finding.

The viability of the cells in the vehicle control was 91±5%, while that of the 1 µM doxorubicin-treated cells at the same 20% oxygen condition (air containing 5% CO_2) was 60±10%. The viability of the 1 µM doxorubicin-treated cells exposed to the cycling oxygen profile (3h at 0% oxygen followed by 1h at 10% oxygen) was lower than that of the normoxic treatment group at 48±5%, while that of the 1 µM doxorubicin-treated cells exposed to 0.1% oxygen was slightly higher than the normoxic treatment group at 67±6%.

These results are consistent with the trend found by Strese *et al.* [74], who found that anoxic (0.1% oxygen) MCF-7 cells were less sensitive to doxorubicin treatment than normoxic (20% oxygen) MCF-7 cells, and that hypoxic (1% oxygen) MCF-7 cells were more sensitive than their normoxic counterparts. Strese *et al.* evaluated the change in the IC_{50}, while in this experiment we evaluate cell viability. We also find that anoxic cells may be less sensitive to doxorubicin, and our preliminary finding that the cells exposed to the cycling hypoxic profile (with an average oxygen level of 2.5%) may be more sensitive to doxorubicin is consistent with the finding of Strese *et al.* that 1% oxygen increases the sensitivity to doxorubicin. These findings, although preliminary, demonstrate the utility of the microfluidic system for analyzing the effects of various hypoxic profiles on doxorubicin efficacy.
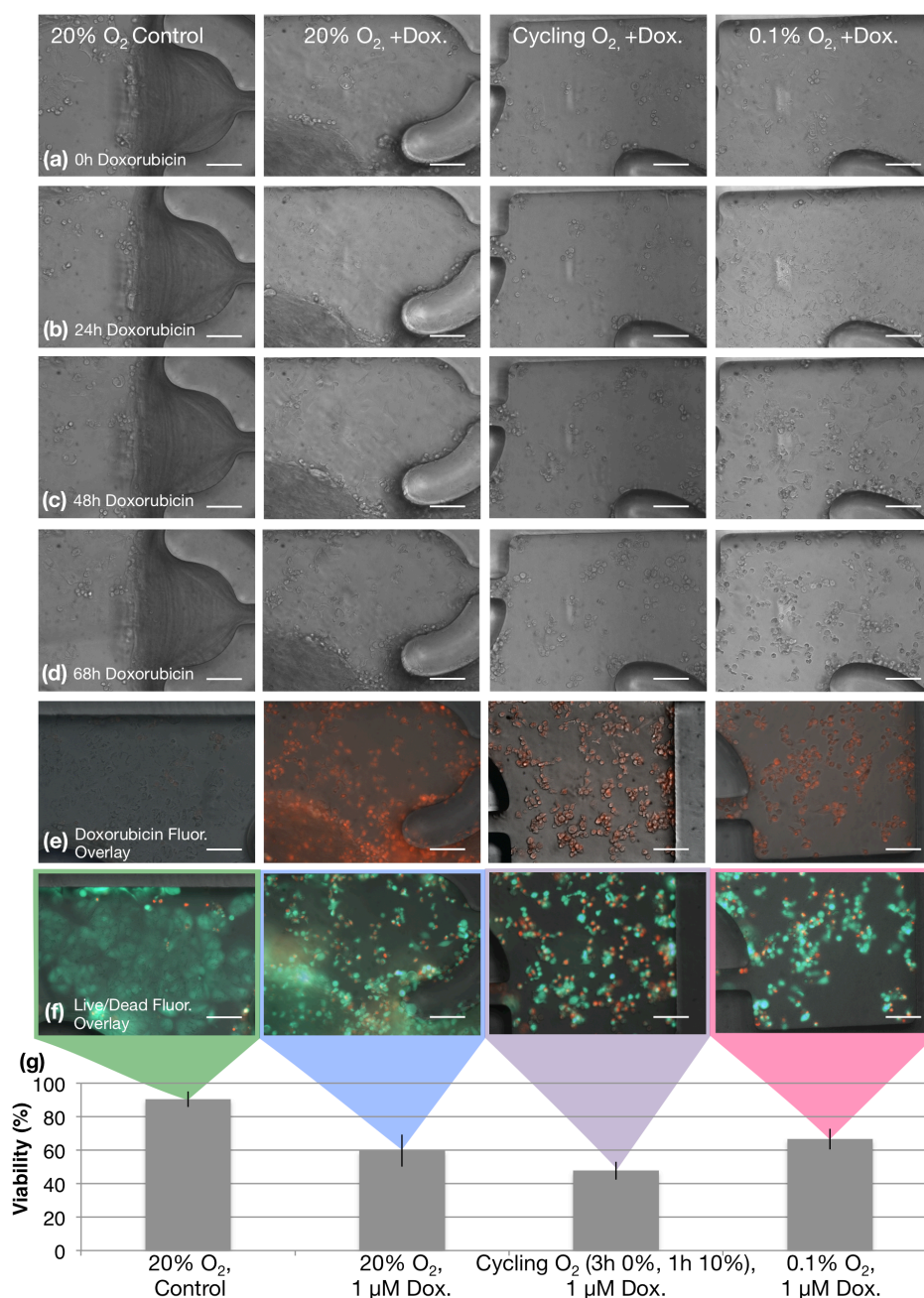
Figure 5.4. Results of on-chip study to investigate the response of MCF-7 breast cancer cells in 2-D monolayer to doxorubicin under different oxygen profiles. Image columns indicate different experimental conditions (oxygen profile as well as either vehicle control or 1 μM doxorubicin; from left to right: vehicle control, at 20% O_2 (air containing 5% CO_2), 1 μM doxorubicin at 20% O_2, 1 μM doxorubicin at a profile of cycling hypoxia (0% O_2 for 3h followed by 10% O_2 for 10h), 1 μM doxorubicin at 0.1% O_2). All gases were supplied on-chip through the duration of the doxorubicin treatment and contained 5% CO_2. **(a-d)** Brightfield images of 4 different microchannels exposed to 3 different oxygen profiles, at different times during the experiment: **(a)** just prior to doxorubicin loading; **(b)** 24h after doxorubicin introduction; **(c)** 48h after doxorubicin introduction; **(d)** 68h after doxorubicin introduction. **(e)** Overlay images of brightfield and doxorubicin fluorescence, after 3-day doxorubicin treatment. **(f)** Overlay images of brightfield and Live/Dead® staining fluorescence, after 3-day doxorubicin treatment. Live cells are stained green with Calcein, while dead cells are stained red with Ethidium Homodimer-1. **(g)** Average cell viability, calculated from the Live/Dead® staining images, for each of the experimental conditions. Error bars represent one standard deviation calculated from measurements of at least 5 locations within the channel.

5.2 3-D Cell Studies

In order to demonstrate compatibility with 3-D cell culture, we also conducted experiments using 3-D cell cultures as described in Chapter 2. We first studied whether 3-D cultures could survive and proliferate on chip, and present this study in section 5.2.1. We then exposed 3-D cell cultures to changing oxygen profiles and monitored their response; the results of this study are presented in section 5.2.1. In order to better understand the spheroids' response to the cycling oxygen profiles, we used two-photon microscopy and cell membrane staining while monitoring the spheroids' response to changing oxygen and present the results of this experiment in section 5.2.3. Finally, we carried out a preliminary investigation of the effects of doxorubicin on tumour cells in 3-D culture; this study is presented in section 5.2.4.

5.2.1 Spheroid Culture in Devices Containing Optical Oxygen Sensors

One concern regarding the use of optical oxygen sensors in cell culture environments is their potential to leach dye molecules or generate reactive oxygen species that could be harmful to cells [223]. In order to ensure that the cells in our microfluidic device were able to survive in close proximity to the optical oxygen sensors, we cultured breast cancer tumour spheroids within a microfluidic device containing the patterned ratiometric optical oxygen sensors described in section 3.4 and stained the spheroids for viability at the end of the experiment.

5.2.1.1 Experimental

Microfluidic Device Preparation: The microfluidic oxygen control device described in Chapter 4 with a layer 1 channel height of approximately 300 μm was fabricated as described in section 4.4 and integrated with patterned optical oxygen sensors as described in section 4.4.2. To facilitate long-term cell culture, the device was degassed as described in section 5.1.1.1. As this process involved heating the chip to 65°C under water, a thin PDMS membrane was spin-coated on top of the patterned sensors on the glass substrate prior to bonding with the microfluidic chip to avoid sensor delamination during the heat treatment, as described in section 4.4.2. After the degassing process was complete, the cell culture channel of the microfluidic device was sterilized by flowing 1 mL ethanol followed by 4 mL PBS and 2 mL cell culture media (DMEM/F-12-HAM completed with 5% FBS, 2.5 mM L-Glutamine and 1X anti-anti). The

device's two hydration channels were connected to syringes containing PBS, and PBS was supplied at a constant rate of 0.5 µL/min for the extent of the cell culture experiment.

Cell Culture: To create the 3-D cultures, parental MCF-7 cells kindly donated by the group of Dr. Calvin Roskelley were suspended in a mixture of 140 µL 2% alginate in HBSS, 180 µL 9.2 mg/mL collagen I, 180 µL Matrigel®, and 7 µL NaHCO$_3$; this mixture was used as the core solution in the hydrogel bead generation process described in section 2.2.2. The cell-laden beads were cultured for 11 days in DMEM/F-12-HAM cell culture media completed with 5% FBS, 2.5 mM L-Glutamine and 1X anti-anti, within hydrophobic cell culture flasks (Sarstedt, Nümbrecht, Germany) prior to loading into the microfluidic device.

To trap the beads on chip, the beads were loaded into a syringe, connected to the cell culture channel inlet, and flowed into the device. After the beads were trapped, the inlet tubing was clamped using pinch clamps (Cole-Parmer) to avoid backflow that could dislodge the beads, and the syringe was changed to one containing completed, conditioned media (a 1:1 mixture of fresh completed media and media that had been used by the same beads for two days during their culture in the flask). 10 µL/min flow by syringe pump was used for 10 minutes to rinse away untrapped beads, and the flow rate was switched to 0.5 µL/min for the remainder of the cell culture.

The three gas control channels were connected to the gas supply system described in section 3.3, and a cycling gas profile of 2 hours at 0% oxygen, 2 hours at 1% oxygen, and 1 hour at 10% oxygen was supplied to all three channels for three days while the device and oxygen sensors were monitored with brightfield and fluorescence microscopy every 30 minutes. During fluorescence measurements, a mercury arc fluorescence excitation source (Nikon Intensilight) passed through a fluorescence filter block (Omega Optics XF115-2) to excite the sensor films. The microfluidic device was maintained within a microscope stage-top incubator (Live Cell Instrument Chamlide) with temperature control to 37°C.

Viability Staining: After approximately 66 hours of culture, the spheroids were stained for viability on-chip, using the Live/Dead assay described in section 5.1.2.1.1. A solution of 10 µM

Calcein-AM and 10 μM ethidium homodimer-1 (EthD-1) in serum-free DMEM/F-12-HAM was perfused into the cell culture channel at a rate of 10 μL/min for 30 minutes, and then flowed at 0.5 μL/min for 1.5 hours. The longer staining time compared to the monolayer assay described in section 5.1.2.1.1 was used to allow the stain to penetrate into the spheroids.

The spheroids were then imaged using fluorescence microscopy using a Nikon Intensilight mercury arc excitation source and triple-band DAPI/FITC/TRITC RGB filter (Chroma 61000v2), with excitation bands centred near 400 nm, 483 nm, and 554 nm and emission bands centred near 453 nm, 516 nm, and 605 nm, was used to observe the fluorescence. Spheroids were subsequently also imaged using confocal microscopy, using a 488 nm and 543 nm excitation lasers and emission filters at 515 nm (30 nm bandpass) and 590 nm (50 nm bandpass).

5.2.1.2   Results and Discussion

The results of the cell culture experiment for three spheroids are presented in Figure 5.5. Brightfield images of the spheroids at the beginning of the experiment and after 65 hours of culture are presented, showing that the spheroid size increased during the experiment and indicating on-chip proliferation.

Wide-field and confocal fluorescence images of the spheroids after live/dead staining are also presented. All three spheroids appear mostly green in the fluorescence images, which indicates high viability. The green colour of the fluorescence differs between the wide-field and confocal fluorescence images because Calcein also emits in the blue channel of the RGB filter used for the wide-field measurements, while the confocal does not have a blue channel. No apparent difference in the stained images was observed between spheroids in close proximity to the optical oxygen sensors (e.g. (c)) and those farther away (e.g. (a-b)).
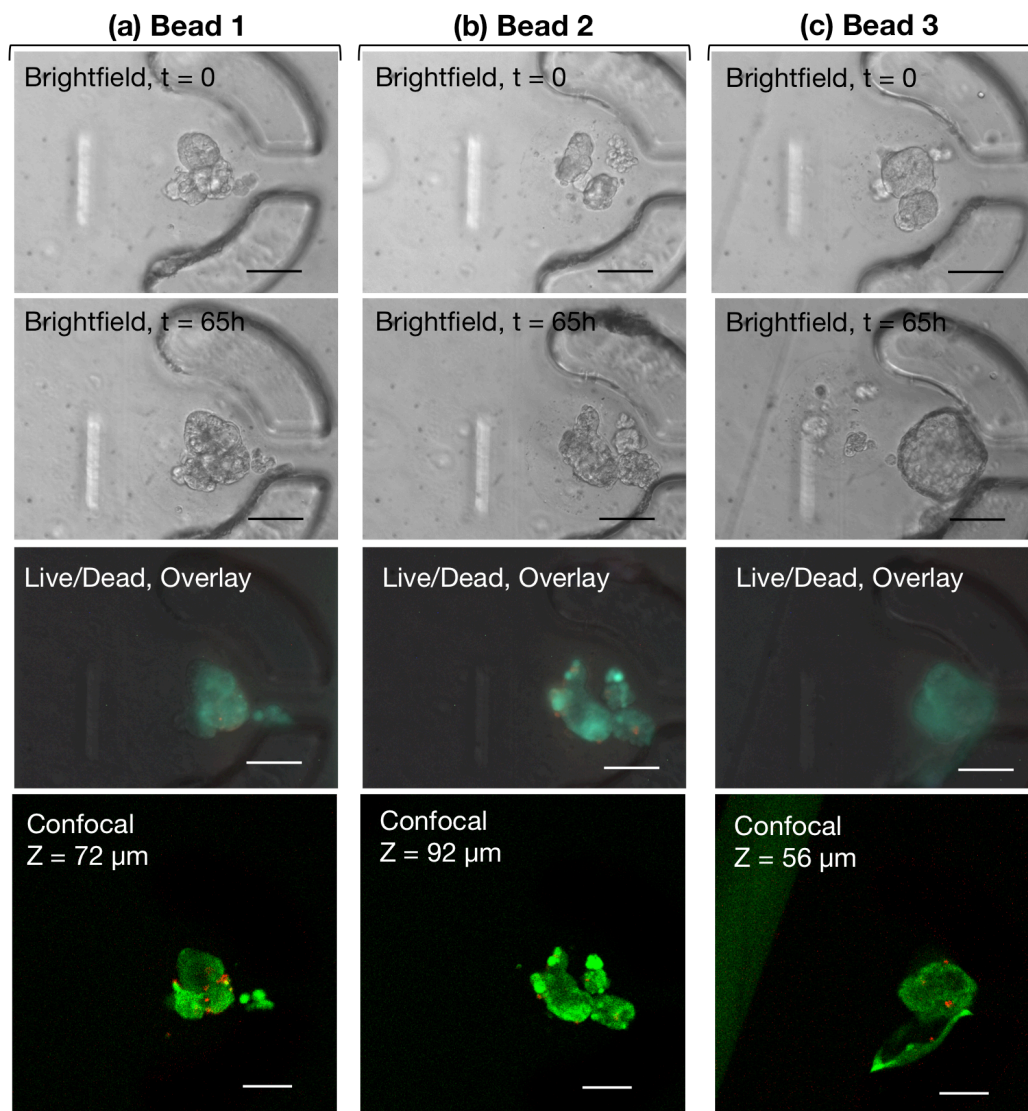
Figure 5.5. Results of on-chip spheroid culture in devices containing optical oxygen sensors. **(a-c)** show images of three different spheroids within the same microfluidic device. Image columns show images of the same spheroid. Brightfield images of the spheroids at the beginning of the experiment (t = 0; just after 0% oxygen began being supplied to the device) and after 65 hours culture (t = 65h; after approximately 1 hour of 10% oxygen supply to the device) are shown. During the culture period, all three spheroids increased in size (indicating proliferation), and the spheroid in bead 3 (c) proliferated out of the hydrogel bead. Wide-field fluorescence and confocal fluorescence images of the live/dead staining are also presented for each spheroid. In these images, green fluorescence indicates live cells, while red fluorescent nuclei indicate dead cells. Scale bars represent 100 μm.

Both the apparent on-chip spheroid proliferation during the experiment and the high viability at the end of the experiment suggest that the use of the optical oxygen sensors does not have an observable effect on the spheroid viability. It is possible that the constant perfusion and short imaging time compared to the imaging interval (500 ms exposure for each of 8 stage locations, for a total exposure time of approximately 10 seconds each 30 minute interval) reduced the effect

178

of any generated reactive oxygen species. If future experiments require longer imaging times, higher exposure doses, or shorter imaging intervals, the effects of the oxygen sensors may need to be re-evaluated.

5.2.2   Reversible Tumour Spheroid Swelling Behaviour in Response to Cycling Oxygen Profiles

To demonstrate the utility of our oxygen control and cell culture platform, we exposed MCF-7 breast cancer tumour spheroids to cycling oxygen profiles of 0%, 3%, and 10% oxygen. We monitored their response to the oxygen profiles and observed reversible swelling behaviour in tumour spheroids: growing at 0% and shrinking at 3% and 10% using brightfield and wide-field fluorescence microscopy techniques. This reversible swelling behaviour has not, to our knowledge, been previously reported in the literature; the unique capability of our microfluidic platform to expose 3-D cultures to cycling oxygen profiles and monitor their response facilitates the observation of this effect.

5.2.2.1   Methods

Microfluidic Device Preparation: The microfluidic oxygen control device detailed in Chapter 4 was used to culture the tumour spheroids and control the oxygen levels over the cell culture. The hydration channels between the cell culture and gas control channels were perfused with phosphate buffered saline (PBS) to preserve osmolarity and deter bubble formation within the cell culture channel. This device did not contain integrated optical oxygen sensors; however, we have previously demonstrated excellent oxygen control down to 0.05% by the gas control channels, independent of input fluid oxygenation and environment outside the chip, for flow rates ≤1 μL/min using simulations and integrated optical oxygen sensors (Chapter 4, [280]). Oxygen switching times of ~10 minutes were also measured and simulated in a similar device with 150 μm layer 1 height (vs. 276 μm here) [280]. The device is presented in Figure 5.6 (a,b).

The PDMS microfluidic device was degassed using the degassing procedure described in section 5.1.1.1 before use, to fill the channels with water and reduce the likelihood of bubble formation during the experiment. Before use, the cell culture channel was rinsed with 70% ethanol to reduce the likelihood of contamination before rinsing with sterile PBS and cell culture media.

The hydration channels were connected to syringes filled with PBS degassed by heating to 47°C and then desiccating and perfused at a rate of 0.5 μL/min for the course of the experiment.

Cell Culture: The results of three separate experiments will be presented in this section. In all three experiments, MCF-7 breast cancer tumour spheroids expressing the FUCCI cell cycle indicator [268] grown within microfluidically-generated alginate-collagen-Matrigel® beads [265] (as described in section 2.2 and section 5.2.1.1) were used. The cell-laden beads from two different batches were trapped on-chip various times (14 days, 21 days, 30 days) after bead formation using a process like that described in section 2.4.1 and section 5.2.1.1. Again, tubing was clamped while the fluid input was changed to degassed, completed DMEM/F-12-HAM cell culture media in order to reduce the potential for backflow, which could dislodge the beads.

The three gas control channels surrounding the cell culture channel were supplied with mixed gases with automatically switching oxygen levels using the system described in section 3.3, permitting spatiotemporal control of oxygen within the device. In three separate experiments, the spheroids were supplied with cycling oxygen profiles between 0%, 3%, and 10% oxygen at different intervals. The CO_2 was controlled to 5% during the extent of each experiment. The chip was immersed in PBS and maintained within a microscope stage-top incubator (Live Cell Instrument Chamlide) which controlled the temperature to 37°C. The spheroids were monitored by imaging with brightfield and fluorescence microscopy every 10 or 20 minutes using the automated imaging system described in section 3.3. Media and PBS briefly heated to 47°C and degassed in vacuum to reduce bubbles were perfused to the cell culture channel and hydration channels at a rate of 0.5 μL/min.

Imaging and Data Analysis: Brightfield and wide-field fluorescence microscopy images of the spheroids were acquired using a Nikon TE-2000-U microscope throughout the experiment. Brightfield and wide-field fluorescence were chosen for this long-term experiment instead of two-photon (2-P) imaging due to the availability of the microscope stage-top incubator system on the Nikon microscope (whereas temperature control is not available on the 2-P system). A Nikon Intensilight mercury arc excitation source and triple-band DAPI/FITC/TRITC RGB filter (Chroma 61000v2), with excitation bands centred near 400 nm, 483 nm, and 554 nm and

emission bands centred near 453 nm, 516 nm, and 605 nm, was used to observe the FUCCI fluorescence. Brightfield images of the spheroids were first registered (StackReg [321], ImageJ) to compensate for slight movements, and then analyzed using an intensity-thresholding and edge detection segmentation protocol implemented in MATLAB$^®$. Spheroid size was determined from the area of the segmented projected regions (outlined in white in Figure 5.6 (c)).
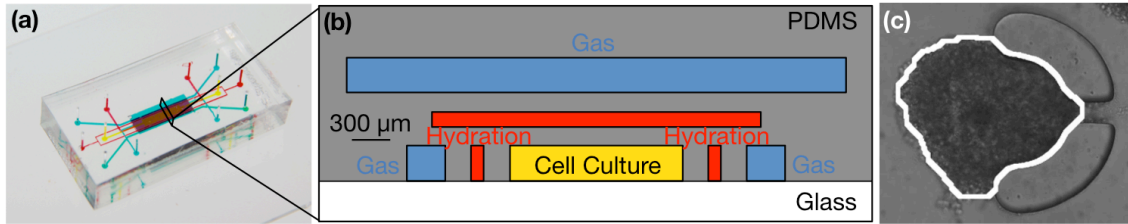
Figure 5.6. Experimental details for cyclic spheroid swelling observation. Photograph (a) and cross-section (b) of the oxygen control device. (c) segmented spheroid. Figure previously published in [322].

5.2.2.2 Results and Discussion

Figure 5.7 presents the effects of a cycling oxygen profile of 2 hours 0%, 6 hours 3%, and 4 hours 10% oxygen on a MCF-7 breast cancer cell spheroid. This spheroid was trapped on chip 30 days after bead formation, and so it was very large (approximately 400 μm in diameter) and no longer within its hydrogel bead at the beginning of the experiment.
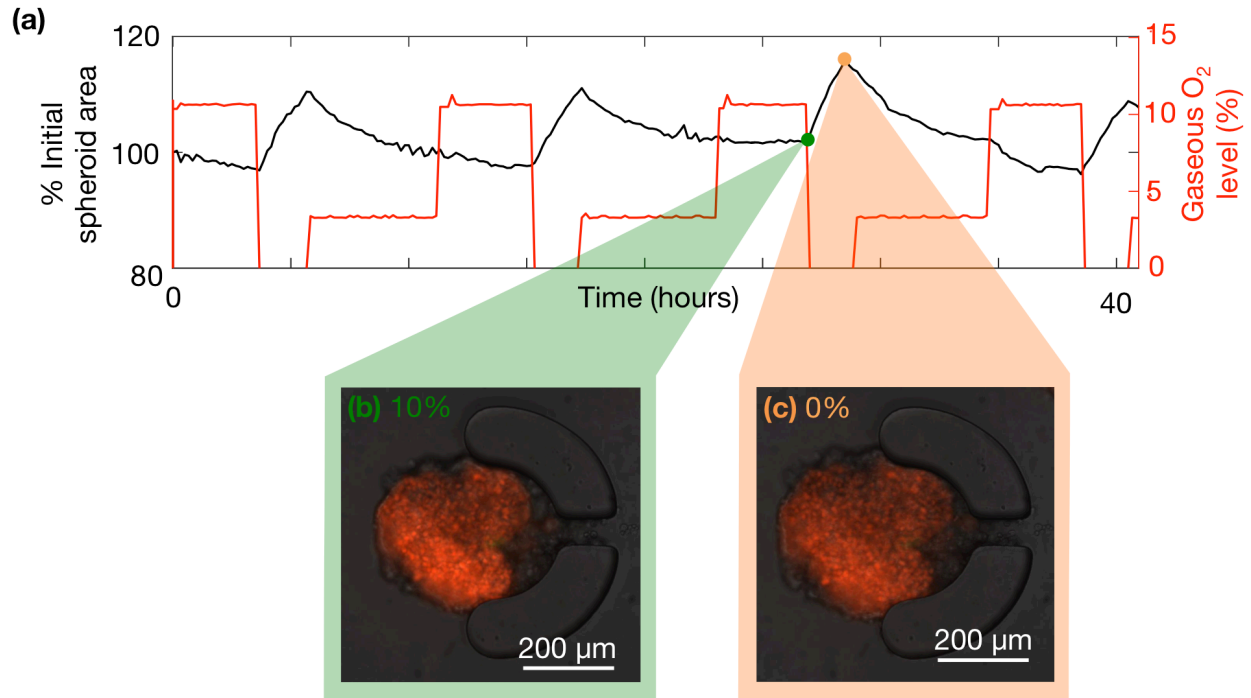
Figure 5.7. Reversible spheroid swelling behaviour in a spheroid 30 days after bead formation. **(a)** Spheroid size (% of initial segmented area 69 787 μm^2, black line) as well as gaseous oxygen level (red line) supplied to gas channels vs. time over ~40h. The spheroids tend to swell at 0% oxygen and shrink at 3% and 10%. **(b,c)** Fluorescence/brightfield overlay images at 10% and 0% oxygen (green, orange circles in (a)). The spheroid is larger and fluorescent nuclei farther apart in (c) than (b). Figure previously published in [322].

We observe spheroid cyclic swelling in time-lapse videos acquired of the chip: the spheroids increase in size during the 2-hour exposure to 0% oxygen, and then shrink again at 3% and 10%. FUCCI-expressing nuclei (orange in Figure 5.7 (b,c)) appear to move farther apart during the 0% exposure, and back together at 3% and 10%. This reversible spheroid swelling was observed to varying degrees in almost all spheroids trapped on chip over >5 experiments with different cycling rates. Figure 5.8 presents a similar plot for five separate spheroids within the same microfluidic device during the same experiment as that shown in Figure 5.7 (note that the spheroid in Figure 5.7 is spheroid 1 in Figure 5.8).

182
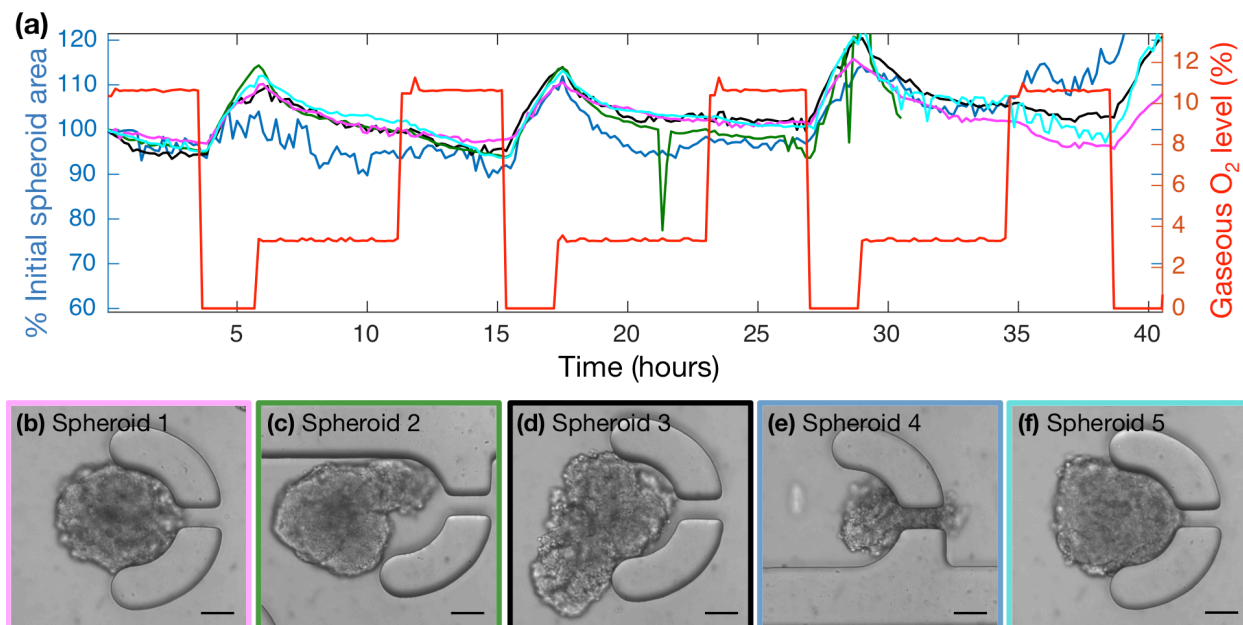
Figure 5.8. Reversible spheroid swelling in multiple spheroids 30 days after bead formation. **(a)** Spheroid size (magenta, green, black, blue, and cyan lines) as well as gaseous oxygen level (red line) supplied to gas channels vs. time over ~40h. Spheroid 1 was the same as that presented in **Figure 5.7**. All spheroids in this experiment tend to swell at 0% oxygen and shrink at 3% and 10%. **(b-f)** Brightfield images of the 5 spheroids analyzed at the beginning of the experiment. Image outline colours in (b-f) match the line colours in (a) for each spheroid. Scale bar represents 100 μm.

Figure 5.8 shows that the 5 spheroids within the same microfluidic device swell and shrink at a similar rate in response to the cycling oxygen profile. Some of the aberrations (such as the peak in spheroid 2's size plot at approximately t = 2450 minutes) are due to inaccuracies in the brightfield segmentation; however, overall the segmentation does a good job of reflecting the spheroid size changes observed in time-lapse videos of the spheroids.

A more detailed look at the cyclic spheroid swelling behaviour in a spheroid trapped on chip 21 days after hydrogel bead formation (and still within its hydrogel bead) is presented in Figure 5.9. This spheroid was exposed to a cycling oxygen profile of 3 hours at 0% oxygen followed by 6 hours at 10% oxygen. Figure 5.9 (a) again shows the segmented spheroid area increasing during exposure to 0% oxygen and decreasing during exposure to 10% oxygen, consistent with the results presented in Figure 5.7 and Figure 5.8. Figure 5.9 (b-f) show brightfield images of the spheroid, with the segmented area visible as a thin white line around the spheroid in each image. These brightfield images show the spheroid size increases and decreases during the experiment,

and that the segmentation follows the spheroid size change to a reasonable accuracy. The hydrogel shell does expand slightly with the swelling and shrinking spheroid (to a lesser degree than the spheroid itself), and from the time-lapse videos it appears to be being pushed outward by the swelling spheroid.
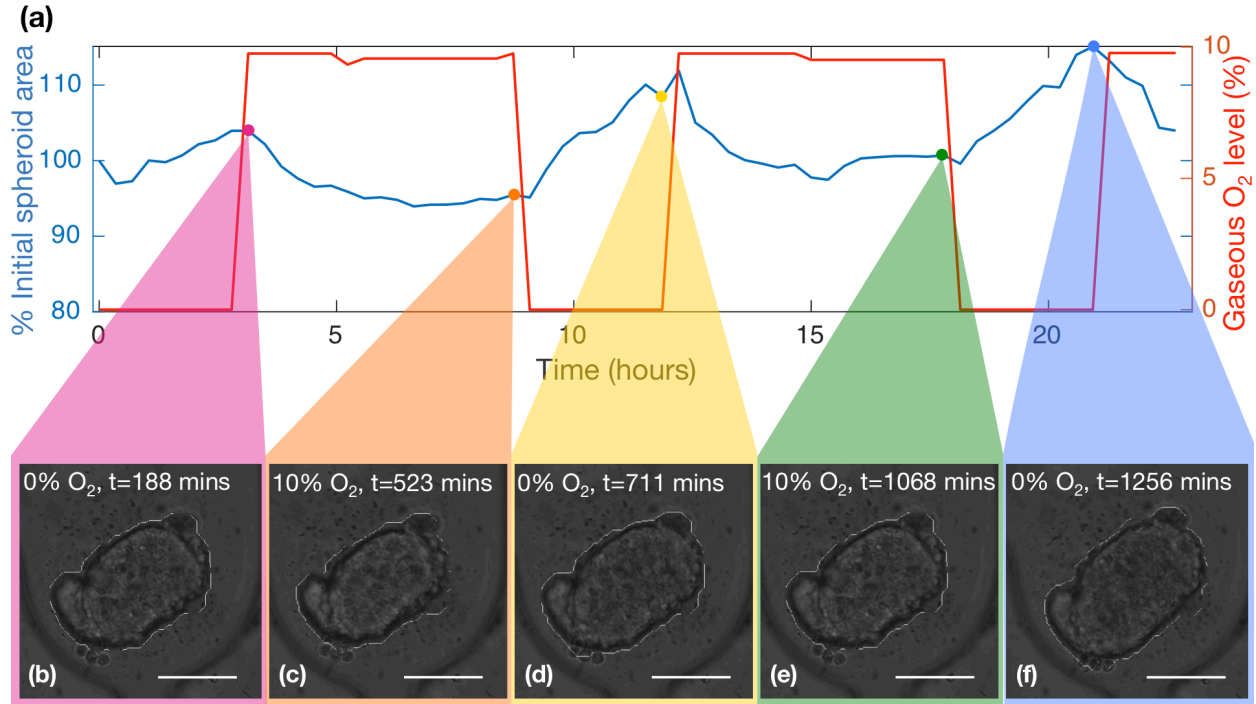
Figure 5.9. Reversible swelling in a spheroid 21 days after bead formation. **(a)** Spheroid size (blue line) as well as gaseous oxygen level (red line) supplied to gas channels vs. time over ~22 hours. **(b-f)** Brightfield images of the spheroid at various times during the experiment, showing the swelling effect as well as the segmentation result (thin white line). Coloured overlays depict the time on the plot of (a) at which each image was taken. Scale bars represent 100 μm.

In a third experiment, hydrogel beads containing smaller spheroids were trapped on chip 14 days after bead formation. The results of this experiment are presented in Figure 5.10. In this experiment the hydrogel shells did not appear to move with the swelling spheroids, potentially because the spheroids were relatively smaller in comparison to the hydrogel shell size than that depicted in Figure 5.9.
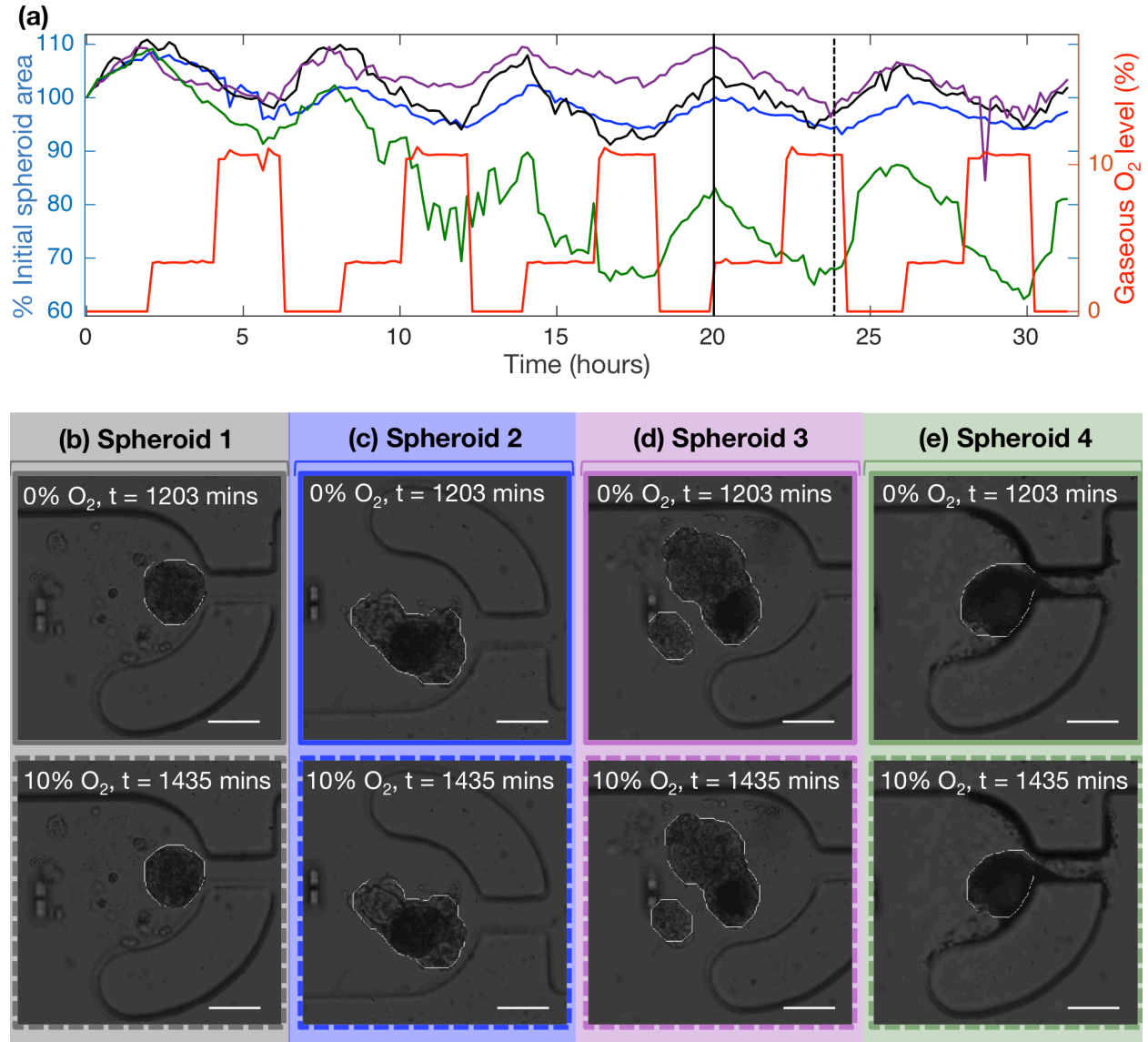
Figure 5.10. Reversible swelling in four spheroids trapped 14 days after bead formation. **(a)** Spheroid size (black, blue, purple, and green lines) as well as gaseous oxygen level (red line) supplied to gas channels vs. time over ~32 hours. **(b-e)** Brightfield images of the four different spheroids, each showing one image at the end of the 2-hour exposure to 0% oxygen (top) and showing one image at the end of the 2-hour exposure to 10% oxygen (bottom). 'Spheroid 3' was actually two separate spheroids within the same hydrogel bead; the spheroid area reported is the sum of the areas of the two spheroids. The swelling effect and the segmentation result (thin white line) are visible in each of these image sets. Coloured overlays and image outline colours for each spheroid match the line colours for the segmented area plotted in (a). Image outline line styles match the times indicated by the vertical black lines shown in (a) and indicate the time at which the images were taken. All spheroids are smaller in the bottom image than the top, showing the reversible swelling effect. Scale bars represent 100 μm.

Figure 5.10 (a) shows that again the spheroids increase in size when exposed to 0% oxygen, and decrease in size when exposed to 3% and 10%. Although the segmentation algorithm has trouble segmenting the spheroid outside of the hydrogel bead that is very close to the trapping structure

185

(spheroid 4 shown in Figure 5.10 (e)) during the beginning of the experiment, all four spheroids show this swelling effect.

The brightfield images shown in Figure 5.10 show the spheroids at two time points during the experiment: one at the end of their 2-hour exposure to 0% oxygen and one at the end of their 2-hour exposure to 10% oxygen. The time points at which the images were taken are indicated in Figure 5.10 (a) by the vertical black lines. The brightfield images again show a size change between the two time points for each spheroid, and the segmentation result (thin white line around each spheroid in the brightfield images) again gives a good indication of the spheroid size. Spheroid 4 appears to swell and shrink to a slightly greater degree than the other three spheroids; this could be in part due to the absence of the alginate shell around it, which could apply pressure to the cells [323] and reduce the magnitude of the swelling behaviour. Analyzing the swelling between t = 14 hours and t = 30 hours (three shrink-swell cycles) shows that the average swelling for the first three spheroids (within shells) is 9±4%, while that for spheroid 4 (outside of the shell) is 21±5% (errors represent one standard deviation of the area change from three shrink-swell cycles of three spheroids for the spheroids in shells and one spheroid for the spheroid outside of the shell).

The results of Figure 5.7-Figure 5.10 show that the MCF-7 spheroids tend to swell and shrink in size in response to changing oxygen levels, with 0% oxygen inducing swelling behaviour within one hour after the change in oxygen level. Different spheroids appear to exhibit the swelling behaviour to different degrees, with spheroid size and roundness (uniformity) having an effect on how readily the swelling can be observed in time-lapse videos. The presence of the alginate shell around the spheroids may also affect their swelling.

Although this interesting cyclic swelling behaviour has not, to our knowledge, been previously reported in the literature, there are known consequences of hypoxia that could lead to this effect. The increase in size in response to low oxygen is consistent with cytoplasmic swelling within the packed cells in the spheroid, which can occur as a result of failing ion pumps (due to inadequate adenosine triphosphate (ATP); the cell's reservoir of chemical energy) and subsequent loss of membrane function in hypoxia/anoxia [324]. Cytoplasmic swelling could also be mediated by

186

changes in the expression of aquaporins, which are water transport channel proteins in the cell membrane [325]. There is some evidence in the literature that aquaporin-1 expression may be correlated with hypoxia in tumour cells [326, 327], so staining for aquaporin under different hypoxic profiles could be an interesting avenue for future work.

Hypoxia can also stimulate migration of tumour cells [84]; an apparent increase in spheroid size could also be due to reduction of cell-cell adhesion within the spheroid as the cells start to break apart from each other. Skiles *et al.* have also reported regions of cytoplasmic swelling as well as loss of cellular cohesion (contacts) in fixed, sectioned spheroids grown at 1% and 2% oxygen for 4 days, which could also be consistent with our observed changes in spheroid size [328]. The loss of cellular cohesion observed by Skiles *et al.* could also be evidence of reduction of cell-cell adhesion, so the changes in spheroid size that we observe as reversible swelling behaviour could be due to cytoplasmic swelling, reduction of cell-cell adhesion, or both.

5.2.3   Two-Photon Microscopy Analysis of Reversible Swelling Behaviour

After observing the reversible swelling behaviour in spheroids exposed to cycling oxygen profiles presented in section 5.2.1, we wished to better understand the phenomena driving this effect. Specifically, we wished to determine whether the reversible spheroid swelling was driven by the swelling of individual cells within the spheroids, by migration of the individual cells within the spheroids, or by some other effect. To discern between these potential causes, we used high-resolution two-photon (2-P) microscopy, combined with a cell membrane stain, to track individual cells within the spheroids during a change in oxygen level. This section presents a summary of this experiment.

5.2.3.1   Methods

MCF-7 breast cancer tumour spheroids were grown in alginate/collagen/Matrigel® beads formed using the flow-focusing process described in section 2.2.2. The solution that formed the core of the beads was made up of 180 μL Matrigel®, 180 μL collagen I, and 140 μL 2% alginate solution in HBSS. A confluent T75 flask of MCF-7 cells was suspended in media after trypsinization, and 3/10 of this flask was centrifuged and resuspended in the core solution.

15 days after bead formation, the spheroids were rinsed twice in HBSS without calcium or magnesium in order to dissolve the alginate shell around the spheroids. The spheroids were then rinsed in serum-free media and resuspended in 1 mL of the same media in preparation for staining. 1 μL of CellMask™ Green plasma membrane stain solution (Thermo Fisher) was added to the spheroids in media, and the spheroids were incubated for 1.5h at 37°C. After staining, the spheroids were rinsed three times in serum-free media to remove excess stain.

The microfluidic oxygen control device described in Chapter 4 was bonded to a #1.5 glass cover slip (0.17 mm thickness) using a 75s air plasma exposure prior to bringing the PDMS and glass surfaces together. After leaving the bonded device in the oven at 65°C overnight to complete the bonding, the channels were filled with 70% ethanol and then ultrapure water and then the device was immersed in ultrapure water and desiccated for >60 minutes. The device was left in water overnight at 65°C, and subsequently brought down to ~45°C before desiccating again for >30 minutes. Ethanol and PBS were then flowed through the cell culture channel of the device to remove contamination. The spheroids, after staining, were loaded into the traps of the cell culture channel by syringe perfusion after the device was degassed. Un-trapped spheroids were rinsed away by flow of fresh serum-free DMEM/F-12-HAM media with 2.5 mM L-Glutamine and 1X anti-anti that had been heated to 50°C for 20 minutes and then desiccated for 30 minutes to degas. Throughout the experiment, the microfluidic device was perfused with this degassed serum-free media using a syringe pump. PBS was also degassed using the same process as the media for perfusion into the hydration channels of the microfluidic device. The device was loaded onto the Olympus FV1000 MPE BX61WI two-photon microscope system described in section 2.5.1.1.3 and imaged using an excitation wavelength of 810 nm and a 25X water-immersion objective (yielding diffraction-limited x-y and z-resolutions of $\omega_{xy} = 0.18$ μm and $\omega_z = 0.60$ μm, respectively, via equation 1). After the spheroids were imaged once, flow of nitrogen containing 5% carbon dioxide (with 0% oxygen) was started in the gas control channels, and the spheroids were monitored with two-photon microscopy for 8 hours. A 2 μm objective z-step slice spacing was used for z-stack acquisition.

In a separate experiment, the same spheroid staining and loading procedures were followed, but the gas channels were perfused with a mixture of air (21% oxygen) containing 5% carbon

dioxide (resulting in 20% oxygen) for 2 hours before switching to 0% oxygen. The purpose of this experiment was to test whether spheroid swelling effects were indeed due to the spheroids' hypoxic environment and not another part of the experimental setup during the two-photon measurements. For this experiment, some of the trapped beads still had their alginate shells, while others were removed, which enabled the visualization of the response of spheroids both in and out of the hydrogel beads. The same imaging parameters were used for this study as that described above. Unfortunately, at the start of this experiment the spheroids remained at room temperature for approximately 6 hours prior to the start of imaging due to system issues, which could have impacted their response. A limitation of the use of the two-photon system for these long-term experiments is its lack of temperature control like the stage-top incubator used for the other studies in this chapter.

To analyze the results of the two-photon imaging experiment, the two-photon z-stacks were first histogram-adjusted in ImageJ to ensure visibility of the membrane stain. The images acquired at the later time points in particular needed to be adjusted as the membrane stain had lost intensity over time, potentially due to photobleaching, leaching into solution, and internalization into the cells. Additionally, the membrane fluorescence of apparently swollen cells tended to be a lower intensity than that of non-swollen cells; the brightness was increased to ensure visibility of these cells. Scale bars were added to select images from the stacks, and the resulting images were exported using ImageJ. To visualize the z-stacks as 3-D renderings, histogram-adjusted TIFF z-stacks were exported using ImageJ and then visualized in 3-D using BioView3D [329].

5.2.3.2   Results and Discussion

Within one hour of starting the flow of nitrogen containing 5% CO_2, the spheroid began to visibly increase in size. Examining the two-photon slices showed that the cells within the spheroid had begun to swell. The cells at the free edge of the spheroid (not subject to pressure from the trapping structure) began to swell, protruding from that side of the spheroid. This effect is evident in the images from several time points of this experiment presented in Figure 5.11. The transmitted light differential interference contrast images depicted in Figure 5.11 (a-d) (providing information similar to that shown in the brightfield images analyzed in section 5.2.1) show the spheroid becoming larger and the edge boundaries becoming less uniform during its exposure to

0% oxygen. The corresponding two-photon slices visualizing the plasma membrane stain fluorescence (presented in Figure 5.11 (e-h)) show that the individual cells within the spheroid become visibly swollen over the course of the experiment. The cells at the right edge of the spheroid become larger over time, eventually breaking away from their contacts with the other cells and becoming near-perfect spheres at the spheroid edge.

Figure 5.11. Monitoring of tumour spheroid swelling under 0% oxygen using two-photon microscopy and lipid membrane staining. This spheroid was not within an alginate shell. **(a-d)** depict transmitted light differential interference contrast images of the spheroid in the microfluidic trapping structure at different times during the experiment: **(a)** prior to starting the flow of anoxic nitrogen gas including 5% CO_2, **(b)** after 1h of anoxic flow, **(c)** after 2.5h of anoxic flow, **(d)** after 5.25h of anoxic flow. **(e-h)** depict two photon fluorescence images of the CellMask™ Green plasma membrane stain, showing a slice approximately 50 μm into the 150 μm initial diameter spheroid, again at different time points corresponding to those in (a-d). Images have been brightness and contrast adjusted to ensure visibility in print, with the images acquired later in the experiment brightened to a greater degree due to reduction of the membrane stain fluorescence during the experiment. **(i-k)** depict 3-D renderings of the two-photon image stacks: **(i)** prior to starting the flow of the anoxic nitrogen plus 5% CO_2, **(j)** after 2.5h of anoxic flow, and **(k)** after 5.25h of anoxic flow. All three 3-D renderings are depicted as viewed from the same angle. It is evident in all three sets of images that over time after the anoxic flow was started, the cells within the spheroid (particularly those near the edges not in contact with the trapping structure) begin to swell. The cells at the edge of the spheroid become very swollen over time, and the spheroid as visualized in the 3-D renderings start to look larger as well as less well-packed. All scale bars represent 50 μm.

The 3-D renderings of the two-photon z-stack (depicted in in Figure 5.11 (i-k)) show that the smooth-edged packing of the cells in the spheroid at the beginning of the experiment gives way to a rougher appearance over time as the cells become less packed and the spheroid increases in size. The spheroid becomes visibly larger over time, and the swollen cells at the spheroid edges are clearly visible. All three 3-D renderings are depicted as viewed from the same angle.

The results presented in Figure 5.11 suggest that cytoplasmic swelling is the dominant effect driving the reversible spheroid swelling behaviour detailed in section 5.2.2. Individual cells within the spheroid appear to be swelling over time when exposed to 0% oxygen within the microfluidic device. It is also possible that hypoxia-induced cytoplasmic swelling could be the cause of the changes in brightfield image contrast of the cell boundaries observed in the monolayer study of section 5.1.1.2.

The results of the second experiment, wherein the gas control channels were first perfused with air containing 5% CO_2 (~20% oxygen) as a control and subsequently perfused with the nitrogen containing 5% CO_2 (0% oxygen), are depicted in Figure 5.12. The spheroid did not appear to swell during the 1.5h exposure to 20%, suggesting that the spheroid swelling observed in Figure 5.11 could be due to the effects of the hypoxic exposure. Less spheroid swelling was observed in this experiment once the anoxic flow was started, and the swelling appeared slower than in the previous experiment (Figure 5.11). After 1.5h of anoxic flow, only minimal if any spheroid and cellular swelling was visible, and although the spheroid had visibly swelled after 7.5h of anoxic exposure, the cells at the spheroid edges had not become as round and detached as those after 5.5h of exposure in the previous experiment. We believe that the difference between these experiments could be due to the spheroids' exposure to room temperature for several hours before beginning imaging in this second experiment, due to system issues. This exposure to room temperature is also potentially problematic because there is also evidence that hypothermia can lead to similar effects as hypoxia, including cellular swelling [330]. The fact that significant swelling is not visible at the start of imaging or after 1.5h of exposure to 20% oxygen, and the consistency between the brightfield images of section 5.2.1 (which were acquired with temperature control) and the transmitted light images of Figure 5.11, suggests that the observed

191

swelling is in fact a result of the hypoxic exposure; however, further experiments (ideally with temperature control) will be necessary for a conclusive understanding.
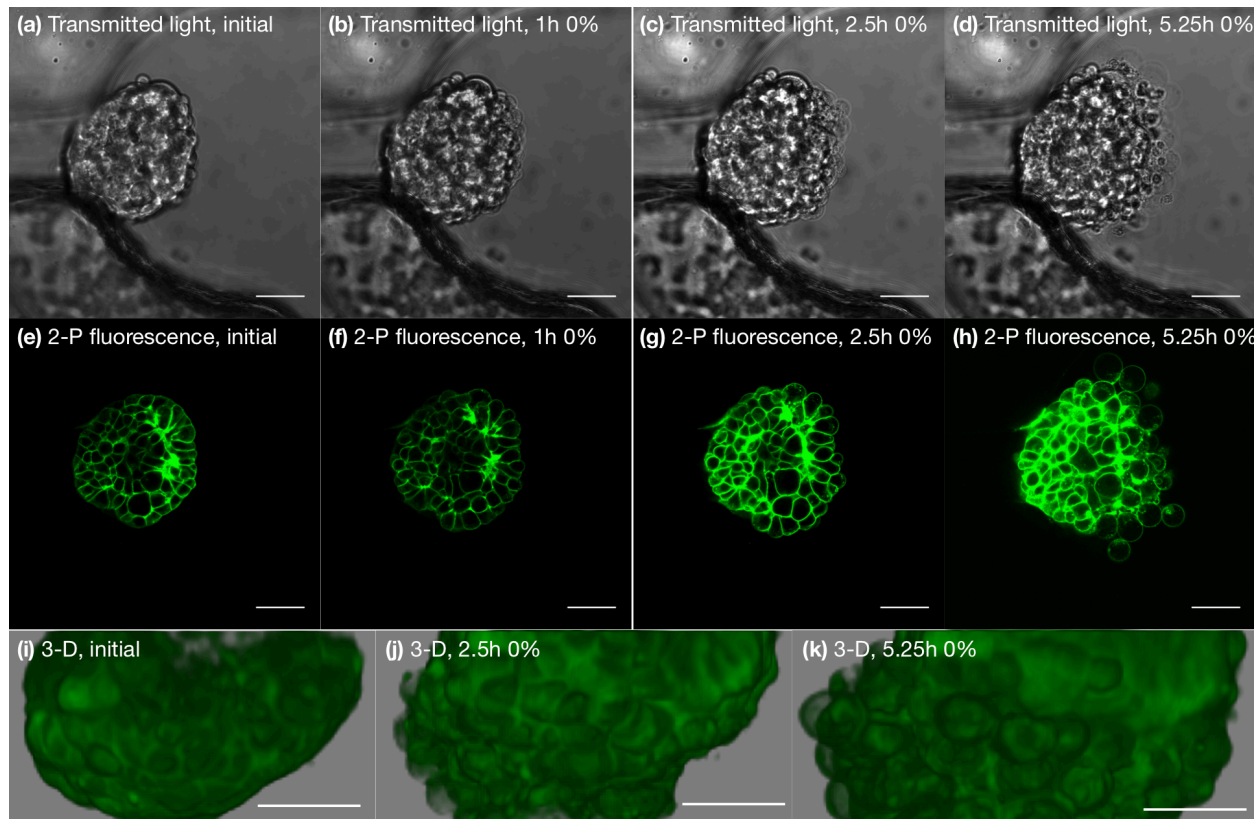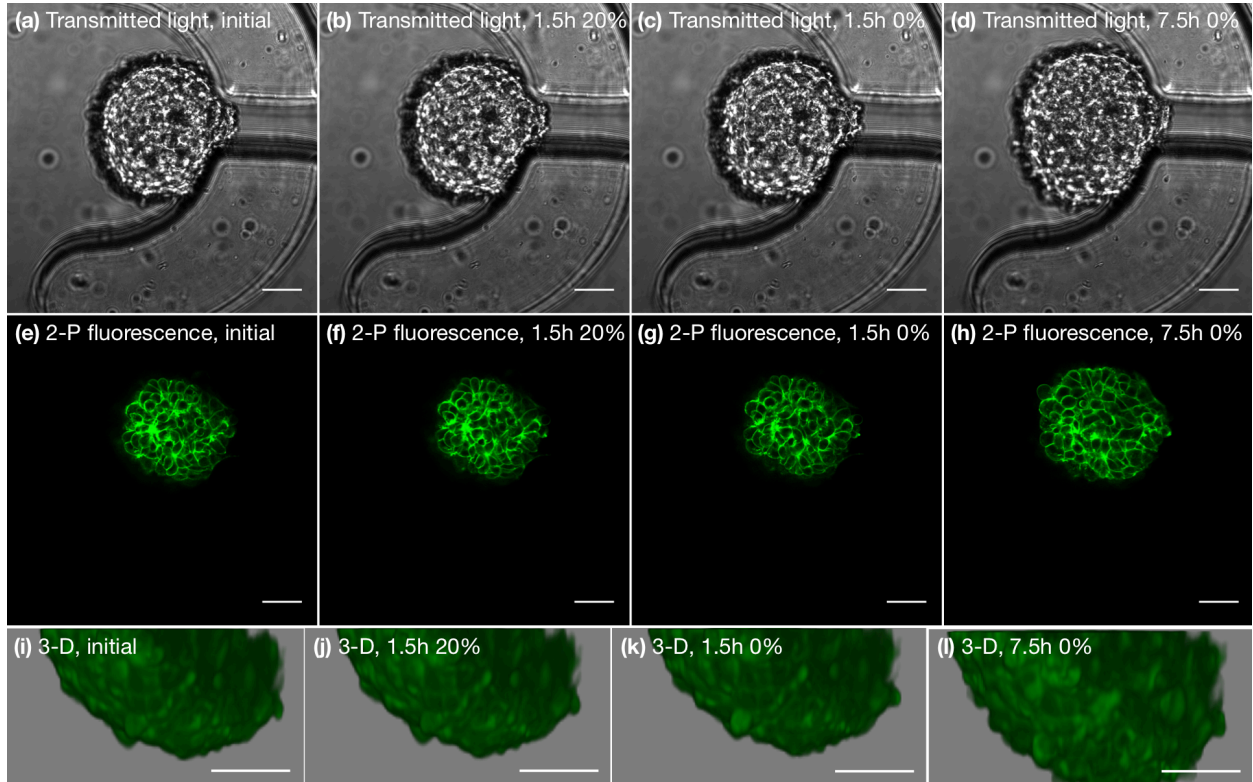

Figure 5.12. Monitoring of spheroid swelling under 20% and 0% oxygen using two-photon microscopy and membrane staining. This spheroid was not within an alginate shell. **(a-d)** depict transmitted light differential interference contrast images of the spheroid in the microfluidic trapping structure at different times during the experiment: **(a)** prior to starting the flow of anoxic nitrogen gas including 5% CO_2, **(b)** after 1.5h of air containing 5% CO_2 (20% oxygen), **(c)** after 1.5h of anoxic flow, **(d)** after 7.5h of anoxic flow. **(e-h)** depict two photon fluorescence images of the CellMask™ Green plasma membrane stain, showing a slice approximately 60 μm into the 180 μm initial diameter spheroid, again at different time points corresponding to those in (a-d). Images have been brightness and contrast adjusted to ensure visibility in print, with the images acquired later in the experiment brightened to a greater degree due to reduction of the membrane stain fluorescence during the experiment. **(i-l)** depict 3-D renderings of the two-photon image stacks: **(i)** prior to starting the on-chip gas flow, **(j)** after 1.5h of 20% oxygen flow, **(k)** after 1.5h of anoxic flow, and **(l)** after 7.5h of anoxic flow. Some swelling is apparent in these images, with the spheroid appearing to increase in size and individual cells appearing swollen after 7.5h of anoxic flow. No swelling is evident during the flow of 20% oxygen; however, only slight if any swelling is visible after 1.5h of anoxic flow in this experiment. All scale bars represent 50 μm.

At the start of the second experiment, we loaded some spheroids that still retained their alginate shells and other spheroids which no longer had alginate shells. The spheroid depicted in Figure 5.12 did not have an alginate shell, while the one depicted in Figure 5.13 does still have the shell (visible in the transmitted light images (a-d)). Although a small amount of swelling is visible after 7 hours of anoxic flow, the swelling is not nearly as apparent as that in Figure 5.11 or

Figure 5.12. We believe that this lessened swelling behaviour could be due to the small amount of pressure exerted on the spheroid by the alginate shell, which could simulate intratumoural pressure *in vivo*.
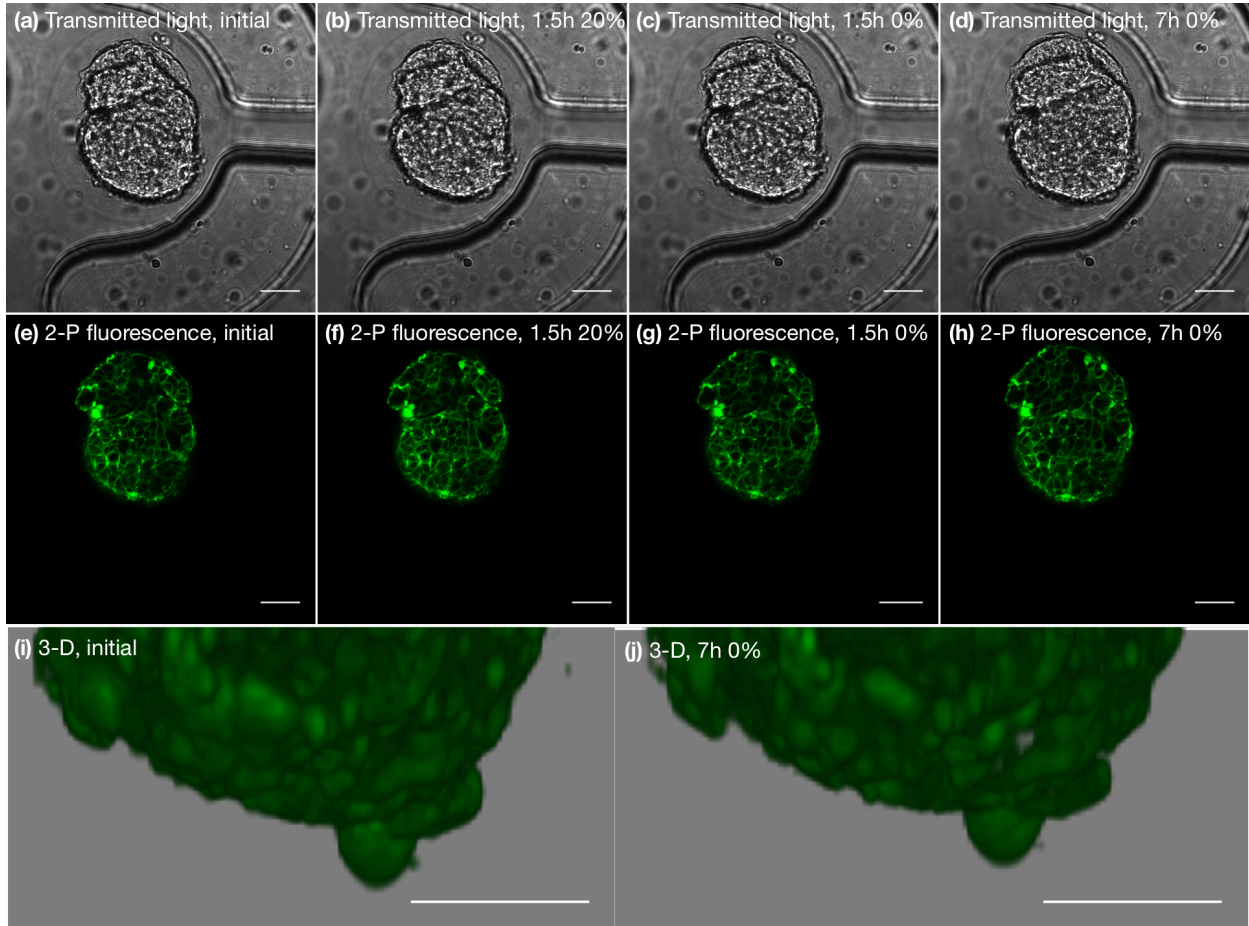
Figure 5.13. Monitoring of spheroid swelling within an alginate bead under 20% and 0% oxygen using two-photon microscopy and membrane staining. This spheroid was within an alginate shell. **(a-d)** depict transmitted light differential interference contrast images of the spheroid in the microfluidic trapping structure at different times during the experiment: **(a)** prior to starting the flow of anoxic nitrogen gas including 5% CO_2, **(b)** after 1.5h of air containing 5% CO_2 (20% oxygen), **(c)** after 1.5h of anoxic flow, **(d)** after 7.5h of anoxic flow. **(e-h)** depict two photon fluorescence images of the CellMask™ Green plasma membrane stain, showing a slice approximately 60 µm into the 180 µm initial diameter spheroid, again at different time points corresponding to those in (a-d). Images have been brightness and contrast adjusted to ensure visibility in print, with the images acquired later in the experiment brightened to a greater degree due to reduction of the membrane stain fluorescence during the experiment. **(i-j)** depict 3-D renderings of the two-photon image stacks: **(i)** prior to starting the on-chip gas flow, **(j)** after 7h of anoxic flow. The spheroid within the alginate shell does not swell as noticeably as that without.

5.2.4   Effects of Doxorubicin on Tumour Spheroids under Varying Oxygen Conditions

Building upon the 2-D monolayer experiments presented in section 5.1.2, the effects of a 1 µM doxorubicin treatment on parental MCF-7 spheroids under varying oxygen conditions was

studied. The purpose of this experiment was to serve a preliminary evaluation of whether drug-screening studies were compatible with 3-D culture within the microfluidic system, as well as to identify existing challenges and directions for future work.

5.2.4.1 Experimental

Cell Culture Device Preparation: The microfluidic cell culture and oxygen control device described in section 4.2 with hydration and gas control channels, and a cell culture channel height of approximately 300 μm was used for this study. Six multilayer microfluidic devices without oxygen sensors were fabricated using the fabrication process described in section 4.4.1, and bonded to the same glass coverslip and connected to inlets and outlets as described in section 5.1.2.1.2. The chips were prepared as described for the monolayer experiment of section 5.1.2.1.2, with the exception of the collagen treatment as cell attachment was not necessary for the 3-D study.

Microfluidic Bead Loading and Cell Culture: Cell-laden beads were produced using parental MCF-7 cells as described in section 5.2.1 and cultured in cell culture flasks for 16 days prior to loading into the microfluidic devices. The beads were loaded and chips rinsed with conditioned cell culture media (in this case a 1:1 mixture of fresh and used completed DMEM/F-12-HAM that had been used in bead culture for 6 days) as described in section 5.2.1, and bead culture under different oxygen profiles was immediately begun. Degassed PBS was flowed through the hydration channels of all devices at 0.5 μL/min for the extent of the experiment.

Two microfluidic devices were perfused with air containing 5% CO_2, two microfluidic devices were perfused with 0.1% oxygen with 5% CO_2, one device was perfused with a cycling gas profile of 3 hours at 0% oxygen followed by 1 hour at 10% oxygen, both with 5% CO_2, and one device was perfused with 1% oxygen with 5% CO_2. Beads were cultured on chip for 20 hours under the different oxygen conditions prior to introducing the drug.

Drug Treatment: 1 μM doxorubicin was used as the drug treatment concentration, and 3 mL of drug and control solutions in completed DMEM/F-12-HAM were prepared, degassed, and connected to the microfluidic system as described in section 5.1.2.1.2. Throughout the three-day

194

treatment process, two stage locations per device were imaged with low-intensity brightfield illumination every 30 minutes to monitor the cells' response to the drug.

Viability Staining and Data Analysis: As described in section 5.2.1.1, the cells in all six microfluidic devices were stained for viability at the end of the 3-day treatment using a solution of 10 µM Live/Dead® stain (Thermo Fisher Scientific) in Hank's Balanced Salt Solution (HBSS) containing calcium and magnesium. The spheroids were then imaged using brightfield, fluorescence, and confocal fluorescence microscopy as described in section 5.2.1.1.

5.2.4.2   Results and Discussion

The viability-stained images of the spheroids showed no obvious difference between any of the test conditions (oxygen level or presence of drug). Brightfield/wide-field fluorescence overlay and confocal z-intensity projection images of representative spheroids from each test condition are presented in Figure 5.14. Difference in green stain colour between the two sets of images is due to the presence of the blue channel in the RGB filter used in wide-field fluorescence, as Calcein emits in both the green and blue channels. Although both live (green) and dead (red) cells are visible in all test cases, there does not appear to be a significant decrease in viability induced by the doxorubicin treatment, even though the same doxorubicin concentration (1 µM) did decrease the viability of monolayer cultures within the same microfluidic system (section 5.1.2). Multicellular resistance can reduce sensitivity to drugs such as doxorubicin, as discussed in section 2.2; as such, it is likely possible that a higher concentration of doxorubicin will be required to differentiate between the effects of the drug on spheroids within different oxygen conditions.
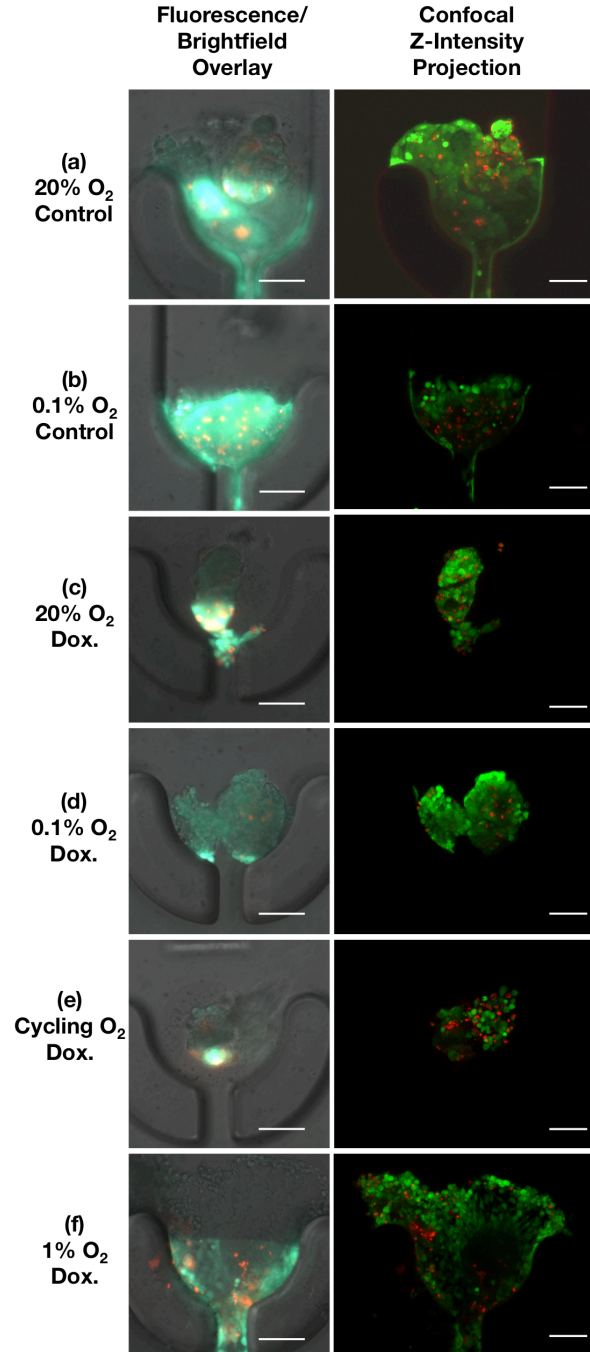
Figure 5.14. Effect of 1 μM doxorubicin treatment on viability of tumour spheroids under varying oxygen conditions. **(a)** 20% oxygen vehicle control, **(b)** 0.1% oxygen vehicle control, **(c)** 20% oxygen with 1 μM doxorubicin, **(d)** 0.1% oxygen with 1 μM doxorubicin, **(e)** cycling oxygen (3 hours at 0% oxygen and 1 hour at 10% oxygen) with 1 μM doxorubicin, **(f)** 1% oxygen with 1 μM doxorubicin. All gas test conditions contained 5% CO_2. For each case, a wide-field fluorescence/brightfield overlay image and a confocal z-intensity projection image are shown. Green staining (Calcein) indicates live cells, while red staining (EthD-1) indicates dead cells. No obvious difference is visible between test groups. Scale bars represent 100 μm.

To test this assertion, we ran an off-chip study (conducted by Mr. S. Soroush Nasseri in collaboration with the author) to observe the effects of a three-day treatment at various doxorubicin concentrations on the viability of cells in monolayer and 3-D culture within standard normoxic polystyrene well plate culture. This experiment (summarized in Figure 5.15) showed that at the 1 μM concentration used in the on-chip study, the monolayer cells had responded by detaching from the substrate and more dead cells were visible in comparison with the control, while the spheroid viability at the 1 μM concentration did not appear significantly different from that of the control.
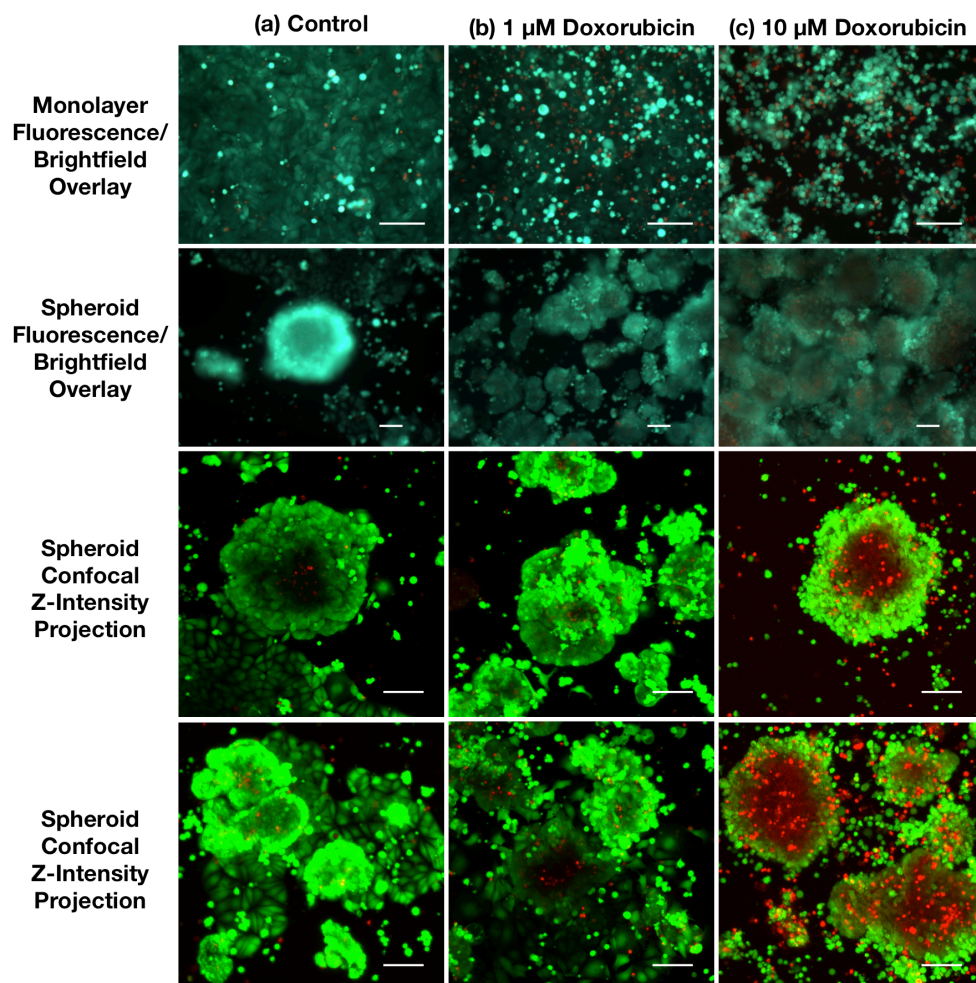
Figure 5.15. Off-chip, normoxic (20% oxygen) experiment comparing monolayer and spheroid viability in response to doxorubicin treatment. Wide-field fluorescence images are shown of the live/dead staining of a 2-D monolayer and a 3-D spheroid, and confocal z-intensity projection images are shown of two representative spheroids for each of **(a)** the vehicle control (no drug), **(b)** 1 μM doxorubicin, **(c)** 10 μM doxorubicin. In all images, green staining indicates live cells (Calcein), while red staining indicates dead cells (EthD-1). Scale bars represent 100 μm.

197

At 10 μM doxorubicin, the spheroid viability appeared to have dropped, with the cells in the interior of the spheroids appearing to be less viable than those in the periphery. There does, however, appear to be a Calcein-AM stain penetration problem that could be accentuating this effect, as the centres of some of the larger control spheroids also appear dark.

The results of the off-chip study of Figure 5.15 support the findings presented in Figure 5.14, as multicellular resistance appears to be decreasing the sensitivity of the cells to 1 μM doxorubicin, which is consistent with the observation of no obvious difference between the viability of treated and untreated spheroids on chip. In future work, higher doxorubicin concentrations such as 10 μM will be used for spheroid studies, so that differences in the sensitivity to doxorubicin that could potentially be introduced by different oxygen conditions can be characterized.

5.3   Summary

This chapter has presented several proof-of-concept biological studies demonstrating the utility of the microfluidic platform detailed in Chapters 2-4. We have demonstrated both 2-D and 3-D cell culture within the microfluidic device with oxygen control and observed a correlation between oxygen levels and GFP fluorescence intensity within MCF-7-GFP-LC3 cells. In exposing tumour spheroids to cycling oxygen profiles, we have observed a new reversible swelling phenomenon in response to the changing oxygen levels, with spheroids increasing in size at 0% oxygen and decreasing at 3% and 10%. Although there is evidence in the literature that could explain this behaviour, we believe that we are the first to observe it dynamically, and the unique capabilities of the oxygen control platform described in this thesis facilitated this observation. Finally, we have demonstrated a preliminary experiment showing that drug screening studies may be carried out within this platform to study the effects of various oxygen profiles on drug efficacy. These studies, using image-based quantification of viability due to its potential to report spatial variations within spheroids as well as its ease-of-use in the microfluidic system, present a proof-of-concept of the microfluidic system for drug screening applications. Future work could include recovering spheroids form the microfluidic devices after drug treatment to study other metrics of drug response (potentially using other viability assays or colony-forming assays) to validate and complement the image-based results.

Chapter 6 Conclusion

6.1 Contributions

This thesis has demonstrated significant steps towards a platform to study tumour cell and tumour spheroid response to chronic and cycling hypoxia. Over the course of this work, I have made the following 6 major contributions:

1. I have developed a device for 2-D and 3-D cell culture and monitoring, suitable for multi-day long-term cultures and optimized for the study of tumour cells and tumour spheroids. We have also made progress towards improving the analysis of data from 3-D cell cultures, which is crucial to future studies in which these 3-D cultures are exposed to hypoxic profiles to study the effects of hypoxia on tumour cell behaviour and response to treatment. We have developed novel imaging protocols as well as on-chip tissue clearing processes to increase the depths into spheroids that can be imaged and improve intensity uniformity in the resulting image stacks. The microfluidic devices developed as a part of this work allowed us to monitor both the spheroid growth and the progress of the tissue clearing processes, observing for the first time dynamic changes in tissue size in response to clearing reagents.

2. I have developed a novel microfluidic oxygen control device with integrated ratiometric oxygen sensors suitable for long-term cell culture applications. With both finite-element modeling and experimental data from the integrated sensors I have shown that the complete device permits excellent control of the oxygen levels in a chamber designed for cell culture, independent of the environmental oxygenation outside the chip, down to 0.05%.

3. I have demonstrated the creation of spatially- and temporally-varying oxygen levels inside the microfluidic device, mimicking the oxygen profiles found inside breast tumours. I studied the effects of oxygenated media flow rates on the simulated and measured oxygen profiles, and found an operating regime for the device (flow rates of 0.5-1 µL/min) wherein the oxygen levels in the cell culture channel after the entrance length are independent of flow rate or oxygenation of the flowing media. The device showed an oxygen equilibration time of less than 10 minutes (with excellent agreement between modeled and measured equilibration times), permitting the creation of complex time-varying oxygen profiles with switching times on biologically-relevant timescales of a few cycles/hour.

4. I have developed two novel fabrication processes for optical oxygen sensors to be integrated into the oxygen control device. Both processes are maskless and applicable to rapid-prototyping applications. I have also characterized the robustness and suitability of the sensors for long-term studies, demonstrating fluidic experiments lasting up to 31 hours, with individual chips and sensors in use for several days during multiple experiments. Long-term experiments with oxygen monitoring require good sensor stability over long periods of time with repeated measurements; I have demonstrated how sensor stability can be improved by using ratiometric (instead of intensity-only) sensors, as well as by pre-photobleaching the sensors and by using a microscope shutter to limit excitation exposure of the dye.

5. The microfluidic platform has allowed us to observe and monitor a reversible spheroid swelling phenomenon that had not been previously reported, in which tumour spheroids increase in size when exposed to low oxygen levels, and then decrease in size again when exposed to higher oxygen levels. Similar to how our microfluidic device allowed us to monitor dynamic spheroid changes in response to tissue clearing in Chapter 2, it also facilitated the observation of reversible spheroid swelling in response to changing oxygen levels, for the first time. Using staining of the cell membrane and two-photon microscopy, we found that this swelling phenomenon appears to be predominantly caused by cytoplasmic swelling of the cells within the spheroid in response to hypoxia. Using our system, we also observed changes in cellular GFP fluorescence in response to changing oxygen levels consistent with those previously reported in the literature.

6. We have conducted a preliminary evaluation of the feasibility of drug screening tests on 2-D and 3-D cell cultures using the microfluidic system and found the microfluidic device to be compatible with studies examining the effects of doxorubicin, a commonly-used cancer treatment, on the viability of breast tumour cells. Although this study is very preliminary, it opens the door for future drug screening studies using this platform.

6.2   Conclusions and Future Work

This thesis presents a platform that is able to expose 2-D and 3-D cell cultures to a variety of chronic and transient oxygen profiles as well as monitor and study their response. The platform has the potential for wide utility in the study of biological systems; however several limitations

to the system remain. Building upon the work presented in this thesis, this section outlines both the limitations to the current work and suggestions for potential avenues for future work.

6.2.1   Challenges Remaining

This thesis has presented several major contributions towards the study of tumour cells and tumour spheroids under varying automated hypoxic profiles; however, challenges remain to be addressed in order to improve the system's utility for drug screening applications. The analysis of the data from 3-D image stacks remains a chief limitation to the use of 3-D spheroids for drug screening studies. Segmentation algorithms to count live and dead cells as well as quantify other characteristics such as autophagosomes, cell size, shape, or protein expression would greatly improve ease of analysis. Furthermore, the penetration of some stains (such as Calcein-AM) into spheroids limits the data that can be acquired from the spheroid centres; improved staining protocols may be necessary to acquire data from these regions, in addition to the imaging protocols investigated as a part of this work.

Additionally, although we did not observe doxorubicin adsorption or absorption by the PDMS device during our proof-of-concept drug studies, the possibility remains for PDMS to interact with other cancer drugs or analytes and deplete them from the solution. If such issues are observed, strategies such as employing thin coatings (such as Teflon or polystyrene) on the PDMS channel surfaces, or modifying the fluid flow rate (and gas control design if necessary to maintain control over the new flow rate) could be employed to address them.

Finally, additional improvements to the modelling and the system could improve the degree of control provided by the system. Taking the cellular consumption of oxygen into account in the finite-element modelling could provide additional information as to the oxygen levels within the cell culture channel as well as within spheroids, and improving the automated gas control system to mix gases to a higher precision could improve its utility for cell-based studies at low oxygen levels (for which premixed cylinders were used in this work). Finally, small fluctuations in atmospheric pressure as well as the pressures in the microfluidic channels were not taken into account in this work. Although these fluctuations should influence the oxygen partial pressure by less than 5% of its value (e.g. the error induced on a pO_2 value of 1% of 1 atm would be

0.05% of 1 atm, and that on 0.1% of 1 atm would be 0.005% of 1 atm), accounting for them in the model and measurement would further improve the precision of oxygen control in this system.

6.2.2 Future Studies Investigating the Effects of Oxygen on Cell Behaviour

The platform presented in this thesis opens the door to a great many future studies involving cells exposed to different oxygen profiles. One logical avenue for future work is further study of the spheroid swelling behaviour. Further experiments using membrane staining and two-photon microscopy with temperature control could facilitate a longer-term study of this behaviour, as well as perhaps a quantitative comparison of spheroid size change and cell size change. Automated segmentation algorithms could facilitate this study. Additionally, it may be interesting to study the mechanism of this cyclic swelling behaviour, perhaps by monitoring ATP or pH. Hypoxia-induced swelling in single glioblastoma cells has been very recently found to result in increased swelling-activated chloride currents, which contribute to cell volume regulation and survival and could present a therapeutic target [331]; our observation of spheroid shrinkage after the periods of hypoxia could be consistent with this volume regulation, so it may be interesting to use the patch-clamp technique to determine whether hypoxia-induced swelling activates swelling-activated chloride channels in MCF-7 cells. It may also be useful to investigate the effects of an inhibitor of swelling-activated chloride currents such as verapamil (which has been found to inhibit swelling-activated chloride currents in MCF-7 cells in response to hypotonic solutions [332]) on the reversible spheroid swelling behaviour. If swelling-activated chloride currents are involved in the spheroid shrinkage after hypoxic swelling, their inhibition could change the reversibility of the cyclic swelling behaviour (perhaps the magnitude of the spheroid shrinkage during exposure to higher oxygen levels could decrease, or the magnitude of the subsequent swelling cycles could increase).

Building upon the work on reversible spheroid swelling, different cell types could be studied to observe differences in their swelling or migration behaviour (perhaps comparing the luminal-type MCF-7 cells with a more invasive basal B cell line such as MDA-MB-231 [333]). Other properties of the spheroids such as cell-cell junctions could also be monitored (perhaps using cadherin staining or by transmission electron microscopy on fixed, sectioned, recovered

spheroids [334]) during reversible swelling under cycling oxygen. It would also be interesting to study the effect of different alginate shell stiffnesses on the reversible swelling behaviour, as these alginate shells could simulate intratumoural pressure [323], which exists in the body. The effects of different collagen or Matrigel® concentrations, or drugs, on the swelling behaviour could be studied as well. It could also be interesting to study the effect of the reversible swelling behaviour on drug penetration into the spheroid, as the swelling could cause the packing density of the cells in the spheroid to decrease, potentially changing the mass transport characteristics of drug penetration.

Other metrics, such as cell proliferation and migration within varying 3-D gel scaffolds, could be studied under different oxygen profiles, and the perfusion media could be collected and analyzed to study cellular secretions under different oxygen conditions. As mentioned in section 5.2.2.2, staining for aquaporin expression on the cell membranes under different hypoxic profiles could help to further understand the reversible spheroid swelling effect. Cellular remodelling of collagen within the 3-D culture environment could be studied to determine whether oxygen availability affects this behaviour. It may also be interesting to create co-cultures of different cell types and monitor the effects of changing oxygen profiles on the different cells and their interactions. Integration of microvasculature into the platform could also be a fascinating avenue for future work, as the influence of hypoxic profiles, 3-D culture matrices, and different cell types could all be studied. The platform is also not limited to studying tumour cells; other oxygen-dependent studies could also be investigated. The differentiation of stem cells, or behaviour of corneal cells or brain cells that might be exposed to events resulting in changes in oxygen level, could also be studied in similar platforms.

6.2.3 Future Studies Investigating the Effects of Hypoxic Profiles on Cancer Treatment Efficacy

One of the next steps will be to apply the platform to screening cancer treatments on 3-D cell cultures under different oxygen conditions with tissue clearing at the study endpoint. We have presented a proof of concept drug screening study using doxorubicin, which is a well-studied cancer treatment. In addition to continuing to investigate well-studied drugs, the platform could be applied in the future to study new cancer treatments. Tissue clearing along with optical

sectioning microscopy and image processing techniques could permit quantitative analysis of viability at the study endpoint. The system could be used to compare treatment efficacy on 2-D and 3-D cell cultures under different oxygen conditions, and determine the effect that cycling hypoxia has on the efficacy of various treatments. The penetration of cancer drugs, or of drug-containing lipid nanoparticle formulations, could also be studied under various oxygen conditions using microscopy. Additionally, the platform could be applied to high-content screening applications while screening under various oxygen conditions.

It could be beneficial to compare various viability staining protocols to find one that has (1) good stain penetration into spheroids, (2) easily quantifiable results (ideally by automated image segmentation), (3) fluorescence spectra that could be combined with other fluorophores (like lipophilic carbocyanine dyes that can be used in lipid nanoparticles) and fluorescent proteins that could be of interest, and (4) fixable properties, so that the viability staining could be analyzed after fixation and tissue clearing. It would also be potentially valuable to recover the spheroids and cells after drug testing experiments for use in other types of assays to validate and complement the image-based analysis used in this thesis. For example, colony-forming assays could be run on the recovered cells to compare with results of similar assays in the literature.

6.2.4 Improvements to Non-Microfluidic Platform Components

The limitation to the precision of the oxygen control is currently imposed by the gas supply system (section 3.3), which has a mixing precision of approximately 0.5%. Moving to more precise gas flow meters and more precise reference sensors, along with potential improvements to the software, could improve this precision. In the meantime, the system can also be used to switch between premixed gas cylinders purchased from gas supply companies such as Praxair. The other potential limitation is our use of syringe pumps to provide fluid flow in this work. Although we have not observed issues in our characterization of the oxygen control device, fluid flow provided by syringe pump is known to be pulsatile. Because of the known flow rate dependence of the oxygen control within this device, pulsatile flow has the potential to cause disturbances to the oxygen levels within the microfluidic cell culture area. Moving to alternative fluid flow sources such as pulseless syringe pumps or pressure-driven flow could reduce this effect if it proves problematic in future studies.

6.2.5 Additional Oxygen Control Modeling

Modeling the oxygen consumption of cells within the microfluidic platform would shed insight onto the oxygen gradients that may be present within tumour spheroids in the microfluidic system. The consumption of both monolayers and tumour spheroids could be modeled based on published data [62, 63, 251] or by conducting measurements using integrated oxygen sensors, and this could lead to an even further improved understanding of the oxygen conditions existing within the microfluidic device.

6.2.6 Adaptations to the Oxygen Control Device

The microfluidic oxygen control system could be optimized for future cell-based assays. These types of assays can require many experimental conditions and replicates, so the oxygen control device could be tailored for specific applications in order to better-suit these studies. For example, if spatial oxygen gradients were not required, the three gas control channels and two hydration channels of the current form of the device could be connected to reduce the required tubing inputs to the system. Additional, separate, cell culture chambers exposed to the same gas control and hydration channels could be added to the device to ease parallelization of experiments (e.g., to study different concentrations of drug). Devices of a specific footprint could be designed to permit analysis by commonly used equipment such as the IN Cell Analyzer (GE Healthcare Life Sciences) for high-content analysis. To address the issue of potential overestimation of viability due to 2-D cell detachment into the perfused liquid, it may be worthwhile to implement a design similar to that demonstrated by Lecault *et al.* [320], which separates the cells from the perfusion path by using chambers below the flow path for cell culture. Multiple chambers could be integrated into each gas control device to ease parallelization and provide technical replicates.

In order to improve the usability of the system, it could be helpful to integrate on-chip bubble trapping into the microfluidic system. In the current implementation we avoid many bubble issues by using an extensive degassing procedure for both the chips and the media and PBS perfused through the chip for long-term experiments using microfluidic chips both with and without gas control. By preheating the media and desiccating, we reduce the nucleation of

bubbles in the syringe and tubing in the warm room and stage-top incubator. It appears from monitoring the experiment using microscopy that most of the bubbles that appear in the system come from the input fluid. It is possible that this degassing procedure could be avoided by integrating inline, on-chip vacuum-based trapping structures for bubbles such as those demonstrated by Lochovsky *et al.* [335]. This would add additional inputs to the device for the vacuum input but could improve ease-of-use. Inline commercial bubble traps could also be employed; however, these could potentially be problematic for use with cancer drugs (which can adsorb to tubing) as they may be difficult to completely clean between experiments.

Another useful addition to the oxygen control device could be the addition of on-chip temperature control. On-chip temperature control could facilitate longer-term two-photon studies with constant monitoring and without the need to move the device into an incubator. We are already able to currently carry out long-term studies using brightfield, wide-field, and confocal fluorescence imaging with temperature control using a stage-top incubator system; however, using the two-photon microscopy improves image quality and reduces sample damage. Gas control and channel hydration are already implemented on chip; as such, on-chip temperature control is the final step necessary to implement incubator-independent operation.

6.2.7   Adaptations to the Oxygen Sensors

The optical oxygen sensors could also be optimized for future studies. A more extensive investigation into the biocompatibility of the sensors would be prudent before their use in the dynamic monitoring of cell studies; however, there are several interesting avenues for future work that could use the sensors to study cell behaviour such as oxygen consumption and transport *in situ*.

If the oxygen levels are to be analyzed in 2-D (for example for studying cellular oxygen consumption as a function of position), utilizing a full pixel-by-pixel calibration of the sensor patches could yield improved measurement results by accounting for differences in quenching behaviour in the different sensor regions. Additionally, pixel binning or averaging of adjacent pixels could help to reduce noise in the 2-D oxygen measurements. Studies requiring the precise measurement of very low oxygen levels below 0.1% could also require more sensitive oxygen

sensors. Future work could also include the investigation of different oxygen-sensitive indicators with higher sensitivities and more precise limits of detection; either PdTFPP, which has approximately twice the sensitivity of PtTFPP [296, 297], or perhaps other, ultra-sensitive, sensors [298], could be employed. It should be kept in mind, however, that potential measurement artifacts characteristic of optical oxygen sensors can become more problematic at very low oxygen levels (sub-nanomolar concentrations), as recently discussed by Lehner *et al.* [336].

Oxygen sensors, in the form of microparticles embedded in the 3-D cell culture or water-soluble indicators perfused into the system, could also be used to measure oxygen levels in 3-D. This type of sensing system could be useful to measure time-varying spatial oxygen gradients that could exist in spheroids exposed to a cycling oxygen profile and help to understand differences in cell response within the spheroid. Lifetime-based luminescent sensors would likely be required for this application to minimize the effects of scattering within the spheroid (ratiometric sensors may not be feasible due to wavelength-dependent scattering and absorption effects).

Bibliography

[1]   D. C. Swinney and J. Anthony, "How were new medicines discovered?," *Nature Revews Drug Discovery,* vol. 10, pp. 507-519, 2011.

[2]   G. P. Nolan, "What's wrong with drug screening today," *Nat Chem Biol,* vol. 3, pp. 187-91, 2007.

[3]   L. Moreno and A. D. Pearson, "How can attrition rates be reduced in cancer drug discovery?," *Expert Opin Drug Discov,* vol. 8, pp. 363-8, 2013.

[4]   J. G. Moffat, J. Rudolph, and D. Bailey, "Phenotypic screening in cancer drug discovery - past, present and future," *Nat Rev Drug Discov,* vol. 13, pp. 588-602, 2014.

[5]   D. C. Swinney, "Phenotypic vs. target-based drug discovery for first-in-class medicines," *Clin Pharmacol Ther,* vol. 93, pp. 299-301, 2013.

[6]   R. Macarron, M. N. Banks, D. Bojanic, D. J. Burns, D. A. Cirovic, T. Garyantes*, et al.*, "Impact of high-throughput screening in biomedical research," *Nat Rev Drug Discov,* vol. 10, pp. 188-95, 2011.

[7]   F. Zanella, J. B. Lorens, and W. Link, "High content screening: seeing is believing," *Trends Biotechnol,* vol. 28, pp. 237-45, 2010.

[8]   J. Comley, "3D Cell Culture: easier said than done!," *Drug Discovery World,* vol. Fall 2010, pp. 25-41, 2010.

[9]   W. Mueller-Klieser, "Three-dimensional cell cultures: from molecular mechanisms to clinical applications," *American Journal of Physiology - Cell Physiology,* vol. 273, pp. C1109-C1123, 1997.

[10]   L. A. Kunz-Schughart, J. P. Freyer, F. Hofstaedter, and R. Ebner, "The Use of 3-D Cultures for High-Throughput Screening: The Multicellular Spheroid Model," *Journal of Biomolecular Screening,* vol. 9, pp. 273-285, 2004.

[11]   F. Pampaloni, N. Ansari, and E. H. Stelzer, "High-resolution deep imaging of live cellular spheroids with light-sheet-based fluorescence microscopy," *Cell Tissue Res,* vol. 352, pp. 161-77, 2013.

[12]   P. L. Olive and R. E. Durand, "Drug and radiation resistance in spheroids: cell contact and kinetics," *Cancer and Metastasis Reviews,* vol. 13, pp. 121-138, 1994.

[13]   R. Warden, J. Saunders, and A. Tsourkas, "Two-photon imaging of multicellular tumor spheroids: a novel method for evaluating the efficacy of CDC25 phosphatase inhibitors," *Cancer Biology & Therapy,* vol. 8, pp. 2237-8, 2009.

[14]   K. Groebe and W. Mueller-Klieser, "On the relation between size of necrosis and diameter of tumor spheroids," *Int J Radiat Oncol Biol Phys,* vol. 34, pp. 395-401, 1996.

[15]   P. Indovina, M. Collini, G. Chirico, and M. T. Santini, "Three-dimensional cell organization leads to almost immediate HRE activity as demonstrated by molecular imaging of MG-63 spheroids using two-photon excitation microscopy," *FEBS Lett,* vol. 581, pp. 719-26, 2007.

[16]   A. M. Ballangrud, W. H. Yang, A. Dnistrian, N. M. Lampen, and G. Sgouros, "Growth and characterization of LNCaP prostate cancer cell spheroids," *Clin Cancer Res,* vol. 5, pp. 3171s-3176s, 1999.

[17]   J. P. Celli, I. Rizvi, A. R. Blanden, I. Massodi, M. D. Glidden, B. W. Pogue*, et al.*, "An imaging-based platform for high-content, quantitative evaluation of therapeutic response in 3D tumour models," *Sci Rep,* vol. 4, p. 3751, 2014.

[18]   K. Trumpi, D. A. Egan, T. T. Vellinga, I. H. Borel Rinkes, and O. Kranenburg, "Paired image- and FACS-based toxicity assays for high content screening of spheroid-type tumor cell cultures," *FEBS Open Bio,* vol. 5, pp. 85-90, 2015.

[19]   H. L. Ma, Q. Jiang, S. Han, Y. Wu, J. Cui Tomshine, D. Wang*, et al.*, "Multicellular tumor spheroids as an in vivo-like tumor model for three-dimensional imaging of chemotherapeutic and nano material cellular penetration," *Mol Imaging,* vol. 11, pp. 487-98, 2012.

[20]   P. Hargrave, P. W. Nicholson, D. T. Delpy, and M. Firbank, "Optical properties of multicellular tumour spheroids," *Phys Med Biol,* vol. 41, pp. 1067-72, 1996.

[21]   W. R. Zipfel, R. M. Williams, and W. W. Webb, "Nonlinear magic: multiphoton microscopy in the biosciences," *Nat Biotechnol,* vol. 21, pp. 1369-77, 2003.

[22]   D. W. Piston, T. J. Fellers, and M. W. Davidson. (2013). *Fundamentals and Applications in Multiphoton Excitation Microscopy*. Available: http://www.microscopyu.com/articles/fluorescence/multiphoton/multiphotonintro.html. Accessed: April 2 2014.

[23]   W. Zipfel. *Estimating the diffraction-limited resolution of your objective lens.* Available: http://www.biotech.cornell.edu/sites/default/files/uploads/Documents/OpticalResolution Calculation.pdf. Accessed: April 2 2014.

[24]   A. Periasamy and American Physiological Society (1887-). *Methods in cellular imaging*. Oxford ; New York: Published for the American Physiological Society by Oxford University Press, 2001.

[25]   C. Frongia, C. Lorenzo, F. Gianni, G. P. Prevost, B. Ducommun, and V. Lobjois, "3D imaging of the response to CDC25 inhibition in multicellular spheroids," *Cancer Biol Ther,* vol. 8, pp. 2230-36, 2009.

[26]   L. le Roux, A. Volgin, D. Maxwell, K. Ishihara, J. Gelovani, and D. Schellingerhout, "Optimizing Imaging of Three-Dimensional Multicellular Tumor Spheroids with Fluorescent Reporter Proteins Using Confocal Microscopy," *Molecular Imaging,* vol. 7, pp. 214-221, 2008.

[27]   D. Zhu, K. V. Larin, Q. Luo, and V. V. Tuchin, "Recent progress in tissue optical clearing," *Laser Photon Rev,* vol. 7, pp. 732-757, 2013.

[28]   E. A. Susaki, K. Tainaka, D. Perrin, F. Kishino, T. Tawara, T. M. Watanabe*, et al.*, "Whole-Brain Imaging with Single-Cell Resolution Using Chemical Cocktails and Computational Analysis," *Cell,* vol. 157, pp. 726-739, 2014.

[29]   K. Chung, J. Wallace, S. Y. Kim, S. Kalyanasundaram, A. S. Andalman, T. J. Davidson*, et al.*, "Structural and molecular interrogation of intact biological systems," *Nature,* vol. 497, pp. 332-337, 2013.

[30]   R. Tomer, L. Ye, B. Hsueh, and K. Deisseroth, "Advanced CLARITY for rapid and high-resolution imaging of intact tissues," *Nat Protoc,* vol. 9, pp. 1682-97, 2014.

[31]   K. Becker, N. Jahrling, S. Saghafi, R. Weiler, and H. U. Dodt, "Chemical Clearing and Dehydration of GFP Expressing Mouse Brains," *Plos One,* vol. 7, p. e33916, 2012.

[32]   M.-T. Ke, S. Fujimoto, and T. Imai, "SeeDB: a simple and morphology-preserving optical clearing agent for neuronal circuit reconstruction," *Nature neuroscience,* vol. 16, pp. 1154-61, 2013.

[33]   T. Kuwajima, A. a. Sitko, P. Bhansali, C. Jurgens, W. Guido, and C. Mason, "ClearT: a detergent- and solvent-free clearing method for neuronal and non-neuronal tissue," *Development (Cambridge, England),* vol. 140, pp. 1364-8, 2013.

[34] H. Hama, H. Kurokawa, H. Kawano, R. Ando, T. Shimogori, H. Noda, *et al.*, "Scale: a chemical approach for fluorescence imaging and reconstruction of transparent mouse brain," *Nat Neurosci,* vol. 14, pp. 1481-8, 2011.

[35] H. Hama, H. Hioki, K. Namiki, T. Hoshida, H. Kurokawa, F. Ishidate, *et al.*, "ScaleS: an optical clearing palette for biological imaging," *Nat Neurosci,* vol. 18, pp. 1518-29, 2015.

[36] B. Hou, D. Zhang, S. Zhao, M. Wei, Z. Yang, S. Wang, *et al.*, "Scalable and DiI-compatible optical clearance of the mammalian brain," *Frontiers in Neuroanatomy,* vol. 9, pp. 1-11, 2015.

[37] M. E. Boutin and D. Hoffman-Kim, "Application and Assessment of Optical Clearing Methods for Imaging of Tissue-Engineered Neural Stem Cell Spheres," *Tissue Engineering Part C-Methods,* vol. 21, pp. 292-302, 2015.

[38] R. Das, A. Agrawal, M. P. Upton, and E. J. Seibel, "Optically clearing tissue as an initial step for 3D imaging of core biopsies to diagnose pancreatic cancer," *Optical Interactions with Tissue and Cells Xxv; and Terahertz for Biomedical Applications,* vol. 8941, pp. 89410N1-11, 2014.

[39] P. S. Dittrich and A. Manz, "Lab-on-a-chip: microfluidics in drug discovery," *Nature Reviews Drug Discovery,* vol. 5, pp. 210-218, 2006.

[40] M. H. Wu, S. B. Huang, and G. B. Lee, "Microfluidic cell culture systems for drug research," *Lab Chip,* vol. 10, pp. 939-56, 2010.

[41] P. Neuzi, S. Giselbrecht, K. Lange, T. J. Huang, and A. Manz, "Revisiting lab-on-a-chip technology for drug discovery," *Nat Rev Drug Discov,* vol. 11, pp. 620-32, 2012.

[42] A. Sin, K. C. Chin, M. F. Jamil, Y. Kostov, G. Rao, and M. L. Shuler, "The design and fabrication of three-chamber microscale cell culture analog devices with integrated dissolved oxygen sensors," *Biotechnology Progress,* vol. 20, pp. 338-345, 2004.

[43] S. N. Bhatia and D. E. Ingber, "Microfluidic organs-on-chips," *Nat Biotechnol,* vol. 32, pp. 760-72, 2014.

[44] L. Yu, M. C. W. Chen, and K. C. Cheung, "Droplet-Based Microfluidic System for Multicellular Tumor Spheroid Formation and Anticancer Drug Testing," *Lab on a Chip,* vol. 10, pp. 2424-2432, 2010.

[45] L. Yu and K. C. Cheung, "Characterization of Drug Induced Autophagy and Cytotoxicity in MCF7 Cells on Multi-layer Microfluidic Device," in *15th International Conference on Miniaturized Systems for Chemistry and Life Sciences (MicroTAS 2011)*, Seattle, USA, 2011, pp. 103-105.

[46] M. C. Chen, M. Gupta, and K. C. Cheung, "Hydrogel-based microfluidic systems for co-culture of cells," *Conference proceedings : Annual International Conference of the IEEE Engineering in Medicine and Biology Society.IEEE Engineering in Medicine and Biology Society.Conference,* vol. 2008, pp. 4848-4851, 2008.

[47] C. Bayly, L. Yu, and K. C. Cheung, "Alginate Encapsulation of Cell-Laden Beads for Microfluidic Tumor Spheroid Culture," presented at the The 17th International Conference on Miniaturized Systems for Chemistry and Life Sciences, MicroTAS 2013 Freiburg, Germany, 2013.

[48] R. M. Sutherland, H. A. Eddy, B. Bareham, K. Reich, and D. Vanantwerp, "Resistance to adriamycin in multicellular spheroids," *International journal of radiation oncology, biology, physics,* vol. 5, pp. 1225-1230, 1979.

[49] B. Desoize and J.-C. Jardillier, "Multicellular resistance: a paradigm for clinical resistance?," *Critical Reviews in Oncology/Hematology,* vol. 36, pp. 193-207, 2000.

[50] M. Höckel and P. Vaupel, "Tumor Hypoxia: Definitions and Current Clinical, Biologic, and Molecular Aspects," *Journal of the National Cancer Institute,* vol. 93, pp. 266-276, 2001.

[51] A. L. Harris, "Hypoxia – a key regulatory factor in tumour growth," *Nature Reviews Cancer,* vol. 2, pp. 38-47, 2002.

[52] R. Thomlinson and L. Gray, "The histological structure of some human lung cancers and the possible implications for radiotherapy," *Br J Cancer,* vol. 9, pp. 539-549, 1955.

[53] P. Rubin and G. Casarett, "Microcirculation of tumors Part I: Anatomy, function, and necrosis," *Clinical Radiology,* vol. 17, pp. 220-229, 1966.

[54] J. Brown, "Evidence for acutely hypoxic cells in mouse tumours and a possible mechanism of reoxygenation," *Br J Radiol,* vol. 52, pp. 650-656, 1979.

[55] A. I. Minchinton, L. Cobb, and J. Brown, "Intermittent hypoxia: Its presence in tumours of different histological grade," *Microvasc Res,* 1997.

[56] D. J. Chaplin, P. L. Olive, and R. E. Durand, "Intermittent Blood Flow in a Murine Tumor: Radiobiological Effects," *Cancer Research,* vol. 47, pp. 597-601, 1987.

[57] A. I. Minchinton, R. E. Durand, and D. J. Chaplin, "Intermittent blood flow in the KHT sarcoma - flow cytometry studies using Hoechst 33342," *Br J Cancer,* vol. 62, pp. 195-200, 1990.

[58] P. Vaupel, "Metabolic microenvironment of tumor cells: a key factor in malignant progression," *Experimental Oncology,* vol. 32, pp. 125-127, 2010.

[59] L. I. Cárdenas-Navia, D. Yu, R. D. Braun, D. M. Brizel, T. W. Secomb, and M. W. Dewhirst, "Tumor-dependent Kinetics of Partial Pressure of Oxygen Fluctuations during Air and Oxygen Breathing," *Cancer Research,* vol. 64, pp. 6010-6017, 2004.

[60] M. W. Dewhirst, Y. Cao, and B. Moeller, "Cycling hypoxia and free radicals regulate angiogenesis and radiotherapy response," *Nature Reviews Cancer,* vol. 8, pp. 425-437, 2008.

[61] P. Subarsky and R. Hill, "Graded hypoxia modulates the invasive potential of HT1080 fibrosarcoma and MDA MB231 carcinoma cells," *Clinical & Experimental Metastasis,* vol. 25, pp. 253-264, 2008.

[62] C. J. Koch, "Measurement of absolute oxygen levels in cells and tissues using oxygen sensors and 2-nitroimidazole EF5," *Methods Enzymol,* vol. 352, pp. 3-31, 2002.

[63] D. R. Grimes, C. Kelly, K. Bloch, and M. Partridge, "A method for estimating the oxygen consumption rate in multicellular tumour spheroids," *J R Soc Interface,* vol. 11, p. 20131124, 2014.

[64] P. N. Span and J. Bussink, "Biology of Hypoxia," *Seminars in Nuclear Medicine,* vol. 45, pp. 101-109, 2015.

[65] W. R. Wilson and M. P. Hay, "Targeting hypoxia in cancer therapy," *Nature Reviews Cancer,* vol. 11, pp. 393-410, 2011.

[66] J. C. Mottram, "On the Alteration in the Sensitivity of Cells Towards Radiation Produced by Cold and by Anærobiosis," *The British Journal of Radiology,* vol. 8, pp. 32-39, 1935.

[67] L. H. Gray, A. D. Conger, M. Ebert, S. Hornsey, and O. C. A. Scott, "The Concentration of Oxygen Dissolved in Tissues at the Time of Irradiation as a Factor in Radiotherapy," *British Journal of Radiology,* vol. 26, pp. 638-648, 1953.

[68] B. A. Teicher, "Hypoxia and drug resistance," *Cancer Metastasis Rev,* vol. 13, pp. 139-68, 1994.

[69]   A. M. Shannon, D. J. Bouchier-Hayes, C. M. Condron, and D. Toomey, "Tumour hypoxia, chemotherapeutic resistance and hypoxia-related therapies," *Cancer Treat Rev,* vol. 29, pp. 297-307, 2003.

[70]   N. Rohwer and T. Cramer, "Hypoxia-mediated drug resistance: novel insights on the functional interaction of HIFs and cell death pathways," *Drug Resist Updat,* vol. 14, pp. 191-201, 2011.

[71]   B. A. Teicher, J. S. Lazo, and A. C. Sartorelli, "Classification of antineoplastic agents by their selective toxicities toward oxygenated and hypoxic tumor cells," *Cancer Res,* vol. 41, pp. 73-81, 1981.

[72]   B. A. Teicher, S. A. Holden, A. Alachi, and T. S. Herman, "Classification of Antineoplastic Treatments by Their Differential Toxicity toward Putative Oxygenated and Hypoxic Tumor Subpopulations Invivo in the Fsaiic Murine Fibrosarcoma," *Cancer Research,* vol. 50, pp. 3339-3344, 1990.

[73]   R. Sullivan, G. C. Paré, L. J. Frederiksen, G. L. Semenza, and C. H. Graham, "Hypoxia-induced resistance to anticancer drugs is associated with decreased senescence and requires hypoxia-inducible factor-1 activity," *Molecular Cancer Therapeutics,* vol. 7, pp. 1961-1973, 2008.

[74]   S. Strese, M. Fryknas, R. Larsson, and J. Gullbo, "Effects of hypoxia on human cancer cell line chemosensitivity," *BMC Cancer,* vol. 13, p. 331, 2013.

[75]   K. Balamurugan, "HIF-1 at the crossroads of hypoxia, inflammation, and cancer," *Int J Cancer,* vol. 138, pp. 1058-66, 2016.

[76]   A. Carreau, B. El Hafny-Rahbi, A. Matejuk, C. Grillon, and C. Kieda, "Why is the partial oxygen pressure of human tissues a crucial parameter? Small molecules and hypoxia," *Journal of Cellular and Molecular Medicine,* vol. 15, pp. 1239-1253, 2011.

[77]   E. Favaro, S. Lord, A. Harris, and F. Buffa, "Gene expression and hypoxia in breast cancer," *Genome Medicine,* vol. 3, p. 55, 2011.

[78]   D. M. Brizel, G. S. Sibley, L. R. Prosnitz, R. L. Scher, and M. W. Dewhirst, "Tumor hypoxia adversely affects the prognosis of carcinoma of the head and neck," *International Journal of Radiation Oncology*Biology*Physics,* vol. 38, pp. 285-289, 1997.

[79]   S. M. Evans, K. D. Judy, I. Dunphy, W. T. Jenkins, W.-T. Hwang, P. T. Nelson*, et al.*, "Hypoxia Is Important in the Biology and Aggression of Human Glial Brain Tumors," *Clinical Cancer Research,* vol. 10, pp. 8177-8184, 2004.

[80]   P. Vaupel, "Hypoxia and Aggressive Tumor Phenotype: Implications for Therapy and Prognosis," *The Oncologist,* vol. 13, pp. 21-26, 2008.

[81]   N. Chaudary and R. P. Hill, "Hypoxia and Metastasis in Breast Cancer," *Breast Disease,* vol. 26, pp. 55-64, 2007.

[82]   E. O. Pettersen, P. Ebbesen, R. G. Gieling, K. J. Williams, L. Dubois, P. Lambin*, et al.*, "Targeting tumour hypoxia to prevent cancer metastasis. From biology, biosensing and technology to drug development: the METOXIA consortium," *J Enzyme Inhib Med Chem,* vol. 30, pp. 689-721, 2015.

[83]   C. Koumenis and B. G. Wouters, ""Translating" Tumor Hypoxia: Unfolded Protein Response (UPR)–Dependent and UPR-Independent Pathways," *Molecular Cancer Research,* vol. 4, pp. 423-436, 2006.

[84] A. Nagelkerke, J. Bussink, H. Mujcic, B. Wouters, S. Lehmann, F. Sweep, *et al.*, "Hypoxia stimulates migration of breast cancer cells via the PERK/ATF4/LAMP3-arm of the unfolded protein response," *Breast Cancer Research,* vol. 15, p. R2, 2013.

[85] J. M. Gleadle and P. J. Ratcliffe, "Induction of Hypoxia-Inducible Factor-1, Erythropoietin, Vascular Endothelial Growth Factor, and Glucose Transporter-1 by Hypoxia: Evidence Against a Regulatory Role for Src Kinase," *Blood,* vol. 89, pp. 503-509, 1997.

[86] G. Bellot, R. Garcia-Medina, P. Gounon, J. Chiche, D. Roux, J. Pouysségur, *et al.*, "Hypoxia-Induced Autophagy Is Mediated through Hypoxia-Inducible Factor Induction of BNIP3 and BNIP3L via Their BH3 Domains," *Molecular and Cellular Biology,* vol. 29, pp. 2570-2581, 2009.

[87] M. C. Simon and B. Keith, "The role of oxygen availability in embryonic development and stem cell function," *Nature Reviews Molecular Cell Biology,* vol. 9, pp. 285-296, 2008.

[88] J. R. Millman, J. H. Tan, and C. K. Colton, "The effects of low oxygen on self-renewal and differentiation of embryonic stem cells. ," *Current Opinion in Organ Transplantation,* vol. 14, pp. 694-700, 2009.

[89] G. Helmlinger, F. Yuan, M. Dellian, and R. K. Jain, "Interstitial pH and pO(2) gradients in solid tumors in vivo: High-resolution measurements reveal a lack of correlation," *Nature Medicine,* vol. 3, pp. 177-182, 1997.

[90] K. Erickson, R. A. Braun, D. H. Yu, J. Lanzen, D. Wilson, D. M. Brizel, *et al.*, "Effect of longitudinal oxygen gradients on effectiveness of manipulation of tumor oxygenation," *Cancer Research,* vol. 63, pp. 4705-4712, 2003.

[91] L. Cárdenas-Navia, D. Mace, R. Richardson, D. Wilson, S. Shan, and M. Dewhirst, "The Pervasive Presence of Fluctuating Oxygenation in Tumors," *Cancer Research,* vol. 68, pp. 5812-5819, 2008.

[92] S. A. Hill and D. J. Chaplin, "Detection of Microregional Fluctuations in Erythrocyte Flow Using Laser Doppler Microprobes," in *Oxygen Transport to Tissue XVII.* vol. 388, C. Ince, J. Kesecioglu, L. Telci, and K. Akpir, Eds., ed: Springer US, 1996, pp. 367-371.

[93] R. A. Cairns, T. Kalliomaki, and R. P. Hill, "Acute (Cyclic) Hypoxia Enhances Spontaneous Metastasis of KHT Murine Tumors," *Cancer Research,* vol. 61, pp. 8903-8908, 2001.

[94] C. Bayer and P. Vaupel, "Acute versus chronic hypoxia in tumors. Controversial data concerning time frames and biological consequences," *Strahlentherapie Und Onkologie,* vol. 188, pp. 616-627, 2012.

[95] P. Vaupel and A. Mayer, "Hypoxia in Tumors: Pathogenesis-Related Classification, Characterization of Hypoxia Subtypes, and Associated Biological and Clinical Implications," *Oxygen Transport to Tissue Xxxvi,* vol. 812, pp. 19-24, 2014.

[96] M. Koritzinsky and B. G. Wouters, "The Roles of Reactive Oxygen Species and Autophagy in Mediating the Tolerance of Tumor Cells to Cycling Hypoxia," *Seminars in Radiation Oncology,* vol. 23, pp. 252-261, 2013.

[97] S. Matsumoto, H. Yasui, J. B. Mitchell, and M. C. Krishna, "Imaging Cycling Tumor Hypoxia," *Cancer Research,* vol. 70, pp. 10019-10023, 2010.

[98] M. W. Dewhirst, "Relationships between Cycling Hypoxia, HIF-1, Angiogenesis and Oxidative Stress," *Radiation Research,* vol. 172, pp. 653-665, 2009.

[99]   D. M. Ragan, E. E. Schmidt, I. C. MacDonald, and A. C. Groom, "Spontaneous cyclic contractions of the capillary wall in vivo, impeding red cell flow: a quantitative analysis. Evidence for endothelial contractility," *Microvasc Res,* vol. 36, pp. 13-30, 1988.

[100]   P. Subarsky and R. Hill, "The hypoxic tumour microenvironment and metastatic progression," *Clinical & Experimental Metastasis,* vol. 20, pp. 237-250, 2003.

[101]   T. G. Graeber, C. Osmanian, T. Jacks, D. E. Housman, C. J. Koch, S. W. Lowe*, et al.*, "Hypoxia-mediated selection of cells with diminished apoptotic potential in solid tumours," *Nature,* vol. 379, pp. 88-91, 1996.

[102]   D. Verduzco, M. Lloyd, L. Xu, A. Ibrahim-Hashim, Y. Balagurunathan, R. A. Gatenby*, et al.*, "Intermittent Hypoxia Selects for Genotypes and Phenotypes That Increase Survival, Invasion, and Therapy Resistance," *PLoS ONE,* vol. 10, p. e0120958, 2015.

[103]   S. M. Ehsan and S. C. George, "Vessel network formation in response to intermittent hypoxia is frequency dependent," *Journal of Bioscience and Bioengineering,* vol. 120, pp. 347-350, 2015.

[104]   M. B. Byrne, M. T. Leslie, H. R. Gaskins, and P. J. A. Kenis, "Methods to study the tumor microenvironment under controlled oxygen conditions," *Trends in Biotechnology,* vol. 32, pp. 556-563, 2014.

[105]   A. H. Kyle, J. H. Baker, and A. I. Minchinton, "Targeting quiescent tumor cells via oxygen and IGF-I supplementation," *Cancer Res,* vol. 72, pp. 801-9, 2012.

[106]   D. Wu and P. Yotnda, "Induction and testing of hypoxia in cell culture," *J Vis Exp,* 2011.

[107]   S. M. Grist, L. Chrostowski, and K. C. Cheung, "Optical Oxygen Sensors for Applications in Microfluidic Cell Culture," *Sensors,* vol. 10, pp. 9286-9316, 2010.

[108]   O. Stern and M. Volmer, "The fading time of fluorescence," *Physikalische Zeitschrift,* vol. 20, pp. 183-188, 1919.

[109]   B. Ungerbock, V. Charwat, P. Ertl, and T. Mayr, "Microfluidic oxygen imaging using integrated optical sensor layers and a color camera," *Lab on a Chip,* vol. 13, pp. 1593-1601, 2013.

[110]   L. C. Clark and C. Lyons, "Electrode Systems for Continuous Monitoring in Cardiovascular Surgery," *Annals of the New York Academy of Sciences,* vol. 102, pp. 29-45, 1962.

[111]   J. M. Arbeit, J. M. Brown, K. S. C. Chao, J. D. Chapman, W. C. Eckelman, A. W. Fyles*, et al.*, "Hypoxia: Importance in tumor biology, noninvasive measurement by imaging, and value of its measurement in the management of cancer therapy," *International Journal of Radiation Biology,* vol. 82, pp. 699-757, 2006.

[112]   C. C. Wu, T. Yasukawa, H. Shiku, and T. Matsue, "Fabrication of miniature Clark oxygen sensor integrated with microstructure," *Sensors and Actuators B-Chemical,* vol. 110, pp. 342-349, 2005.

[113]   S. Suresh, V. C. Srivastava, and I. M. Mishra, "Techniques for oxygen transfer measurement in bioreactors: a review," *Journal of Chemical Technology & Biotechnology,* vol. 84, pp. 1091-1103, 2009.

[114]   D. B. Papkovsky, T. O'Riordan, and A. Soini, "Phosphorescent porphyrin probes in biosensors and sensitive bioassays," *Biochemical Society transactions,* vol. 28, pp. 74-77, 2000.

[115]   S. Gatti, T. Brey, W. E. G. Muller, O. Heilmayer, and G. Holst, "Oxygen microoptodes: a new tool for oxygen measurements in aquatic animal ecology," *Marine Biology,* vol. 140, pp. 1075-1085, 2002.

[116] A. Mills, "Optical Oxygen Sensors," *Platinum Metals Review,* vol. 41, pp. 115-127, 1997.

[117] P. Hartmann, W. Ziegler, G. Holst, and D. W. Lubbers, "Oxygen flux fluorescence lifetime imaging," *Sensors and Actuators B-Chemical,* vol. 38, pp. 110-115, 1997.

[118] E. J. Park, K. R. Reid, W. Tang, R. T. Kennedy, and R. Kopelman, "Ratiometric fiber optic sensors for the detection of inter- and intra-cellular dissolved oxygen," *Journal of materials chemistry,* vol. 15, pp. 2913-2919, 2005.

[119] B. Konig, O. Kohls, G. Holst, R. N. Glud, and M. Kuhl, "Fabrication and test of sol-gel based planar oxygen optodes for use in aquatic sediments," *Marine Chemistry,* vol. 97, pp. 262-276, 2005.

[120] I. Bergman, "Rapid-Response Atmospheric Oxygen Monitor Based on Fluorescence Quenching," *Nature,* vol. 218, p. 396, 1968.

[121] D. F. Wilson and S. A. Vinogradov, "Tissue Oxygen Measurements Using Phosphorescence Quenching," in *Handbook of Biomedical Fluorescence*, M.-A. Mycek and B. W. Pogue, Eds., ed New York, NY, USA: Marcel Dekker, 2003, pp. 637-662.

[122] Y. Amao, "Probes and Polymers for Optical Sensing of Oxygen," *Microchimica Acta,* vol. 143, pp. 1-12, 2003.

[123] C. McDonagh, C. S. Burke, and B. D. MacCraith, "Optical chemical sensors," *Chemical reviews,* vol. 108, pp. 400-422, 2008.

[124] R. A. Yotter, L. A. Lee, and D. M. Wilson, "Sensor technologies for monitoring metabolic activity in single cells - Part I: Optical, methods," *IEEE sensors journal,* vol. 4, pp. 395-411, 2004.

[125] S. A. Pfeiffer and S. Nagl, "Microfluidic platforms employing integrated fluorescent or luminescent chemical sensors: a review of methods, scope and applications," *Methods and Applications in Fluorescence,* vol. 3, p. 034003, 2015.

[126] S. Sun, B. Ungerbock, and T. Mayr, "Imaging of oxygen in microreactors and microfluidic systems," *Methods and Applications in Fluorescence,* vol. 3, p. 034002, 2015.

[127] G. Holst, O. Kohls, I. Klimant, B. Konig, M. Kuhl, and T. Richter, "A modular luminescence lifetime imaging system for mapping oxygen distribution in biological samples," *Sensors and Actuators B-Chemical,* vol. 51, pp. 163-170, 1998.

[128] T. Itoh, K. Yaegashi, T. Kosaka, T. Kinoshita, and T. Morimoto, "In-Vivo Visualization of Oxygen-Transport in Microvascular Network," *American Journal of Physiology-Heart and Circulatory Physiology,* vol. 36, pp. H2068-H2078, 1994.

[129] V. Nock, R. J. Blaikie, and T. David, "Patterning, integration and characterisation of polymer optical oxygen sensors for microfluidic devices," *Lab on a chip,* vol. 8, pp. 1300-1307, 2008.

[130] W. L. Rumsey, J. M. Vanderkooi, and D. F. Wilson, "Imaging of Phosphorescence - a Novel Method for Measuring Oxygen Distribution in Perfused Tissue," *Science,* vol. 241, pp. 1649-1651, 1988.

[131] D. A. Chang-Yen, A. Badardeen, and B. K. Gale, "Spin-assembled nanofilms for gaseous oxygen sensing," *Sensors and Actuators B-Chemical,* vol. 120, pp. 426-433, 2007.

[132] Y.-E. L. Koo, Y. Cao, R. Kopelman, S. M. Koo, M. Brasuel, and M. A. Philbert, "Real-Time Measurements of Dissolved Oxygen Inside Live Cells by Organically Modified Silicate Fluorescent Nanosensors," *Analytical Chemistry,* vol. 76, pp. 2498-2505, 2004.

[133] C. O'Donovan, J. Hynes, D. Yashunski, and D. B. Papkovsky, "Phosphorescent oxygen-sensitive materials for biological applications," *Journal of materials chemistry,* vol. 15, pp. 2946-2951, 2005.

[134] Z. Lin, T. Cherng-Wen, P. Roy, and D. Trau, "In-situ measurement of cellular microenvironments in a microfluidic device," *Lab on a chip,* vol. 9, pp. 257-262, 2009.

[135] R. H. W. Lam, M.-C. Kim, and T. Thorsen, "A microfluidic oxygenator for biological cell culture," presented at the Transducers & Eurosensors `07, Lyon, France, 2007.

[136] R. H. Lam, M. C. Kim, and T. Thorsen, "Culturing aerobic and anaerobic bacteria and mammalian cells with a microfluidic differential oxygenator," *Analytical Chemistry,* vol. 81, pp. 5918-5924, 2009.

[137] A. D. Elder, S. M. Matthews, J. Swartling, K. Yunus, J. H. Frank, C. M. Brennan*, et al.*, "The application of frequency-domain Fluorescence Lifetime Imaging Microscopy as a quantitative analytical tool for microfluidic devices," *Optics Express,* vol. 14, pp. 5456-5467, 2006.

[138] G. Holst, R. N. Glud, M. Kuhl, and I. Klimant, "A microoptode array for fine-scale measurement of oxygen distribution," *Sensors and Actuators B-Chemical,* vol. 38, pp. 122-129, 1997.

[139] I. Klimant, M. Kuhl, R. N. Glud, and G. Holst, "Optical measurement of oxygen and temperature in microscale: strategies and biological applications," *Sensors and Actuators B-Chemical,* vol. 38, pp. 29-37, 1997.

[140] D. B. Papkovsky, G. V. Ponomarev, W. Trettnak, and P. O'Leary, "Phosphorescent Complexes of Porphyrin Ketones: Optical Properties and Application to Oxygen Sensing," *Analytical Chemistry,* vol. 67, pp. 4112-4117, 1995.

[141] G. Liebsch, I. Klimant, B. Frank, G. Holst, and O. S. Wolfbeis, "Luminescence lifetime imaging of oxygen, pH, and carbon dioxide distribution using optical sensors," *Applied Spectroscopy,* vol. 54, pp. 548-559, 2000.

[142] K. Kellner, G. Liebsch, I. Klimant, O. S. Wolfbeis, T. Blunk, M. B. Schulz*, et al.*, "Determination of oxygen gradients in engineered tissue using a fluorescent sensor," *Biotechnology and Bioengineering,* vol. 80, pp. 73-83, 2002.

[143] G. Holst and B. Grunwald, "Luminescence lifetime imaging with transparent oxygen optodes," *Sensors and Actuators B: Chemical,* vol. 74, pp. 78-90, 2001.

[144] P. Urayama, W. Zhong, J. A. Beamish, F. K. Minn, R. D. Sloboda, K. H. Dragnev*, et al.*, "A UV-visible-NIR fluorescence lifetime imaging microscope for laser-based biological sensing with picosecond resolution," *Applied Physics B-Lasers and Optics,* vol. 76, pp. 483-496, 2003.

[145] X. F. Wang, T. Uchida, D. M. Coleman, and S. Minami, "A 2-Dimensional Fluorescence Lifetime Imaging-System Using a Gated Image Intensifier," *Applied Spectroscopy,* vol. 45, pp. 360-366, 1991.

[146] W. Zhong, P. Urayama, and M. A. Mycek, "Imaging fluorescence lifetime modulation of a ruthenium-based dye in living cells: the potential for oxygen sensing," *Journal of Physics D-Applied Physics,* vol. 36, pp. 1689-1695, 2003.

[147] G. Marriott, R. M. Clegg, D. J. Arndtjovin, and T. M. Jovin, "Time Resolved Imaging Microscopy - Phosphorescence and Delayed Fluorescence Imaging," *Biophysical Journal,* vol. 60, pp. 1374-1387, 1991.

[148] R. K. P. Benninger, O. Hofmann, J. McGinty, J. Requejo-Isidro, I. Munro, M. A. A. Neil*, et al.*, "Time-resolved fluorescence imaging of solvent interactions in microfluidic devices," *Optics Express,* vol. 13, pp. 6275-6285, 2005.

[149] R. D. Shonat, D. F. Wilson, C. E. Riva, and M. Pawlowski, "Oxygen Distribution in the Retinal and Choroidal Vessels of the Cat as Measured by a New Phosphorescence Imaging Method," *Applied Optics,* vol. 31, pp. 3711-3718, 1992.

[150] D. Sud, W. Zhong, D. G. Beer, and M. A. Mycek, "Time-resolved optical imaging provides a molecular snapshot of altered metabolic function in living human cancer cell models," *Optics Express,* vol. 14, pp. 4412-4426, 2006.

[151] G. Mehta, K. Mehta, D. Sud, J. W. Song, T. Bersano-Begey, N. Futai*, et al.*, "Quantitative measurement and control of oxygen levels in microfluidic poly(dimethylsiloxane) bioreactors during cell culture," *Biomed. Microdevices,* vol. 9, pp. 123-134, 2007.

[152] M. Kuhl, L. F. Rickelt, and R. Thar, "Combined imaging of bacteria and oxygen in biofilms," *Applied and Environmental Microbiology,* vol. 73, pp. 6289-6295, 2007.

[153] J. R. Lakowicz and K. W. Berndt, "Lifetime-Selective Fluorescence Imaging Using an Rf Phase-Sensitive Camera," *Review of Scientific Instruments,* vol. 62, pp. 1727-1734, 1991.

[154] M. E. Lippitsch, J. Pusterhofer, M. J. P. Leiner, and O. S. Wolfbeis, "Fibre-Optic Oxygen Sensor with the Fluorescence Decay Time as the Information Carrier," *Analytica Chimica Acta,* vol. 205, pp. 1-6, 1988.

[155] K. W. Berndt and J. R. Lakowicz, "Electroluminescent Lamp-Based Phase Fluorometer and Oxygen Sensor," *Analytical Biochemistry,* vol. 201, pp. 319-325, 1992.

[156] W. Trettnak, C. Kolle, F. Reininger, C. Dolezal, and P. OLeary, "Miniaturized luminescence lifetime-based oxygen sensor instrumentation utilizing a phase modulation technique," *Sensors and Actuators B-Chemical,* vol. 36, pp. 506-512, 1996.

[157] L. Yao, R. Khan, V. P. Chodavarapu, V. S. Tripathi, and F. V. Bright, "Sensitivity-Enhanced CMOS Phase Luminometry System Using Xerogel-Based Sensors," *Ieee Transactions on Biomedical Circuits and Systems,* vol. 3, pp. 304-311, 2009.

[158] A. P. Vollmer, R. F. Probstein, R. Gilbert, and T. Thorsen, "Development of an integrated microfluidic platform for dynamic oxygen sensing and delivery in a flowing medium," *Lab on a chip,* vol. 5, pp. 1059-1066, 2005.

[159] N. Szita, P. Boccazzi, Z. Y. Zhang, P. Boyle, A. J. Sinskey, and K. F. Jensen, "Development of a multiplexed microbioreactor system for high-throughput bioprocessing," *Lab on a chip,* vol. 5, pp. 819-826, 2005.

[160] A. Zanzotto, N. Szita, P. Boccazzi, P. Lessard, A. J. Sinskey, and K. F. Jensen, "Membrane-aerated microbioreactor for high-throughput bioprocessing," *Biotechnology and Bioengineering,* vol. 87, pp. 243-254, 2004.

[161] Y. Cao, Y.-E. Lee Koo, and R. Kopelman, "Poly(decyl methacrylate)-based fluorescent PEBBLE swarm nanosensors for measuring dissolved oxygen in biosamples," *Analyst,* vol. 129, pp. 745-750, 2004.

[162] S. M. Borisov and I. Klimant, "Luminescent nanobeads for optical sensing and imaging of dissolved oxygen," *Microchimica Acta,* vol. 164, pp. 7-15, 2009.

[163] B. Ungerböck, G. Mistlberger, V. Charwat, P. Ertl, and T. Mayr, "Oxygen imaging in microfluidic devices with optical sensors applying color cameras," *Procedia Engineering,* vol. 5, pp. 456-459, 2010.

[164] T. Mayr, S. M. Borisov, T. Abel, B. Enko, K. Waich, G. Mistlberger, *et al.*, "Light Harvesting as a Simple and Versatile Way to Enhance Brightness of Luminescent Sensors," *Analytical Chemistry,* vol. 81, pp. 6541-6545, 2009.

[165] J. Ehgartner, H. Wiltsche, S. M. Borisov, and T. Mayr, "Low cost referenced luminescent imaging of oxygen and pH with a 2-CCD colour near infrared camera," *Analyst,* vol. 139, pp. 4924-33, 2014.

[166] P. Babilas, G. Liebsch, V. Schacht, I. Klimant, O. S. Wolfbeis, R. M. Szeimies, *et al.*, "In vivo phosphorescence imaging of pO2 using planar oxygen sensors," *Microcirculation (New York, N.Y.: 1994),* vol. 12, pp. 477-487, 2005.

[167] M. Stucker, L. Schulze, G. Pott, P. Hartmann, D. W. Lubbers, A. Rochling, *et al.*, "FLIM of luminescent oxygen sensors: clinical applications and results," *Sensors and Actuators B-Chemical,* vol. 51, pp. 171-175, 1998.

[168] D. B. Papkovsky, A. N. Ovchinnikov, V. I. Ogurtsov, G. V. Ponomarev, and T. Korpela, "Biosensors on the basis of luminescent oxygen sensor: the use of microporous light-scattering support materials," *Sensors and Actuators B: Chemical,* vol. 51, pp. 137-145, 1998.

[169] P. Hartmann and W. Trettnak, "Effects of Polymer Matrices on Calibration Functions of Luminescent Oxygen Sensors Based on Porphyrin Ketone Complexes," *Analytical Chemistry,* vol. 68, pp. 2615-2620, 1996.

[170] T. C. O'Riordan, H. Voraberger, J. P. Kerry, and D. B. Papkovsky, "Study of migration of active components of phosphorescent oxygen sensors for food packaging applications," *Analytica Chimica Acta,* vol. 530, pp. 135-141, 2005.

[171] V. Nock, R. J. Blaikie, and T. David, "Micro-patterning of polymer-based optical oxygen sensors for lab-on-chip applications," in *BIOMEMS and Nanotechnology III; Proceedings of the Society of Photo-Optical Instrumentation Engineers (SPIE)*, Canberra, ACT, Australia 2008, pp. 1-10.

[172] V. Nock, M. Alkaisi, and R. J. Blaikie, "Photolithographic patterning of polymer-encapsulated optical oxygen sensors," *Microelectronic Engineering,* vol. 87, pp. 814-816, 2010.

[173] R. Ambekar, J. Park, D. B. Henthorn, and C.-S. Kim, "Photopatternable Polymeric Membranes for Optical Oxygen Sensors," *IEEE sensors journal,* vol. 9, pp. 169-175, 2009.

[174] D. A. Chang-Yen and B. K. Gale, "An integrated optical oxygen sensor fabricated using rapid-prototyping techniques," *Lab on a chip,* vol. 3, pp. 297-301, 2003.

[175] I. Klimant, V. Meyer, and M. Kuhl, "Fiber-optic Oxygen Microsensors, a New Tool in Aquatic Biology," *Limnology and Oceanography,* vol. 40, pp. 1159-1165, 1995.

[176] I. Klimant, F. Ruckruh, G. Liebsch, C. Stangelmayer, and O. S. Wolfbeis, "Fast response oxygen micro-optodes based on novel soluble ormosil glasses," *Mikrochimica Acta,* vol. 131, pp. 35-46, 1999.

[177] C. S. Burke, O. McGaughey, J. M. Sabattie, H. Barry, A. K. McEvoy, C. McDonagh, *et al.*, "Development of an integrated optic oxygen sensor using a novel, generic platform," *Analyst,* vol. 130, pp. 41-45, 2005.

[178] Y. E. K. Lee, R. Smith, and R. Kopelman, "Nanoparticle PEBBLE Sensors in Live Cells and In Vivo," *Annual Review of Analytical Chemistry,* vol. 2, pp. 57-76, 2009.

[179] Y. E. K. Lee and R. Kopelman, "Optical nanoparticle sensors for quantitative intracellular imaging," *Wiley Interdisciplinary Reviews-Nanomedicine and Nanobiotechnology,* vol. 1, pp. 98-110, 2009.

[180] A. S. Kocincova, S. Nagl, S. Arain, C. Krause, S. M. Borisov, M. Arnold*, et al.*, "Multiplex bacterial growth monitoring in 24-well microplates using a dual optical sensor for dissolved oxygen and pH," *Biotechnol Bioeng,* vol. 100, pp. 430-8, 2008.

[181] J. M. Vanderkooi, G. Maniara, T. J. Green, and D. F. Wilson, "An Optical Method for Measurement of Dioxygen Concentration Based Upon Quenching of Phosphorescence," *Journal of Biological Chemistry,* vol. 262, pp. 5476-5482, 1987.

[182] D. F. Wilson and G. J. Cerniglia, "Localization of Tumors and Evaluation of Their State of Oxygenation by Phosphorescence Imaging," *Cancer Research,* vol. 52, pp. 3988-3993, 1992.

[183] I. P. Torres Filho and M. Intaglietta, "Microvessel pO2 Measurements by Phosphorescence Decay Method," *American Journal of Physiology,* vol. 265, pp. H1434-H1438, 1993.

[184] S. A. Vinogradov, L. W. Lo, W. T. Jenkins, S. M. Evans, C. Koch, and D. F. Wilson, "Noninvasive imaging of the distribution in oxygen in tissue in vivo using near-infrared phosphors," *Biophysical Journal,* vol. 70, pp. 1609-1617, 1996.

[185] L. M. Smith, A. S. Golub, and R. N. Pittman, "Interstitial pO2 determination by phosphorescence quenching microscopy," *Microcirculation,* vol. 9, pp. 389-395, 2002.

[186] D. F. Wilson, S. A. Vinogadov, P. Grosul, N. Sund, M. N. Vacarezza, and J. Bennett, "Imaging oxygen pressure in the rodent retina by phosphorescence lifetime," *Oxygen Transport to Tissue Xxvii,* vol. 578, pp. 119-124, 2006.

[187] S. V. Apreleva, D. F. Wilson, and S. A. Vinogradov, "Tomographic imaging of oxygen by phosphorescence lifetime," *Applied Optics,* vol. 45, pp. 8547-8559, 2006.

[188] A. Y. Lebedev, A. V. Cheprakov, S. Sakadzic, D. A. Boas, D. F. Wilson, and S. A. Vinogradov, "Dendritic Phosphorescent Probes for Oxygen Imaging in Biological Systems," *Acs Applied Materials & Interfaces,* vol. 1, pp. 1292-1304, 2009.

[189] D. Sud, G. Mehta, K. Mehta, J. Linderman, S. Takayama, and M.-A. Mycek, "Optical imaging in microfluidic bioreactors enables oxygen monitoring for continuous cell culture," *Journal of Biomedical Optics,* vol. 11, pp. 0505041-3, 2006.

[190] J. E. Aubin, "Autofluorescence of Viable Cultured Mammalian-Cells," *Journal of Histochemistry & Cytochemistry,* vol. 27, pp. 36-43, 1979.

[191] D. B. Papkovsky and T. C. O'riordan, "Emerging applications of phosphorescent metalloporphyrins," *Journal of Fluorescence,* vol. 15, pp. 569-584, 2005.

[192] J. R. Bacon and J. N. Demas, "Determination of Oxygen Concentrations by Luminescence Quenching of a Polymer-Immobilized Transition-Metal Complex," *Analytical Chemistry,* vol. 59, pp. 2780-2785, 1987.

[193] C. McDonagh, C. Kolle, A. K. McEvoy, D. L. Dowling, A. A. Cafolla, S. J. Cullen*, et al.*, "Phase fluorometric dissolved oxygen sensor," *Sensors and Actuators B-Chemical,* vol. 74, pp. 124-130, 2001.

[194] X. Lu, B.-H. Han, and M. A. Winnik, "Characterizing the Quenching Process for Phosphorescent Dyes in Poly[((n-butylamino)thionyl)phosphazene] Films," *The Journal of Physical Chemistry B,* vol. 107, pp. 13349-13356, 2003.

[195] J. Q. Brown, R. Srivastava, and M. J. McShane, "Encapsulation of glucose oxidase and an oxygen-quenched fluorophore in polyelectrolyte-coated calcium alginate microspheres as optical glucose sensor systems," *Biosensors & bioelectronics,* vol. 21, pp. 212-6, 2005.

[196] I. Klimant and O. S. Wolfbeis, "Oxygen-Sensitive Luminescent Materials Based on Silicone-Soluble Ruthenium Diimine Complexes," *Analytical Chemistry,* vol. 67, pp. 3160-3166, 1995.

[197] K. Mongey, J. G. Vos, B. D. Maccraith, and C. M. Mcdonagh, "The photophysical properties of ruthenium polypyridyl complexes within a sol-gel matrix," *Journal of Sol-Gel Science and Technology,* vol. 8, pp. 979-983, 1997.

[198] D. Eastwood and Gouterma.M, "Porphyrins : XVIII. Luminescence of (Co), (Ni), Pd, Pt complexes," *Journal of Molecular Spectroscopy,* vol. 35, pp. 359-375, 1970.

[199] D. B. Papkovsky, J. Olah, I. V. Troyanovsky, N. A. Sadovsky, V. D. Rumyantseva, A. F. Mironov*, et al.*, "Phosphorescent Polymer-Films for Optical Oxygen Sensors," *Biosensors & Bioelectronics,* vol. 7, pp. 199-206, 1992.

[200] D. B. Papkovsky, G. V. Ponomarev, and O. S. Wolfbeis, "Longwave luminescent porphyrin probes," *Spectrochimica Acta Part a-Molecular and Biomolecular Spectroscopy,* vol. 52, pp. 1629-1638, 1996.

[201] M. Quaranta, S. M. Borisov, and I. Klimant, "Indicators for optical oxygen sensors," *Bioanal Rev,* vol. 4, pp. 115-157, 2012.

[202] S. A. Vinogradov and D. F. Wilson, "Metallotetrabenzoporphyrins - New Phosphorescent Probes for Oxygen Measurements," *Journal of the Chemical Society-Perkin Transactions 2,* pp. 103-111, 1995.

[203] I. Dunphy, S. A. Vinogradov, and D. F. Wilson, "Oxyphor R2 and G2: phosphors for measuring oxygen by oxygen-dependent quenching of phosphorescence," *Analytical Biochemistry,* vol. 310, pp. 191-198, 2002.

[204] S. M. Borisov, G. Nuss, and I. Klimant, "Red Light-Excitable Oxygen Sensing Materials Based on Platinum(II) and Palladium(II) Benzoporphyrins," *Analytical Chemistry,* vol. 80, pp. 9435-9442, 2008.

[205] L. H. Hutter, B. J. Muller, K. Koren, S. M. Borisov, and I. Klimant, "Robust optical oxygen sensors based on polymer-bound NIR-emitting platinum(II)-benzoporphyrins," *Journal of Materials Chemistry C,* vol. 2, pp. 7589-7598, 2014.

[206] B. J. Muller, T. Burger, S. M. Borisov, and I. KlimantGraz, "High performance optical trace oxygen sensors based on NIR-emitting benzoporphyrins covalently coupled to silicone matrixes," *Sensors and Actuators B-Chemical,* vol. 216, pp. 527-534, 2015.

[207] D. F. Wilson, W. L. Rumsey, T. J. Green, and J. M. Vanderkooi, "The Oxygen Dependence of Mitochondrial Oxidative-Phosphorylation Measured by a New Optical Method for Measuring Oxygen Concentration," *Journal of Biological Chemistry,* vol. 263, pp. 2712-2718, 1988.

[208] G. J. Cerniglia, D. F. Wilson, M. Pawlowski, S. Vinogradov, and J. Biaglow, "Intravascular oxygen distribution in subcutaneous 9L tumors and radiation sensitivity," *Journal of Applied Physiology,* vol. 82, pp. 1939-1945, 1997.

[209] L. W. Lo, C. J. Koch, and D. F. Wilson, "Calibration of oxygen-dependent quenching of the phosphorescence of Pd-meso-tetra (4-carboxyphenyl) porphine: A phosphor with general application for measuring oxygen concentration in biological systems," *Analytical Biochemistry,* vol. 236, pp. 153-160, 1996.

[210] T. Johannes, E. G. Mik, and C. Ince, "Dual-wavelength phosphorimetry for determination of cortical and subcortical microvascular oxygenation in rat kidney," *Journal of Applied Physiology,* vol. 100, pp. 1301-1310, 2006.

[211] T. Johannes, E. G. Mik, and C. Ince, "Nonresuscitated Endotoxemia Induces Microcirculatory Hypoxic Areas in the Renal Cortex in the Rat," *Shock,* vol. 31, pp. 97-103, 2009.

[212] E. G. Mik, T. Johannes, and C. Ince, "Monitoring of renal venous Po-2 and kidney oxygen consumption in rats by a near-infrared phosphorescence lifetime technique," *American Journal of Physiology-Renal Physiology,* vol. 294, pp. F676-F681, 2008.

[213] T. A. Orth, J. A. Allen, J. G. Wood, and N. C. Gonzalez, "Exercise training prevents the inflammatory response to hypoxia in cremaster venules," *Journal of Applied Physiology,* vol. 98, pp. 2113-2118, 2005.

[214] R. Pirow, C. Baumer, and R. J. Paul, "Crater landscape: two-dimensional oxygen gradients in the circulatory system of the microcrustacean Daphnia magna," *Journal of Experimental Biology,* vol. 207, pp. 4393-4405, 2004.

[215] D. C. Poole, B. J. Behnke, P. McDonough, R. M. McAllister, and D. F. Wilson, "Measurement of muscle microvascular oxygen pressures: Compartmentalization of phosphorescent probe," *Microcirculation,* vol. 11, pp. 317-326, 2004.

[216] D. F. Wilson, S. M. Evans, W. T. Jenkins, S. A. Vinogradov, E. Ong, and M. W. Dewhirst, "Oxygen distributions within R3230Ac tumors growing in dorsal flap window chambers in rats," *Oxygen Transport to Tissue Xx,* vol. 454, pp. 603-609, 1998.

[217] D. F. Wilson, W. M. F. Lee, S. Makonnen, S. Apreleva, and S. A. Vinogradov, "Oxygen pressures in the interstitial space of skeletal muscle and tumors in vivo," *Oxygen Transport to Tissue Xxix,* vol. 614, pp. 53-62, 2008.

[218] D. F. Wilson, W. M. F. Lee, S. Makonnen, O. Finikova, S. Apreleva, and S. A. Vinogradov, "Oxygen pressures in the interstitial space and their relationship to those in the blood plasma in resting skeletal muscle," *Journal of Applied Physiology,* vol. 101, pp. 1648-1656, 2006.

[219] D. F. Wilson, S. A. Vinogradov, B. W. Dugan, D. Biruski, L. Waldron, and S. A. Evans, "Measurement of tumor oxygenation using new frequency domain phosphorometers," *Comparative Biochemistry and Physiology a-Molecular and Integrative Physiology,* vol. 132, pp. 153-159, 2002.

[220] L. S. Ziemer, W. M. F. Lee, S. A. Vinogradov, C. Sehgal, and D. F. Wilson, "Oxygen distribution in murine tumors: characterization using oxygen-dependent quenching of phosphorescence," *Journal of Applied Physiology,* vol. 98, pp. 1503-1510, 2005.

[221] M. A. Yaseen, V. J. Srinivasan, S. Sakadzic, W. Wu, S. Ruvinskaya, S. A. Vinogradov*, et al.*, "Optical monitoring of oxygen tension in cortical microvessels with confocal microscopy," *Optics Express,* vol. 17, pp. 22341-22350, 2009.

[222] J. W. Dobrucki, "Interaction of oxygen-sensitive luminescent probes Ru(phen)(3)(2+) and Ru(bipy)(3)(2+) with animal and plant cells in vitro - Mechanism of phototoxicity and conditions for non-invasive oxygen measurements," *Journal of Photochemistry and Photobiology B-Biology,* vol. 65, pp. 136-144, 2001.

[223] P. C. Thomas, M. Halter, A. Tona, S. R. Raghavan, A. L. Plant, and S. P. Forry, "A noninvasive thin film sensor for monitoring oxygen tension during in vitro cell culture," *Analytical Chemistry,* vol. 81, pp. 9239-9246, 2009.

[224] P. Kiernan, C. McDonagh, B. D. Maccraith, and K. Mongey, "Ruthenium-doped sol-gel derived silica films: Oxygen sensitivity of optical decay times," *Journal of Sol-Gel Science and Technology,* vol. 2, pp. 513-517, 1994.

[225] S. K. Lee and I. Okura, "Photostable optical oxygen sensing material: Platinum tetrakis(pentafluorophenyl)porphyrin immobilized in polystyrene," *Analytical Communications,* vol. 34, pp. 185-188, 1997.

[226] Y. Amao, K. Asai, and I. Okura, "Oxygen sensing based on lifetime of photoexcited triplet state of platinum porphyrin-polystyrene film using time-resolved spectroscopy," *Journal of Porphyrins and Phthalocyanines,* vol. 4, pp. 292-299, 2000.

[227] D. B. Papkovsky, "Luminescent Porphyrins as Probes for Optical (Bio)Sensors," *Sensors and Actuators B-Chemical,* vol. 11, pp. 293-300, 1993.

[228] P. Lavin, C. M. Mcdonagh, and B. D. Maccraith, "Optimization of Ormosil films for optical sensor applications," *Journal of Sol-Gel Science and Technology,* vol. 13, pp. 641-645, 1998.

[229] C. McDonagh, B. D. MacCraith, and A. K. McEvoy, "Tailoring of sol-gel films for optical sensing of oxygen in gas and aqueous phase," *Analytical Chemistry,* vol. 70, pp. 45-50, 1998.

[230] V. I. Ogurtsov and D. B. Papkovsky, "Application of frequency spectroscopy to fluorescence-based oxygen sensors," *Sensors and Actuators B-Chemical,* vol. 113, pp. 608-616, 2006.

[231] V. S. Tripathi, V. B. Kandimalla, and H. X. Ju, "Preparation of ormosil and its applications in the immobilizing biomolecules," *Sensors and Actuators B-Chemical,* vol. 114, pp. 1071-1082, 2006.

[232] B. J. Basu, "Optical oxygen sensing based on luminescence quenching of platinum porphyrin dyes doped in ormosil coatings," *Sensors and Actuators B-Chemical,* vol. 123, pp. 568-577, 2007.

[233] V. Sunkara, D. K. Park, H. Hwang, R. Chantiwas, S. A. Soper, and Y. K. Cho, "Simple room temperature bonding of thermoplastics and poly(dimethylsiloxane)," *Lab on a chip,* vol. 11, pp. 962-965, 2011.

[234] L. Tang and N. Y. Lee, "A facile route for irreversible bonding of plastic-PDMS hybrid microdevices at room temperature," *Lab on a chip,* vol. 10, pp. 1274-1280, 2010.

[235] B. Y. Xu, X. N. Yan, J. J. Xu, and H. Y. Chen, "One step high quality poly(dimethylsiloxane)-hydrocarbon plastics bonding," *Biomicrofluidics,* vol. 6, pp. 016507–016507-8, 2012.

[236] E. Sinkala and D. T. Eddington, "Oxygen sensitive microwells," *Lab Chip,* vol. 10, pp. 3291-5, 2010.

[237] H. X. Zhu, Y. Q. Tian, S. Bhushan, F. Y. Su, and D. R. Meldrum, "High Throughput Micropatterning of Optical Oxygen Sensor," *2010 IEEE SENSORS,* pp. 2053-2056, 2010.

[238] V. Nock, L. M. Murray, M. M. Alkaisi, and R. J. Blaikie, "Patterning of polymer-encapsulated optical oxygen sensors by electron beam lithography," presented at the Nanoscience and Nanotechnology (ICONN), 2010 International Conference on, Sydney, NSW, 2010.

[239] S. M. Grist, N. Oyunerdene, J. Flueckiger, J. Kim, P. C. Wong, L. Chrostowski*, et al.,* "Fabrication and laser patterning of polystyrene optical oxygen sensor films for lab-on-a-chip applications," *Analyst,* vol. 139, pp. 5718-5727, 2014.

[240] T. W. Molter, S. C. McQuaide, M. T. Suchorolski, T. J. Strovas, L. W. Burgess, D. R. Meldrum*, et al.*, "A microwell array device capable of measuring single-cell oxygen consumption rates," *Sensors and Actuators B-Chemical,* vol. 135, pp. 678-686, 2009.

[241] J. R. Etzkorn and et al., "Using micro-patterned sensors and cell self-assembly for measuring the oxygen consumption rate of single cells," *Journal of Micromechanics and Microengineering,* vol. 20, p. 095017, 2010.

[242] C. Gartner, B. Ungerbock, I. Schulz, T. Jahn, A. Mosig, T. Mayr*, et al.*, "Sensor enhanced microfluidic devices for cell based assays and organs on chip," *Smart Biomedical and Physiological Sensor Technology Xii,* vol. 9487, 2015.

[243] J. Ehgartner, P. Sulzer, T. Burger, A. Kasjanow, D. Bouwes, U. Krühne*, et al.*, "Online analysis of oxygen inside silicon-glass microreactors with integrated optical sensors," *Sensors and Actuators B: Chemical,* vol. 228, pp. 748-757, 2016.

[244] G. Mehta, J. Lee, W. Cha, Y. C. Tung, J. J. Linderman, and S. Takayama, "Hard Top Soft Bottom Microfluidic Devices for Cell Culture and Chemical Analysis," *Analytical Chemistry,* vol. 81, pp. 3714-3722, 2009.

[245] A. Groisman, M. Adler, M. Polinkovsky, and E. Gutierrez, "Generation of oxygen gradients with arbitrary shapes in a microfluidic device," *Lab on a chip,* vol. 10, pp. 388-391, 2010.

[246] K. Funamoto, I. K. Zervantonakis, Y. C. Liu, C. J. Ochs, C. Kim, and R. D. Kamm, "A novel microfluidic platform for high-resolution imaging of a three-dimensional cell culture under a controlled hypoxic environment," *Lab on a chip,* vol. 12, pp. 4855-4863, 2012.

[247] P. C. Thomas, S. R. Raghavan, and S. P. Forry, "Regulating Oxygen Levels in a Microfluidic Device," *Analytical Chemistry,* vol. 83, pp. 8821-8824, 2011.

[248] S. P. Forry and L. E. Locascio, "On-chip CO2 control for microfluidic cell culture," *Lab on a Chip,* vol. 11, pp. 4041-6, 2011.

[249] Y. A. Chen, A. D. King, H. C. Shih, C. C. Peng, C. Y. Wu, W. H. Liao*, et al.*, "Generation of oxygen gradients in microfluidic devices for cell culture using spatially confined chemical reactions," *Lab on a chip,* vol. 11, pp. 3626-3633, 2011.

[250] L. Wang, W. Liu, Y. Wang, J. C. Wang, Q. Tu, R. Liu*, et al.*, "Construction of oxygen and chemical concentration gradients in a single microfluidic device for studying tumor cell-drug interactions in a dynamic hypoxia microenvironment," *Lab on a Chip,* vol. 13, pp. 695-705, 2013.

[251] M.-C. Kim, R. W. Lam, T. Thorsen, and H. H. Asada, "Mathematical analysis of oxygen transfer through polydimethylsiloxane membrane between double layers of cell culture channel and gas chamber in microfluidic oxygenator," *Microfluidics and Nanofluidics,* pp. 1-12, 2013.

[252] D. K. Wood, A. Soriano, L. Mahadevan, J. M. Higgins, and S. N. Bhatia, "A biophysical indicator of vaso-occlusive risk in sickle cell disease," *Science Translational Medicine,* vol. 4, p. 123ra26, 2012.

[253] M. D. Brennan, M. L. Rexius-Hall, L. J. Elgass, and D. T. Eddington, "Oxygen control with microfluidics," *Lab Chip,* vol. 14, pp. 4305-18, 2014.

[254] A. Groisman, M. Polinkovsky, E. Gutierrez, and A. Levchenko, "Fine temporal control of the medium gas content and acidity and on-chip generation of series of oxygen concentrations for cell cultures," *Lab on a chip,* vol. 9, pp. 1073-1084, 2009.

[255] S. C. Oppegard, K. H. Nam, J. R. Carr, S. C. Skaalure, and D. T. Eddington, "Modulating Temporal and Spatial Oxygenation over Adherent Cellular Cultures," *Plos One,* vol. 4, p. e6891, 2009.

[256] S. C. Oppegard, A. J. Blake, J. C. Williams, and D. T. Eddington, "Precise control over the oxygen conditions within the Boyden chamber using a microfabricated insert," *Lab on a chip,* vol. 10, pp. 2366-2373, 2010.

[257] J. F. Lo, Y. Wang, A. Blake, G. Yu, T. A. Harvat, H. Jeon*, et al.*, "Islet preconditioning via multimodal microfluidic modulation of intermittent hypoxia," *Anal Chem,* vol. 84, pp. 1987-93, 2012.

[258] G. Mauleon, C. P. Fall, and D. T. Eddington, "Precise Spatial and Temporal Control of Oxygen within In Vitro Brain Slices via Microfluidic Gas Channels," *Plos One,* vol. 7, 2012.

[259] S. Martewicz, F. Michielin, E. Serena, A. Zambon, M. Mongillo, and N. Elvassore, "Reversible alteration of calcium dynamics in cardiomyocytes during acute hypoxia transient in a microfluidic platform," *Integr Biol (Camb),* vol. 4, pp. 153-64, 2012.

[260] L. Wang, M. A. Acosta, J. B. Leach, and R. L. Carrier, "Spatially monitoring oxygen level in 3D microfabricated cell culture systems using optical oxygen sensing beads," *Lab on a chip,* vol. 13, pp. 1586-1592, 2013.

[261] A. A. Jaeger, C. K. Das, N. Y. Morgan, R. H. Pursley, P. G. McQueen, M. D. Hall*, et al.*, "Microfabricated polymeric vessel mimetics for 3-D cancer cell culture," *Biomaterials,* vol. 34, pp. 8301-13, 2013.

[262] C. M. Ghajar and M. J. Bissell, "Tumor Engineering: The Other Face of Tissue Engineering," *Tissue Engineering Part A,* vol. 16, pp. 2153-2156, 2010.

[263] A. D. Stroock and C. Fischbach, "Microfluidic Culture Models of Tumor Angiogenesis," *Tissue Engineering Part A,* vol. 16, pp. 2143-2146, 2010.

[264] M. C. Chen, M. Gupta, and K. C. Cheung, "Alginate-based microfluidic system for tumor spheroid formation and anticancer agent screening," *Biomedical Microdevices,* vol. 12, pp. 647-54, 2010.

[265] L. Yu, S. M. Grist, S. S. Nasseri, E. Cheng, Y. C. E. Hwang, C. Ni*, et al.*, "Core-shell hydrogel beads with extracellular matrix for tumor spheroid formation," *Biomicrofluidics,* vol. 9, p. 024118, 2015.

[266] L. Yu, C. Ni, S. Grist, C. Bayly, and K. Cheung, "Alginate core-shell beads for simplified three-dimensional tumor spheroid culture and drug screening," *Biomedical Microdevices,* vol. 17, p. 33, 2015.

[267] S. M. Grist*, S. S. Nasseri*, T. Poon, M.-C. Liu, C. Roskelley, and K. C. Cheung, "Two-photon imaging for long-term tumor model monitoring in a microfluidic device," presented at the The 19th International Conference on Miniaturized Systems for Chemistry and Life Sciences (MicroTAS 2015), Gyeongju, Korea, 2015.

[268] A. Sakaue-Sawano, H. Kurokawa, T. Morimura, A. Hanyu, H. Hama, H. Osawa*, et al.*, "Visualizing Spatiotemporal Dynamics of Multicellular Cell-Cycle Progression," *Cell,* vol. 132, pp. 487-498, 2008.

[269] A. Sakaue-Sawano, K. Ohtawa, H. Hama, M. Kawano, M. Ogawa, and A. Miyawaki, "Tracing the silhouette of individual cells in S/G2/M phases with fluorescence," *Chem Biol,* vol. 15, pp. 1243-8, 2008.

[270] H. G. Hall, D. A. Farson, and M. J. Bissell, "Lumen formation by epithelial cell lines in response to collagen overlay: a morphogenetic model in culture," *Proc Natl Acad Sci U S A,* vol. 79, pp. 4672-6, 1982.

[271] M. Swamydas, J. M. Eddy, K. J. Burg, and D. Dreau, "Matrix compositions and the development of breast acini and ducts in 3D cultures," *In Vitro Cell Dev Biol Anim,* vol. 46, pp. 673-84, 2010.

[272] Amalgaam. (2010). *FUCCI: fluorescent ubiquination-based cell cycle indicator*. Available: http://www.amalgaam.co.jp/products/advanced/fucci.html. Accessed: March 1 2014.

[273] J. J. Dirckx, L. C. Kuypers, and W. F. Decraemer, "Refractive index of tissue measured with confocal microscopy," *J Biomed Opt,* vol. 10, p. 44014, 2005.

[274] S. M. Grist*, E. Cheng*, L. F. Yu, and K. C. Cheung, "Modulated two-photon imaging of whole spheroids for three-dimensional cell cultures," presented at the The 18th International Conference on Miniaturized Systems for Chemistry and Life Sciences (MicroTAS 2014), San Antonio, Texas, 2014.

[275] G. Hamilton, "Multicellular spheroids as an in vitro tumor model," *Cancer Letters,* vol. 131, pp. 29-34, 1998.

[276] S. Y. Kim, K. Chung, and K. Deisseroth, "Light microscopy mapping of connections in the intact brain," *Trends in Cognitive Sciences,* vol. 17, pp. 596-599, 2013.

[277] S. M. Grist*, S. S. Nasseri*, C. Ni, C. Roskelley, and K. C. Cheung, "μSee3D: On-chip tissue clearing for imaging 3-D cell cultures," presented at the The 19th International Conference on Miniaturized Systems for Chemistry and Life Sciences (MicroTAS 2015), Gyeongju, Korea, 2015.

[278] N. Otsu, "Threshold Selection Method from Gray-Level Histograms," *Ieee Transactions on Systems Man and Cybernetics,* vol. 9, pp. 62-66, 1979.

[279] D. S. Richardson and J. W. Lichtman, "Clarifying Tissue Clearing," *Cell,* vol. 162, pp. 246-57, 2015.

[280] S. Grist, J. Schmok, M.-C. Liu, L. Chrostowski, and K. Cheung, "Designing a Microfluidic Device with Integrated Ratiometric Oxygen Sensors for the Long-Term Control and Monitoring of Chronic and Cyclic Hypoxia," *Sensors,* vol. 15, p. 20030, 2015.

[281] E. Cheng, C. Song, L. Yu, and K. C. Cheung, "Automated Analysis of Collagen Reorganization Over Time in Three-Dimensional Cell Cultures," presented at the 18th International Conference on Miniaturized Systems for Chemistry and Life Sciences (MicroTAS 2014), San Antonio, Texas, USA, 2014.

[282] L. Wang, L. Lei, X. F. Ni, J. Shi, and Y. Chen, "Patterning bio-molecules for cell attachment at single cell levels in PDMS microfluidic chips," *Microelectronic Engineering,* vol. 86, pp. 1462-1464, 2009.

[283] S. Jung, Y. G. Choo, and T. Ji, "Lift-Off Photolithographic Top-Contact OTFTs Using a Bilayer of PVA and SU8," *Ieee Electron Device Letters,* vol. 33, pp. 603-605, 2012.

[284] K. A. Addae-Mensah, R. S. Reiserer, and J. P. Wikswo, "Poly(vinyl alcohol) as a structure release layer for the microfabrication of polymer composite structures," *Journal of Micromechanics and Microengineering,* vol. 17, pp. N41-N46, 2007.

[285] S. M. Grist, L. Chrostowski, and K. C. Cheung, "Thin film patterning using a water-soluble etch mask," presented at the The 16th International Conference on Miniaturized Systems for Chemistry and Life Sciences, Okinawa, Japan, 2012.

[286]   M. Tsunekawa, S. Nishio, and H. Sato, "Multiphoton Ionization Mass-Spectrometric Study on Laser-Ablation of Polymethylmethacrylate and Polystyrene at 308-Nm," *Japanese Journal of Applied Physics Part 1-Regular Papers Short Notes & Review Papers,* vol. 34, pp. 218-225, 1995.

[287]   M. Tsunekawa, S. Nishio, and H. Sato, "Laser-Ablation of Polymethylmethacrylate and Polystyrene at 308-Nm - Demonstration of Thermal and Photothermal Mechanisms by a Time-of-Flight Mass Spectroscopic Study," *Journal of Applied Physics,* vol. 76, pp. 5598-5600, 1994.

[288]   M. A. Hopcroft, "MAT-Test: A New Method for Thin-Film Materials Characterization," MPhil PhD Thesis, Engineering, Cambridge University, United Kingdom, 2002.

[289]   S. R. I. Gabran, R. R. Mansour, and M. M. A. Salama, "Maskless pattern transfer using 355 nm laser," *Optics and Lasers in Engineering,* vol. 50, pp. 710-716, 2012.

[290]   S. Bhattacharya, A. Datta, J. M. Berg, and S. Gangopadhyay, "Studies on surface wettability of poly(dimethyl) siloxane (PDMS) and glass under oxygen-plasma treatment and correlation with bond strength," *Journal of Microelectromechanical Systems,* vol. 14, pp. 590-597, 2005.

[291]   S. Gawad, "Development of a microscope automation system for cancer cell analysis," Master's of Engineering, Electrical and Computer Engineering, The University of British Columbia and École Polytechnique Fédérale de Lausanne, Vancouver, Canada, 2013.

[292]   S. M. Grist, S. Gawad, C. Bayly, L. F. Yu, L. Chrostowski, and K. C. Cheung, "3D cell culture with integrated oxygen control and measurement," presented at the CMBEC 37 Conference, Vancouver, 2014.

[293]   AquaServ. (2010). *The fundamentals of oxygen scavengers*. Available: http://hvac-talk.com/vbb/attachment.php?attachmentid=137901&d=1289782733. Accessed: December 1 2015.

[294]   R. R. Cavano. (2007). *Sulfites for oxygen control*. Available: http://www.natcoll.com/wp-content/uploads/Sulfites-for-Oxygen-Control.pdf. Accessed: December 1 2015.

[295]   D. A. Armbruster and T. Pry, "Limit of blank, limit of detection and limit of quantitation," *Clin Biochem Rev,* vol. 29 Suppl 1, pp. S49-52, 2008.

[296]   K. Koren, S. M. Borisov, and I. Klimant, "Stable optical oxygen sensing materials based on click-coupling of fluorinated platinum(II) and palladium(II) porphyrins-A convenient way to eliminate dye migration and leaching," *Sens Actuators B Chem,* vol. 169, pp. 173-181, 2012.

[297]   C. S. Chu and Y. L. Lo, "Ratiometric fiber-optic oxygen sensors based on sol-gel matrix doped with metalloporphyrin and 7-amino-4-trifluoromethyl coumarin," *Sensors and Actuators B-Chemical,* vol. 134, pp. 711-717, 2008.

[298]   P. Lehner, C. Staudinger, S. M. Borisov, and I. Klimant, "Ultra-sensitive optical oxygen sensors for characterization of nearly anoxic systems," *Nature Communications,* vol. 5, 2014.

[299]   H. Bruus, *Theoretical microfluidics*. Oxford ; New York: Oxford University Press, 2008.

[300]   D. A. Markov, E. M. Lillie, S. P. Garbett, and L. J. McCawley, "Variation in diffusion of gases through PDMS due to plasma surface treatment and storage conditions," *Biomed Microdevices,* vol. 16, pp. 91-6, 2014.

[301]   J. Park, T. Bansal, M. Pinelis, and M. M. Maharbiz, "A microsystem for sensing and patterning oxidative microgradients during cell culture," *Lab Chip,* vol. 6, pp. 611-22, 2006.

[302]   E. Toolbox. (2015). *Coefficients of Linear Thermal Expansion*. Available: http://www.engineeringtoolbox.com/linear-expansion-coefficients-d_95.html. Accessed: November 24 2015.

[303]   J. H. Koschwanez, R. H. Carlson, and D. R. Meldrum, "Thin PDMS films using long spin times or tert-butyl alcohol as a solvent," *PLoS One,* vol. 4, p. e4572, 2009.

[304]   A. B. Cubitt, R. Heim, S. R. Adams, A. E. Boyd, L. A. Gross, and R. Y. Tsien, "Understanding, Improving and Using Green Fluorescent Proteins," *Trends in Biochemical Sciences,* vol. 20, pp. 448-455, 1995.

[305]   D. C. Prasher, "Using GFP to See the Light," *Trends in Genetics,* vol. 11, pp. 320-323, 1995.

[306]   D. Ehrhardt, "GFP technology for live cell imaging," *Curr Opin Plant Biol,* vol. 6, pp. 622-8, 2003.

[307]   C. Coralli, M. Cemazar, C. Kanthou, G. M. Tozer, and G. U. Dachs, "Limitations of the reporter green fluorescent protein under simulated tumor conditions," *Cancer Res,* vol. 61, pp. 4784-90, 2001.

[308]   M. A. Qadir, B. Kwok, W. H. Dragowska, K. H. To, D. Le, M. B. Bally*, et al.*, "Macroautophagy inhibition sensitizes tamoxifen-resistant breast cancer cells and enhances mitochondrial depolarization," *Breast Cancer Res Treat,* vol. 112, pp. 389-403, 2008.

[309]   D. Vordermark, T. Shibata, and J. M. Brown, "Green fluorescent protein is a suitable reporter of tumor hypoxia despite an oxygen requirement for chromophore formation," *Neoplasia,* vol. 3, pp. 527-534, 2001.

[310]   M. C. Hansen, R. J. Palmer, C. Udsen, D. C. White, and S. Molin, "Assessment of GFP fluorescence in cells of Streptococcus gordonii under conditions of low pH and low oxygen concentration," *Microbiology-Sgm,* vol. 147, pp. 1383-1391, 2001.

[311]   P. M. S. Roma, L. Siman, F. T. Amaral, U. Agero, and O. N. Mesquita, "Total three-dimensional imaging of phase objects using defocusing microscopy: Application to red blood cells," *Applied Physics Letters,* vol. 104, p. 251107, 2014.

[312]   N. Mizushima, T. Yoshimori, and B. Levine, "Methods in mammalian autophagy research," *Cell,* vol. 140, pp. 313-26, 2010.

[313]   S. Barth, D. Glick, and K. F. Macleod, "Autophagy: assays and artifacts," *J Pathol,* vol. 221, pp. 117-24, 2010.

[314]   O. Tacar, P. Sriamornsak, and C. R. Dass, "Doxorubicin: an update on anticancer molecular action, toxicity and novel drug delivery systems," *J Pharm Pharmacol,* vol. 65, pp. 157-70, 2013.

[315]   G. Takemura and H. Fujiwara, "Doxorubicin-induced cardiomyopathy from the cardiotoxic mechanisms to management," *Prog Cardiovasc Dis,* vol. 49, pp. 330-52, 2007.

[316]   S. Doublier, D. C. Belisario, M. Polimeni, L. Annaratone, C. Riganti, E. Allia*, et al.*, "HIF-1 activation induces doxorubicin resistance in MCF7 3-D spheroids via P-glycoprotein expression: a potential model of the chemo-resistance of invasive micropapillary carcinoma of the breast," *BMC Cancer,* vol. 12, p. 4, 2012.

[317]   L. Panasci, B. J. Jean-Claude, D. Vasilescu, A. Mustafa, S. Damian, Z. Damian*, et al.*, "Sensitization to doxorubicin resistance in breast cancer cell lines by tamoxifen and megestrol acetate," *Biochem Pharmacol,* vol. 52, pp. 1097-102, 1996.

[318]   E. Berthier, E. W. Young, and D. Beebe, "Engineers are from PDMS-land, Biologists are from Polystyrenia," *Lab Chip,* vol. 12, pp. 1224-37, 2012.

[319]   D. Curry, H. Scheller, M. Lu, M. Mkandawire, M. R. Servos, S. Cui*, et al.*, "Prevention of doxorubicin sorptive losses in drug delivery studies using polyethylene glycol," *RSC Advances,* vol. 5, pp. 25693-25698, 2015.

[320]   V. Lecault, M. Vaninsberghe, S. Sekulovic, D. J. Knapp, S. Wohrer, W. Bowden*, et al.*, "High-throughput analysis of single hematopoietic stem cell proliferation in microfluidic cell culture arrays," *Nat Methods,* vol. 8, pp. 581-6, 2011.

[321]   P. Thevenaz, U. E. Ruttimann, and M. Unser, "A pyramid approach to subpixel registration based on intensity," *Ieee Transactions on Image Processing,* vol. 7, pp. 27-41, 1998.

[322]   S. M. Grist, J. C. Schmok, M.-C. A. Liu, L. Chrostowski, and K. C. Cheung, "A Microfluidic Platform to Study Real-time Tumour Spheroid Response to Chronic/Transient Hypoxia," presented at the The 19th International Conference on Miniaturized Systems for Chemistry and Life Sciences (MicroTAS 2015), Gyeongju, Korea, 2015.

[323]   K. Alessandri, B. R. Sarangi, V. V. Gurchenkov, B. Sinha, T. R. Kiessling, L. Fetler*, et al.*, "Cellular capsules as a tool for multicellular spheroid production and for investigating the mechanics of tumor progression in vitro," *Proceedings of the National Academy of Sciences of the United States of America,* vol. 110, pp. 14843-14848, 2013.

[324]   J. P. Cobb, R. S. Hotchkiss, I. E. Karl, and T. G. Buchman, "Mechanisms of cell injury and death," *British Journal of Anaesthesia,* vol. 77, pp. 3-10, 1996.

[325]   L. Cassimeris, V. R. Lingappa, G. Plopper, and B. Lewin, *Lewin's cells*, 2nd ed. Sudbury, Mass.: Jones and Bartlett Publishers, 2011.

[326]   T. J. Yin, S. Y. Yu, L. Xiao, J. Zhang, C. Liu, Y. P. Lu*, et al.*, "Correlation between the expression of aquaporin 1 and hypoxia-inducible factor 1 in breast cancer tissues," *Journal of Huazhong University of Science and Technology-Medical Sciences,* vol. 28, pp. 346-348, 2008.

[327]   L. Tie, N. Lu, X. Y. Pan, Y. Pan, Y. An, J. W. Gao*, et al.*, "Hypoxia-induced up-regulation of aquaporin-1 protein in prostate cancer cells in a p38-dependent manner," *Cell Physiol Biochem,* vol. 29, pp. 269-80, 2012.

[328]   M. L. Skiles, S. Sahai, L. Rucker, and J. O. Blanchette, "Use of culture geometry to control hypoxia-induced vascular endothelial growth factor secretion from adipose-derived stem cells: optimizing a cell-based approach to drive vascular growth," *Tissue Eng Part A,* vol. 19, pp. 2330-8, 2013.

[329]   K. Kvilekval, D. Fedorov, B. Obara, A. Singh, and B. S. Manjunath, "Bisque: a platform for bioimage analysis and management," *Bioinformatics,* vol. 26, pp. 544-52, 2010.

[330]   R. G. Boutilier, "Mechanisms of cell survival in hypoxia and hypothermia," *J Exp Biol,* vol. 204, pp. 3171-81, 2001.

[331]   L. Sforna, M. Cenciarini, S. Belia, A. Michelucci, M. Pessia, F. Franciolini*, et al.*, "Hypoxia Modulates the Swelling-Activated Cl Current in Human Glioblastoma Cells: Role in Volume Regulation and Cell Survival," *J Cell Physiol,* 2016.

[332]   M. Marin, A. Poret, G. Maillet, F. Leboulenger, and F. Le Foll, "Regulation of volume-sensitive Cl- channels in multi-drug resistant MCF7 cells," *Biochem Biophys Res Commun,* vol. 334, pp. 1266-78, 2005.

[333] R. M. Neve, K. Chin, J. Fridlyand, J. Yeh, F. L. Baehner, T. Fevr*, et al.*, "A collection of breast cancer cell lines for the study of functionally distinct cancer subtypes," *Cancer Cell,* vol. 10, pp. 515-27, 2006.

[334] A. S. Yap, M. Michael, and R. G. Parton, "Seeing and believing: recent advances in imaging cell-cell interactions," *F1000Res,* vol. 4, p. 273, 2015.

[335] C. Lochovsky, S. Yasotharan, and A. Gunther, "Bubbles no more: in-plane trapping and removal of bubbles in microfluidic devices," *Lab Chip,* vol. 12, pp. 595-601, 2012.

[336] P. Lehner, C. Staudinger, S. M. Borisov, J. Regensburger, and I. Klimant, "Intrinsic Artefacts in Optical Oxygen Sensors—How Reliable are our Measurements?," *Chemistry – A European Journal,* vol. 21, pp. 3978-3986, 2015.

Appendix

Appendix A Full List of Publications During Graduate Program

This Appendix presents the full list of publications to which I contributed during my graduate program.

a) Articles Published or Accepted in Refereed Journals (13)

1. **S. Grist,** J. Schmok, M.-C. Liu, L. Chrostowski, and K. Cheung, "Designing a Microfluidic Device with Integrated Ratiometric Oxygen Sensors for the Long-Term Control and Monitoring of Chronic and Cyclic Hypoxia," *Sensors,* vol. 15, p. 20030, 2015. (Graduate Work, Invited Feature Paper)

2. L. Yu, **S. M. Grist**, S. S. Nasseri, E. Cheng, Y. C. E. Hwang, C. Ni and K. C. Cheung. *Core-shell hydrogel beads with extracellular matrix for tumor spheroid formation.* Biomicrofluidics, 2015, 9. (Graduate Work)

3. L. Yu, C. Ni, **S. M. Grist**, C. Bayly and K. C. Cheung. *Alginate core-shell beads for simplified three-dimensional tumor spheroid culture and drug screening.* Biomedical Microdevices, 2015, 17, 9918. (Graduate Work)

4. Valentina Donzella, Ahmed Sherwali, Jonas Flueckiger, **Samantha M. Grist**, Sahba Talebi Fard, and Lukas Chrostowski. *Design and fabrication of SOI micro-ring resonators based on sub-wavelength grating waveguides.* Optics Express, 2015, 23, 4791-4803. (Graduate Work)

5. S. T. Fard, K. Murray, M. Caverley, V. Donzella, J. Flueckiger, **S. M. Grist**, E. Huante-Ceron, S. A. Schmidt, E. Kwok, N. A. F. Jaeger, A. P. Knights and L. Chrostowski, *Silicon-on-insulator sensors using integrated resonance-enhanced defect-mediated photodetectors*, *Optics Express,* 22, 28517-28529, Nov 17 2014. (Graduate Work)

6. V. Donzella, A. Sherwali, J. Flueckiger, S. T. Fard, **S. M. Grist**, and L. Chrostowski, *Sub-wavelength grating components for integrated optics applications on SOI chips*, Optics Express, 22, 21037-21050, Aug 25 2014. (Graduate Work)

7. **S. M. Grist**, N. Oyunerdene, J. Flueckiger, J. Kim, P. C. Wong, L. Chrostowski and K. C. Cheung, "Fabrication and laser patterning of polystyrene optical oxygen sensor films for lab-on-a-chip applications," *Analyst,* vol. 139, pp. 5718-5727, Nov 21 2014. (Graduate Work)

8. Sahba Talebi Fard, Valentina Donzella, Shon A. Schmidt, Jonas Flueckiger, **Samantha M. Grist**, Pouria Talebi Fard, Yichen Wu, Rick J. Bojko, Ezra Kwok, Nicolas A. F. Jaeger, Daniel M. Ratner, and Lukas Chrostowski. *Performance of ultra-thin SOI-based resonators for sensing applications*. Optics Express. 22. 14166-14179. June 16 2014. (Graduate Work)

9. X. Wang, **S. Grist**, J. Flueckiger, N. A. F. Jaeger, and L. Chrostowski. *Silicon photonic slot waveguide Bragg gratings and resonators*, Optics Express. 21. 19029-19039. Aug 12 2013. (Graduate Work)

10. X. Wang, J. Flueckiger, S. Schmidt, **S. Grist**, S. T. Fard, J. Kirk, M. Doerfler, K. C. Cheung, D. M. Ratner, and L. Chrostowski. *A silicon photonic biosensor using phase-shifted Bragg gratings in slot waveguide*. Journal of Biophotonics. 6, 821-828, Apr 11 2013. (Graduate Work)

11. **S. M. Grist**[†], S. A. Schmidt[†], J. Flueckiger, V. Donzella, W. Shi, S. Talebi Fard, J. T. Kirk, D. M. Ratner, K. C. Cheung, and L. Chrostowski. *Silicon photonic micro-disk resonators for label-free biosensing*. Optics Express. 21. 7994-8006. Apr 8 2013. (Graduate Work)

12. Xu Wang, Wei Shi, Han Yun, **Samantha Grist,** Nicolas A. F. Jaeger, Lukas Chrostowski. *Narrow-band waveguide Bragg gratings on SOI wafers with CMOS-compatible fabrication process*. Optics Express. 20(14). 15547-15558. (Graduate Work)

13. **Samantha M. Grist**, Lukas Chrostowski and Karen C. Cheung. 2010. *Optical Oxygen Sensors for Applications in Microfluidic Cell Culture*. Sensors 2010, 10(7). (Graduate Work)

b) Conference Papers, Presentations, and Posters (13)

14. **Samantha Marie Grist*,** S. Soroush Nasseri, Jonathan Schmok, Loïc Laplatine, Meng-Chi (Andy) Liu, Lukas Chrostowski, and Karen C. Cheung. *A microfluidic platform for 3-D cell-based screening of cancer treatments under chronic and transient hypoxia*. Presented orally at SLAS 2016. Awarded a Tony B. Academic Travel Award. (Graduate Work, International)

15. **Samantha M. Grist***, Jonathan C. Schmok, S. Soroush Nasseri, Meng-Chi (Andy) Liu, Lukas Chrostowski, and Karen C. Cheung. *A Microfluidic Platform to Study Real-time Tumour Spheroid Response to Chronic/Transient Hypoxia* Presented as a poster at MicroTAS 2015 in October 2015. pp. 2081-2082. (Graduate Work, International)

16. **Samantha M. Grist***[†], S. Soroush Nasseri*[†], Tak Poon, Cynthia Ni, Calvin Roskelley, and Karen C. Cheung. *μSee3D: On-chip tissue clearing for imaging 3D cell cultures*. Presented orally at MicroTAS 2015 in October 2015. pp. 308-310. (Graduate Work, International)

17. **Samantha Grist***[†], S. Soroush Nasseri*[†], Tak Poon, Meng-Chi (Andy) Liu, Calvin Roskelley, and Karen C. Cheung. *Two-photon imaging for long-term tumor model monitoring in a microfluidic device*. Presented as a poster at MicroTAS 2015 in October 2015. pp. 594-596. (Graduate Work, International)

18. **Samantha M. Grist***, Andy Liu, Selim Gawad, Lukas Chrostowski, and Karen C. Cheung. *A microfluidic device with integrated oxygen sensors for the cell-based screening of cancer treatments under transient hypoxia*. SLAS 2015. Awarded a Tony B. Academic Travel Award and Best Student Poster Award. (Graduate Work, International)

19. **S. M. Grist***[†]**,** E. Cheng*[†], L. F. Yu, and K. C. Cheung, *Modulated two-photon imaging of whole spheroids for three-dimensional cell cultures*, presented at the 18th International Conference on Miniaturized Systems for Chemistry and Life Sciences (MicroTAS 2014), San Antonio, Texas, 2014. pp. 551-553. (Graduate Work, International)

20. **Samantha M. Grist***, Selim Gawad, Carmen Bayly, Linfen Yu, Lukas Chrostowski, and Karen C. Cheung. *3D Cell culture with integrated oxygen control and measurement*. Proceedings of the CMBEC 37 conference. 2014. 862909-862909-14. Awarded 3rd place in Best Student Paper competition. (Graduate Work, National)

21. S. Talebi Fard*, **S. M. Grist**, V. Donzella, S. A. Schmidt, J. Flueckiger, X. Wang, W. Shi, A. Millspaugh, M. Webb, D. M. Ratner, K. C. Cheung, and L. Chrostowski. *Label-free silicon photonic biosensors for use in clinical diagnostics*. Proc. SPIE, Silicon Photonics VIII, Volume 8629, Issue 862909, p.862909--14 (2013). (Graduate Work, International)

22. **Samantha M. Grist*,** Lukas Chrostowski, Karen C. Cheung, *Thin film patterning using a water-soluble etch mask*, The 16th International Conference on Miniaturized Systems for Chemistry and Life Sciences, Okinawa, Japan, October 26-November 1, 2012. pp. 668-670. (Graduate Work, International)

23. **Samantha Grist**, Linfen Yu, Lukas Chrostowski, Karen C. Cheung*. *Microfluidic cell culture systems with integrated sensors for drug screening*. Proceedings of SPIE Volume 8251; Microfluidics, BioMEMS, and Medical Microsystems X, 01/2012. (Graduate Work, International)

24. Lukas Chrostowski*, **Samantha Grist**, Jonas Flueckiger, Wei Shi, Xu Wang, Eric Ouellet, Han Yun, Mitch Webb, Ben Nie, Zhen Liang, Karen C. Cheung, Shon A. Schmidt, Daniel M. Ratner, Nicolas A. F. Jaeger, *Silicon photonic resonator sensors and devices*, Proceedings of SPIE Volume 8236; Laser Resonators, Microresonators, and Beam Control XIV, 01/2012. (Graduate Work, International)

25. Jonas Flueckiger*, **Samantha M. Grist***, Eric Ouellet, Lukas Chrostowski, Karen C. Cheung, *Label-Free Biosensing Using Cascaded Silicon-on-Insulator Micro-Racetrack Resonators Integrated With PDMS Microfluidic Channels*, The 15th International Conference on Miniaturized Systems for Chemistry and Life Sciences, Seattle, Washington, USA, 10/2011. pp. 565-567. (Graduate Work, International)

26. Xu Wang*, Wei Shi, **Samantha Grist**, Han Yun, Nicolas A. F. Jaeger, Lukas Chrostowski, *Narrow-Band Transmission Filter using Phase-Shifted Bragg Gratings in SOI Waveguide*, IEEE Photonics Conference, pp. ThZ1, 10/2011 (Graduate Work, International)

c) Non-refereed contributions (5)

27. **Samantha M. Grist**, Linfen Yu, Carmen Bayly, Leaminn Ma, and Karen C. Cheung. *Microfluidic 3-D cell culture and control of microenvironment for high-throughput drug screening*. First annual BC Stem Cell and Regenerative Medicine Retreat, Vancouver, BC, Canada. January 2013. (Graduate Work)

28. Lukas Chrostowski, **Samantha M. Grist**, Shon Schmidt and Daniel Ratner. *Assessing silicon photonic biosensors for home healthcare*. SPIE Biomedical Optics and Imaging Article, SPIE Newsroom. doi: 10.1117/2.1201202.004131. March 1 2012. (Graduate Work)

29. Jonas Flueckiger*, **Samantha M. Grist**, Gurpal Bisra, Lukas Chrostowski, Karen C. Cheung, *Cascaded silicon-on-insulator microring resonators for the detection of biomolecules in PDMS microfluidic channels*, Proc. SPIE, Vol 7929; SPIE Microfluidics, BioMEMS, and Medical Microsystems IX, 01/2011. (Graduate Work)

30. **Samantha M. Grist***, Jonas Flueckiger, Jiali Yu, Wei Shi, Karen C. Cheung, Lukas Chrostowski, *Silicon-on-insulator resonators integrated with PDMS microfluidic channels for applications in biosensing*, Pacific Center for Advanced Materials and Microstructures (PCAMM) 15th Annual Meeting, 2010. (Graduate Work)

31. Miguel Guillen*, Han Yun, **Samantha Grist**, Xu Wang, Wei Shi, Robert Boeck, Charlie Li, Jiali Yu, Nicolas A. F. Jaeger, Lukas Chrostowski, *SOI Nanophotonics Fabrication Course*, Pacific Centre for Advanced Materials and Microstructures (PCAMM) Annual Meeting, 11/12/2010. (Graduate Work)